Optical Properties and Wave Propagation in Semiconductor-Based Two-Dimensional Photonic Crystals

by

Mario Agio

A thesis submitted to the graduate faculty

in partial fulfillment of the requirements for the degree of

DOCTOR OF PHILOSOPHY IN PHYSICS

Università degli Studi di Pavia
Pavia, Italy

Iowa State University
Ames, Iowa

Dottorato di Ricerca

– CICLO XV –

Dottorato di Ricerca
Università degli Studi di Pavia

Graduate College
Iowa State University

This is to certify that the doctoral thesis of

Mario Agio

has met the thesis requirements of Università degli Studi di Pavia and of Iowa State University

Supervisors:

Lucio C. Andreani

Costas M. Soukoulis

To Marta

TABLE OF CONTENTS

LIST OF TABLES v

LIST OF FIGURES vii

ABSTRACT xxi

INTRODUCTION 1

CHAPTER 1. PHOTONIC BANDS 11

1.1 History 11

1.2 Maxwell Equations for a Photonic Crystal 20

1.2.1 The Bloch-Floquet Theorem 23

1.2.2 The Band Structure 26

1.2.3 The Photonic Band Gap 28

1.2.4 The Plane-Wave Expansion Method 31

1.3 Two-Dimensional Photonic Crystals 34

1.3.1 The Band Structure 37

1.3.2 Symmetry Properties 41

1.4 Two-Dimensional Photonic-Crystal Slabs 46

1.4.1 Numerical Method 48

1.4.2 The Photonic Band Structure 51

1.4.3 Vertical Confinement Effects 54

1.4.4 Symmetry Properties 59

1.5 Linear Defects in Two-Dimensional Photonic Crystals 61

1.5.1 The Super-Cell Method 62

1.5.2 The Dispersion Relation 63

CHAPTER 2. OPTICAL PROPERTIES 67

2.1 History 69

2.2 The Variable-Angle Reflectance 70

2.2.1 Basic Ideas 71

2.2.2 The Scattering Matrix Method 74

2.2.3 Reflection, Transmission and Diffraction 83

2.3 Two-Dimensional Photonic Crystals 86

2.3.1 Macro-Porous Silicon Photonic Crystals 87

2.3.2 Reflectance and Selection Rules 89

2.4 Two-Dimensional Photonic-Crystal Slabs 95

2.4.1 The Air Bridge 96

2.4.2 GaAs-based Photonic Crystals 99

2.5 Out-of-Plane Losses 113

2.5.1 Vertical Confinement Effects 115

2.5.2 Dependence on the Filling Factor 117

2.5.3 Dependence on the Etch Depth 118

CHAPTER 3. WAVE PROPAGATION 121

3.1 History 122

3.2 The Finite-Difference Time-Domain Method 125

3.2.1 Basic Ideas 125

3.2.2 Finite-Difference Expressions for Maxwell's curl equations 128

3.2.3 Modelling Out-of-Plane Losses 131

3.3 GaAs- and InP-based Two-Dimensional Photonic Crystals 132

3.3.1 Fabrication Methods and Etch Depth 135

3.3.2 Validation of the Two-Dimensional Approximation 138

3.4 W1 and W3 Straight Waveguides 140

3.4.1 The W1 Waveguide 142

3.4.2 The W3 Waveguide 145

3.5 Bends in W1 and W3 Waveguides . . . 147
3.5.1 The W1 Waveguide . . . 149
3.5.2 The W3 Waveguide . . . 150
3.6 Modelling of Bends in W3 Waveguides . . . 152
3.6.1 Moving holes . . . 153
3.6.2 The Modal Transmission . . . 156
3.6.3 Taper . . . 159
3.6.4 Slits . . . 162
3.7 Splitters and Combiners . . . 166
3.7.1 Using W3 Waveguides . . . 167
3.7.2 Using W3 and W7 Waveguides . . . 170
3.7.3 Demonstrator . . . 171
CONCLUSIONS AND PERSPECTIVES . . . 177
BIBLIOGRAPHY . . . 183
ACKNOWLEDGEMENTS . . . 203

LIST OF TABLES

Table 3.1 Combiner designs for the demonstrator. 172

LIST OF FIGURES

Figure 1 An example of one-dimensional (1D) (left), two-dimensional (2D) (center) and three-dimensional (3D) (right) photonic crystal. Images taken from the book *Photonic crystals – molding the flow of light*, by Joannopoulos, J. D., *et al.* (1995). 2

Figure 2 Side view of a photonic-crystal slab. The light gray region is air, the black region is the core layer, and the gray-green region is the substrate. Air holes have been etched down to the substrate. 5

Figure 3 SEM micrograph of a dielectric photonic crystal waveguide; courtesy of Talneau, A., Laboratoire de Photonique et Nanostructures (LPN) - Centre National pour la Recherche Scientifique (CNRS), France. 6

Figure 1.1 Brillouin zone for the photonic crystals of Fig. 1: 1D (left), 2D (center), 3D (right). The bold lines represent the primitive vectors $\mathbf{g}_i$ of the reciprocal space. The gray shaded areas correspond to the irreducible Brillouin zone. . 27

Figure 1.2 The formation of a band gap in a 1D photonic crystal. Left: the multilayer as 1D photonic crystal; a is the lattice constant and l_1, l_2 are the thicknesses of the layers. Right: (a) Free-photon dispersion relation for a medium with $\epsilon_{\mathrm{d}} = 13$ folded in the 1D Brillouin zone. (b) Photonic bands of a multilayer; parameters: $\epsilon_1 = 11$, $\epsilon_2 = 13$ and $l_2/l_1 = 1$. n is the band index. 29

Figure 1.3 Top view of a 2D photonic crystal made of a triangular lattice of air holes, with radius r, in a medium with dielectric function ϵ (left panel). The corresponding 2D reciprocal space and the hexagonal Brillouin zone with symmetry points and lines (right panel). $a = |\mathbf{a}_i|$ is the direct space unit vector and $b = |\mathbf{g}_i|$ is the reciprocal space unit vector. 35

Figure 1.4 Even (a) and odd (b) modes with respect to a symmetry plane α. For in-plane propagation in a 2D photonic crystal, the electromagnetic field can be decomposed into H-modes (a) and E-modes (b). 36

Figure 1.5 Photonic bands of a 2D photonic crystal made of a triangular lattice of air holes, with radius $r = 0.3a$, in a dielectric medium with $\epsilon = 12$. Solid (dashed) lines refer to H-modes (E-modes). 37

Figure 1.6 Gap map for the photonic crystal of Fig. 1.5. The regions delimited by solid (dashed) lines refer to H-modes (E-modes). A complete photonic band gap opens for $r > 0.41a$ (gray shaded area). 40

Figure 1.7 Empty lattice bands for the photonic crystal shown in Fig. 1.3. The average dielectric constant is $\epsilon_{\|} = 10.4$, the lattice constant is $a = 3\mu$m and the energies are in electron-Volt (eV). The symmetry labels refer to E-modes. . 42

Figure 1.8 Photonic bands of the 2D photonic crystal of Fig. 1.3: (a) E-modes, (b) H-modes. The lattice constant is $a = 3\mu$m, the hole radius is $r = 0.2a$ and the material dielectric constant is $\epsilon = 12$. 43

Figure 1.9 Upper panels: (a) slab waveguide of thickness d patterned with a triangular lattice of air holes, (b) top view, (c) the 2D Brillouin zone with symmetry points. Lower panels: (d) strong-confinement symmetric waveguide, i.e. patterned self-standing dielectric membrane (*air bridge*), (e) weak-confinement symmetric waveguide (e.g. patterned *AlGaAs-GaAs-AlGaAs* system), (f) patterned asymmetric waveguide (e.g. *silicon-on-insulator*). . . 47

Figure 1.10 Left (right) panel: empty-lattice (photonic) bands for a self-standing dielectric membrane, patterned with a 1D lattice with air filling ratio $f = 30\%$. The width of the waveguide is $d/a = 0.5$ and the core dielectric function is $\epsilon = 12$. The dashed lines delimit the guided-mode region (white area) and refer to the dispersion of light in air and in the effective core material ($\epsilon = 8.7$). Light gray is for the leaky mode region, dark gray is where no solutions can exist. 51

Figure 1.11 Photonic bands for the air-bridge structure of Fig. 1.9d, with hole radius $r = 0.24a$. (a) Waveguide thickness $d = 0.3a$; (b) waveguide thickness $d = 0.6a$; (c) ideal 2D case. Solid (dashed) lines represent modes that are even (odd) with respect to the xy mirror plane. The dotted lines in (a) and (b) refer to the light lines in air and in the effective waveguide material. . . 54

Figure 1.12 Photonic bands for the weak-confinement structure of Fig. 1.9e, with hole radius $r = 0.24a$. (a) Waveguide thickness $d = 0.3a$; (b) $d = 0.6a$; (c) $d = 1.0a$. Solid (dashed) lines represent modes that are even (odd) with respect to the xy mirror plane. The dotted lines refer to the light lines in the effective core and cladding materials. 56

Figure 1.13 Gap maps for the air bridge structure of Fig. 1.9d. (a) Waveguide thickness $d = 0.3a$; (b) waveguide thickness $d = 0.6a$; (c) ideal 2D case. Solid (dashed) lines represent the edges of photonic bands that are even (odd) with respect to the xy mirror plane. The dotted line in (b) refers to the cut-off of the second-order waveguide mode. 57

Figure 1.14 Gap maps for the weak-confinement structure of Fig. 1.9e. (a) Waveguide thickness $d = 0.3a$; (b) $d = 0.6a$; (c) $d = 1.0a$. Solid (dashed) lines represent the edges of photonic bands that are even (odd) with respect to the xy mirror plane. 58

Figure 1.15 Left: a photonic crystal waveguide along the $\Gamma - K$ direction of a triangular lattice of air holes in a dielectric material. w defines the width of the waveguide, a is the lattice constant. Right: an example of super-cell for the calculation of the photon dispersion for this system. 62

Figure 1.16 Dispersion relation for the photonic crystal waveguide of Fig. 1.15 with $w = \sqrt{3}a$, $f = 60\%$, and $\epsilon_{\text{diel}} = 11.56$. The gray area is the projected band structure of the bulk photonic crystal. The solid lines correspond to guided H-modes that are spatially even with respect to the waveguide axis. 64

Figure 2.1 Description of the Variable-Angle Reflectance technique. Polarized monochromatic light impinges the surface of a 2D photonic crystal with an angle θ. The reflected beam contains information on the photonic modes of the system. The azimuth is chosen in order to sample the symmetry lines of the 2D Brillouin zone (the example regards a square lattice). 72

Figure 2.2 Experimental realization of the Variable-Angle Reflectance technique. The elliptical mirror allows to vary the angle of incidence θ. Courtesy of Galli, M., Università degli Studi di Pavia, Italy. 74

Figure 2.3 Kinematics of reflection r and diffraction d in air. The diffraction angles, θ' and ϕ', are determined by energy and momentum conservation. i is the incident beam with polar angles (θ, ϕ) and $\hat{\mathbf{n}}$ is the normal to the surface α. 81

Figure 2.4 TM-polarized transmission, reflection and diffraction for the air bridge one-dimensional photonic crystal of Fig. 1.10. Parameters: $\epsilon = 12$, $d = 0.5a$, and $f = 30\%$. Incident wave: $\theta = 50°$, $\phi = 0°$ and TM-polarization. Diffr. (R) and Diffr. (T) mean diffraction above and below the membrane, respectively. 84

Figure 2.5 Reflection and diffraction for the air bridge one-dimensional photonic crystal of Fig. 1.10. Parameters: $\epsilon = 12$, $d = 0.5a$, and $f = 30\%$. Incident wave: $\theta = 50°$, $\phi = 30°$ and TM-polarized. 85

Figure 2.6 AFM image of a macro-porous silicon photonic crystal (dimensions: $10 \times 8.4\mu$m). The lattice constant is $a = 2\mu$m and the hole radius is $r = 0.24a$. Courtesy of Patrini, M., Università degli Studi di Pavia, Italy, and Bettotti, P., Università degli Studi di Trento, Italy. 88

Figure 2.7 Calculated reflectance for the macro-porous silicon sample of Fig. 2.6 with TE polarized light incident along the $\Gamma - K$ orientation. The angle of incidence is varied from 5° to 60° with a step of 5°. Vertical bars mark the positions of 2D photonic modes for 5° and 60°. 90

Figure 2.8 (a),(c): experimental reflectance of the sample of Fig. 2.6 for light incident along the $\Gamma - K$ orientation, for TE and TM polarizations; courtesy of Galli, M., Università degli Studi di Pavia, Italy. (b),(d): calculated reflectance. The angle of incidence is varied from 5° to 60° with a step of 5°. The curves at 5°, 10° and 15° are slightly off-set for clarity. Inset to (b): diffracted intensity corresponding to the allowed mode at $\theta = 5°$ (onset marked by arrows). 91

Figure 2.9 Top panels: photonic bands of a triangular lattice of air holes in silicon with $a = 2\mu$m, $r = 0.24a$; (a) E-modes, (b) H-modes. 92

Figure 2.10 Measured dispersion of the photonic bands (points), derived from the structures in reflectance curves; the solid and dashed lines are the same photonic bands of Fig. 2.9, separated according to parity with respect to the plane of incidence: (a) TE polarization, odd modes, (b) TM polarization, even modes. The open triangles in (b) represent diffraction in air and must be compared with the folded free-photons dispersion (dotted lines). 94

Figure 2.11 Reflectance and photonic bands of the air bridge system of Fig. 1.9d, with thickness $d = 0.3a$ and hole radius $d = 0.24a$. (a) Calculated surface reflectance for a TM-polarized plane wave incident along the Γ-K orientation of the two-dimensional lattice. The angle of incidence is varied from $\theta = 0°$ to $\theta = 60°$ with a step of 5°. (b) Photonic bands. Lines represent the bands calculated from the expansion in waveguide modes, while points are extracted from the calculated reflectance. Solid lines and closed circles: even modes with respect to a vertical mirror plane $(\mathbf{k}, z)$, probed by TM-polarized light. Dashed lines and open circles: odd modes with respect to a vertical mirror plane $(\mathbf{k}, z)$, probed by TE-polarized light. The dotted line represents the dispersion of light in air. Both reflectance and photonic bands have been calculated employing 109 plane waves. 98

Figure 2.12 Cross-section of a typical GaAs-based photonic crystal. 100

Figure 2.13 (Left panels) The chessboard lattice: (a) dielectric rods in air, (b) air rods in dielectric. The dashed lines mark the unit cell, a is the lattice constant and b is the rod diagonal; (c) the Brillouin zone with symmetry points, Γ, X, M. (Right panel) Gap map for the chessboard-lattice two-dimensional photonic crystal for a background dielectric constant $\epsilon_{\text{diel}} = 12$. A black spot corresponds to the existence of a band gap for both polarizations. . . . 102

Figure 2.14 (a) SEM image of the chessboard lattice X-ray mask, with $a = 564$nm. (b) Detailed SEM image of the epitaxial AlGaAs slab after the etching process. Courtesy of Romanato, F. *et al.*, NNL - INFM, Italy. 103

Figure 2.15 Sample L2: unit cell (left) and SEM image (right). Courtesy of Romanato, F. *et al.*, NNL - INFM, Italy. 105

Figure 2.16 Experimental (a) and calculated (b) variable angle reflectance for TE-polarized light incident along the $\Gamma - M$ direction. The angle of incidence is varied in steps of 5°. The different curves are vertically shifted for clarity. Experimental data courtesy of Galli, M., Università degli Studi di Pavia, Italy. . . 106

Figure 2.17 Experimental (left panel) and calculated (right panel) photonic modes for different polarizations with respect to the plane of incidence: TE (blue), TM (red). The dotted lines represent the dispersion of light in air, in the core and cladding. 108

Figure 2.18 Sample RUN3: unit cell (left) and SEM image (right). Courtesy of Romanato, F. *et al.*, NNL - INFM, Italy. 109

Figure 2.19 Experimental (a) and calculated (b) variable angle reflectance for TE polarized light incident along the $\Gamma - X$ direction. The angle of incidence is varied in steps of 5°. The different curves are vertically shifted for clarity. Experimental data courtesy of Galli, M., Università degli Studi di Pavia, Italy. 110

Figure 2.20 Experimental (left panel) and calculated (right panel) photonic modes for different polarizations with respect to the plane of incidence: TE (blue), TM (red). The dotted lines represent the dispersion of light in air, in the core and cladding. 111

Figure 2.21 TM-polarized reflectance for a GaAs-based photonic crystal and a patterned air bridge. Both the air bridge and the GaAs/AlGaAs heterostructure are patterned with a triangular lattice of air holes, with $r = 0.24a$. Air bridge: air (semi-infinite), patterned core ($\epsilon = 12$, $d = 0.3a, 0.9a$), air (semi-infinite). GaAs/AlGaAs heterostructure: air (semi-infinite), patterned AlGaAs ($\epsilon = 11$, $d = 0.5a$), patterned GaAs ($\epsilon = 12$, $d = 0.3a, 0.9a$), patterned AlGaAs ($\epsilon = 11$, semi-infinite). Incident wave: $\theta = 50°$, $\phi = 0°$ and TM-polarized. For clarity, the curve corresponding to the $0.9a$-thick GaAs has been shifted upwards by 0.2. 114

Figure 2.22 TM-polarized reflectance as a function of the core thickness d/a for the air bridge and the GaAs/AlGaAs heterostructure described in the caption of Fig. 2.21: (top panel) air bridge, (bottom panel) GaAs/AlGaAs. For clarity, the curves for the air bridge are vertically shifted by 1.0 and those for the GaAs/AlGaAs waveguide by 0.1. Incident wave: $\theta = 50°$, $\phi = 0°$ and TM-polarized. 116

Figure 2.23 TM-polarized reflectance as a function of the hole radius r/a for the GaAs/AlGaAs heterostructure described in the caption of Fig. 2.21, where the GaAs core layer has now thickness $d = 0.9a$. For clarity, the reflectance curves are vertically shifted by 0.1. Incident wave: $\theta = 50°$, $\phi = 0°$ and TM-polarized. 117

Figure 2.24 TM-polarized reflectance as a function of the etch depth h/a for a GaAs/AlGaAs heterostructure: air (semi-infinite), patterned AlGaAs ($\epsilon = 11$, $d = 0.5a$), patterend GaAs ($\epsilon = 12$, $d = 0.9a$), patterned AlGaAs ($\epsilon = 11$, $h/a = 0.5 - \infty$) and AlGaAs substrate ($\epsilon = 11$, semi-infinite). All patterned layers have air holes with radius $r = 0.32a$. For clarity, the reflectance curves are vertically shifted by 0.09. Incident wave: $\theta = 50°$, $\phi = 0°$ and TM-polarized. 119

Figure 3.1 Positions of the H-polarized field components for the central-difference derivatives. Each field component is defined on a uniform rectangular mesh with displacements Δx and Δy. Each mesh is shifted by $\Delta x/2$ or $\Delta y/2$ from the others so that if H_z is positioned at the lattice points $(i, i\pm1, \ldots, i\pm m; j, j\pm 1, \ldots, j\pm n)$, E_x will be at $(i, i\pm1, \ldots, i\pm m; j+1/2, j+1/2\pm1, \ldots, j+1/2\pm n)$ and E_y at $(i+1/2, i+1/2\pm1, \ldots, i+1/2\pm m; j, j\pm1, \ldots, j\pm n)$. 127

Figure 3.2 FDTD simulation of a simple crystal along the $\Gamma - M$ direction. A plane wave is launched from the left (arrow) and it is collected by a line detector (D) after the photonic crystal. The black-thick edges truncate the computational mesh using Liao absorbing boundary conditions. The other edges use Bloch boundary conditions. 130

Figure 3.3 InP/GaInAsP waveguide heterostructure. Two strain-compensated GaInAsP quantum wells emitting at two different near-infrared wavelengths are embedded in the core layer. Courtesy of Ferrini, R., EPFL, Switzerland. 134

Figure 3.4 Refractive index profile of the InP/GaInAsP waveguide heterostructure of Fig. 3.3 and squared field profile $\zeta^2(z)$ of the fundamental TE mode calculated for $\lambda = 1.55\mu$m. Courtesy of Ferrini, R., EPFL, Switzerland. 134

Figure 3.5 SEM micrographs of a photonic crystal with lattice constant a=400nm fabricated using CAIBE etching. The images were taken before the SiO_2 mask removal. Courtesy of Ferrini, R., EPFL, Switzerland, Mulot, M., KTH, Sweden, and Talneau, A., LPN - CNRS, France. 136

Figure 3.6 Examples of simple two-dimensional photonic crystals. 138

Figure 3.7 3D vs 2D FDTD simulations. Transmission along the $\Gamma-K$ direction for a 8-unit-cell long photonic crystal; H-polarization. Parameters of the 2D FDTD simulation: $\epsilon = 10.3$, $f = 38\%$ and $\epsilon'' = 0.05$ (0.12) for the cylindrical-hole (conical-hole) case; 3D FDTD simulation: $f = 35\%$, a=420nm, etch-depth=2.5μm and index profile taken from Fig. 3.4. 3D calculations courtesy of Kasesaki, M., IESL - FORTH, Crete, Greece. 138

Figure 3.8 (a) FDTD simulation of a W3 photonic crystal waveguide. The source (S) has a Gaussian profile perpendicular to the waveguide axis. The detector (D) covers the exit of the waveguide. The edges of the computational mesh are terminated with Liao absorbing boundary conditions (black). (b) SEM micrograph of a W1 waveguide; courtesy of Talneau, A., LPN - CNRS, France. 141

Figure 3.9 Transmission spectra for various lengths of the W1 waveguide described in section 1.5.2: H-polarization, $\epsilon = 11.56$, and $f = 60\%$ (as in Fig. 1.16). The bold solid (dotted) line delimits the $\Gamma-K$ ($\Gamma-M$) H-modes band gap of the bulk photonic crystal. The solid, dotted, and dashed lines correspond to the transmission along the waveguide with length $10a$, $30a$, and $60a$, respectively. 143

Figure 3.10 Normalized intensity of the electric field for the frequencies corresponding to the low-frequency mini-stop band (a) and high-frequency mini-stop band (b) of Fig. 3.9. 144

Figure 3.11 (a) Dispersion relation for a W3 waveguide, with $\epsilon = 10.5$, and $f = 35\%$. The solid lines refer to H-modes that are spatially even with respect to the waveguide axis; the odd modes are not shown. The gray areas are the projected H-modes of the bulk photonic crystal. (b) H-polarized transmission for the same W3 waveguide of length $40a$ and loss parameter $\epsilon'' = 0.1$. . . . 146

Figure 3.12 Sharp bends in W1 and W3 waveguides. 147

Figure 3.13 (a) The same dispersion relation of Fig. 1.16. Solid (dotted) lines refer to H-modes that are spatially even (odd) with respect to the waveguide axis. (b) Normalized intensity of the electric field at $a/\lambda = 0.2607$ for a sharp bend in a W1 waveguide. Structure parameters as in Fig. 1.16. 149

Figure 3.14 (a) The same dispersion relation of Fig. 3.11a. Solid (dotted) lines refer to H-modes that are spatially even (odd) with respect to the waveguide axis. (b) Normalized intensity of the electric field at $a/\lambda = 0.2297$ for a sharp bend in a W3 waveguide. Structure parameters as in Fig. 3.11. Note: in this case $\epsilon = 11.56$ instead of 10.5. 150

Figure 3.15 Smoothing a bend moving holes at the corner. 152

Figure 3.16 Experimental spectra (black curves) and calculated spectra (gray curves) for a corresponding set of bend designs (left panels). From top to bottom: sharp bend, one-hole-moved, three-holes-moved. The gray areas refer to the mini-stop band region. The simulations were performed choosing $\epsilon = 10.5$, $f = 35\%$, and $\epsilon'' = 0.1$. The calculated spectra were slightly stretched to fit the experiments, yielding an effective dielectric function $\epsilon = 10.4$ instead of 10.5. The experimental data are courtesy of Moosburger, J., University of Würzburg, Germany and Olivier, S., EPP, France. 153

Figure 3.17 Experimental spectra (black curves) and calculated spectra (gray curves) for a corresponding set of bend designs (right panels). From top to bottom: six-holes-moved, ten-holes-moved, fifteen-holes-moved. The gray areas refer to the mini-stop band region. The simulations were performed choosing $\epsilon = 10.5$, $f = 35\%$, and $\epsilon'' = 0.1$. The calculated spectra were slightly stretched to fit the experiments, yielding an effective dielectric function $\epsilon = 10.4$ instead of 10.5. The experimental data are courtesy of Moosburger, J., University of Würzburg, Germany and Olivier, S., EPP, France. 154

Figure 3.18 Modal transmission for a three-holes-moved bend (a) and a ten-holes-moved bend (b). The black line refer to the total transmission. The red (blue) line corresponds to the transmission into spatially even (odd) modes with respect to the waveguide axis. Parameters: $\epsilon = 10.5$, $f = 35\%$, and $\epsilon'' = 0.1$. 157

Figure 3.19 Poynting vector as a function of frequency and distance from the waveguide axis for the transmission into spatially even modes. y=1 corresponds to $y = 3\sqrt{3}/2a$. (a) three-holes-moved bend; (b) ten-holes-moved bend. Parameters as in Fig. 3.18. 158

Figure 3.20 (a) SEM micrograph of a W3 $\rightarrow$ W1 tapering section; courtesy of Talneau, A., LPN - CNRS, France. (b) Dispersion relation for a W1-30% waveguide (left panel) and a W3 waveguide (right panel). Solid (dashed) lines refer to spatially even (odd) H-modes with respect to the waveguide axis. Photonic-crystal parameters: $\epsilon = 10.5$, $f = 40\%$. 160

Figure 3.21 Normalized intensity of the electric field through a tapered sharp bend connecting two W3 waveguides. Parameters: $a/\lambda = 0.2515$, $\epsilon = 10.5$, $f = 40\%$ and $\epsilon'' = 0$. 161

Figure 3.22 (a) A one-hole-moved double bend in a W3 waveguide. (b) Left panel: one-slit bend design; right panel: two-slits bend design. 162

Figure 3.23 (a) Transmission through a double bend in a W3 waveguide. The black line refers to the two-slits bend design. The red (blue) line corresponds to the one-slit (three-holes-moved) bend design. Parameters: $\epsilon = 10.5$, $f = 38\%$ and $\epsilon'' = 0.1$. (b) Normalized intensity of the electric field at $a/\lambda = 0.2487$ for the one-slit design. 163

Figure 3.24 (a) Slit-taper bend designs. (b) Normalized intensity of the electric field at $a/\lambda = 0.24$ for a slit-taper double bend. Parameters: $\epsilon = 10.5$, $f = 38\%$ and $\epsilon'' = 0.05$. 164

Figure 3.25 (a) Transmission through a slit-taper double bend in a W3 waveguide. The black (red) line refers to the total transmission for $\epsilon'' = 0.05$ ($\epsilon'' = 0.1$). The blue (orange) line corresponds to the even and odd transmission for $\epsilon'' = 0.1$. (b) Poynting vector as a function of frequency and distance from the waveguide axis for the transmission into spatially even modes. y=1 corresponds to $y = 3\sqrt{3}/2a$. Parameters: $\epsilon = 10.5$, $f = 38\%$ and $\epsilon'' = 0.1$. . 165

Figure 3.26 (a) Combiner/splitter with W3 waveguide sections. (b) Experimental spectra (black curves) and calculated spectra (gray curves) for a bend and a splitter respectively (right panels). The transmission for the splitter has been multiplied by a factor of 2. The gray areas refer to the mini-stop band region. The simulations were performed choosing $\epsilon = 10.5$, $f = 35\%$, and $\epsilon'' = 0.1$. The calculated spectra were slightly stretched to fit the experiments, yielding an effective dielectric constant ϵ=10.4 instead of 10.5. The experimental data are courtesy of Moosburger, J., University of Würzburg, Germany and Olivier, S., EPP, France. 168

Figure 3.27 (a) Splitter transmission for the system of Fig. 3.26a; i.e. $\mathbf{B} \rightarrow \mathbf{A}$ or $\mathbf{B} \rightarrow \mathbf{C}$. The transmission has been multiplied by a factor of 2. (b) Combiner transmission for the system of Fig. 3.26a for three, six and ten holes displaced at the junction. $\mathbf{A} \rightarrow \mathbf{B}$ transmission (top) and $\mathbf{A} \rightarrow \mathbf{C}$ transmission (bottom). Parameters: $\epsilon = 10.5$, $f = 35\%$, and $\epsilon'' = 0.1$. 169

Figure 3.28 W3 $\rightarrow$ W7 slit combiner: (a) structure, (b) transmission. The solid (dashed) line correspond to $\mathbf{A} \rightarrow \mathbf{B}$ ($\mathbf{A} \rightarrow \mathbf{C}$) transmission. Parameters: $\epsilon = 10.5$, $f = 35\%$, and $\epsilon'' = 0.1$. 170

Figure 3.29 SEM micrograph of the combiner used for the multi-wavelength photonic crystal laser; courtesy of Happ, T., University of Würzburg, Germany. . . . 171

Figure 3.30 Combiner slit designs: (a) W3W7s, (b) W3W3s. 172

Figure 3.31 Transmission (a) and cross-talk (b) for the demonstrator combiners. Parameters: $\epsilon = 10.5$, $f = 38\%$, and $\epsilon'' = 0.1$. 173

Figure 3.32 W3W3s combiner design: even/odd transmission. Parameters: $\epsilon = 10.5$, $f = 38\%$, and $\epsilon'' = 0.1$. 174

Figure 3.33 W3W3s combiner design: field pattern for $a/\lambda = 0.287$. Parameters: $\epsilon = 10.5$, $f = 38\%$, and $\epsilon'' = 0.1$. 174

ABSTRACT

This work is a theoretical investigation on the physical properties of semiconductor-based two-dimensional photonic crystals, in particular for what concerns systems embedded in planar dielectric waveguides (GaAs/AlGaAs, GaInAsP/InP heterostructures, and self-standing membranes) or based on macro-porous silicon. The photonic-band structure of photonic crystals and photonic-crystal slabs is numerically computed and the associated light-line problem is discussed, which points to the issue of intrinsic out-of-plane diffraction losses for the photonic bands lying above the light line. The photonic states are then classified by the group theory formalism: each mode is related to an irreducible representation of the corresponding small point group. The optical properties are investigated by means of the scattering matrix method, which numerically implements a variable-angle-reflectance experiment; comparison with experiments is also provided. The analysis of surface reflectance proves the existence of selection rules for coupling an external wave to a certain photonic mode. Such rules can be directly derived from symmetry considerations. Lastly, the control of wave propagation in weak-index contrast photonic-crystal slabs is tackled in view of designing building blocks for photonic integrated circuits. The proposed designs are found to comply with the major requirements of low-loss propagation, high and single-mode transmission. These notions are then collected to model a photonic-crystal combiner for an integrated multi-wavelength-source laser.

INTRODUCTION

Since the pioneering works of Yablonovitch, E. (1987) and John, S. (1987) on inhibited spontaneous emission and on light localization in periodic dielectric structures, respectively, the term *photonic crystal* has been the appellation for any system characterized by a dielectric function ϵ that is periodic in one or more dimensions, as shown in Fig. 1. Accordingly, the classification into one-, two-, or three-dimensional photonic crystals depends on whether ϵ is periodic in one, two, or three dimensions. A typical example of one-dimensional photonic crystal is the so-called Bragg mirror, which has been studied since a long time before the proposal of Yablonovitch, E. and John, S. [Yariv, A., *et al.* (1984)] and, nowadays, is employed in several optical and optoelectronic devices. Except this case, poor research was done on the physics of periodic dielectric structures, if compared to the intense research activity that started after 1987 and still grows every year. Indeed, since the very beginning, photonic crystals appeared as promising candidates for applications in various areas of optics and optoelectronics. Just for the sake of curiosity, mother nature, as often does, already knows how to exploit photonic crystals, for instance to make beautiful wings for butterflies or beautiful opals for ladies. However, apart a few other examples, photonic crystals are not so common in nature and they can be thus considered as artificial materials. For example, as shown in Fig. 1, a photonic crystal can be simply fabricated by arranging two different dielectric media according to a desired pattern.

The idea that leads to the concept of photonic crystal can be easily understood by following the analogy between photons in a periodic dielectric potential and electrons in a crystal. It is well known [Bassani, F., *et al.* (1975); Cardona, M., *et al.* (1996)] that the periodicity of the electronic potential is the reason for the existence of the electronic band structure. Therefore, like a periodic potential leads to allowed bands and band gaps for electrons, for photons, a periodic dielectric function leads to the so-called *photonic bands* and *photonic band gap*. A photonic band refers to

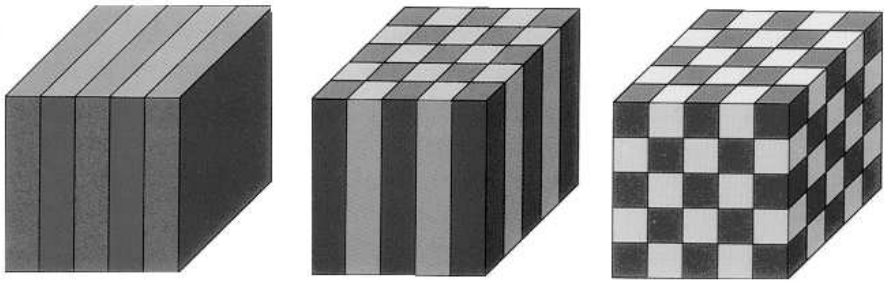

Figure 1 An example of one-dimensional (1D) (left), two-dimensional (2D) (center) and three-dimensional (3D) (right) photonic crystal. Images taken from the book *Photonic crystals – molding the flow of light*, by Joannopoulos, J. D., *et al.* (1995).

modes that can propagate inside the photonic crystal, while the photonic band gap represents a frequency domain, where photons cannot exist. Indeed, one of the most attracting features of photonic crystals is the existence of a photonic band gap, because of the possibility to control the electromagnetic radiation. For example, the spontaneous emission of atoms embedded in a photonic crystal can be inhibited, if the emission frequency lies within the photonic band gap [Yablonovitch, E. (1987); Koenderink, A. F., *et al.* (2002)]. On the contrary, the emission pattern can be enhanced or reshaped by photonic-band-structure effect [Fan, S., *et al.* (1998); Busch, K., *et al.* (2000); Erchak, A. A., *et al.* (2001)]. Also, the band gap can be exploited to fabricate high reflective mirrors, which is in fact the principle of operation of a Bragg mirror.

Ideally, the photonic band gap is in one, two, or three dimensions depending on the periodicity of the dielectric function, though the rule is not valid for any structure. Now, the fact that photonic crystals are artificial materials opens infinite possibilities on the choice of the dielectric pattern. Furthermore, by designing defects in the otherwise periodic structure, one wishes to create defect states within the photonic band gap. Roughly speaking, according to the dimensionality of the defect itself and to the dimensionality of the photonic band gap, various degrees of light localization can be obtained [Joannopoulos, J. D., *et al.* (1995, 1997)]: for three-dimensional photonic crystals, a point defect represents a three-dimensional cavity, a linear defect acts like a waveguide, while a planar defect is, accordingly, a planar waveguide; similarly, for a two-dimensional photonic crystal, a point defect (in the plane of periodicity) makes a two-dimensional cavity, and a linear defect

forms a planar waveguide. Finally, for a one-dimensional photonic crystal, a point defect (along the direction of periodicity) is in practice a Fabry-Pérot resonator between two Bragg mirrors. Thus, all the above functionalities are implemented by appropriate tailoring of a photonic band gap material. This concept envisages that several optical components (resonators, waveguides, add/drop filters, splitters, combiners, lasers, etc.) could be designed on a single photonic-crystal chip to process optical signals just like "conventional" chips do for electrical pulses. Such a powerful expression of the potentiality of photonic crystals is one of the motivations that make them so attracting to physicists, engineers... and to managers. Following a roadmap towards the fabrication of photonic integrated circuits, the recently past years have provided important results as regards theory and experiment of passive and active photonic-crystal building blocks: micro-cavities [Villeneuve, P. R., *et al.* (1996); Foresi, J. S., *et al.* (1997); Painter, O., *et al.* A (1999); Pottier, P., *et al.* (1999); Benisty, H., *et al.* (1999); Kramper, P., *et al.* (2001)], straight waveguides [Baba, T., *et al.* (1999, 2001); Lončar, M., *et al.* B (2000); Johnson, S. G., *et al.* (2000); Leonard, S. W., *et al.* (2000); Olivier, S., *et al.* A (2001); Talneau, A., *et al.* (2001)], bent waveguides [Mekis, A., *et al.* (1996); Lin, S.-Y., *et al.* B (1998); Tokushima, M., *et al.* (2000); Lončar, M., *et al.* A (2000); Chutinan, A., *et al.* (2000, 2002); Chow, E., *et al.* (2001); Moosburger, J., *et al.* (2001); Talneau, A., *et al.* B (2002)], add/drop filters [Fan, S., *et al.* (1998, 1999); Boscolo, S., *et al.* (2002)], and lasers [Ryu, H.-Y., *et al.* (2002); Shkunov, M. N., *et al.* (2002); Cao, J. R., *et al.* (2002); Imada, M., *et al.* (2002)].

Besides the objective of making integrated optical circuits, photonic crystals are interesting for other reasons too. For instance, there are efforts to exploit the band gap properties for fabricating low-loss photonic-crystal fibers. By leaving for a moment the physics related to the existence of a photonic band gap, one realizes that also photonic bands exhibit important features. Indeed, the photonic band structure is characterized by a variety of dispersion curves that makes the electromagnetic properties of photonic crystals quite unique. The possibility of tailoring the dispersion of light, by working on the structure design, leads to the availability of artificial media, with peculiar features. In this sense, photonic crystals may enhance the separating power of a prism, making a super-prism [Kosaka, H., *et al.* (1998)], or exhibit an anomalous refraction behavior [Notomi, M, *et al.* (2000); Luo, C., *et al.* (2002); Pertsch, T., *et al.* (2002)]. In a similar manner, the

band dispersion can be designed to provide a dielectric lens able to focus light down to micron-size spots [Kosaka, H., *et al.* (2000)]. The dispersion properties of photonic crystals are also interesting in non-linear optics for obtaining phase-matching and enhancement of second- or third-harmonic generation [Martorell, J., *et al.* (1997); Cowan, A. R., *et al.* (2002); Dumeige, Y., *et al.* (2002)]. In this case, the photonic crystal has to be made of a periodic arrangement of at least one non-linear medium [Berger, V. (1998)].

The implementation of such beautiful ideas relies on a deep knowledge of the physical properties of photonic crystals. Many efforts have been devoted to theory, experiment and fabrication of these artificial materials [see the feature issues *J. Opt. Soc. Am. B, 10* (2); *J. Opt. Soc. Am. B, 19* (9); *J. Lightwave Technol., 17* (11); *IEEE J. Quantum Electronics, 38* (7) and the *NATO - ASI* conference proceedings edited by Weisbuch, C., and Rarity, J. (1996); Soukoulis, C. M. (1996, 2001) for a collection of papers]. While theorists have to face the fundamental problem of solving Maxwell's equation [Jackson, J. D. (1975)] for a variety of photonic crystals, with or without defect states, experimentalists are committed with the not easy task of characterizing the samples and discovering new effects not accounted by theory. Last but not least, fabricators have to methods for obtaining regular dielectric patterns with the desired shape. These objectives are particularly challenging, specially for what concerns experiment and fabrication, if one wants photonic crystals to operate at the telecommunication wavelength of 1.55μm or, in general, in the frequency domain of optical and optoelectronic devices. Indeed, this implies that the lattice constant of the dielectric mesh shrinks down to a few microns up to a few hundreds of nanometers, since the band-gap effects are effective for wavelengths comparable or smaller than the periodicity of the dielectric constant. To this purpose, even if much attention has been devoted to the problem of finding three-dimensional structures that forbid light propagation in all directions [Leung, K. M., *et al.* B (1990); Ho, K. M., *et al.* (1990, 1994); Yablonovitch, E., *et al.* (1991); Busch, K., *et al.* (1998)], in particular, with noticeable achievements for artificial opals [Thijssen, M. S., *et al.* (1999); Blanco, A., *et al.* (2000); Vlasov, Y. A., *et al.* (2001)], two-dimensional photonic crystals have attracted more interest [Meade, R. D., *et al.* (1992); Villeneuve, P. R., *et al.* (1992); Padjen, R., *et al.* (1994); Cassagne, D., *et al.* (1996); Anderson, C. M., *et al.* (1997); Li, Z.-Y., *et al.* (1998); Wang, X.-H., *et al.* (1999); Agio, M. (1999); Agio, M., *et al.* A (2000)], though they allow to control light only

in two dimensions, because they are much easier to fabricate in the optical region. Nevertheless, by embedding a two-dimensional photonic crystal in a waveguide configuration [Meade, R. D., *et al.* (1994)], one attains both in-plane control of light propagation, by means of the two-dimensional band gap, and vertical control, by conventional dielectric confinement [Saleh, B. E. A., *et al.* (1991)]. The above concept is particularly suitable for being implemented in semiconductor heterostructures, where the desired two-dimensional pattern is transferred to the planar waveguide by lithographic etching [Gourley, P. L., *et al.* (1994); Krauss T. F., *et al.* (1996); Chow, E., *et al.* (2000); Sondergaard, T., *et al.* (2000); Silvestre, E., *et al.* (2000); Kawai, N., *et al.* (2001); Romanato, F., *et al.* (2002); Peyrade, D., *et al.* (2002)]. As displayed in Fig. 2, a typical waveguide-based two-dimensional photonic crystal is composed by a guiding layer (black), sandwiched between two low-index materials, in this case air (light-gray) and the substrate (gray-green). Whereas the pattern controls the flow of light in two dimensions, the presence of a core layer provides vertical confinement. Such feature places photonic crystal slabs in between three- and two-dimensional photonic crystals.

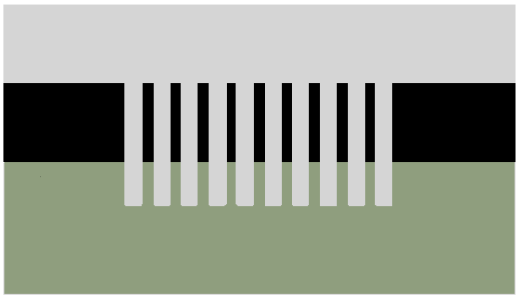

Figure 2 Side view of a photonic-crystal slab. The light gray region is air, the black region is the core layer, and the gray-green region is the substrate. Air holes have been etched down to the substrate.

The fabrication of micron-size two-dimensional photonic-crystal waveguides based on Si/SiO_2, GaAs/AlGaAs, GaInAsP/InP and other common semiconductor heterostructures, has made possible the measurement of photonic bands in the near-infrared frequency domain [Labilloy, D., *et al.* A (1997); Astratov, V. N., *et al.* A (1999); Astratov, V. N., *et al.* (2000); Pacradouni, V., *et al.* (2000); Coquillat, D., *et al.* (2001); Galli, M., *et al.* B (2002); Patrini, M., *et al.* A (2002); Ferrini, R., *et al.* (2002)]. Likewise, the characterization of photonic-crystal channel

waveguides in the near-infrared regime, see the SEM micrograph of Fig. 3, including sharp bends or resonant cavities, has been attained thanks to the availability of the appropriate samples and refined experimental techniques [Foresi, J. S., *et al.* (1997); Lin, S.-Y., *et al.* B (1998); Pottier, P., *et al.* (1999); Baba, T., *et al.* (1999, 2001); Benisty, H., *et al.* (1999); Benisty, H., *et al.* B (2002); Tokushima, M., *et al.* (2000); Lončar, M., *et al.* B (2000); Smith, C. J. M., *et al.* (2000); Chow, E., *et al.* (2001); Moosburger, J., *et al.* (2001); Talneau, A., *et al.* A (2002)].

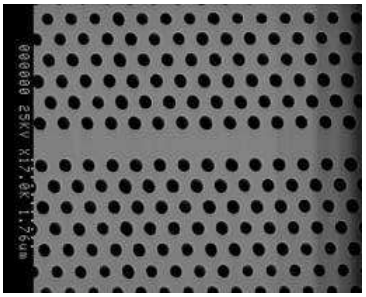

Figure 3 SEM micrograph of a dielectric photonic crystal waveguide; courtesy of Talneau, A., Laboratoire de Photonique et Nanostructures (LPN) - Centre National pour la Recherche Scientifique (CNRS), France.

However, embedding two-dimensional photonic crystals in a waveguide configuration has raised serious issues that, in part, have yet to be solved. First of all, the calculation of the photonic band structure has to account for the vertical profile of the planar waveguide. To this purpose, theorists have devised numerical techniques [Johnson, S. G., *et al.* (1999, 2000); Lončar, M., *et al.* A (2000); Ochiai, T., *et al.* A (2001); Andreani, L. C. (2002)], to overcome the impossibility of treating photonic-crystal slabs with the conventional *plane-wave expansion method* [John, S., *et al.* (1988); Leung, K. M., *et al.* B (1990); Ho, K. M., *et al.* (1990)], which represents the standard for computing the mode dispersion in bulk photonic crystals. Secondly, the photonic-crystal pattern has the effect of coupling the guided modes of the system to radiation modes, whenever the corresponding bands lie above the light lines of the cladding media (often air and dielectric substrate); in other words the spectrum of a photonic-crystal slab is composed by truly guided modes, below the light line, and resonances, above the light line, which are also called quasi-guided modes. Since quasi-guided modes are subject to intrinsic propagation losses [D'Urso, B., *et al.* (1998); Benisty, H., *et al.* (1999); Lalanne, Ph., *et al.* (2001); Bogaerts, W., *et al.* (2001); Ochiai, T., *et al.* A (2001)] one

would rather choose to work with truly guided modes. Unfortunately, truly guided modes are supported by almost only photonic-crystal slabs with a high-index contrast between core and cladding, like a suspended dielectric membrane (air bridge) [Kawai, N., *et al.* (2001)], a silicon-on-insulator waveguide [Baba, T., *et al.* (2001)] or a GaAs/Al_2O_3 waveguide [Chow, E., *et al.* (2000)]; on the other hand, photonic crystals based on weak-index-contrast heterostructures, like GaAs/AlGaAs [Krauss T. F., *et al.* (1996)] or GaInAsP/InP [Ferrini, R., *et al.* (2002)] can support only quasi-guided modes. Since propagation losses represent an unwanted feature, the solution seems to be simple: fabricate photonic crystals using strong-confinement waveguides. However, the picture is not as trivial as it appears. Indeed, any time that a guided mode encounters a defect, be a bend, a resonant cavity or simply roughness, some power is lost because of the defect that couples to radiation modes. Now, a photonic-crystal integrated circuit is definitely plenty of defects, which are there to accomplish a precise functionality. In this case, also by employing strong-confinement waveguides, one expects to have losses. Since it has been argued that losses are proportional to the square power of the dielectric contrast between core and cladding [Benisty, H., *et al.* (2000)], the situation gets blurred: is it better to employ strong-confinement photonic-crystals, which support guided modes, though lead to higher losses in correspondence of defects, or better to choose for weak-confinement photonic-crystals, whose quasi-guided modes exhibit reasonable losses with or without defects? The question is challenging and the photonic-crystal research community has yet to find which is the correct answer. Indeed, besides the difficulty of calculating the amount of losses, which became possible only very recently [Lalanne, Ph., *et al.* (2001); Ochiai, T., *et al.* A (2001); Bogaerts, W., *et al.* (2001)] there are many aspects that one has to consider for designing the optimal photonic-crystal structure, for example the ease of fabrication. All in all, much depends on what purpose the sample is made for. However, it is clear that the previously cited results on waveguides, bends and resonant cavities have to be weighted with the awareness that the way towards a *"killer" application*, which will make photonic crystals enter our everyday life, likewise the transistor did for silicon about fifty years ago, might be still long.

The present work would like to contribute to the frenzied research in this area, by offering some results on the optical properties and on wave propagation in semiconductor-based two-dimensional

photonic crystals. The aim is to lead the reader from the basic concepts that are with the photonic band picture, up to the modelling issues of complex building blocks for photonic-integrated circuits, with emphasis on the guiding and optical properties of quasi-guided modes. Particular attention is devoted to highlighting differences or similarities between two-dimensional photonic crystals and two-dimensional photonic-crystal slabs, in particular, as regards the photonic band structure, the symmetry properties and the selection rules that concern the coupling to radiative modes. The wish is to provide strong arguments to convince the reader that quasi-guided modes may be effectively harnessed in both fundamental research and photonic-crystal applications: their dispersion can be very efficiently measured by surface reflectance [Astratov, V. N., *et al.* A (1999)], making the characterization of samples easier than with other methods [Yablonovitch, E., *et al.* (1989); Robertson, W. M., *et al.* A (1993); Labilloy, D., *et al.* (1999)], specially in the near-infrared/optical regime; with the same technique, one can have a direct insight on the selection rules and, thus, on the symmetry properties of quasi-guided modes [Ochiai, T., *et al.* A (2001); Andreani, L. .C., *et al.* (2001); Galli, M., *et al.* B (2002)]; finally, the surface reflectance can also provide information of their guiding properties [Galli, M., *et al.* B (2002)]. In other words, one could say that quasi-guided modes are "optically active", in the sense that they do respond to an optical excitation, while guided modes are "hidden" below the light cone and are thus more difficult to access. For what concerns wave propagation, the quasi-guided modes of weak-confinement photonic crystals may be better than guided modes for the reasons discussed in the previous paragraph. Moreover, since weak-confinement implies that the mode dispersion be similar to that of an ideal two-dimensional photonic crystal [Andreani, L. C. (2002); Qiu, M. (2002); Kafesaki, M., *et al.* (2002)], one could take advantage of such feature, to model wave propagation in weak-confinement photonic-crystal slabs within a two-dimensional approximation [Qiu, M. (2002)], with obvious benefits.

The work is organized into three chapters. Each chapter begins with a bibliographic review on the arguments that will be discussed in there. The intention is to provide the reader with some background, before tackling the inner sections. The first chapter is dedicated to the study of the photonic band structure of two-dimensional photonic crystals and photonic-crystal slabs, with emphasis on vertical-confinement effects and on the symmetry properties of the energy eigenstates.

The concept of quasi-guided mode is also introduced. The last section briefly discusses linear defects in two-dimensional photonic crystals, whose concepts will be recalled and extended while dealing with wave propagation. The second chapter carries on the comparison between photonic crystals and photonic-crystal slabs, by dealing with the optical properties and the determination of the photonic band structure by means of the surface-reflectance method, proposed by Astratov, V. N., *et al.* A (1999). Moreover, the selection rules for coupling to external radiation are discussed. Finally, surface reflectance is employed for studying the dependence of the propagation losses of quasi-guided modes on the waveguide geometry. This analysis leads to the third chapter, which entirely concerns wave propagation of quasi-guided modes in weak-confinement photonic-crystal slabs, based on GaAs/AlGaAs and GaInAsP/InP heterostructures. Starting from the transmission properties of straight channel waveguides, like the one of Fig. 3, the study is then extended to waveguides with sharp bends. The discussion is centered on the issue of attaining single-mode transmission in multi-mode waveguides, because they exhibit lower propagation losses than single-mode waveguides. To this purpose, several bend designs are investigated. After that, the attention is focussed on other building blocks, like splitters and combiners. The final objective is to gather these results in the design of a photonic-crystal combiner for a multi-wavelength-source laser, which would aim to demonstrate the feasibility of photonic-crystal devices for integrated optics.

Much of the results of Chapter 2 have been carried out thanks to various collaborations and projects on the optical properties of one- and two-dimensional photonic crystals. Macro-porous silicon samples have been grown by the group of Pavesi L. at the Department of Physics, Università degli Studi di Trento, Italy, in the framework of a MIUR-Cofin 2000 project involving Trento and Pavia. GaAs-based photonic-crystal slabs (samples L2 and RUN3) have been fabricated by the groups of Di Fabrizio E. and De Vittorio M. at National Nanotechnology Laboratory (NNL) - Istituto Nazionale di Fisica della Materia (INFM), Italy, within an INFM-PAIS 2001 research project involving Lecce, Trieste and Pavia. The variable-angle-reflectance experiments have been performed by the groups of Guizzetti G. and Marabelli F. at the Department of Physics "A. Volta", Università degli Studi di Pavia, Italy, while the theoretical work is by Andreani L. C. and Agio M., always at the Department of Physics "A. Volta".

Chapter 3, instead, partially reports on the activity of a European Union Information Societies Technology (IST) program, whose acronym is Photonic Crystal Integrated Circuits (PCIC), which involves eight institutions: Ecole Polytechnique de Palaiseau (EPP), France; Ecole Polytechnique Fédérale de Lausanne (EPFL), Switzerland; Würzburg Universität, Germany; RIEE, Prague; Laboratoire de Photonique et Nanostructures (LPN) - Centre National pour la Recherche Scientifique (CNRS), France, Opto+ - Alcatel, France; Kungl Tekniska Högskolan (KTH), Sweden; and Institute of Electronic Structures and Lasers (IESL) - Foundation for Research and Technology Hellas (FORTH), Crete, Greece. The objective of the research project is to put the bases for making photonic-integrated circuits employing InP-based photonic crystals. For what concerns the results discussed in Chapter 3, the InP-samples have been grown by Mulot, M. *et al.* at KTH, Sweden, Thomas H. *et al.* at Würzburg Universität, Germany and people from Opto+ - Alcatel, France. The experimental data are courtesy of Talneau A., LPN - CNRS, France, Olivier S., EPP, France, and Moosburger J., Würzburg Universität, Germany. The numerical modelling has been performed by Agio M. and Kafesaki M. at IESL - FORTH, Crete, Greece.

The part of the work that is more related to fundamental research (Chapters 1 and 2) has been carried out mainly at the Department of Physics "A. Volta", Università degli Studi di Pavia, under the guidance of prof. Lucio C. Andreani. Instead, the part that is more application oriented (Chapter 3) has been accomplished at the Department of Physics, Iowa State University, supervised by prof. Costas M. Soukoulis, thanks to the "Memorandum of Agreement - International Doctorate" between the Departments of Physics of Università degli Studi di Pavia and Iowa State University.

Pavia, November 2002

CHAPTER 1. PHOTONIC BANDS

The concept of photonic band is fundamental for understanding photonic crystals. This will be more evident in the following chapters, when optical properties and wave propagation will be analyzed. The aim is to provide the reader with a physical background on the band structure of two-dimensional photonic crystals and photonic crystal slabs made of air holes in semiconductor materials.

The chapter is organized as follows. Section 1.1 is an historical overview of photonic crystals, with emphasis on the calculation of photonic bands and their symmetry properties. A short review on the dispersion properties of photonic crystal waveguides is also present. Section 1.2 starts from the problem of solving Maxwell's equations in a periodic dielectric structure using the plane-wave expansion method. The photonic band picture and the concept of photonic band gap are introduced. Section 1.3 is dedicated to two-dimensional photonic crystals, in particular to the case of a triangular lattice of air holes in a dielectric material. A subsection describes the classification of bands according to group-theory. Section 1.4 concerns two-dimensional photonic crystal slabs. A numerical method for computing the bands is given and the light-line problem is discussed. Examples are considered for both strong and weak vertical confinement structures. The issue of out-of-plane diffraction losses is postponed to the next chapters. Section 1.5 is about the dispersion relation of dielectric linear defects in two-dimensional photonic crystals.

1.1 History

Since the very beginning of research in photonic band-gap materials, many efforts have been devoted to the study of photonic bands [John, S., *et al.* (1988); Leung, K. M., *et al.* B (1990); Ho, K. M., *et al.* (1990); Yablonovitch, E., *et al.* (1991)]. The main purpose was to design

structures exhibiting a complete photonic band gap in three dimensions, to achieve a full control over spontaneous emission and light localization. Indeed, the papers that first proposed photonic crystals concerned these subjects [Yablonovitch, E. (1987); John, S. (1987)].

Calculating the band structure of a three-dimensional photonic crystal was not an easy task, also because of the vector nature of Maxwell's equations. Strangely enough, the study did not start from the simplest cases (one- and two-dimensional photonic crystals), but researchers tried hard to solve the full three-dimensional problem. Yablonovitch, E., *et al.* (1989) and Leung, K. M., *et al.* A (1990) proposed a numerical method, called the plane-wave method, based on the expansion of the electromagnetic field on plane waves and the diagonalization of the resultant eigenvalue problem. In these work, using the scalar wave approximation, it was shown that a face-centered-cubic lattice of dielectric spheres in air has a complete band gap. A couple of years later, Leung, K. M., *et al.* B (1990) reported on the full vector calculation within the plane-wave method and showed that no complete band gap exists for that structure. The discrepancy between the data obtained with and without the scalar wave approximation demonstrated the necessity of preserving the vector nature of the electromagnetic field in numerical computations. Just a month after the publication of this work, Ho, K. M., *et al.* (1990) found that dielectric spheres arranged in the diamond structure possess a full photonic band gap. Subsequently, Yablonovitch, E., *et al.* (1991) designed another system with complete band gap, with a structure more suitable for micro-fabrication.

Even though three-dimensional photonic crystals were much attracting for their novel properties, in view also of revolutionary applications in optical communications, their fabrication was too much demanding yet to reach lattice constants apt for operation at micron and sub-micron wavelengths.

Two-dimensional photonic crystals could be a fair trade-off between a three-dimensional band gap and a more feasible micro-fabrication. Moreover, reducing the problem to two-dimensions was certainly helpful in understanding the new concepts brought by photonic crystals. A complete band gap in two-dimensions was first theoretically predicted and experimentally demonstrated by Meade, R. D., *et al.* (1992) for a triangular lattice of air holes in a dielectric background. Subsequently, many other structures with two-dimensional band gap were theoretically investigated [Villeneuve, P. R., *et al.* (1992); Padjen, R., *et al.* (1994); Cassagne, D., *et al.* (1996); Anderson, C. M., *et al.* (1997); Li, Z.-Y., *et al.* (1998); Wang, X.-H., *et al.* (1999); Agio, M. (1999); Agio, M., *et al.*

A (2000)]. For example, Cassagne, D., *et al.* (1996) studied the formation of a photonic band gap for the graphite and the boron-nitride structures; Anderson, C. M., *et al.* (1997) thoroughly analyzed symmetry-reduction effects in square-lattice photonic crystals; Li, Z.-Y., *et al.* (1998) exploited anisotropy to increase the size of the band gap. At the same time, other numerical methods for band structure calculation were proposed: the Korringa-Kohn-Rastoker (kkr) method by John, S., *et al.* (1988), the transfer-matrix method by Pendry, J. B., *et al.* (1992), the tight-binding parametrization by Lidorikis, E., *et al.* (1998), the finite-difference time-domain method by Qiu, M., *et al.* A (2000) and other methods based on Green's functions [Martin, O. J. F., *et al.* (1999)]. Nevertheless, the plane-wave expansion became the standard numerical method to compute photonic bands.

In a few years of intense work on band structure calculation, there was quite a number of two- and three-dimensional photonic crystals available for fabrication and characterization. The first experiments were performed at the micro-wave frequency regime [Yablonovitch, E., *et al.* (1989); Meade, R. D., *et al.* (1992); Robertson, W. M., *et al.* A (1993); Thijssen, M. S., *et al.* (1999)], but much of the interest in photonic crystals was for the frequency range close to 1.55μm. Experiments on three-dimensional photonic crystals with band gaps at micrometer and sub-micrometer wavelengths, had to wait the advent of self-assembled structures [Busch, K., *et al.* (1998); Blanco, A., *et al.* (2000); Vlasov, Y. A., *et al.* (2001)], which provided a more affordable and efficient fabrication technique, than complicated etching processes. A full photonic band gap near 1.5μm was measured for inverted opals made of silicon [Blanco, A., *et al.* (2000)]. Besides that, interesting results have also been obtained for the so-called layer-by-layer structure: a three-dimensional photonic crystal fabricated by stacking dielectric or metallic rods to form a net with the symmetry of the diamond lattice [Ho, K. M., *et al.* (1994); Lin, S. Y., *et al.* A (1998); Fleming, J. G., *et al.* (2002)]. In order to perform measurements of two-dimensional photonic crystals with micron-size lattice constant, refined etching techniques were necessary as well. Two solutions were found: one based on electrochemical etching, the other based on lithographic methods already developed for semiconductor nano-structures used in micro-electronics. Electrochemical etching is exploited to fabricate macro-porous silicon with a two-dimensional lattice of regular air holes distant from 10μm to 1μm from each other and deep up to 100 μm [Lehmann, V., *et al.* (1990); Grüning, U.,

et al. (1996); Birner, A., *et al.* (1998); Rowson, S., *et al.* (1999)]. Such an high aspect ratio makes macro-porous silicon effectively a real two-dimensional photonic crystals. However, being really two-dimensional carries the flaw of obtaining only a two-dimensional control of light. This can be interesting for fundamental research, but in most cases it is not useful for applications. Another issue is that this etching process is restricted to one material, i.e. to silicon. However, it is worth to mention that there are also attempts to fabricate macro-porous silicon samples yielding a three-dimensional control of light by vertical pore modulation [Schilling, J., *et al.* B (2001)].
Lithographic techniques are not restricted to silicon and they can be applied to many semiconductors, offering more freedom in the choice of the material. They are also more accurate than electrochemical etching, but the etch-depth can be maximum a few microns against 100μm of macro-porous silicon. Considering that wavelength, lattice constant end etch-depth are of the same order of magnitude, the concept of two-dimensional crystal starts to be questionable for these systems. In this sense, the concept of two-dimensional photonic crystal had to be generalized to a new class of structures: the finite-height two-dimensional photonic crystals, also named photonic crystal slabs, see Fig. 2. The first fabrication of a two-dimensional photonic crystal slab operating at near-infrared wavelengths is by Krauss T. F., *et al.* (1996). They showed that a photonic band gap in the range of 800-900nm can be obtained embedding a two-dimensional photonic crystal in a GaAs/AlGaAs waveguide configuration. They also envisaged that the fabrication process should permit straightforward integration of such structures in other optical and optoelectronic devices.

Photonic crystal slabs, contrary to two- and three-dimensional photonic crystals, were first investigated by experiments rather than theory, even though their proposal dates back to Meade, R. D., *et al.* (1994). Indeed, whereas the manufacture of photonic crystal slabs took advantage of a ready-to-use expertise on lithography of semiconductor heterostructures, the complication added by the presence of a finite-size dimension required some time to implement efficient and accurate numerical methods for band structure calculations.
Thanks to the availability of high-quality GaAs-based samples and to a novel experimental technique, Labilloy, D., *et al.* A (1997) were able to perform quantitative measurements of transmission, reflection and diffraction at near-infrared wavelengths of waveguide-based two-dimensional photonic crystals. Also, this work demonstrated that scattering losses out of the waveguide plane do not

disrupt the band gap properties and sharp band edges were found. Besides the GaAs/AlGaAs system [Labilloy, D., *et al.* A (1997); Benisty, H., *et al.* (1999); Astratov, V. N., *et al.* A (1999); Galli, M., *et al.* B (2002)], other types of waveguide are of interest for photonic crystals and are currently under experimental investigation: Si/SiO_2 [Patrini, M., *et al.* A (2002); giapponesi], InP/GaInAsP [Ferrini, R., *et al.* (2002)], self-standing membrane [Pacradouni, V., *et al.* (2000); Silvestre, E., *et al.* (2000); Kawai, N., *et al.* (2001)], and $AlGaAs/Al_2O_3$ [Chow, E., *et al.* (2000)]. Photonic crystal slabs can be divided into two major groups, high and weak vertical-confinement systems, according to the choice of the planar waveguide [Jackson, J. D. (1975); Saleh, B. E. A., *et al.* (1991)]. For example, a self-standing membrane of Si or GaAs builds up a strong vertical confinement, whereas GaAs/AlGaAS and InP/GaInAsP waveguides only provide weak vertical confinement. This feature is related to the issue of out-of-plane scattering losses and to the light-line problem. It is well known that the dispersion diagram of a waveguide is characterized by the guided-mode region, below the light line, and by the leaky-mode region, above the light line, where the light line represents the dispersion of light in the cladding material. In a similar way for photonic crystals slabs, photonic bands can be truly guided modes or resonances with propagation losses. If the waveguide is asymmetric, like for the system of Fig. 2, then there are two light lines: one for the air cladding and one for the dielectric substrate. Thus, there can be modes that leak in the substrate and not in the top cladding, and modes that radiate both in the substrate and in air. Notice that these losses are intrinsic, and must not be confused with scattering related to fabrication issues, as roughness or finite etch-depth.

It is clear that the problem of out-of-plane losses was, and is, one of the major concerns for the application of photonic crystal slabs: which is the structure, with the wanted band gap properties, possessing minimum out-of-plane losses? Hard question when no theoretical methods were available to calculate the photonic bands of finite-height photonic crystals and the propagation losses of such systems. The choice of the waveguide, the choice of the layer thickness, the choice of the etch-depth, and the choice of the patterning itself, were two many parameters to allow answering the above question without the assistance of numerical modelling.

D'Urso, B., *et al.* (1998) tackled the problem of vertical confinement and finite etch-depth in waveguide-based photonic crystals using a three-dimensional finite-difference time-domain method.

Even though the study was conducted on micro-cavities, they gave important hints on how to minimize out-of-plane scattering losses, either by using a self-standing membrane configuration either by deeply etching a waveguide embedded in a semiconductor heterostructure. Johnson, S. G., *et al.* (1999) extended the plane-wave method to two-dimensional photonic crystal slabs by means of a super-cell in the vertical dimension. The study is limited to the guided-mode region though, because the plane-wave method is not able to handle the continuum spectrum of leaky bands. They analyzed the effect of vertical confinement on photonic bands and on the band gap; one of the main findings concerns the dependence of the size of the band gap on the waveguide thickness. The approach of Johnson, S. G., *et al.* (1999) is not applicable to any photonic crystal based on low-index contrast slabs, because the guided-mode region is so narrow that the band gap lies always above the light line. In fact, the most challenging problem was to calculate the dispersion of photonic resonances, i.e. the bands in the radiative region. These bands do not have a discrete frequency, but are characterized by a Lorentzian curve with a mean value, which defines the energy of the band, and a width, which is proportional to out-of-plane losses.

For this class of systems, Benisty, H., *et al.* (2000) proposed a phenomenological model to include losses in a simple two-dimensional calculation. The weak-vertical confinement is taken into account by choosing as material index the effective index of the fundamental guided mode of the unpatterned waveguide. Out-of-plane losses are modelled within first-order perturbation theory, where the perturbation is the patterning of the core layer. The final result is an imaginary part for the dielectric constant that can be easily implemented in a two-dimensional calculation and nicely fits experimental transmission spectra. They also suggested that weak confinement structures cause lower out-of-plane losses than those with strong confinement. Finally, the idea of performing two-dimensional simulations in place of three-dimensional ones seemed a practicable way for reducing the modelling burden. However, many information are lost in the approximation and the method itself had to be validated by comparison with ab-initio numerical results.

Other numerical methods were developed to solve the full electromagnetic problem of two-dimensional photonic crystal slabs, but they did not accomplish the calculation of bands in the radiative region [Whittaker, D. M., *et al.* (1999); Chow, E., *et al.* (2000); Lalanne, Ph., *et al.* (2001)]. The finite-difference time-domain method, a powerful numerical technique, but quite demanding for

three-dimensional problems, seemed to be the last choice. Chutinan, A., *et al.* (2000) and later Ochiai, T., *et al.* A (2001) computed the dispersion relation for an air bridge system patterned with a triangular lattice of air holes, below and above the light line. The latter also evaluated the decay rate of leaky modes, finding that the width of the resonances has a non trivial dependence on the **k** vector and varies from band to band. This was also pointed out by experiments performed on various waveguide systems [Astratov, V. N., *et al.* A (1999); Lončar, M., *et al.* (2002); Patrini, M., *et al.* A (2002); Galli, M., *et al.* B (2002)].

In order to have a deeper insight on photonic bands and on their radiative losses, Ochiai, T., *et al.* B (2001) applied the nearly-free photon approximation [Cassagne, D., *et al.* (1996)] to photonic crystal slabs to obtain analytical formulae for the dispersion relation and for the width of the resonances. The method is in good agreement with finite-difference time-domain simulations, but is limited to slabs where the patterning can be considered a perturbation.

Very recently, Andreani, L. C. (2002) has implemented a fast and accurate numerical method to calculate the band structure of waveguide-based photonic crystals. The formalism, based on the expansion of the electromagnetic field on the guided modes of the unpatterned waveguide, will be discussed in detail in this chapter. In practice, this technique requires nearly the same CPU time than the plane-wave method applied to two-dimensional photonic crystals.

The study of photonic crystals and of their photonic bands can not neglect the importance of symmetry. The definition of photonic crystal itself is based on a symmetry consideration: invariance for discrete translations in one, two, or three dimensions. Moreover, the photonic band picture, as a concept borrowed from Solid State Physics, should be accomplished by the classification of the energy levels based on group theory. Contrary to the thorough classification of electronic states in solids [Koster, G. F., *et al.* (1963); Bassani, F., *et al.* (1975); Cardona, M., *et al.* (1996)], a similar work for photonic crystals remained somewhat marginal until recently.

Apart basic applications, such as defining the irreducible Brillouin zone or writing Maxwell's equations for two independent polarizations [Joannopoulos, J. D., *et al.* (1995); Agio, M. (1999)], the symmetry analysis became an important tool in guiding the investigation of new lattices or bases to design wide-band-gap photonic crystals. Padjen, R., *et al.* (1994) examined how the shape of

the basis influences the photonic bands. Cassagne, D., *et al.* (1996) performed the first symmetry analysis of the photonic states for graphite, boron-nitride and triangular crystals, while Anderson, C. M., *et al.* (1997) studied the symmetry-reduction in group $4mm$ photonic crystals to increase the size of existing photonic band gaps or to create new ones by lifting some band degeneracies. Labelling the empty lattice modes according to the irreducible representations of the crystal point group and comparing them to the corresponding photonic bands helped much in the understanding the band gap formation in two-dimensional photonic crystals [Cassagne, D., *et al.* (1996); Agio, M. (1999)]. In two recent works, Ochiai, T., *et al.* A (2001) extended the same procedure to two-dimensional photonic crystal slabs. In this case, the empty lattice dispersion relation is given by the guided modes of the unpatterned slab.

Concerning the decay rates of resonances, Ochiai, T., *et al.* A (2001) found that the lifetime of several bands is infinite at the Γ point. This phenomenon was explained by means of symmetry considerations: the decoupling of the photonic bands from the diffraction modes in free space originates from symmetry mismatch. Andreani, L. .C., *et al.* (2001), in a thorough study on the symmetry properties of two-dimensional photonic crystals, put in evidence the necessity of group theory in interpreting the optical properties of such systems. In fact, group theory gained the deserved attention in combination with variable-angle reflectance experiments on two-dimensional photonic crystals [Astratov, V. N., *et al.* A (1999); Galli, M., *et al.* A (2002); Patrini, M., *et al.* A (2002)]. The reflectance spectra depend on the coupling of the free space field with the photonic modes in the crystal. The coupling strength, which is inversely proportional to the band lifetime, can be zero when symmetry mismatch occurs[1].

As a final remark, it is worth to mention that also three-dimensional photonic crystals are underway as regards symmetry characterization. López-Tejeira, F., *et al.* (2002) used group theory to classify the eigenstates in opal systems. Similarly to two-dimensional photonic crystal, the study allowed to identify photonic bands that do not couple to the external field.

One of the motivations for investing research in photonic crystals is the possibility of *molding the flow of light* [Joannopoulos, J. D., *et al.* (1995)]. The existence of a frequency range where

[1] An historical overview on this technique will be given in the next chapter.

light propagation is forbidden, can be exploited by engineering defects into the bulk crystal. As mentioned in the introductory chapter, a linear defect can be seen as a waveguide: the photonic band gap provides lateral confinement, whereas the defect itself constitutes the core. On the other hand, a point defect acts as a micro-cavity. Both micro-cavities and waveguides are the building-blocks of optical communication and optoelectronics. In order to model effective integrated devices based on photonic crystals, being able to calculate defect modes and their dispersion relation is of primary interest.

The super-cell method was found to be suitable for this purpose [Meade, R. D., *et al.* (1994); Joannopoulos, J. D., *et al.* (1995); Benisty, H. (1996); Villeneuve, P. R., *et al.* (1996)]. The defect is embedded in large unit cell, so that the eigenstates do not overlap, and the eigenfrequencies are computed by means of the plane-wave method. Another choice is to use the finite-difference time-domain method [Qiu, M., *et al.* B (2000); Chutinan, A., *et al.* (2000)].

The dispersion relation of photonic-crystal waveguides was investigated since the early years of research on photonic crystals; see *J. Opt. Soc. Am. B, 10* (2) for a collection of works on this subject. Benisty, H. (1996) carefully studied the guided modes of dielectric two-dimensional photonic-crystal waveguides, focussing, in particular, on the role of the edge corrugations. In fact, modes in corrugated waveguides can undergo contradirectional coupling (optical feedback), which is characterized by a stop band. The existence of stop bands in the mode dispersion of photonic-crystal waveguides was theoretically investigated also by Mekis, A., *et al.* (1998) and experimentally confirmed by Olivier, S., *et al.* A (2001). Such stop bands are also called mode gaps or mini-stop bands.

As a peculiarity with respect to conventional dielectric waveguides, photonic-crystal waveguides can support two types of modes: index-guided modes and band-gap-guided modes. The formers can exist only if the waveguide core has an index of refraction greater than that of the surrounding photonic crystal. This is the same case of guided modes in dielectric waveguides. On the contrary, band-gap-guided modes do not need a high-index core, because the confinement is provided by the band gap. Thus, the occurrence of both index-guided and band-gap-guided modes in photonic-crystal waveguides is likely to happen when the linear defect is created by removing air holes in a photonic crystal etched in semiconductors. As a consequence, a photonic-crystal waveguide can be

easily multi-mode even for small widths of the dielectric channel [Agio, M., *et al.* (2001)].

Meade, R. D., *et al.* (1994) suggested that dielectric waveguides in two-dimensional photonic-crystal slabs could be easily fabricated. Likewise for photonic bands, the modes of linear waveguides in photonic-crystal slabs are either truly guided, below the light line, either resonances, above the light line. The application of the super-cell method within the plane-wave expansion faces the same issues previously described for the calculation of photonic bands. Chutinan, A., *et al.* (2000) used the finite-difference time-domain method to compute the dispersion relation of a photonic-crystal waveguide in a self-standing dielectric membrane. One month later, Johnson, S. G., *et al.* (2000) published a systematic analysis of different families of waveguides in photonic crystal slabs, giving the conditions that must be applied in order to achieve single-mode operation. Since they used the super-cell method, the study concerned only truly guided modes. Lončar, M., *et al.* A (2000), instead, performed a comprehensive work on design and fabrication of waveguides in silicon-on-insulator photonic crystal slabs. The design parameters were found by means of three-dimensional finite-difference time-domain simulations, including the leaky modes region.

As discussed for bulk photonic-crystal slabs, the amount of out-of-plane losses for the waveguide modes could preclude the application to real devices. The quantification of propagation losses in photonic crystal waveguides, i.e. the width of the resonances in the waveguide dispersion relation, was done experimentally by Lončar, M., *et al.* (2002). They were able to trace the dispersion relation for leaky modes from 1440 to 1590 nm and found that the propagation losses decrease as approaching to the mini-stop band located at 1500 nm. Recently, Andreani, L. C., *et al.* B (2002) calculated the diffraction losses of line-defect modes in high-index-contrast photonic-crystal slabs, confirming the above trend.

1.2 Maxwell Equations for a Photonic Crystal

The calculation of photonic bands is essentially the solution of Maxwell's equations in a medium with spatial periodicity in either the dielectric function, either the magnetic permeability or both. The problem is treated with a formalism borrowed from Solid State Physics, following the analogy with electrons in a periodic potential. Recasting Maxwell's equations in a closed form for the

magnetic field yields an eigenvalue problem similar to the time-independent Schrödinger equation. The photonic band picture is the natural consequence of such formalism.

For linear media, Maxwell's equations can be written in a general form as

$$\nabla \cdot \mathbf{B} = 0\,, \qquad \nabla \times \mathbf{E} + \frac{1}{c}\frac{\partial}{\partial t}\mathbf{B} = 0\,, \tag{1.1a}$$

$$\nabla \cdot \mathbf{D} = 4\pi\rho\,, \qquad \nabla \times \mathbf{H} - \frac{1}{c}\frac{\partial}{\partial t}\mathbf{D} = \frac{4\pi}{c}\mathbf{j}\,, \tag{1.1b}$$

where Eqs. (1.1a) are the homogenous equations and Eqs. (1.1b) are the non homogenous ones. The tensor dielectric function $\bar{\epsilon}(\mathbf{r}, t)$ relates the electric field $\mathbf{E}$ with the electric displacement field $\mathbf{D}$ through the constitutive relation

$$\mathbf{D}(\mathbf{r}, t) = \int \bar{\epsilon}(\mathbf{r}, t - t') \cdot \mathbf{E}(\mathbf{r}, t')\mathrm{d}t'\,. \tag{1.2}$$

A similar relation connects the magnetic field $\mathbf{H}$ to the magnetic induction field $\mathbf{B}$ through the tensor magnetic permeability $\bar{\mu}(\mathbf{r}, t)$. In this context, it is assumed that the media composing the photonic crystal are isotropic, i.e. the dielectric and magnetic tensors reduce to scalars $\bar{\epsilon}(\mathbf{r}, t) \Rightarrow \epsilon(\mathbf{r}, t)$ and $\bar{\mu}(\mathbf{r}, t) \Rightarrow \mu(\mathbf{r}, t)$, the dielectric function is non dispersive $\epsilon(\mathbf{r}, t - t') = \epsilon(\mathbf{r})\delta(t - t')$, real and non negative, the media are non magnetic, i.e. $\mathbf{B} = \mathbf{H}$, and no free charges nor currents $\rho = 0$ and $\mathbf{j} = 0$. With these hypotheses, Maxwell's equations are simplified to

$$\nabla \cdot \mathbf{H} = 0\,, \qquad \nabla \times \mathbf{E} + \frac{1}{c}\frac{\partial}{\partial t}\mathbf{H} = 0\,, \tag{1.3a}$$

$$\nabla \cdot \epsilon(\mathbf{r})\mathbf{E} = 0\,, \qquad \nabla \times \mathbf{H} - \frac{1}{c}\frac{\partial}{\partial t}\epsilon(\mathbf{r})\mathbf{E} = 0\,. \tag{1.3b}$$

Thanks to the linearity of Maxwell's equations, it is convenient to look for solutions for harmonic fields

$$\mathbf{E}(\mathbf{r}, t) = \mathbf{E}(\mathbf{r})e^{-\imath\omega t}\,, \qquad \mathbf{H}(\mathbf{r}, t) = \mathbf{H}(\mathbf{r})e^{-\imath\omega t}\,. \tag{1.4}$$

The general solution can be obtained as a superposition of harmonic modes. Plugging the formulae (1.4) into Eqs. (1.3a) and (1.3b), in a few simple steps it is possible to recast Maxwell's equations in a closed form for either the magnetic or the electric fields

$$\nabla \cdot \mathbf{H}(\mathbf{r}) = 0 \qquad \nabla \times \left(\frac{1}{\epsilon(\mathbf{r})}\nabla \times \mathbf{H}(\mathbf{r})\right) = \frac{\omega^2}{c^2}\mathbf{H}(\mathbf{r}) \tag{1.5a}$$

$$\nabla \cdot \epsilon(\mathbf{r})\mathbf{E}(\mathbf{r}) = 0 \qquad \nabla \times \nabla \times \mathbf{E}(\mathbf{r}) = \frac{\omega^2}{c^2}\epsilon(\mathbf{r})\mathbf{E}(\mathbf{r})\,, \tag{1.5b}$$

where the equations at the right side are the analog of the time-independent Schrödinger equation. Notice that in this case, the potential $\epsilon(\mathbf{r})$ enters as a multiplication factor, instead of being summed to the free "hamiltonian", as it is for electrons. Moreover, whereas the Schrödinger wave-function is a scalar, the electric and magnetic field have three components that are mixed by the spatial dependent dielectric function. These features make Eqs. (1.5a) and (1.5b) more complex than the single-electron Schrödinger equation. It is more convenient to work with Eqs. (1.5a), because the magnetic field is transverse and the master equation has the form of an eigenvalue problem. On the contrary, the divergence equation for the electric field involves the dielectric function and the "hamiltonian" equation is more complicated, being a generalized eigenvalue problem. For this reason, the solution of the electromagnetic problem will be carried out using Eqs. (1.5a), which is the standard choice adopted by the research community. For the other possibility, namely Eqs. (1.5b), please refer to Agio, M. (1999).

Up to now, the derivation of the master equation is valid for any system for which the initial assumptions are fulfilled, without further specifications. To solve the electromagnetic problem for a photonic crystal, it is necessary to impose that the dielectric function is periodic. The periodicity can be in one, two, or three dimensions and, correspondingly, the photonic crystal is one-, two-, or three-dimensional. Looking at Fig. 1, notice that the dielectric function of a photonic crystal is made of a unit cell repeated in space according to a well defined pattern. All of that can be reduced to two concepts: basis and lattice. The lattice defines the spatial arrangement of the unit cell; the basis specifies the content of the unit cell[2]. For example, the basis of a three-dimensional photonic crystal can be a dielectric sphere in air or a dielectric cube in air. The lattice is generated by linear combination of the so-called primitive vectors $\mathbf{a}_i$, which are determined by the minimum translations that leave the dielectric function unchanged. Choosing a reference frame and placing a lattice point at the origin of it, any other lattice point is in one-to-one correspondence with a vector $\mathbf{R}$, linear combination of $\mathbf{a}_i$; in mathematical terms, the lattice is defined by a vector space $\mathbb{V}$, with basis $\{\mathbf{a}_i\}$. The dimensionality of $\mathbb{V}$ equals the number of dimensions in which the dielectric function is periodic. Therefore, a one-dimensional photonic crystal will have one primitive vector, a two-dimensional photonic crystal will have two primitive vectors, and so on. The unit cell has

[2]Notice that, given lattice and basis, the choice of the unit cell is not unique.

the same dimensions of $\mathbb{V}$ and the space A_c that occupies is determined by the primitive vectors:

$$A_c = \begin{cases} |\mathbf{a}_1|\,, & \text{1D;} \\ |\mathbf{a}_1 \times \mathbf{a}_2|\,, & \text{2D;} \\ |\mathbf{a}_1 \cdot (\mathbf{a}_2 \times \mathbf{a}_3)|\,, & \text{3D.} \end{cases} \tag{1.6}$$

In this framework, the dielectric function of a photonic crystal has the property

$$\forall\, \mathbf{R} \in \mathbb{V},\ \epsilon(\mathbf{r}+\mathbf{R}) = \epsilon(\mathbf{r})\,. \tag{1.7}$$

In other words, the photonic crystal is invariant for any discrete translation defined by a vector $\mathbf{R} \in \mathbb{V}$. To understand the implications of the invariance for discrete translations, it is helpful to work in terms of symmetry transformations and use the operator formalism.

The master equation for the magnetic field can be rewritten in a general form as

$$\hat{\mathbf{O}}(\mathbf{r})\mathbf{H}(\mathbf{r}) = \lambda \mathbf{H}(\mathbf{r})\,, \text{with } \hat{\mathbf{O}}(\mathbf{r}) = \nabla \times \left(\frac{1}{\epsilon(\mathbf{r})}\nabla \times\ \right., \text{ and } \lambda = \frac{\omega^2}{c^2}\,.$$

It is easy to show that $\hat{\mathbf{O}}$ is an hermitian positive definite operator. This guarantees that the eigenvalues are real and non negative, and that a complete set of orthonormal eigenfunctions does exist. Being $\hat{\mathbf{T}}_{\mathbf{R}}$ the unitary operator[3] associated to a discrete translation $\mathbf{R}$, the rule for the transformation reads

$$\hat{\mathbf{O}}' = \hat{\mathbf{T}}_{\mathbf{R}} \hat{\mathbf{O}}\, \hat{\mathbf{T}}_{\mathbf{R}}^{-1} \qquad \epsilon' = \hat{\mathrm{T}}_{\mathbf{R}} \epsilon\, \hat{\mathrm{T}}_{\mathbf{R}}^{-1} \qquad \mathbf{H}'(\mathbf{r}) = (\hat{\mathbf{T}}_{\mathbf{R}}\mathbf{H})(\hat{\mathbf{T}}_{\mathbf{R}}^{-\mathbf{1}}\mathbf{r})\,. \tag{1.8}$$

Since the photonic crystal is invariant for this kind of transformation, i.e. is a symmetry transformation for the system, the operator $\hat{\mathbf{O}}$ and the dielectric function ϵ are left unchanged: $\hat{\mathbf{O}}' = \hat{\mathbf{O}}$ and $\epsilon' = \epsilon$. What happens to $\mathbf{H}'$?

1.2.1 The Bloch-Floquet Theorem

The application of the operator $\hat{\mathbf{T}}_{\mathbf{R}}$ to the master equation yields a new eigenvalue problem for the transformed field $\mathbf{H}'$, but, since $\hat{\mathbf{O}}$ commutes with $\hat{\mathbf{T}}_{\mathbf{R}}$, it is easy to show that $\mathbf{H}'$ must satisfy

[3] The operator acts also on the field components of $\mathbf{H}$. For the dielectric function, instead, the operator $\mathrm{T}_{\mathbf{R}}$ acts only on the spatial coordinates.

the same equation for $\mathbf{H}$.

$$\hat{\mathbf{O}}(\mathbf{r})\mathbf{H}(\mathbf{r}) = \lambda\mathbf{H}(\mathbf{r}) \qquad \Longleftrightarrow \qquad \hat{\mathbf{O}}(\mathbf{r})\hat{\mathbf{T}}_{\mathbf{R}}\mathbf{H}(\mathbf{r}) = \lambda\hat{\mathbf{T}}_{\mathbf{R}}\mathbf{H}(\mathbf{r})\,.$$

Such condition is fulfilled if $\mathbf{H}'$ is equal to $\mathbf{H}$ within a multiplication factor, which implies that $\mathbf{H}$ is, in the most general form, a linear combination of degenerate eigenfunctions of the translation operator $\hat{\mathbf{T}}_{\mathbf{R}}$

$$\hat{\mathbf{T}}_{\mathbf{R}}\mathbf{H}(\mathbf{r}) = \alpha\mathbf{H}(\mathbf{r})\,. \tag{1.9}$$

The eigenfunctions of $\hat{\mathbf{T}}_{\mathbf{R}}$ are plane waves and the eigenvalues are complex numbers of unitary modulus:

$$\mathbf{f}_{\mathbf{k}}(\mathbf{r}) = \hat{\mathbf{f}}e^{\imath\mathbf{k}\cdot\mathbf{r}} \qquad \hat{\mathbf{T}}_{\mathbf{R}}\mathbf{f}_{\mathbf{k}}(\mathbf{r}) = e^{-\imath\mathbf{k}\cdot\mathbf{R}}\mathbf{f}_{\mathbf{k}}(\mathbf{r}) \qquad \alpha = e^{-\imath\mathbf{k}\cdot\mathbf{R}}\,,$$

where $\mathbf{k}$ is the wave-vector. Notice that all the eigenfunctions $\mathbf{f}_{\mathbf{k}'}(\mathbf{r})$ and $\mathbf{f}_{\mathbf{k}}(\mathbf{r})$, with $\mathbf{k}' = \mathbf{k} + \mathbf{G}$ so that $\mathbf{G}\cdot\mathbf{R} = 2n\pi$, are degenerate. The condition

$$\mathbf{G}\cdot\mathbf{R} = 2n\pi \tag{1.10}$$

is not only a mere scalar product, but defines the dual space $\mathbb{G}$ of the vector space $\mathbb{V}$. If $\{\mathbf{a}_i\}$ is the basis for $\mathbb{V}$, the basis of the dual space (co-basis) is $\{\mathbf{g}_i\}$; any dual-space vector $\mathbf{G}$ can be obtained as a linear combination of $\mathbf{g}_i$. Therefore, two eigenfunctions $\mathbf{f}_{\mathbf{k}'}(\mathbf{r})$ and $\mathbf{f}_{\mathbf{k}}(\mathbf{r})$ are degenerate if $\mathbf{k}' - \mathbf{k} \in \mathbb{G}$. The general solution of the master equation is therefore

$$\mathbf{H}_{\mathbf{k}}(\mathbf{r}) = \sum_{\mathbf{G}\in\mathbb{G}} c(\mathbf{k}+\mathbf{G})\mathbf{f}_{\mathbf{k}+\mathbf{G}}(\mathbf{r})\,. \tag{1.11}$$

The divergence condition $\nabla\cdot\mathbf{H}_{\mathbf{k}}(\mathbf{r}) = 0$ is automatically fulfilled if $(\mathbf{k}+\mathbf{G})\cdot\mathbf{f}_{\mathbf{k}+\mathbf{G}} = 0$, i.e. $\mathbf{f}_{\mathbf{k}+\mathbf{G}}(\mathbf{r})$ is also transverse. Since $\mathbf{H}_{\mathbf{k}}(\mathbf{r})$ is also eigenfunction of $\hat{\mathbf{T}}_{\mathbf{R}}$ with the same eigenvalue α of $\mathbf{f}_{\mathbf{k}}(\mathbf{r})$, the application of $\hat{\mathbf{T}}_{\mathbf{R}}$ to $\mathbf{H}_{\mathbf{k}}(\mathbf{r})$ yields

$$\hat{\mathbf{T}}_{\mathbf{R}}\mathbf{H}_{\mathbf{k}}(\mathbf{r}) = \mathbf{H}_{\mathbf{k}}(\mathbf{r}-\mathbf{R}) = e^{-\imath\mathbf{k}\cdot\mathbf{R}}\mathbf{H}_{\mathbf{k}}(\mathbf{r})\,. \tag{1.12}$$

Eq. (1.12) represents the so-called *Bloch-Floquet theorem*, which can be written also as

$$\mathbf{u}_{\mathbf{k}}(\mathbf{r}) = e^{-\imath\mathbf{k}\cdot\mathbf{r}}\sum_{\mathbf{G}\in\mathbb{G}} c(\mathbf{k}+\mathbf{G})\mathbf{f}_{\mathbf{k}+\mathbf{G}}(\mathbf{r}) \qquad \Longrightarrow \qquad \mathbf{H}_{\mathbf{k}}(\mathbf{r}) = e^{\imath\mathbf{k}\cdot\mathbf{r}}\mathbf{u}_{\mathbf{k}}(\mathbf{r})\,. \tag{1.13}$$

It is easy to show that $\mathbf{u_k}(\mathbf{r})$ has the same periodicity of the dielectric function. The Bloch-Floquet theorem states that *the general solution of a master equation invariant under* $\hat{\mathbf{T}}_\mathbf{R}$ *is a periodic function multiplied by a phase factor* $\exp(\imath\mathbf{k}\cdot\mathbf{r})$. *The period of* $\mathbf{u_k}(\mathbf{r})$ *is determined by* $\hat{\mathbf{T}}_{\mathbf{a}_i}$.

The operator formalism and the use of symmetry have helped in finding the general form for the solution of Maxwell's equation in a photonic crystal. What has been derived is also valid for the electric field $\mathbf{E_k}(\mathbf{r})$. Nevertheless, the knowledge of one field, determines the other one by straightforward application of Maxwell's equations.

From Eq. (1.11), it is evident that $\mathbf{H_{k'}}(\mathbf{r}) = \mathbf{H_k}(\mathbf{r})$ if $\mathbf{k'} - \mathbf{k} \in \mathbb{G}$, because of the sum over the $\mathbf{G}$ vectors. In other words, to two different $\mathbf{k}$ do not necessarily correspond different solutions $\mathbf{H_k}(\mathbf{r})$. This feature is due to the invariance of the system under discrete translations and the physical meaning is that in a photonic crystal the momentum $\mathbf{k}$ is conserved within a vector $\mathbf{G}$, i.e. $\mathbf{k}$ is not a "good quantum number" for the system.

The wave-vectors $\mathbf{k}$ span the so-called reciprocal space, which is the dual space of the Euclidean space $\mathbb{R}^3$. The reciprocal space $\mathbb{K}^3$ can be divided into classes of equivalence $[\mathbf{k}]$, according to the relation of equivalence $\mathcal{R} = \{(\mathbf{k}, \mathbf{k'}) \in \mathbb{K}^3 \times \mathbb{K}^3 : \mathbf{k'} - \mathbf{k} = \mathbf{G} \in \mathbb{G}\}$. Now, each class of equivalence $[\mathbf{k}]$ points to different $\mathbf{H_k}(\mathbf{r})$, where this time $\mathbf{k}$ is a representative of the class. The class of equivalence $[\mathbf{k}]$ of the momentum $\mathbf{k}$ is conserved in a photonic crystal, i.e. $[\mathbf{k}]$ is now a "good quantum number". The representative for each class $[\mathbf{k}]$ is called *the Bloch vector* $\mathbf{k}$. The choice of the Bloch vector is not unique, because it is just an element of its class of equivalence. Nevertheless, it is convenient to work with Bloch vectors that lend themselves to a "physical interpretation". Usually, the Bloch vector is taken as the smallest element of the class, in modulus. The ensemble of such Bloch vectors defines the so-called first Brillouin zone, shortly Brillouin zone (B.Z.)

$$\text{B.Z.} \doteq \left\{ \mathbf{k} \in \mathbb{K}^3 : |\mathbf{k}| = \min_{\mathbf{z}\in[\mathbf{k}]}(|\mathbf{z}|) \right\} . \tag{1.14}$$

Similarly to what has been done for the photonic crystal in real space, it is possible to define a unit cell in the reciprocal space. Correspondingly, there will be a reciprocal lattice that determines how the unit cell tiles the reciprocal space. Again, the choice of the unit cell is not unique. The direct lattice is associated to the vector space $\mathbb{V}$, the reciprocal lattice is associated to its dual space $\mathbb{G}$. The primitive vectors are $\mathbf{a_i}$ for the direct lattice and $\mathbf{g}_i$ for the reciprocal lattice. An expression

for $\mathbf{g}_i$ in terms of $\mathbf{a}_i$ is readily given by solving Eq. (1.10) for the primitive vectors,

$$\mathbf{a}_i \cdot \mathbf{g}_j = 2\pi \qquad \Longrightarrow \qquad \begin{cases} \mathbf{g}_i = 2\pi \dfrac{\mathbf{a}_j \times \mathbf{a}_k}{\mathbf{a}_i \cdot (\mathbf{a}_j \times \mathbf{a}_k)}, & \text{3D;} \\ \mathbf{g}_i = 2\pi \lim\limits_{\delta \to 0} \dfrac{\mathbf{a}_j \times \delta\hat{\mathbf{k}}}{\mathbf{a}_i \cdot (\mathbf{a}_j \times \delta\hat{\mathbf{k}})}, & \text{2D;} \\ \mathbf{g}_1 = \dfrac{2\pi}{|\mathbf{a}_1|}\hat{\mathbf{a}}_1, & \text{1D;} \end{cases} \tag{1.15}$$

where $\hat{\mathbf{k}}$ gives the direction of the z axis and i, j, k label the primitive vectors. According to the definition of Eq. (1.14), the Brillouin zone is the region delimited by cutting the reciprocal space with planes perpendicular to the primitive vectors and distant $|\mathbf{g}_i/2|$ from the origin. Thus, once the primitive vectors of the reciprocal lattice have been calculated, the Brillouin zone can be easily drawn. For a cubic (3D) or square (2D) lattice, the reciprocal primitive vectors are simply $\mathbf{g}_i = \frac{2\pi}{|\mathbf{a}_i|}\hat{\mathbf{a}}_i$. This is not the case for other lattices, like the triangular lattice for instance. Fig. 1.1 shows the Brillouin zone for the photonic crystals displayed in Fig. 1. For the one-dimensional photonic crystal, the Brillouin zone is B.Z. $= \{\mathbf{k} = (k_1, 0, 0) \in \mathbb{K}^3 : 2k_1 \in (-g_1, g_1]\}$, where k_1 is the x component of the Bloch vector and g_1 is the modulus of the primitive vector $\mathbf{g}_1$, which has been aligned parallel to the x axis. For the two-dimensional photonic crystal, the Brillouin zone[4] B.Z. $= \{\mathbf{k} = (k_1, k_2, 0) \in \mathbb{K}^3 : 2k_1 \in (-g_1, g_1] \wedge 2k_2 \in (-g_2, g_2]\}$; for the three-dimensional photonic crystal, the Brillouin zone is B.Z. $= \{\mathbf{k} = (k_1, k_2, k_3) \in \mathbb{K}^3 : 2k_1 \in (-g_1, g_1] \wedge 2k_2 \in (-g_2, g_2] \wedge 2k_3 \in (-g_3, g_3]\}$.

1.2.2 The Band Structure

The eigenfunctions of the master equation can be classified by means of the Bloch vector $\mathbf{k}$. Besides the eigenfunctions, the Bloch vector can also label the corresponding eigenvalues λ. As $\mathbf{k}$ varies inside the Brillouin zone, the eigenvalues obey to a certain dispersion relation $\lambda = \lambda(\mathbf{k})$. There is no one-to-one correspondence between the Bloch vector and the solutions of the master equation. In fact, it is possible that two solutions $\mathbf{H}_\mathbf{k}(\mathbf{r})$ have the same Bloch vector, but different expansion coefficients $c(\mathbf{k} + \mathbf{G})$ in Eq. (1.11). There are infinite choices for $c(\mathbf{k} + \mathbf{G})$ yielding

[4]Notice that the Brillouin zone is $(-g_1, g_1]$, because, since $|-\mathbf{g}_1| = \mathbf{g}_1$, $\pm\mathbf{g}_1$ belong to the same class of equivalence.

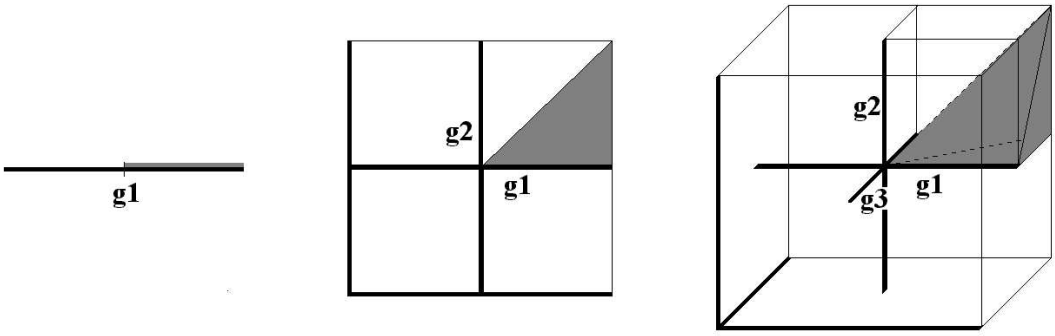

Figure 1.1 Brillouin zone for the photonic crystals of Fig. 1: 1D (left), 2D (center), 3D (right). The bold lines represent the primitive vectors $\mathbf{g}_i$ of the reciprocal space. The gray shaded areas correspond to the irreducible Brillouin zone.

independent linear combinations of the basis functions $\mathbf{f}_{\mathbf{k}+\mathbf{G}}(\mathbf{r})$. The ensemble of the independent linear combinations has the same cardinality of the group $\mathbb{G} = \{\mathbf{G} = l\mathbf{g}_1 + m\mathbf{g}_2 + n\mathbf{g}_3; (l, m, n) \in \mathbb{Z}^3\}$, isomorphous to $\mathbb{Z}^3$. By simply counting the number of triplets $(l, m, n) \in \mathbb{Z}^3$, it is evident that $\mathbb{Z}^3$ has the same cardinality of $\mathbb{N}^\star$. Therefore, it is consistent to add a label $n \in \mathbb{N}^\star$ to $\mathbf{H}_\mathbf{k}(\mathbf{r})$ to represent a certain linear combination of the basis functions. At the same time, the label is also attached to the corresponding eigenvalue λ.

$$\mathbf{H}_{\mathbf{k},n}(\mathbf{r}) = \sum_{\mathbf{G}\in\mathbb{G}} c_n(\mathbf{k}+\mathbf{G})\mathbf{f}_{\mathbf{k}+\mathbf{G}}(\mathbf{r}) \qquad\qquad \lambda = \lambda_n(\mathbf{k})\,. \tag{1.16}$$

In addition to the Bloch vector and the index n, there is also another important degree of freedom that characterizes the solutions of the master equation: the polarization σ. The magnetic field is a three-vector component, but only two components are independent because of the divergence equation. As a consequence, for each choice of $\mathbf{k}, n$ there are two independent solutions with different polarization. However, it is found that, in general, the polarization is not independent of the Bloch vector: $\sigma = \sigma(\mathbf{k})$. This is because the polarization conservation relies on a plane of symmetry, which might change with the Bloch vector. For such reason, it is convenient to absorb the polarization degree of freedom in the index n. Only in specific cases, where at least one polarization is independent of the Bloch vector, the index σ is used to label the eigenfunctions and the eigenfrequencies. For instance, it will be shown that this is the case for in-plane propagation in two-dimensional photonic crystals.

The "quantum numbers" $\mathbf{k}, n$ are therefore used to classify the eigenfunctions and the eigenvalues of the master equation. The step to the concept of photonic band is short. The eigenfrequencies $\omega/c = \sqrt{\lambda}$ take on the labels $\mathbf{k}, n \Longrightarrow \omega = \omega_n(\mathbf{k})$. Calling n the band index, *the n-th photonic band is defined as the portion of the spectrum λ with dispersion $\omega_n(\mathbf{k})$, as $\mathbf{k}$ varies inside the* B.Z.. The photonic band structure is just the ensemble of photonic bands, with n running from 1 to ∞.

Before proceeding, it is worth to remark that the spectrum λ can be further classified by considering other symmetry properties of the photonic crystal [Joannopoulos, J. D., *et al.* (1995); Agio, M. (1999)]. For instance, the invariance of the master equation under time reversal yields $\omega_n(\mathbf{k}) = \omega_n(-\mathbf{k})$. This means that the band structure can be calculated reducing the B.Z. to non-negative Bloch vectors, since the other part has exactly the same spectrum. The invariance under discrete translations has already been considered and it leads to the Bloch theorem. Instead, the symmetry transformations with a fixed point (rotations, inversion, reflections), gathered in the point group of the crystal, have not been used yet. Thanks to these transformations, the calculation of the band structure can be reduced up to the so-called *irreducible Brillouin zone*. In Fig. 1.1, the irreducible Brillouin zone is marked with gray. Notice that the irreducible zone can be much smaller than the whole Brillouin zone, specially for three-dimensional photonic crystals.
Furthermore, to avoid solving the master equation for every point of the irreducible Brillouin zone, it is often enough to do it along the symmetry lines, because they correspond to a higher degree of symmetry with respect to the internal points and, for this reason, they are more representative.

1.2.3 The Photonic Band Gap

A photon with energy ω propagates in a photonic crystal, only if $\exists\,(\mathbf{k}, n) : \omega = \omega_n(\mathbf{k})$. Thus, *the spectral region $[\omega_1, \omega_2]$ for which $\forall\,\omega \in [\omega_1, \omega_2], \nexists\,(\mathbf{k}, n) : \omega = \omega_n(\mathbf{k})$ is called the photonic band gap.* Photonic band gap means that in the frequency window $[\omega_1, \omega_2]$ there is a null density Of states (D.O.S.) $\rho(\omega)$, which is defined as

$$\rho(\omega) = \sum_n \sum_{\mathbf{k}\in \text{B.Z.}} \delta(\omega - \omega_n(\mathbf{k})) \tag{1.17}$$

The D.O.S. is another important quantity characterizing the photonic crystal. Contrary to the smooth D.O.S. for an homogenous medium, the D.O.S. of a photonic crystal presents jumps with peaks and dips around a mean value given by the effective medium theory [Kirchner, A., *et al.* (1998)]. The calculation of the D.O.S. is an important check for the existence of a photonic band gap, because it accounts for all the Bloch vectors in the B.Z., whereas the band structure is often limited to the symmetry lines of the B.Z.. However, the present discussion deals only with results on the band structure.

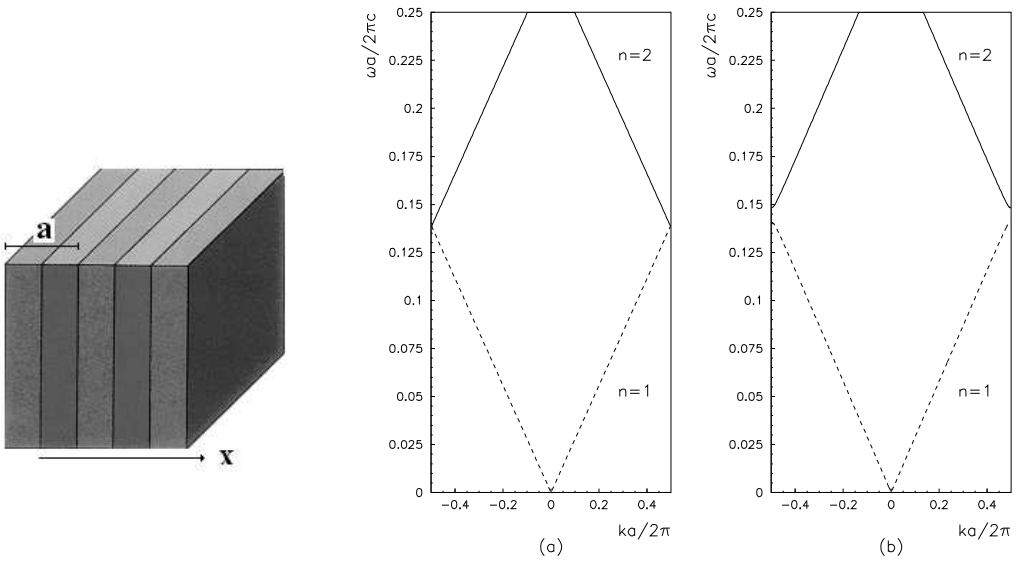

Figure 1.2 The formation of a band gap in a 1D photonic crystal. Left: the multilayer as 1D photonic crystal; a is the lattice constant and l_1, l_2 are the thicknesses of the layers. Right: (a) Free-photon dispersion relation for a medium with $\epsilon_{\rm d} = 13$ folded in the 1D Brillouin zone. (b) Photonic bands of a multilayer; parameters: $\epsilon_1 = 11$, $\epsilon_2 = 13$ and $l_2/l_1 = 1$. n is the band index.

To better understand the concept of photonic band structure and the formation of a photonic band gap, it is convenient to consider the photonic band structure of a simple one dimensional system: the multilayer. The left image in Fig. 1.2 is an example of a one-dimensional photonic crystal obtained stacking layers of two dielectric media. The lattice constant is a and the periodicity is along the x axis; the system is homogenous in the other directions y, z. Recalling Eqs. (1.14)

and (1.15) the B.Z. is $(-\pi/a, \pi/a]$. The right panel of Fig. 1.2 compares the band structure of an homogenous medium (a), with the band structure of a multilayer (b) for propagation along the x axis, i.e. $\mathbf{k} = (k, 0, 0)$. The material parameters for both systems are given in the caption. The band structure (a) is obtained by simply folding the dispersion relation $\omega/c = k/\sqrt{\epsilon_{\rm d}}$ when it reaches the edge of the B.Z.. The band structure (b), instead, is calculated by numerical solution of the master equation. Notice that for the case (b) a band gap opens between the first two bands. The mathematical reason is that the free-photon bands n_1, n_2, which are degenerate for $k = \pi/a$, are split by the potential due to the periodic dielectric function, according to the perturbation theory of degenerate states. Physically, the modes with ω in the band gap undergo destructive interference that causes exponential decay as they travel through the layers. Indeed, for a wave propagating in a photonic crystal with $k = \pi/a$, the phase shift of the forward-mode after m unit cells is exactly $\exp(\imath kma) = (-1)^m$. The phase shift of the backward-mode, reflected at the m-th unit cell, is $-(-1)^m$, because of the -1 gained upon reflection. The backward-mode has to travel other m unit cells before returning to the starting point and accumulates another phase shift $(-1)^m$. The total phase shift for the backward-mode is $-(-1)^m(-1)^m = -1$. Therefore, the backward-mode returns always with destructive interference, independently of the unit cell where it was reflected.

Particular attention is needed for the two modes belonging to the lower and upper band edge: $\omega_1(\pi/a)$ and $\omega_2(\pi/a)$. They are extended modes since they are Bloch waves, but, at the same time, they should undergo destructive interference because of $k = \pi/a$. Actually, these modes are not propagating modes, their group velocity $\mathbf{v}_g = \hat{\mathbf{x}}\partial\omega(k)/\partial k$ is zero, but rather stationary waves[5].

As regards the first band, as $k \to 0$, also $\omega \to 0$. This is the long-wavelength limit, according to which, the photonic crystal can be treated has an effective homogenous medium, with a linear dispersion $\omega/c = k/\sqrt{\epsilon_{\rm eff}}$, where $\epsilon_{\rm eff}$ is the effective dielectric function. For a multilayer, $\epsilon_{\rm eff}$ has an analytical expression: $\epsilon_{\rm eff} = (\epsilon_1 l_1 + \epsilon_2 l_2)/a$ [Agranovich, V. M., *et al.* (1985)]. For papers on the effective dielectric function in two- and three-dimensional photonic crystals, refer to Datta, S., *et al.* (1993); Kirchner, A., *et al.* (1998); Halevi, P., *et al.* (1999).

[5] A propagating wave has only one phase factor $(\mathbf{k}\cdot\mathbf{r} - \omega t)$, whereas a stationary wave possesses two phase factors, one in space $(\mathbf{k}\cdot\mathbf{r})$ and another one in time (ωt).

Scaling properties

One of the differences between photonic crystals and conventional crystals is that photons, contrary to electrons, do not have a fundamental length. For electrons, the fundamental length is the Bohr radius $a_\circ$. This feature leads to the scaling invariance for the macroscopic Maxwell's equations. The photonic crystal can be expanded or reduced via the following transformation

$$\epsilon'(s\mathbf{r}) = \epsilon(\mathbf{r})\,, \tag{1.18}$$

with s as scaling parameter. It is easy to show that the eigenfunctions and the eigenvalues of the master equation scale with $\epsilon(\mathbf{r})$: $\mathbf{H}'(s\mathbf{r}) = \mathbf{H}(\mathbf{r})$ and $\omega' = \omega/s$. This property is of particular interest for experimentalist, because it allows the so-called lithographic tuning [Labilloy, D., *et al.* A (1997)]. The lithographic tuning consists of sampling a portion of the spectrum not by changing the wavelength of the source, but changing the lattice constant of the photonic crystal.
Another scaling properties is the following. Assume that the dielectric function is multiplied by a factor s,

$$\epsilon'(\mathbf{r}) = s^2\epsilon(\mathbf{r})\,. \tag{1.19}$$

In this case the eigenvectors do not change, whereas the eigenvalues scale according to s: $\omega' = \omega/s$. This implies that for a photonic crystal made of two media ϵ_1, ϵ_2, the eigenfrequencies depend only on the ratio ϵ_1/ϵ_2, within a multiplication factor s.

1.2.4 The Plane-Wave Expansion Method

After a decade of research in photonic-band-gap materials, several techniques have been proposed for solving Maxwell's equations [John, S., *et al.* (1988); Pendry, J. B., *et al.* (1992); Qiu, M., *et al.* A (2000)]. Nevertheless, the plane-wave expansion method has become the standard de facto for computing the band structure of semiconductor-based photonic crystals. The method is based on the truncation of the sum in Eq. (1.11), reducing the master equation to a matrix eigenvalue problem. The coefficients $c_n(\mathbf{k}+\mathbf{G})$ and the eigenfrequencies $\omega_n(\mathbf{k})$ are obtained by standard numerical diagonalization of the resulting "hamiltonian".

Since the basis functions $\mathbf{f_k}(\mathbf{r})$ are plane waves, the Eq. (1.11) is explicitly written as

$$\mathbf{H_k}(\mathbf{r}) = \sum_{\mathbf{G}\in\mathbb{G}} \sum_{\sigma} c_\sigma(\mathbf{k}+\mathbf{G})\hat{\mathbf{f}}_\sigma e^{\imath(\mathbf{k}+\mathbf{G})\cdot\mathbf{r}}\,, \tag{1.20}$$

where $\sigma = \sigma(\mathbf{k}+\mathbf{G})$ represents the two polarizations of $\hat{\mathbf{f}}_\sigma$, with $\hat{\mathbf{f}}_\sigma \cdot (\mathbf{k}+\mathbf{G}) = 0$. By truncating the index $\mathbf{G} \in \mathbb{G}$ to a cut-off $K : |\mathbf{G}| < K$, Eq. (1.20) becomes a finite expansion. The cut-off is the approximation imposed by the numerical method; in fact, it would be impossible to store infinite arrays in the computer memory. Eq. (1.20) is nothing but the Fourier expansion of the magnetic field truncated to a cut-off and $c_\sigma(\mathbf{k}+\mathbf{G})$ are its Fourier coefficients. The next step is to rewrite the master equation (1.5a) in the Fourier space by calculating the matrix elements of the "hamiltonian" operator $\hat{\mathbf{O}}$ on the plane-wave basis. The result is

$$\sum_{\mathbf{G}',\sigma'} \mathcal{H}^{\sigma,\sigma'}_{\mathbf{G},\mathbf{G}'} c_{\sigma'}(\mathbf{k}+\mathbf{G}') = \frac{\omega^2}{c^2} c_\sigma(\mathbf{k}+\mathbf{G})\,, \tag{1.21}$$

where the "hamiltonian" matrix is

$$\mathcal{H}^{\sigma,\sigma'}_{\mathbf{G},\mathbf{G}'} = |\mathbf{k}+\mathbf{G}||\mathbf{k}+\mathbf{G}'|\eta_{\mathbf{G},\mathbf{G}'} \begin{pmatrix} \hat{\mathbf{f}}_{\sigma_2}\cdot\hat{\mathbf{f}}_{\sigma'_2} & -\hat{\mathbf{f}}_{\sigma_2}\cdot\hat{\mathbf{f}}_{\sigma'_1} \\ -\hat{\mathbf{f}}_{\sigma_1}\cdot\hat{\mathbf{f}}_{\sigma'_2} & \hat{\mathbf{f}}_{\sigma_1}\cdot\hat{\mathbf{f}}_{\sigma'_1} \end{pmatrix} \tag{1.22}$$

and the matrix $[\![\eta]\!] = [\![\epsilon]\!]^{-1}$ is the inverse of the dielectric function Fourier transform

$$\epsilon_{\mathbf{G},\mathbf{G}'} = \frac{1}{A_\mathrm{c}} \int_{A_\mathrm{c}} \epsilon(\mathbf{r}) e^{\imath(\mathbf{G}-\mathbf{G}')\cdot\mathbf{r}} \mathrm{d}\mathbf{r}\,, \tag{1.23}$$

where A_c is the space occupied by the unit cell. $[\![\mathcal{H}]\!]$ is a square matrix with dimensions $2N \times 2N$, $[\![\eta]\!]$ and $[\![\epsilon]\!]$ have dimensions $N \times N$ instead; N is the number of $\mathbf{G}$ vectors below the cut-off. Likewise the "hamiltonian" operator $\hat{\mathbf{O}}$ associated to the master equation, $\mathcal{H}$ is hermitian with non-negative eigenvalues.

Eq. (1.22) is the eigenvalue problem for $[\![\mathcal{H}]\!]$. Standard numerical diagonalization of $[\![\mathcal{H}]\!]$ yields the eigenfrequencies $\omega_n(\mathbf{k})$ and, optionally, the coefficients $c_n(\mathbf{k}+\mathbf{G})$. Notice that for each diagonalization, the routine outputs a set $\omega_n(\mathbf{k})$, with $n = 1, \ldots, 2N$, corresponding to the energies of $2N$ bands for a fixed Bloch vector $\mathbf{k}$. In order to calculate the whole band structure, the operation has to be repeated for a certain ensemble of $\mathbf{k}$ vectors in the B.Z., usually the edges of the irreducible B.Z..

The truncation of the sum in Eq. (1.20) is the trick that allowed numerical solution of the master equation. In fact, the exact Fourier transform of the operator $\hat{\mathbf{O}}$ would be a matrix of infinite dimensions, whereas $[\![\mathcal{H}]\!]$ is limited to $2N \times 2N$. For this reason, the matrix eigenvalue problem is an approximation of Maxwell's equations and an error will occur in the calculated eigenfrequencies. Calling $\lambda_n(\mathbf{k})$ the true eigenvalue and $\lambda_n^{(N)}(\mathbf{k})$ the eigenvalue calculated with the numerical routine, the error committed in evaluating the band energies will be $\Delta_n^{(N)}(\mathbf{k}) = |\lambda_n(\mathbf{k}) - \lambda_n^{(N)}(\mathbf{k})|$. As $N \to \infty$, the "hamiltonian" $[\![\mathcal{H}]\!]^{(2N)}$ should approach the true Fourier transform of $\hat{\mathbf{O}}$ and, consequently, the band energies should converge to the true values, i.e. $\forall\, \mathbf{k}, \forall\, n;\ \Delta_n^{(N)}(\mathbf{k}) \to 0$ as $N \to \infty$. Now the issue is: is this statement true or not? Also, if true, how fast is the convergence? The core of the problem consists in the Fourier transform of the dielectric function $\epsilon(\mathbf{r})$, which enters the operator $\hat{\mathbf{O}}$ as $1/\epsilon(\mathbf{r})$. When the master equation is transformed into the Fourier space, there are two choices for the dielectric function: take the Fourier transform of $1/\epsilon(\mathbf{r}) \Rightarrow [\![\eta]\!] = [\![1/\epsilon]\!]$ or take the Fourier transform of $\epsilon(\mathbf{r})$ and invert the matrix $\Rightarrow [\![\eta]\!] = [\![\epsilon]\!]^{-1}$. Contrary to intuition, as $N \to \infty$, $[\![1/\epsilon]\!]^{(N)} \neq [\![\epsilon]\!]^{(N)^{-1}}$. This result stems from the jump discontinuities of the dielectric function at the interfaces among the media of the photonic crystal. The inequality signifies that the convergence of the plane-wave expansion method is not a trivial problem at all. In a paper on the factorization of Fourier series of discontinuous periodic functions, Li, L. (1996) gave mathematical foundations that the correct choice for uniform convergence is $[\![\eta]\!] = [\![\epsilon]\!]^{-1}$, which is called the inverse rule. The fact is that $[\![\epsilon]\!]^{-1}$ uniformly satisfies the boundary conditions for the electromagnetic field, while $[\![1/\epsilon]\!]$ does it only non uniformly. The idea of taking the inverse of the Fourier transform has been used since Ho, K. M., *et al.* (1990), but without the rigorous motivation given by Li, L. (1996). That is why it is also known as Ho's method. For instance, considering two-dimensional photonic crystals, the $\Delta_n^{(N)}(\mathbf{k})$ caused by $[\![\eta]\!] = [\![\epsilon]\!]^{-1}$ is below 1% already with N of the order of 100. With $[\![\eta]\!] = [\![1/\epsilon]\!]$, $\Delta_n^{(N)}(\mathbf{k})$ is still above 1% for more than 300 plane waves. The plane-wave expansion method is thus able to output accurate eigenfrequencies with a moderate CPU time, provided the inverse rule is used. Notice that standard diagonalization and inversion routines are $O(N^3)$ operations; i.e. doubling the number of plane waves increases the CPU time by eight times. That is why the method is very efficiently applied to two-dimensional photonic crystals. For three-dimensional photonic crystals, where the number of $\mathbf{G}$ vectors is of the order of one

thousand or more, the method start to approach its numerical limit as regards the CPU time and the accuracy of the diagonalization process. Nevertheless, improved algorithms of the plane-wave expansion method allow to use thousands of G vectors for an extremely accurate determination of the eigenfrequencies [Meade, R. D., *et al.* (1993)].

It has been shown that the electromagnetic problem for a photonic crystal can be treated within an operator formalism by recasting Maxwell's equations in a closed form for either the electric either the magnetic fields. The translational symmetry of the dielectric function implies that the solutions have to be Bloch waves. The frequency spectrum is organized in the band structure picture, with the classification of the energy levels in terms of Bloch vector $\mathbf{k}$ and band index n. The band structure is obtained by numerical solution of the master equation by means of the plane-wave expansion method. These concepts and tools can now be applied to the study of semiconductor-based two-dimensional photonic crystals.

1.3 Two-Dimensional Photonic Crystals

A two-dimensional photonic crystal is characterized by a dielectric function periodic in a plane and homogeneous in the direction perpendicular to it, see Fig. 1. In other words, choosing a reference frame $x - y - z$, the dielectric function is $\epsilon = \epsilon(x, y)$. Correspondingly, the system has a two-dimensional lattice with two primitive vectors in both direct and reciprocal space. The reciprocal primitive vectors are given by Eq. (1.15). The discussion is focussed on two-dimensional photonic crystals made of a triangular lattice of air holes in a semiconductor material, because it is one of the most attracting structures [Meade, R. D., *et al.* (1992); Labilloy, D., *et al.* A (1997); Kramper, P., *et al.* (2001); Galli, M., *et al.* A (2002)]. Moreover, the band structure is calculated only for in-plane propagation, that is $\mathbf{k} = (k_x, k_y, 0)$. Nevertheless, many results are valid for two-dimensional photonic crystals in general.

Fig. 1.3 shows a top view of the two-dimensional photonic crystal under investigation (left panel) and the corresponding reciprocal lattice, with the Brillouin zone and the symmetry lines (right panel). The holes radius is r, the lattice constant is a and ϵ is the background dielectric

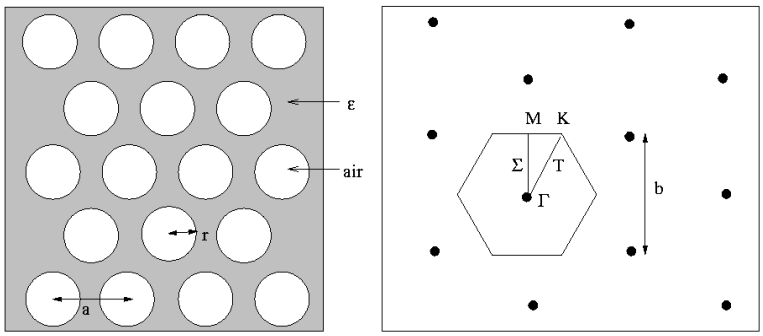

Figure 1.3 Top view of a 2D photonic crystal made of a triangular lattice of air holes, with radius r, in a medium with dielectric function ϵ (left panel). The corresponding 2D reciprocal space and the hexagonal Brillouin zone with symmetry points and lines (right panel). $a = |\mathbf{a}_i|$ is the direct space unit vector and $b = |\mathbf{g}_i|$ is the reciprocal space unit vector.

function. The primitive vectors are $\mathbf{a}_1 = a(1,0)$ and $\mathbf{a}_2 = a\left(\frac{1}{2}, \frac{\sqrt{3}}{2}\right)$, and the unit-cell area is $A_\mathrm{c} = a^2\frac{\sqrt{3}}{2}$. By using Eq. (1.15), the reciprocal-space primitive vectors are $\mathbf{g}_1 = \frac{2\pi}{a}\left(1, -\frac{1}{\sqrt{3}}\right)$ and $\mathbf{g}_2 = \frac{2\pi}{a}\left(0, \frac{2}{\sqrt{3}}\right)$.

For in-plane propagation, the electromagnetic field can be classified into two modes: H-modes and E-modes[6]. H-modes correspond to (E_x, E_y, H_z), E-modes to (E_z, H_x, H_y), where the field components are functions of x, y only; the other components are zero. This result stems from a symmetry property of the system: given a symmetry plane α, the electromagnetic field can be decomposed into modes that are even or odd for reflection with respect to α, see Fig. 1.4. For a two-dimensional photonic crystal, there are infinite mirror planes $\alpha \equiv x - y$ perpendicular to z, i.e. the electromagnetic field has to be even or odd for any plane, $\forall z_\circ \in \mathbb{R}, \alpha : z = z_\circ$. This condition is fulfilled only if the field components do not depend on z. The same result can be obtained working on the master equation (1.5a) and on the plane-wave expansion (1.20). For in-plane propagation, the basis functions $\mathbf{f}_{\mathbf{k}+\mathbf{G}}(\mathbf{r})$ do not depend on z, and so do the fields $\mathbf{E}_\mathbf{k}(\mathbf{r}), \mathbf{H}_\mathbf{k}(\mathbf{r})$. The polarizations σ are $\hat{\mathbf{f}}_{\sigma_1,\mathbf{k}+\mathbf{G}} = (0,0,1)$ and $\hat{\mathbf{f}}_{\sigma_2,\mathbf{k}+\mathbf{G}} = (f_x, f_y, 0) : \hat{\mathbf{f}}_{\sigma_2,\mathbf{k}+\mathbf{G}} \cdot (\mathbf{k}+\mathbf{G}) = 0$. Even though σ_2 depends on the vector $\mathbf{k}+\mathbf{G} = (k_x + G_x, k_y + G_y, 0)$, the distinction between σ_1 and σ_2 is independent

[6]In literature, another nomenclature is often found: TE-modes for H-modes and TM-modes for E-modes [Joannopoulos, J. D., *et al.* (1995)]; also p-modes for H-modes and s-modes for E-modes [Kirchner, A., *et al.* (1998)].

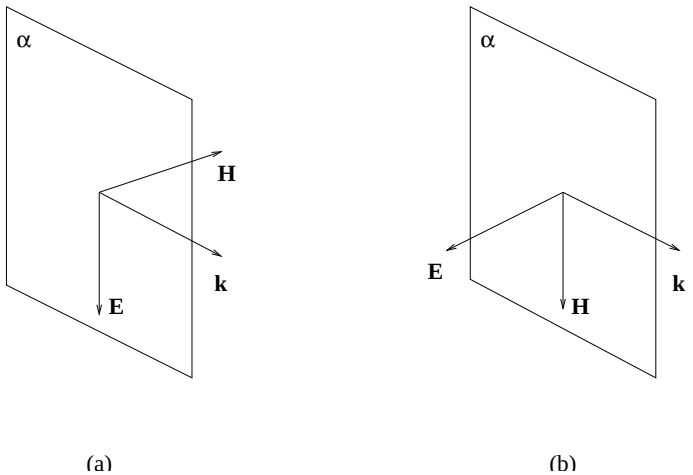

Figure 1.4 Even (a) and odd (b) modes with respect to a symmetry plane α. For in-plane propagation in a 2D photonic crystal, the electromagnetic field can be decomposed into H-modes (a) and E-modes (b).

of $\mathbf{k}+\mathbf{G}$, i.e. $\hat{\mathbf{f}}_{\sigma_1,\mathbf{k}+\mathbf{G}} \cdot \hat{\mathbf{f}}_{\sigma_2,\mathbf{k}+\mathbf{G}'} = 0 \; \forall \, \mathbf{G}, \mathbf{G}' \in \mathbb{G}$. Therefore, σ is a "good quantum number" for the eigenfunctions and the eigenvalues: $\mathbf{H}_{\mathbf{k},n,\sigma}(\mathbf{r})$, $\omega_{n,\sigma}(\mathbf{k})$. σ_1 corresponds to H-modes and σ_2 to E-modes. Plugging the polarizations in the master equation (1.5a), one obtains two different "hamiltonian" for σ_1 and σ_2. In the Fourier space, the master equation is split into

$$\sum_{\mathbf{G}'} (\mathbf{k}+\mathbf{G}) \cdot (\mathbf{k}+\mathbf{G}') \eta_{\mathbf{G},\mathbf{G}'} c_{\sigma_1}(\mathbf{k}+\mathbf{G}') = \frac{\omega^2}{c^2} c_{\sigma_1}(\mathbf{k}+\mathbf{G}) \,, \qquad \text{for } H\text{-modes;} \tag{1.24a}$$

$$\sum_{\mathbf{G}'} |\mathbf{k}+\mathbf{G}||\mathbf{k}+\mathbf{G}'| \eta_{\mathbf{G},\mathbf{G}'} c_{\sigma_2}(\mathbf{k}+\mathbf{G}') = \frac{\omega^2}{c^2} c_{\sigma_2}(\mathbf{k}+\mathbf{G}) \,, \qquad \text{for } E\text{-modes.} \tag{1.24b}$$

Eqs. (1.24a) and (1.24b) lead to two band structures, one for H-modes and one for E-modes respectively. Thus, a two-dimensional photonic crystal may have a band gap for one polarization, or both. In the latter case, the band gap is complete. Notice that the existence of the additional quantum number σ allows "hamiltonian" matrices with dimensions $N \times N$ in the plane-wave expansion method, whereas for out-of-plane propagation the dimensions are $2N \times 2N$, like for three-dimensional photonic crystals, where Eq. (1.21) must be used instead.

1.3.1 The Band Structure

The band structure is calculated along the symmetry lines of the Brillouin zone: $\Gamma - K, \Gamma - M, K - M$, see the right panel of Fig. 1.3, so that the Bloch vectors are given. The $\mathbf{G}$ vectors are constructed by linear combination of the reciprocal-lattice primitive vectors $\mathbf{g}_i$. The last ingredient is the explicit expression of the dielectric function Fourier transform. Performing the integral in Eq. (1.23), the result is

$$\epsilon_{\mathbf{G},\mathbf{G}'} = \begin{cases} (\epsilon_{\text{air}} - \epsilon_{\text{diel}}) \dfrac{2\pi r}{A_{\text{c}} G} J_1(Gr)\,, & \text{if } \mathbf{G} \neq \mathbf{G}'; \\ f\epsilon_{\text{air}} + (1-f)\epsilon_{\text{diel}}\,, & \text{if } \mathbf{G} = \mathbf{G}'; \end{cases} \tag{1.25}$$

where ϵ_{air} is the air dielectric constant (=1), ϵ_{diel} is the material dielectric function ($= \epsilon$), $G = |\mathbf{G} - \mathbf{G}'|$, $J_1(x)$ is the Bessel function of the first order and $f = \pi r^2 / A_{\text{c}}$ is the air filling factor.

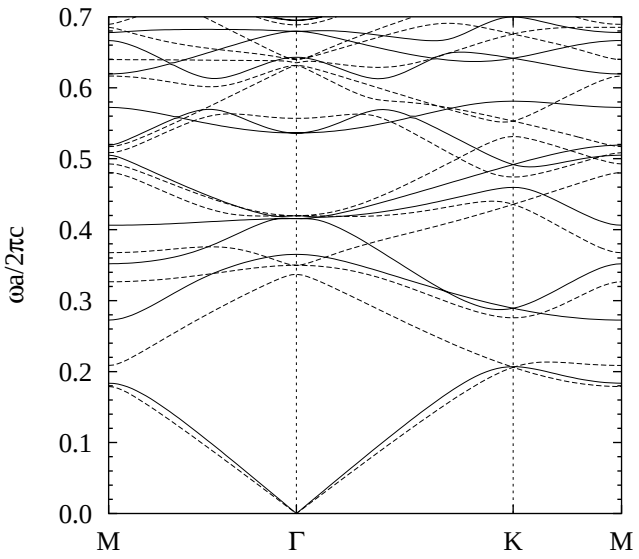

Figure 1.5 Photonic bands of a 2D photonic crystal made of a triangular lattice of air holes, with radius $r = 0.3a$, in a dielectric medium with $\epsilon = 12$. Solid (dashed) lines refer to H-modes (E-modes).

Fig. 1.5 displays the photonic band structure calculated[7] for air holes, with radius $r = 0.3a$, in a dielectric medium with $\epsilon = 12$, typically Si or GaAs in the near-infrared frequency regime. The system exhibits a photonic band gap only for H-modes (solid lines). For E-modes (dashed

[7]The number of plane waves used for the calculation is 109, if not otherwise stated.

lines), the band gap is closed by the second band. Notice that the first bands of both H-modes and E-modes have linear dispersion for $\omega \to 0$. This is the long-wavelength limit, already seen for the multilayer studied in Sec. 1.2.3. The H-modes and E-modes dispersions have different slope for $\omega \to 0$, i.e. the two modes have different effective dielectric function. The effective dielectric function for E-modes is given by the analytical formula

$$\epsilon_{\text{eff}} = f\epsilon_{\text{air}} + (1-f)\epsilon_{\text{diel}} = \epsilon_{\mathbf{G},\mathbf{G}}\,, \tag{1.26}$$

which is exactly the formula for the multilayer, with l_1, l_2 replaced by $f, (1-f)$. The effective dielectric functions for H-modes does not have an analytic expression. Effective medium theory gives two bounds for the effective dielectric function of H-modes. The true value is comprised between the Maxwell-Garnett result

$$\epsilon_{\text{eff}} = \epsilon_{\text{diel}}\left(1 + \frac{2f\alpha}{1-f\alpha}\right)\,, \tag{1.27}$$

where $\alpha = (\epsilon_{\text{air}} - \epsilon_{\text{diel}})/(\epsilon_{\text{air}} + \epsilon_{\text{diel}})$ is the depolarization factor, and the inverse Maxwell-Garnett, obtained by interchanging the filling fractions, f and $1-f$, and the dielectric functions ϵ_{air} and ϵ_{diel}. The correct value is given by numerical solution of complicated equations [Kirchner, A., *et al.* (1998); Halevi, P., *et al.* (1999)]. Thus, in the long-wavelength limit, a two-dimensional photonic crystal behaves like an homogenous uniaxial crystal[8], where the optical axis is along the z direction and the dielectric functions $\epsilon_{\parallel}$ and $\epsilon_{\perp}$ are the effective values for E-modes and H-modes respectively. For two-dimensional photonic crystals $\epsilon_{\parallel} > \epsilon_{\perp}$ always. The effective dielectric tensor reads

$$\overline{\epsilon} = \begin{pmatrix} \epsilon_{\perp} & 0 & 0 \\ 0 & \epsilon_{\perp} & 0 \\ 0 & 0 & \epsilon_{\parallel} \end{pmatrix} \tag{1.28}$$

For finite frequencies the photonic crystal effects become important and the mean field approximation is more complicated [Kirchner, A., *et al.* (1998)]. Nevertheless, it is still meaningful to speak in terms of effective dielectric function as the zero-th term in a perturbative expansion of the band structure [Cassagne, D., *et al.* (1996); Agio, M. (1999)].

[8]That is true for the square and the triangular lattices. For lattices with a lower symmetry the crystal is biaxial, with two effective dielectric functions for H-modes. See Ref. Halevi, P., *et al.* (1999).

Looking again at Fig. 1.5, it is found that H-modes have a photonic band gap also around $\omega a/2\pi c \sim 0.6$. However, the band gaps lying at higher frequencies are more sensitive to disorder, contrary to the first band gap at $\omega a/2\pi c \sim 0.25$. Indeed, for the higher bands, the coefficients $c_\sigma(\mathbf{k}+\mathbf{G})$ with large $\mathbf{k}+\mathbf{G}$ vectors have a stronger weight in the plane-wave expansion, contrary to what happens for the lower bands. Disorder primarily affects the coefficients with large $\mathbf{k}+\mathbf{G}$ vectors, because they correspond to plane waves with small wavelength, more sensitive to roughness and other irregularities. Since disorder is practically unavoidable in real samples, it is important to devise photonic crystals where the desired properties are robust. With the current degree of quality in the manufacturing processes of micron-size photonic crystals, one has to work with the first bands [Benisty, H., *et al.* (1999)]. For a thorough analysis of disorder effects in two-dimensional photonic crystal see Ref. Lidorikis, E., *et al.* (2000).

It has been shown that the band structure of Fig. 1.5 exhibits band gaps only for H-modes. However, this is only the result of a particular choice of r and ϵ. It is interesting to see what happens if one of the two parameters is varied. In theory, one could change the dielectric function ϵ, but in practice, its value is determined by the choice of the material, which is very important and, usually, has the precedence over the other parameters. For the most common semiconductor-based photonic crystals (Si, GaAs, InP), ϵ is within 11-12. For this reason, only the hole radius is considered as a free parameter.

Gap Maps

The existence of a complete photonic band gap is one of the most attracting features of photonic crystals. If one wants to know whether the structure of Fig. 1.3 has a full band gap, or simply locate the band gaps for each polarization, it would be necessary to examine a large number of band structures, one for a given value of the hole radius r. It turns out, that is more convenient and clear to visualize only the edges of the photonic band gap as a function of r in the the so-called *gap map*. Fig. 1.6 shows the band gaps for the parameters of Fig. 1.5, with r/a varying from 0 to 0.5, which corresponds to the closed-packed condition. There is a wide band gap for H-modes (solid lines) that opens for $r \geq 0.17a$ and increases with the hole radius until it reaches the maximum value for $r \sim 0.45a$. Another band gap for H-modes occurs for a smaller range of r and at higher

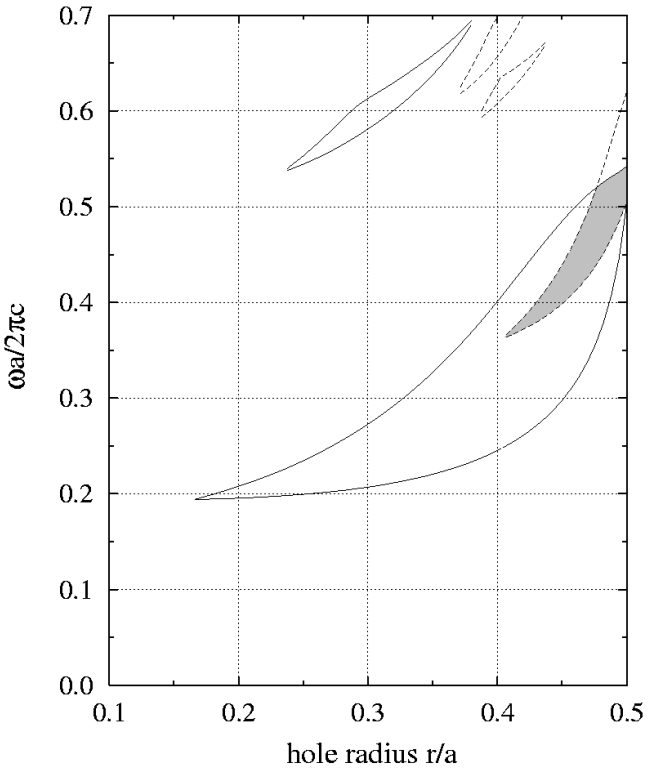

Figure 1.6 Gap map for the photonic crystal of Fig. 1.5. The regions delimited by solid (dashed) lines refer to H-modes (E-modes). A complete photonic band gap opens for $r > 0.41a$ (gray shaded area).

frequencies. This is the second gap seen in the band structure of Fig. 1.5, where $r = 0.3a$.

Concerning the other polarization (dashed lines), the lowest frequency band gap is located around $r = 0.45a$, with a steep profile that covers the frequency range $\omega a/2\pi c \sim 0.35 - 0.6$. Smaller band gaps appear at higher frequencies for $r \sim 0.4a$. The map of the complete band gap is determined by the intersection of the H-modes band gaps with the E-modes band gaps. This happens only for $r > 0.41a$ in the frequency window $\omega a/2\pi c \sim 0.35 - 0.55$ (gray shaded area). It is worth to mention that the gap edges shift towards higher frequencies as the radius increases, in accordance to the reduction of the effective dielectric constants $\epsilon_{\parallel}$ and $\epsilon_{\perp}$.

In order to obtain a complete photonic band gap in this system, it is necessary to have a high air fraction. Such condition might be critical from the experimental point of view, because of intrinsic

limits in the fabrication process. In fact, it would be difficult to reach high aspect ratios with holes walls as thin as membranes. The alternative is to release the requirement of a full band gap and work with a partial band gap using polarized light. For a two-dimensional photonic crystal of air holes in a semiconductor one finds convenient to exploit the wide band gap given for H-polarization. This point will be deepened in the chapter dedicated to wave propagation, where the existence of a band gap is fundamental. Here and in the next chapter the attention addresses the band structure as a whole, so that the peculiarity of a full band gap has a relative importance.

1.3.2 Symmetry Properties

The eigenvalues of the master equation (1.5a) are interpreted in terms of Bloch vector and band index within the photonic band picture. Moreover, for in-plane propagation in two-dimensional photonic crystals, the polarization is used as a further classification of the eigenfrequencies. All of that is founded on certain symmetry properties of the system. The Bloch vector is a consequence of the periodicity of the dielectric function, the separation into H-modes and E-modes stems from a mirror symmetry. In the last paragraph of Sec. 1.2.2, it has already been mentioned how symmetry can be exploited to work out the irreducible Brillouin zone. The aim of this section is to introduce the use of group theory in studying the photonic band structure, in analogy to what has been done for the symmetry analysis of electronic states in solids [Bassani, F., *et al.* (1975)]. The system under investigation is always the two-dimensional photonic crystal of Fig. 1.3; however, in this case, the hole radius is $r = 0.2a$, the lattice constant is given, $a = 3\mu$m, and the energies are expressed in electron-Volt (eV).

Since the Bloch theorem already accounts for the translation invariance, the attention will be focussed only on the *point group* of the system, which contains all the symmetry operations with a fixed point. The photonic bands with Bloch vector $\mathbf{k}$ can be classified according to the *small point group* at $\mathbf{k}$. The small point group is the subgroup that leaves $\mathbf{k}$ invariant (apart from a reciprocal lattice vector). The symmetry of a state $\mathbf{H_k}(\mathbf{r})$ is determined by the transformation rule given in Eqs. (1.8), where $\hat{\mathbf{T}}_\mathbf{R}$ is replaced by the operator associated to a transformation belonging to the small point group. The electric field and the magnetic field components transform like a vector and a pseudo-vector respectively. The symmetry properties related to the spatial coordinate $\mathbf{r}$ are

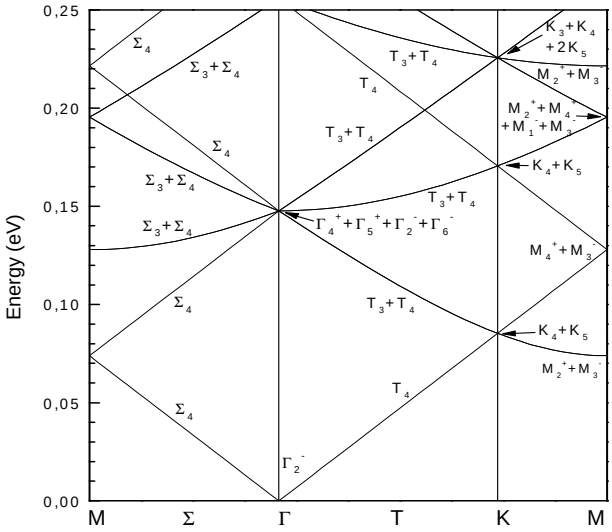

Figure 1.7 Empty lattice bands for the photonic crystal shown in Fig. 1.3. The average dielectric constant is $\epsilon_{\|} = 10.4$, the lattice constant is $a = 3\mu$m and the energies are in electron-Volt (eV). The symmetry labels refer to E-modes.

found looking at the profile of $\mathbf{H_k}(\mathbf{r})$ and $\mathbf{E_k}(\mathbf{r})$. The notation is taken from Koster, G. F., *et al.* (1963).

The point group for a triangular lattice with cylindrical holes is D_{6h}, which is useful to view as the direct product of C_{6v} and C_s. C_{6v} has a six-fold rotation axis (z) and six mirror planes that form 60° angles among each other. C_s contains the identity and the reflection σ_{xy}. The small point groups at the main symmetry points are D_{2h} at M and D_{3h} at K. The small point group along the symmetry lines is C_{2v} for the $\Gamma - M$, $\Gamma - K$ and $M - K$ directions. Notice that the twofold axis of C_{2v} differs for the three cases. For off-plane propagation, the specular reflection σ_{xy} is not a symmetry operation anymore and the point group remains C_{6v} only. The discussion will be restricted to in-plane propagation.

For studying the electronic states in solids, it is often useful to work with the empty-lattice scheme, which consists of the free-electron levels folded in the Brillouin zone for a given Bravais lattice. A similar methodology can be applied to photonic bands, choosing the free-photon dispersion given for an homogenous medium with the effective dielectric tensor of Eq. (1.28). Since the system is

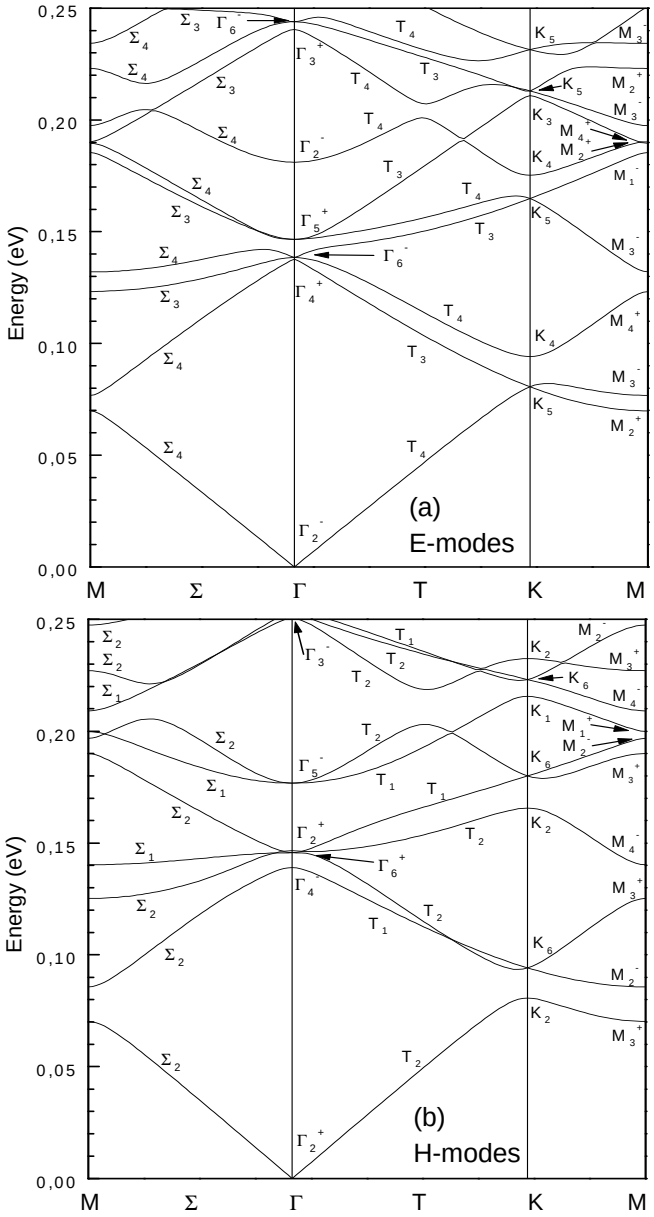

Figure 1.8 Photonic bands of the 2D photonic crystal of Fig. 1.3: (a) E-modes, (b) H-modes. The lattice constant is $a = 3\mu$m, the hole radius is $r = 0.2a$ and the material dielectric constant is $\epsilon = 12$.

uniaxial, H-modes and E-modes have to be studied separately. Nevertheless, since the air fraction is small ($f = 14.5\%$), H-modes can be treated with the same dispersion of E-modes with good approximation: $\epsilon_{\|} \sim \epsilon_{\perp}$.

Fig. 1.7 shows the empty-lattice photonic bands for the considered structure, whose average dielectric function is given by Eq. (1.26), that is $\epsilon_{\|} = 10.4$. The folding of the free-photon dispersion gives rise to degeneracies at the symmetry points and lines. The symmetry labels in Fig. 1.7 refer to E-modes. They are derived by finding the characters of the symmetry operations of the small point group acting on degenerate plane waves, and decomposing the resulting representation into irreducible representations. For clarity, the procedure for the states at the Γ point is reported in detail.

The first state ($\omega = 0$) corresponds to the plane wave with $\mathbf{G} = (0, 0)$, which transforms like the identical representation. Taking into account the symmetry of the transformation properties of the electric field component E_z, the symmetry of this state is Γ_2^-. The next state at Γ consists of the plane waves with $\mathbf{G} = b(0, \pm 1), b(\pm\frac{\sqrt{3}}{2}, \pm\frac{1}{2})$, where $b = \frac{4\pi}{\sqrt{3}a} = |\mathbf{g}_i|$, and is six-fold degenerate. The characters of the symmetry operations, taking into account the spatial dependence of the plane waves as well as the transformation properties of the E_z field component, are

E	C_2	$2C_3$	$2C_6$	$3C_2'$	$3C_2''$	I	σ_h	$2S_6$	$2S_3$	$3\sigma_v$	$3\sigma_d$
6	0	0	0	-2	0	0	-6	0	0	2	0

and can be decomposed into the irreducible representations $\Gamma_4^+ + \Gamma_5^+ + \Gamma_2^- + \Gamma_6^-$. In a similar manner one classifies the other states.

Fig. 1.8 displays the calculated photonic band structure for $\epsilon = 12$ and $r = 0.2a$. Most of the degeneracies of the empty lattice have been removed because of the potential due to the dielectric function. Only the degeneracies imposed by the irreducible representations of the small point group remain. The photonic bands at Γ and at K are non-degenerate or twofold degenerate; the bands at the M point and along the lines are non-degenerate. In particular, notice that the twofold degenerate states at Γ can have Γ_5^+ or Γ_6^- symmetry for E-modes and Γ_5^- or Γ_6^+ symmetry for H-modes. This originates from the different transformation properties of the electric and magnetic field under the inversion operation. Along the lines, bands with the same symmetry anti-cross, while bands

with different symmetry cross each other.

In conclusion, the photonic band structure of a two-dimensional photonic crystal can be classified according the the irreducible representations of the small point group. For in-plane propagation, the main consequence of symmetry is the decoupling of the electromagnetic field into H-modes and E-modes. The use of group theory is helpful in understanding the formation of the photonic band structure, with emphasis on the removal of degeneracy and on the crossing/anti-crossing of photonic bands. These results are also important for the interpretation of the optical properties of photonic crystals; for instance, the coupling of the Bloch waves with the external field.

As regards the photonic band gap, a two-dimensional photonic crystal made of a triangular lattice of air holes in a dielectric medium exhibits a band gap for H-modes in a wide range of the hole radius r. A complete band gap is found only for large filling ratios. Controlling light propagation by means of a full band gap in a two-dimensional photonic crystal is quite a problem, because of the absence of vertical confinement. This issue might preclude the use of two-dimensional photonic crystals for certain functionalities. Moreover, a practical realization of a two-dimensional photonic crystal in the near infrared is available only with macro-porous silicon [Lehmann, V., *et al.* (1990); Birner, A., *et al.* (1998)]. Also, the fabrication process of macro-porous silicon photonic crystals does not easily allow the integration with electronic circuitry or the inclusion of active layers, for instance, making its technological potential somewhat limited.

A plausible solution to all of these problems is the concept of finite-height two-dimensional photonic crystal [Meade, R. D., *et al.* (1994)]. The idea is to etch a two-dimensional photonic crystal in a planar dielectric waveguide so that the in-plane confinement is provided by the band gap, while the vertical confinement is given by the conventional total internal reflection. Such structures can be fabricated with top-down processes using lithographic techniques, which allow the integration of metal contacts, quantum wells and other nano-structures. However, these promising statements involve new issues that has to be understood, like the modification of the photonic band structure with respect to the ideal two-dimensional case or the occurrence of out-of-plane diffraction losses. The next section is aimed to formalize the new concepts and study the band structure of two-dimensional photonic-crystal slabs.

1.4 Two-Dimensional Photonic-Crystal Slabs

A two-dimensional photonic-crystal slab is made of a planar dielectric waveguide that is deeply etched according to a two-dimensional pattern. In other words, the dielectric function is periodic in the $x-y$ plane and is a step-wise function in the vertical direction z: $\forall \mathbf{R} \in \mathbb{V}, \forall z \in \mathbb{R}; \epsilon(\mathbf{x}+\mathbf{R}, z) = \epsilon(\mathbf{x}, z)$, with $\mathbf{x} = (x, y)$ and $\mathbb{V}$ is the vector space associated to the two-dimensional lattice. The number of parameters involved in the characterization of these systems is large: the structure of the planar waveguide (layers, thicknesses, dielectric functions), the two-dimensional photonic crystal (lattice and unit cell) and the etch depth. Nevertheless, there are few representative cases that are able to address all the important features pertaining to two-dimensional photonic-crystal slabs. Since the attention is focussed on the effects due to the planar waveguide, the photonic crystal pattern is chosen una tantum as a triangular lattice of air holes. At this stage, the etch depth is considered as infinite.

Planar waveguides can be divided into two main classes: symmetric and asymmetric waveguides; the symmetry is referred to reflection with respect to a plane placed in the middle of the core layer. For a symmetric waveguide, the cladding layers above and below the core are equal. Then, the waveguide may give strong or weak confinement depending on the dielectric contrast between core and cladding. The configurations that are presented here regard two symmetric waveguides, one with strong confinement and the other one with weak confinement. For the case of an asymmetric waveguide, please refer to Patrini, M., *et al.* A (2002) and Peyrade, D., *et al.* (2002). Fig. 1.9 gives examples of planar waveguides patterned with a triangular lattice of air holes. The thickness of the core layer is d, whereas the cladding layers are considered as semi-infinite. The low panels display three types of planar waveguide: (d) a dielectric self-standing membrane, also known as *air bridge*, (e) waveguide based on a semiconductor heterostructure, for instance a GaAs/AlGaAs system, (f) waveguide with strong asymmetry, like a silicon-on-insulator wafer. The air bridge is a typical strong-confinement waveguide, while the GaAs/AlGaAs system belongs to the weak-confinement case; both waveguides are symmetric. The values of the dielectric function given in Fig. 1.9 are appropriate to typical semiconductors (Si, GaAs, AlGaAs).

The photonic band structure of these systems is more complicated than for ideal two-dimensional

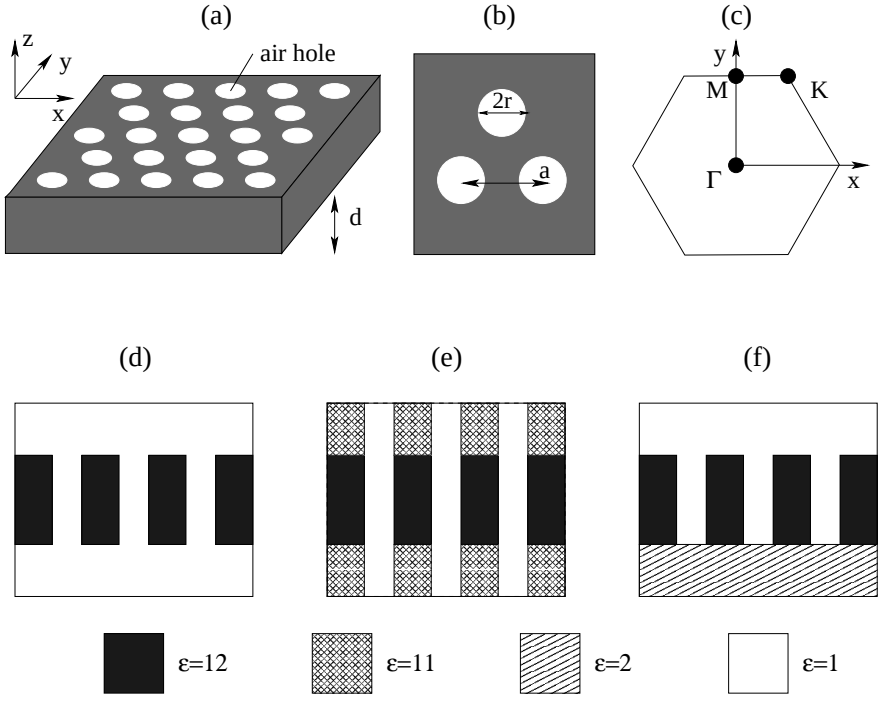

Figure 1.9 Upper panels: (a) slab waveguide of thickness d patterned with a triangular lattice of air holes, (b) top view, (c) the 2D Brillouin zone with symmetry points. Lower panels: (d) strong-confinement symmetric waveguide, i.e. patterned self-standing dielectric membrane (*air bridge*), (e) weak-confinement symmetric waveguide (e.g. patterned *AlGaAs-GaAs-AlGaAs* system), (f) patterned asymmetric waveguide (e.g. *silicon-on-insulator*).

photonic crystals, because of the finite-height of the two-dimensional pattern. For symmetric waveguides, the modes are still even or odd with respect to the mid-plane of the core layer. However, they are not H-modes or E-modes anymore, because the fields are also function of the z coordinate. Nevertheless, it makes sense to call them H-like modes or E-like modes. For asymmetric waveguides such separation breaks down and the band structure has to be calculated by solving the master equation with all the transverse field components. However, the main complication with respect to two-dimensional photonic crystals consists of the so-called *light-line problem* and of the existence of Bloch modes with a cut-off. In fact, these structures support two kinds of modes. If the waveguide thickness is not too small, guided modes exist whose energies lie below the light line of the cladding material (or light lines, if the waveguide is asymmetric). These modes are true stationary Bloch

states and, ideally, they are not subject to propagation losses. Above the light line of the cladding material, the spectrum becomes a continuum of states with resonances called *quasi-guided modes*. Since these modes lie within the leaky modes of the waveguide, they exhibit intrinsic propagation losses due to out-of-plane diffraction. Moreover, the planar waveguide can be mono-mode or multi-mode in the frequency region of interest. If the waveguide is multi-mode, there will be Bloch waves with a cut-off corresponding to the onset of a higher-order mode in the planar waveguide. All of these concepts appear in the photonic band structure.

As already discussed in Sec. 1.1, there are three numerical methods that solve Maxwell's equations for two-dimensional photonic-crystal slabs: the plane-wave expansion method, with a super-cell in the vertical direction that accounts for the waveguide [Johnson, S. G., *et al.* (1999)], the finite-difference time-domain method [Ochiai, T., *et al.* A (2001)], and the scattering matrix method [Whittaker, D. M., *et al.* (1999)]. Each one has its advantages and its flaws. In particular, the plane-wave expansion method with the super-cell is limited to energies below the light line; the finite-difference time-domain method is time consuming and less accurate than frequency-domain methods; the scattering-matrix method does not directly outputs the band structure. In the next section, a novel method is presented [Andreani, L. C. (2002)]; the photonic band structure is calculated by expanding the magnetic field in the basis of guided modes of the planar waveguide, where each layer is taken to have an average dielectric function. The approach goes beyond the nearly-free approximation of Ochiai, T., *et al.* B (2001), since no perturbative assumption is required, and it is valid also for strong modulation of the dielectric function.

1.4.1 Numerical Method

The basic idea underneath this method is the expansion of the magnetic field in terms of the guided modes of an "effective" waveguide, in place of a super-cell with plane-waves. Each basis mode is then folded in the two-dimensional Brillouin zone, where it is coupled by the inverse dielectric tensor $\eta_{\mathbf{G},\mathbf{G}'}$, just like plane waves in a two-dimensional photonic crystal. The eigenstates falling below the light line are identified as guided modes, whereas those above the light line represent the guided resonances.

The importance of using guided modes instead of plane waves is readily explained. Below the light

line, the spectrum is discrete, $\omega_n(\mathbf{k})$, and the modes exhibit exponential decay in the cladding; above it is continuum, $\omega_\rho(\mathbf{k})$, and the modes have an oscillatory profile in the cladding. If the spectrum is discrete, an expansion with N plane waves yields N eigenstates with increasing energy: $\omega_1(\mathbf{k}), \omega_2(\mathbf{k}), \ldots, \omega_N(\mathbf{k})$. Also, if the super-cell is large enough, the overlap among guided modes of nearest super-cells is negligible, because the mode profile decays exponentially in the cladding. When the spectrum becomes continuum, there are two issues with the super-cell method. First of all, since the mode profile is not evanescent in the cladding, there will be interaction among modes of neighboring super-cells, causing an error in the evaluation of the eigenfrequencies. Secondly, the diagonalization of the hamiltonian will give only the states of the continuum that are just above the light line. In fact, if $\omega_{\mathrm{LL}}(\mathbf{k})$ is the frequency of the light line for Bloch vector $\mathbf{k}$, $\forall\, \epsilon > 0, \exists\, \omega_\rho(\mathbf{k}) : \omega_{\mathrm{LL}}(\mathbf{k}) < \omega_\rho(\mathbf{k}) < \omega_{\mathrm{LL}}(\mathbf{k}) + \epsilon$. Thus, given any number N of plane waves, all the eigenfrequencies above the light line will lie in an infinitesimal around of the accumulation point $\omega_{\mathrm{LL}}(\mathbf{k})$. In other words, the plane-wave expansion does not pick up the resonances of the continuum, but it yields the first states, without exception, starting from the light line and within an infinitesimal interval of $\omega_{\mathrm{LL}}(\mathbf{k})$. That is why the plane-wave expansion is valid only for modes below the light line, where the spectrum is discrete, and not for the resonances.

As already mentioned, the numerical method proposed by Andreani, L. C. (2002) avoids the use of a super-cell and expands the electromagnetic field in an orthonormal set of guided modes of an effective waveguide. The great advantage is that the method is able to calculate the dispersion relation of the resonances. Within this approach, both modes above and below the light line are considered as truly guided, so that the spectrum is discrete, formally. This avoids the problem encountered with the plane-wave expansion. Indeed, while plane waves form a complete basis set, the expansion on guided modes is not such, because leaky modes are missing. Therefore, the two "hamiltonian" differ: if $\mathcal{H}$ is the "hamiltonian" in the plane-wave expansion and $\omega_n(\mathbf{k}), \omega_\rho(\mathbf{k})$ is the spectrum (discrete and continuum), the "hamiltonian" in the guided-modes expansion will be $\widetilde{\mathcal{H}}$ with spectrum $\tilde{\omega}_n(\mathbf{k})$ only discrete. Below the light line, the assumption is that $\tilde{\omega}_n(\mathbf{k}) \sim \omega_n(\mathbf{k})$ with good approximation. The eigenfrequencies above the light line simply represent the frequencies of the resonances, $\tilde{\omega}_n(\mathbf{k})$, with zero line-width. The method is not exact, in principle, and its validity relies on the contribution of leaky modes to the eigenfrequencies. The assumption is that

the frequency shift due to coupling with leaky modes of the effective waveguide is small, if not negligible, for both guided and quasi-guided modes. As to the spectrum below the light line, very good agreement has been found in comparison with the super-cell method. Concerning the modes above the light line, the method has been tested with results in the literature [Ochiai, T., *et al.* A (2001)] and, indirectly, with the scattering-matrix method [Andreani, L. C. (2002)]. Also for this case the agreement is very good.

The implementation of this method is not much different from the plane-wave expansion method. The basis set is chosen to consist of the guided modes of an effective planar waveguide, where each layer j has the homogenous dielectric function given by the spatial average of $\epsilon_j(\mathbf{x})$ within the unit cell; i.e. the diagonal elements of the dielectric matrix $\epsilon_{j,\mathbf{G},\mathbf{G}}$, see Eq. (1.26). Therefore, in Eq. (1.20), the plane waves are replaced by the guided modes, and the magnetic field is

$$\mathbf{H}_{\mathbf{k}}(\mathbf{r}) = \sum_{\mathbf{G}\in\mathbb{G}} \sum_{\alpha} c_{\alpha}(\mathbf{k}+\mathbf{G}) \hat{\mathbf{f}}_{\alpha}(z) e^{\imath(\mathbf{k}+\mathbf{G})\cdot\mathbf{x}}\,, \tag{1.29}$$

where $\hat{\mathbf{f}}_{\alpha}(z)e^{\imath(\mathbf{k}+\mathbf{G})\cdot\mathbf{x}}$ represents a guided mode with wave-vector $\mathbf{k}+\mathbf{G}$; α is a discrete index that labels the guided mode, $\mathbf{k}$ is the Bloch vector and $\mathbf{G}$ are reciprocal vectors of the two-dimensional lattice. Likewise for the plane-wave expansion method, the $\mathbf{G}$ vectors are limited by a cut-off K and the master equation is transformed into a linear eigenvalue problem

$$\sum_{\mathbf{G}',\alpha'} \mathcal{H}^{\alpha,\alpha'}_{\mathbf{G},\mathbf{G}'} c_{\alpha'}(\mathbf{k}+\mathbf{G}') = \frac{\omega^2}{c^2} c_{\alpha}(\mathbf{k}+\mathbf{G})\,, \tag{1.30}$$

where the "hamiltonian" matrix is given by

$$\mathcal{H}^{\alpha,\alpha'}_{\mathbf{G},\mathbf{G}'} = \int \frac{1}{\epsilon(\mathbf{r})} \left(\nabla \times \mathbf{f}_{\alpha}(z) e^{-\imath(\mathbf{k}+\mathbf{G})\cdot\mathbf{x}}\right) \left(\nabla \times \mathbf{f}_{\alpha'}(z) e^{\imath(\mathbf{k}+\mathbf{G}')\cdot\mathbf{x}}\right) \mathrm{d}\mathbf{r}\,. \tag{1.31}$$

The matrix elements $\mathcal{H}^{\alpha,\alpha'}_{\mathbf{G},\mathbf{G}'}$ of Eq. (1.31) can be calculated by noting that the $\mathrm{d}\mathbf{x}$ integral in each layer j yields the matrix Fourier transform $[\![\epsilon_j^{-1}]\!]$ of the inverse dielectric function. This is the same quantity that appears in the two-dimensional case and is computed using the inverse method $[\![\epsilon_j^{-1}]\!] \Rightarrow [\![\eta_j]\!]$.

Besides a wave-vector cut-off K, it is also convenient to specify a maximum number of guided modes of the effective waveguide. 109 plane waves are found to give stable photonic bands up to $\omega a/2\pi c \sim 0.7$ in the whole range of hole radii from zero to the close-packing condition $r = 0.5a$.

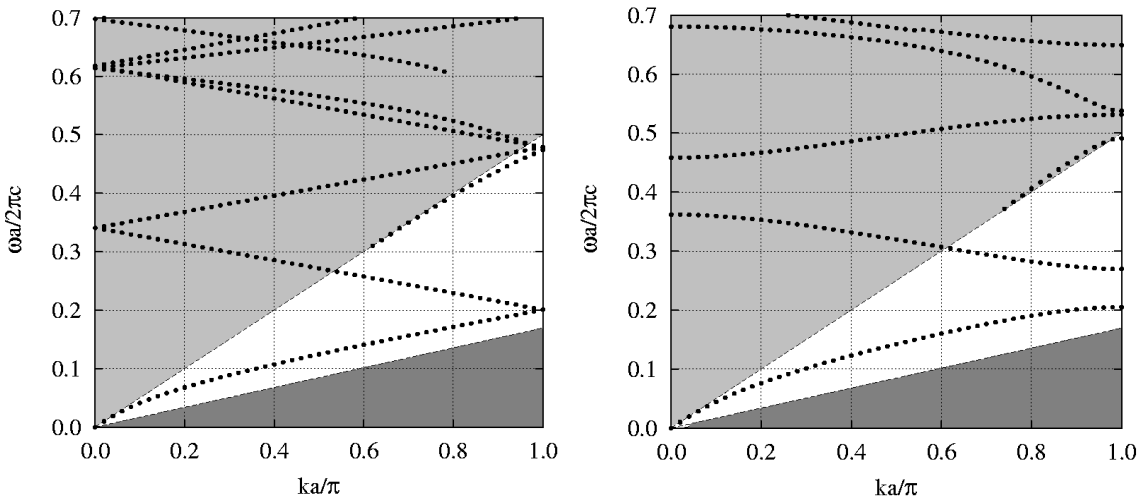

Figure 1.10 Left (right) panel: empty-lattice (photonic) bands for a self-standing dielectric membrane, patterned with a 1D lattice with air filling ratio $f = 30\%$. The width of the waveguide is $d/a = 0.5$ and the core dielectric function is $\epsilon = 12$. The dashed lines delimit the guided-mode region (white area) and refer to the dispersion of light in air and in the effective core material ($\epsilon = 8.7$). Light gray is for the leaky mode region, dark gray is where no solutions can exist.

For symmetric waveguides, keeping four guided modes in each parity sector gives also very good convergence, except when the waveguide is so thick that several higher-order modes are required.

1.4.2 The Photonic Band Structure

The photonic band structure of photonic-crystal slabs is characterized by the light-line problem, which discriminates between guided modes and quasi-guided modes. This is one of the main novelties with respect to conventional photonic crystals. Moreover, it has been mentioned that there can exist Bloch waves with a cut-off, which depends on the waveguide geometry. To get more insight on these concepts and have a better understanding of the photonic band structure, it is useful to study a simple case, namely a self-standing dielectric membrane in air, completely etched with a one-dimensional lattice like a Bragg reflector. The formation of the band structure is explained starting from the guided modes of the effective waveguide, which corresponds to the empty-lattice picture seen for two-dimensional photonic crystals. The core layer is chosen to have

$\epsilon = 12$, the cladding $\epsilon = 1$. The filling factor is $f = 30\%$ and the waveguide thickness is $d = 0.5a$. The effective waveguide, which defines the basis states, is an homogenous self-standing membrane with dielectric constant $\epsilon = 8.7$, given by Eq. (1.26).

The left panel of Fig. 1.10 displays the dispersion relation of the H-like modes for the effective waveguide, folded in the Brillouin zone. The light lines are drawn with dashed lines. The dark gray region is where no solutions can exist. The white region, between the light lines, contains the guided modes. The light gray area corresponds to leaky modes. These guided modes represent the empty-lattice states that are used as basis set in the numerical method. Actually, in order to form a complete basis set, the expansion should include all the waveguide modes that are found for a given Bloch vector $\mathbf{k}$. In this case, the number of states would be infinite, because of the leaky modes continuum, and the expansion would be numerically untractable.

This picture is similar to Fig. 1.2a, where plane waves have been replaced by guided modes, to account for the vertical confinement. There are two main differences with respect to Fig. 1.2a: there exist modes characterized by a cut-off energy that do not reach the long-wavelength limit, and the presence of a continuum spectrum (leaky modes). The long-wavelength limit corresponds to the fundamental waveguide mode, while the states with cut-off are higher-order modes.

The form of the dielectric matrix $[\![\epsilon]\!]$ is the origin of propagation losses in photonic crystal slabs. When a guided mode is folded, it crosses the air light line and enters the leaky mode region. However, the mode remains truly guided, because the coupling with leaky modes is null, since the dielectric tensor of the effective waveguide is diagonal. Indeed, the photonic band picture of the effective waveguide is equivalent to the conventional unfolded dispersion relation, where guided modes never cross the light line. When the effective waveguide is replaced by the photonic crystal slab, the numerical method outputs a discrete spectrum above and below the light line, which is shown in the right panel of Fig. 1.10. Below the light line, the photonic band structure is made of guided Bloch states, which may form a photonic band gap likewise in a one dimensional photonic crystal, see Fig. 1.2b. Once the Bloch mode has crossed the light line, even if it is calculated as a state with zero line-width, in fact, it becomes a resonance, due to the non-zero off-diagonal elements of the dielectric matrix $[\![\epsilon]\!]$, which couple the Bloch mode to the external field. Therefore, these states are subject to intrinsic propagation losses. The physical process that causes losses, is thus

diffraction, since states with different $\mathbf{G}$ vectors are coupled by the off-diagonal elements of $[\![\epsilon]\!]$, and the origin of diffraction is the periodicity of the dielectric function.

The spectrum is thus a continuum of states and the photonic band picture seems to break down. However, assuming that *above the light line, the dispersion relation of photonic crystal slabs is not a mere continuum of states, but it is organized in resonances, with central frequency and width well defined*, the photonic band picture is still valid. In summary, the photonic bands lying below the light line represent the dispersion of guided modes, while those above the light line represent the dispersion of resonances. The numerical method does not provide the width of the resonances, so that, in principle, it is not known if the above statement holds. This issue will be addressed in the next two chapters, to show that the photonic band picture indeed is valid also for modes above the light line, provided that the structure is properly designed [Krauss T. F., *et al.* (1996)].

Also the concept of photonic band gap requires some clarifications. Looking at band structure in the right panel of Fig. 1.10, notice that the band gaps are not characterized by a null density of states. In fact, in Eq. (1.17) the sum is performed over the whole Brillouin zone, which includes the leaky mode region. Considering that above the light line the states are organized in resonances, it is correct to assume that far from the resonances the density of states is almost zero, or at least very small. In this sense, the concept of photonic band gap is reformulated as follows: *the spectral region* $[\omega_1, \omega_2]$ *for which* $\forall\, \omega \in [\omega_1, \omega_2], \nexists\, (\mathbf{k}, n) : \omega = \tilde{\omega}_n(\mathbf{k})$*, where* $\tilde{\omega}_n(\mathbf{k})$ *is either a guided mode or a resonance, is called the photonic band gap.* Therefore, photonic-crystal slabs represent a trade-off also in the sense that the photonic band gap does not exactly imply a null density of states.

Another important feature of the band structure of photonic crystal slabs is that the band gap can be closed also by the onset of a higher order mode, as shown in Fig. 1.10 for the band gap at $\omega a/2\pi c \sim 0.4$. For this reason, it is favorable to work in the frequency region where only the fundamental mode can exist.

As a final remark, it is worth to mention that the choice of the effective waveguide is by no means unique. The effective waveguide determines the guided modes used as basis set. Since the set is not complete, changing the effective waveguide is not irrelevant. However, calculations performed taking different values for the average dielectric functions gave very similar results, apart the cut-off energies of the higher order modes, which strongly depend on the effective waveguide. That is why

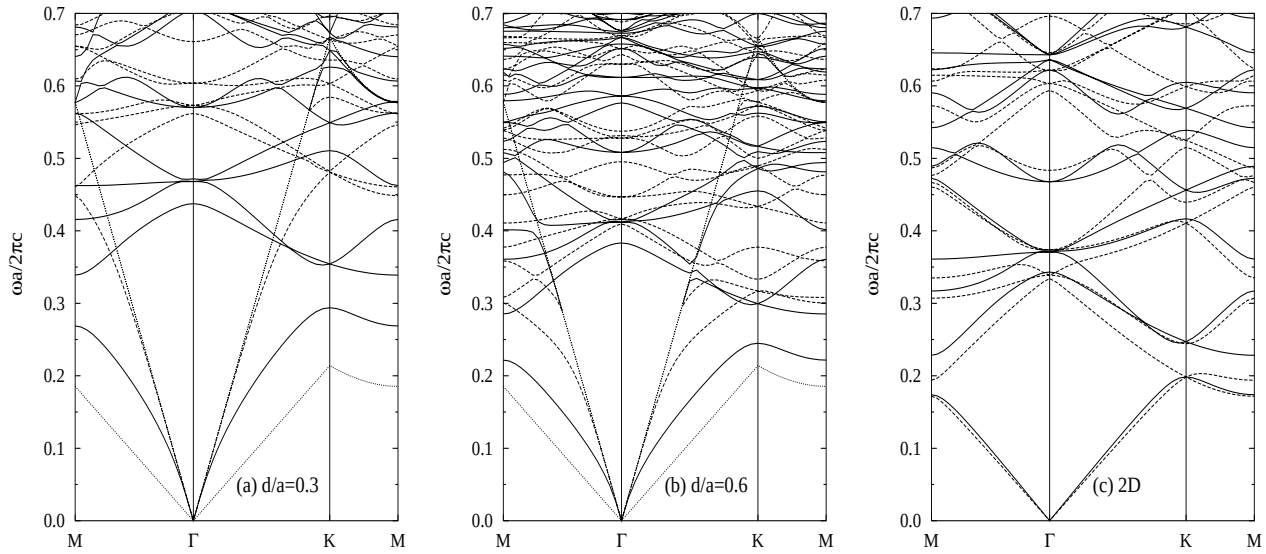

Figure 1.11 Photonic bands for the air-bridge structure of Fig. 1.9d, with hole radius $r = 0.24a$. (a) Waveguide thickness $d = 0.3a$; (b) waveguide thickness $d = 0.6a$; (c) ideal 2D case. Solid (dashed) lines represent modes that are even (odd) with respect to the xy mirror plane. The dotted lines in (a) and (b) refer to the light lines in air and in the effective waveguide material.

the cut-off energies have to be treated with particular care.

1.4.3 Vertical Confinement Effects

Given a numerical method to calculated the band structure and explained what is conceptually different or new with respect to conventional photonic crystals, it is time to return to the structures of Fig. 1.9 and study two representative systems: the strong confinement waveguide (air bridge, Fig. 1.9d) and the weak confinement waveguide (AlGaAs/GaAs/AlGaAs, Fig. 1.9e). The pattern is a triangular lattice of air holes, Fig. 1.9a. The aim is to see the dependence of the photonic band structure on the waveguide thickness d and on the hole radius r for both weak and strong confinement cases. The band structure is calculated along the symmetry lines of the two-dimensional Brillouin zone, Fig. 1.9c. Since these systems are symmetric, the bands are classified in H-like modes and E-like modes.

Bands

Fig. 1.11 shows the photonic band structure of the air bridge for a hole radius $r = 0.24a$ and waveguide thickness $d = 0.3a, 0.6a$, compared with the ideal two-dimensional case. The bands of the two-dimensional system, Fig. 1.11c, exhibit a photonic band gap between the first and second band for even modes (H-modes). The bands of the photonic crystal slab fall partly in to the guided mode region, where they agree with those calculated by Johnson, S. G., *et al.* (1999), and partly in the leaky mode region, where they must be viewed as resonances. For thickness $d = 0.3a$, see Fig. 1.11a, the lowest bands are qualitatively similar to their two-dimensional counterpart, but they are also strongly blue-shifted due to field confinement in the z direction. The gap in the even modes (H-like modes) opens between $\omega a/2\pi c \sim 0.29 - 0.34$, while it is located between 0.2 and 0.23 in the two-dimensional case. The confinement effect is stronger for odd modes. This feature is interpreted as follows: in the long-wavelength limit, the waveguide behaves as a uniaxial medium, with $\epsilon_{\|} \equiv \epsilon_{zz}$, given by Eq. (1.26) and being larger than $\epsilon_{\perp} \equiv \epsilon_{xx} = \epsilon_{yy}$, approximated by Eq. (1.27). In the two-dimensional case, odd modes have the electric field along z and feel the largest dielectric constant $\epsilon_{\|}$: hence they are better confined in the waveguide and have a larger blue-shift compared to even modes.

The six photonic modes at the Γ point in each polarization can be interpreted as the fundamental waveguide mode at the lowest non-zero reciprocal lattice vectors, folded in the Brillouin zone and split by the dielectric matrix. Notice that the in the photonic crystal slab with $d = 0.3a$, the modes up to $\omega a/2\pi c \simeq 0.57$ can be put in one-to-one correspondence with the bands of the two-dimensional case, indicating that the waveguide is mono-mode. A second-order waveguide mode appears above $\omega a/2\pi c \simeq 0.57$. Analogous considerations hold for the case of waveguide thickness $d = 0.6a$, in Fig. 1.11b, where the field confinement is less pronounced. Moreover, a second-order waveguide mode starts already at $\omega a/2\pi c \simeq 0.3$ and the bands at higher frequencies become more complex.

The example allows to discuss the trend with waveguide thickness with fixed hole radius $r = 0.24a$. For a small value of d/a, the waveguide is mono-mode in a wide frequency range and the photonic bands can be interpreted as two-dimensional bands blue-shifted by the field confinement. The

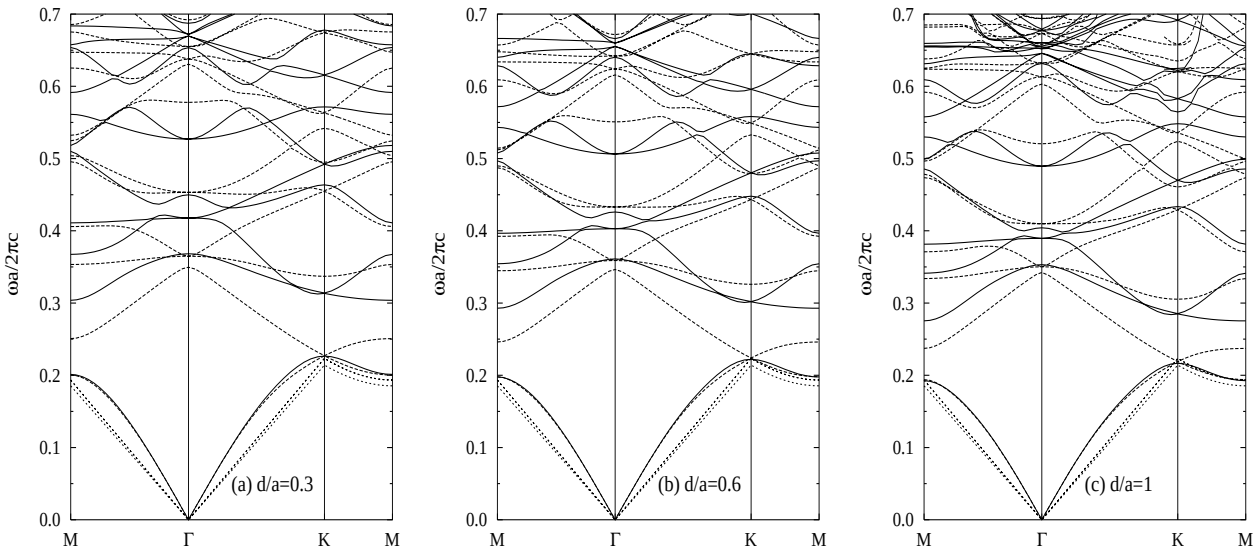

Figure 1.12 Photonic bands for the weak-confinement structure of Fig. 1.9e, with hole radius $r = 0.24a$. (a) Waveguide thickness $d = 0.3a$; (b) $d = 0.6a$; (c) $d = 1.0a$. Solid (dashed) lines represent modes that are even (odd) with respect to the xy mirror plane. The dotted lines refer to the light lines in the effective core and cladding materials.

confinement is stronger for odd modes. On increasing the ratio d/a, the blue-shift is reduced and a second-order waveguide mode occurs with decreasing cut-off frequency. For $d > 0.6a$, the second-order mode falls into the gap of even modes. When defects are present in the band gap, the presence of the second-order mode will contribute to losses. Concerning low-loss wave propagation , it is better to have structures that are mono-mode in the frequency range of interest. For the air bridge system, small values of d/a are more favorable.

Fig. 1.12 displays the photonic bands for the weak-confinement structure of Fig. 1.9e for three values of waveguide thickness. Due to the small dielectric contrast between core and cladding, there are no truly guide modes and all photonic modes lie in the radiative region. The dispersion of quasi-guided modes is very similar to the two-dimensional case of Fig. 1.11c and the blue-shift is much less than for the air bridge. However, it is noticeable that the gap in the even modes is increased compared to the two-dimensional case. The three patterned waveguides are mono-mode for the shown frequency range, except for $d = a$, where a second-order mode occurs for $\omega a/2\pi c \simeq 0.65$. Like for the strong confinement case, the results of Fig. 1.12 suggest that, in order to maximize the

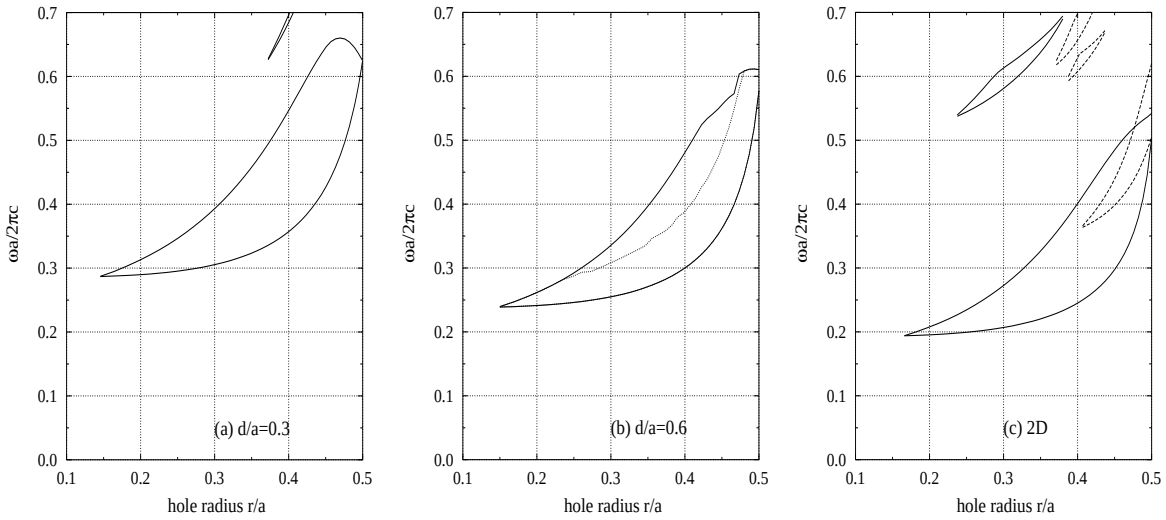

Figure 1.13 Gap maps for the air bridge structure of Fig. 1.9d. (a) Waveguide thickness $d = 0.3a$; (b) waveguide thickness $d = 0.6a$; (c) ideal 2D case. Solid (dashed) lines represent the edges of photonic bands that are even (odd) with respect to the xy mirror plane. The dotted line in (b) refers to the cut-off of the second-order waveguide mode.

even gap, it is more convenient to use small values of waveguide thickness.

Gap Maps

It is also interesting to see the trends of the band gaps with the hole radius. Fig. 1.13 displays the gap maps as a function of hole radius for the air bridge structure of Fig. 1.9d with waveguide thickness $d = 0.3a, 0.6a$ and in the two-dimensional case. The purpose of Fig. 1.13c, which is equal to Fig. 1.6, is to set a reference for the gap maps in a photonic crystal slab. The gap map of the two-dimensional case has already been discussed in Sec. 1.3.1. For the photonic crystal waveguide, Fig. 1.13a,b, there is no gap in the odd modes (dashed lines) for any hole radius and, therefore, no complete band gap. The band gap for even modes (solid lines) occurs at higher frequencies than in two-dimensions, because of the vertical confinement.

It has to be remarked that the upper edge of the gap lies in the radiative region for a hole radius larger than about $0.4a$ so that the even gap is formed partly in the guided mode region and partly in the leaky mode region. The band gaps obtained here are larger than those calculated by Johnson,

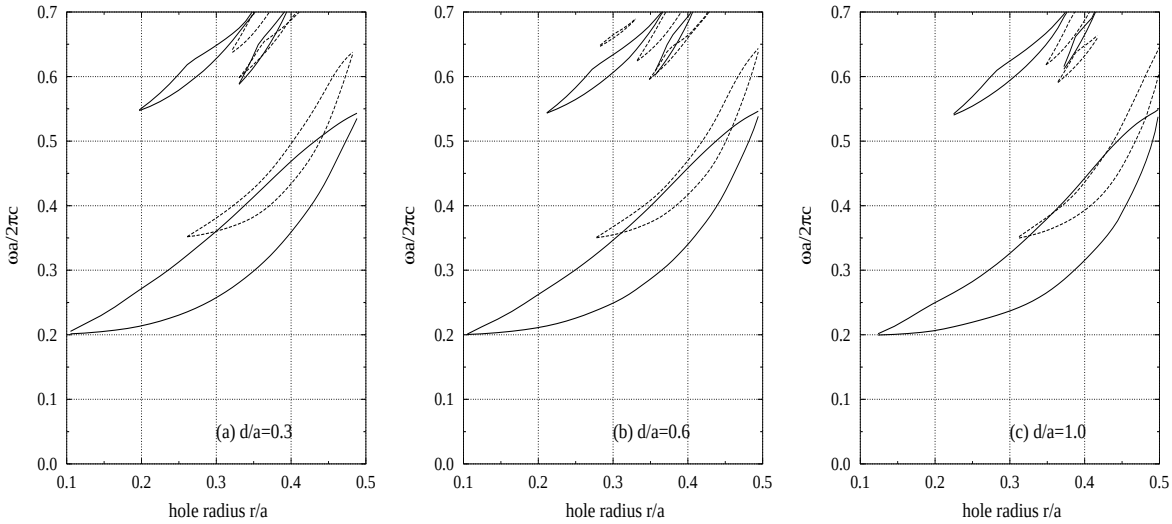

Figure 1.14 Gap maps for the weak-confinement structure of Fig. 1.9e. (a) Waveguide thickness $d = 0.3a$; (b) $d = 0.6a$; (c) $d = 1.0a$. Solid (dashed) lines represent the edges of photonic bands that are even (odd) with respect to the xy mirror plane.

S. G., *et al.* (1999), where only the guided mode region was considered. Moreover, Johnson, S. G., *et al.* (1999) concluded that the optimal waveguide thickness for a gap in the even modes is around $d = 0.6a$ and that the band gap would decrease for smaller thicknesses. By considering both guided and quasi-guided modes, we find instead that the even gap of the triangular lattice of holes remains large even for waveguide thicknesses $d = 0.3a$ and below.

The dotted line of Fig. 1.13b represents the cut-off frequency of a second-order waveguide mode (see also Fig. 1.11b). Strictly speaking, the even gap exists only between the lower gap edge and the second-order cut-off. For $d = a$ (not shown), the second-order cut-off falls below the lower gap edge, closing the even gap. However, since this numerical method does not provide accurate cut-offs, the above statement might be wrong. Again, to avoid complications related to multi-mode waveguides, it is more convenient to choose values of d/a smaller than 0.6.

Fig. 1.14 shows the gap maps for the weak-confinement waveguide of Fig. 1.9e, with waveguide thickness $d = 0.3a, 0.6a, a$. They are rather similar to the two-dimensional case, because the confinement effect is much less important than for the air bridge. It has to be pointed out that the weak-confinement waveguide has no truly guided modes in the considered range of waveguide thicknesses: all modes are resonances and the photonic band gap lies entirely in the radiative

region. Notice that, on decreasing the waveguide thickness, the gap for odd modes opens at smaller values of the hole radius; the same happens for the even gap. Contrary to the strong-confinement waveguide, a full band gap common to both polarizations still exists and it occurs even for hole radii of the order of $0.3a$, if waveguide widths $d \sim 0.3a$ are used.

1.4.4 Symmetry Properties

As regards the symmetry properties of two-dimensional photonic crystal slabs, there is no much more to say with respect to two-dimensional photonic crystals. In Sec. 1.3.2, it has been shown that the point group of a triangular lattice of air holes is D_{6h}, seen as direct product of C_{6v} and C_s. The small point groups at the main symmetry points are D_{2h} at M and D_{3h} at K. Likewise for the point group, it is convenient to write the small point groups as a direct product: $D_{2h} = D_{2v} \otimes C_s$ and $D_{3h} = D_{3v} \otimes C_s$. C_s contains the identity and the reflection with respect to the $x - y$ plane, σ_{xy}. For two-dimensional photonic crystal slabs, with triangular lattice of air holes, the symmetry analysis can be divided into two cases, according to the symmetry with respect to the mid-plane of the core layer. For symmetric waveguides (air bridge, AlGaAs/GaAs/AlGaAs, etc.) the point group and the small point groups are those of two-dimensional photonic crystals (for in-plane propagation). For asymmetric waveguides (silicon-on-insulator, etc.), σ_{xy} is not a symmetry operation anymore and the point group is only C_{6v}; correspondingly, the small point groups are C_{2v} and C_3v. Given the small point groups, the classification of photon states proceeds as described in Sec. 1.3.2 for two-dimensional photonic crystals. However, since above the light line the spectrum is continuum, one would have an infinite number of states to analyze, which is meaningless. The modes of interest are only the central frequencies of the resonances. With the present numerical method, the symmetry properties of resonances are studied by looking at the corresponding eigenvectors, as if the spectrum were discrete.

The photonic bands of two-dimensional photonic crystal slabs have been calculated by means of a numerical method conceptually analogous to the usual plane-wave expansion. The concept of photonic band structure and of photonic band gap have been extended, in order to account for the existence of quasi-guided modes in the radiative region. For strong-confinement waveguides (air

bridge), the photonic modes exhibit a large blue-shifted with respect to the two-dimensional case. The gap maps of the air bridge display only a gap for even modes. The even gap remains large even for small waveguide thickness, while it is closed by a second-order waveguide mode when the thickness reaches $d = 0.6a$. In the weak confinement waveguide (GaAs/AlGaAs system), the bands are similar to the two-dimensional case. However, the single gaps and the complete band gap open for smaller values of the hole radius. Another difference between strong and weak confinement waveguides regards the nature of photonic modes. While strong confinement waveguides support both guided and quasi-guided modes, weak confinement waveguides have practically only quasi-guided modes. These modes are subject to propagation losses, because of the coupling to the external field. Understanding and quantifying out-of-plane losses is very important, since they may preclude the use of photonic crystal slabs towards integrated photonic crystals circuits. One would like to know which is the optimal waveguide design that accounts for minimal out-of-plane losses, ease of fabrication with lithographic methods and appropriate band gap properties. An air bridge system allows to operate with truly guided modes; on the other hand, it is more difficult to fabricate. Two-dimensional photonic crystals embedded in weak confinement waveguides possess a band structure that is more similar to the two-dimensional case and they can be obtained with top-down processes much easily than suspended membranes. These features make weak confinement systems more promising than the strong confinement counterpart, provided they exhibit "small" propagation losses [Benisty, H., *et al.* (2000)].

The next chapter is focussed on the study of radiative modes and on the optical properties of two-dimensional photonic crystals. One of the objectives is to have a deep understanding of out-of-plane losses, with emphasis on weak confinement systems. Following the trend of losses as a function of the structure parameters, may help in finding the optimal design for a two-dimensional photonic crystal slab. This will be accomplished by taking into account also the finite etch depth of the photonic crystal pattern, which is the usual situation for realistic systems.
Before concluding the chapter, a last section is dedicated to the super-cell method and to the dispersion relation of linear defects in photonic crystals. These results will be used in Chapter. 3 to analyze wave propagation in two-dimensional photonic crystals.

1.5 Linear Defects in Two-Dimensional Photonic Crystals

The photonic band gap is so much attracting because of the capability to control wave propagation, besides light emission [Joannopoulos, J. D., *et al.* (1997)]. Such functionality can be achieved by designing defects, which create energy levels within the photonic band gap. Considering the plane of periodicity of two-dimensional photonic crystals, a point defect corresponds to a resonant cavity, while a linear defect corresponds to a waveguide. Resonant cavities and waveguides are among the building blocks of photonic integrated circuits. Since a point defect breaks the periodicity in two dimensions, it is characterized by a dispersion-less spectrum (if only in-plane wave-vectors are considered). On the other hand, a linear defect preserves the periodicity in one dimension, yielding a one dimensional Brillouin zone and a Bloch vector $\mathbf{k}$. Therefore, these defect states will obey to a dispersion relation $\omega = \omega_m(\mathbf{k})$, where m is the order of the guided mode, in analogy to a conventional waveguide with periodic corrugated walls.

Among the all possible linear defects [Joannopoulos, J. D., *et al.* (1995); Johnson, S. G., *et al.* (2000)], the choice falls on those created by removing N adjacent rows of holes in a photonic crystal made of a triangular lattice of air holes in a dielectric material. The motivation is that these systems are the most promising for application in photonic integrated circuits. The so-called WN waveguide, where N is the number of removed rows, is usually created along the $\Gamma - K$ direction, rather than the $\Gamma - M$, because the waveguide walls are smoother. The guides with odd N (W1,W3,...) have symmetric boundaries, while those with even N (W2,W4,...) have boundaries shifted by $a/2$ with respect to each other [Benisty, H. (1996)]. It is convenient to work with odd N, because the waveguide is symmetric with respect to its axis.

Fig. 1.15 shows a W1 waveguide, which is created by removing one row of air holes along the $\Gamma - K$ direction of the triangular lattice. By definition, a WN waveguide is obtained by removing N rows of adjacent holes along $\Gamma - K$. For a W1 waveguide, the width w corresponds to $a\sqrt{3}$, which is generalized to $w = a\sqrt{3}(N+1)/2$ for WN waveguides. The presence of the waveguide breaks the periodicity along $\Gamma - M$. Nevertheless, the system remains periodic along $\Gamma - K$, with lattice constant a, so that the Bloch theorem applies. An efficient numerical technique for calculating the dispersion relation of the guided modes is the super-cell method [Benisty, H. (1996)].

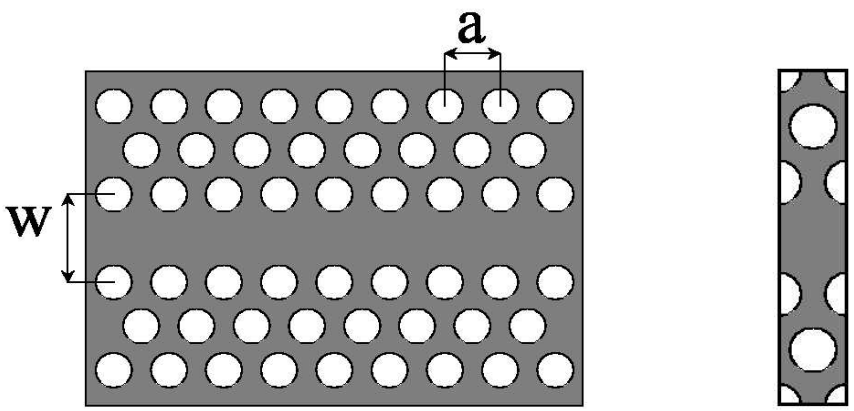

Figure 1.15 Left: a photonic crystal waveguide along the $\Gamma - K$ direction of a triangular lattice of air holes in a dielectric material. w defines the width of the waveguide, a is the lattice constant. Right: an example of super-cell for the calculation of the photon dispersion for this system.

1.5.1 The Super-Cell Method

Consider the unit cell displayed in the right panel of Fig. 1.15, which contains the waveguide defect. The super-cell method consists of assuming a periodic array of waveguides, spaced by bulk photonic crystal, whose unit cell corresponds to the one just mentioned. The spacing is determined by the width of the super cell. A guided mode is characterized by an evanescent field in the direction perpendicular to the Bloch vector. For this reason, if the super-cell is sufficiently large, the guided modes of adjacent unit cells will not overlap (no interaction) and the dispersion relation will be like that one of a single waveguide. The array of waveguides is characterized by two primitive vectors $\mathbf{a}_1, \mathbf{a}_2$. Even if the Brillouin zone is two-dimensional, only the Bloch vector along the waveguide axis represents the true guided-mode wave-vector. Given the unit cell, the reciprocal primitive vectors and the Bloch vector, the dispersion relation is calculated by the usual plane-wave expansion method.

While the primitive vectors are easily found by looking at the super cell: $\mathbf{a}_1 = a(1, 0)$ and $\mathbf{a}_2 = a\sqrt{3}(0, (N + 1)/2 + K)$, where N is for WN and $2K + 1$ is the number of photonic-crystal rows between two waveguide channels, the dielectric matrix $[\![\epsilon]\!]$ of the unit cell is more difficult to calculate. Looking again at Fig. 1.15, notice that the dielectric function inside the super cell can

be obtained from the dielectric function of a single air hole, displaced by well defined vectors

$$\epsilon(\mathbf{x}) = \epsilon_{\text{diel}} + (\epsilon_{\text{air}} - \epsilon_{\text{diel}}) \sum_{\text{v}} \theta\left(|\mathbf{x} - \mathbf{v}| - r\right) \ , \ \mathbf{x} \in \text{unit cell}\,, \tag{1.32}$$

where r is the hole radius, $\mathbf{x} = (x, y)$, and $\mathbf{v}$ are the displacement vectors. $\theta(x)$ is the Heaviside function. Writing the dielectric function in the form of Eq. (1.32) is very convenient for computing the Fourier integral, see Eq. (1.23). Indeed, the Fourier transform of the dielectric function can be expressed as the bulk Fourier transform multiplied by a structure factor,

$$\epsilon_{\mathbf{G},\mathbf{G}'} = \begin{cases} S(\mathbf{G} - \mathbf{G}')F(\epsilon_{\text{air}}, \epsilon_{\text{diel}}, r, G), & \text{if } \mathbf{G} \neq \mathbf{G}'; \\ f'\epsilon_{\text{air}} + (1 - f')\epsilon_{\text{diel}}, & \text{if } \mathbf{G} = \mathbf{G}'; \end{cases} \tag{1.33}$$

with f' as the super-cell filling factor and $\mathbf{G}, \mathbf{G}'$ are the reciprocal vectors of the super-cell lattice. $S(\mathbf{G})$ is the structure factor, while $F(\epsilon_{\text{air}}, \epsilon_{\text{diel}}, r, G)$ is the atomic factor, corresponding to the dielectric-function Fourier transform of the bulk photonic crystal:

$$S(\mathbf{G}) = \frac{A_{\text{c}}}{A} \sum_{\mathbf{v}} e^{\imath \mathbf{G}\cdot\mathbf{v}}\,, \qquad F(\epsilon_{\text{air}}, \epsilon_{\text{diel}}, r, G) = (\epsilon_{\text{air}} - \epsilon_{\text{diel}}) \frac{2\pi r}{A_{\text{c}} G}\, J_1(Gr)\,, \tag{1.34}$$

where A is the area of the super cell, while A_{c} is the area of the bulk crystal unit cell.
Once that the dielectric matrix has been calculated, Eqs. (1.24a) and (1.24b) can be used to find the dispersion relation of guided H-modes and guided E-modes, respectively. Since the waveguide is symmetric with respect to its axis, the guided modes can be further classified as even or odd with respect to a reflection plane σ_{xz}, where x is the waveguide axis and z is the vertical direction. If not otherwise stated, the plane-wave expansion is performed with ~ 500 waves and the width of the super-cell is such that 13 photonic-crystal rows separate the waveguides ($K = 6$).

1.5.2 The Dispersion Relation

Fig. 1.16 shows the dispersion relation of the W1 channel waveguide of Fig. 1.15, for $f = 60\%$ and $\epsilon_{\text{diel}} = 11.56$. The figure displays only guided H-modes that are spatially even with respect to σ_{xz}[9]. The gray regions correspond to modes of the bulk photonic crystal.

Since the waveguide is symmetric, the fundamental guided mode does not have a cut-off. Notice

[9]Notice the nomenclature: the modes are even if one looks at the field pattern, but they are globally odd for the symmetry operation σ_{xz}: $\sigma_{xz} = -1$. Thus the adjective "spatially" to specify when one refers to the symmetry of the field profile only.

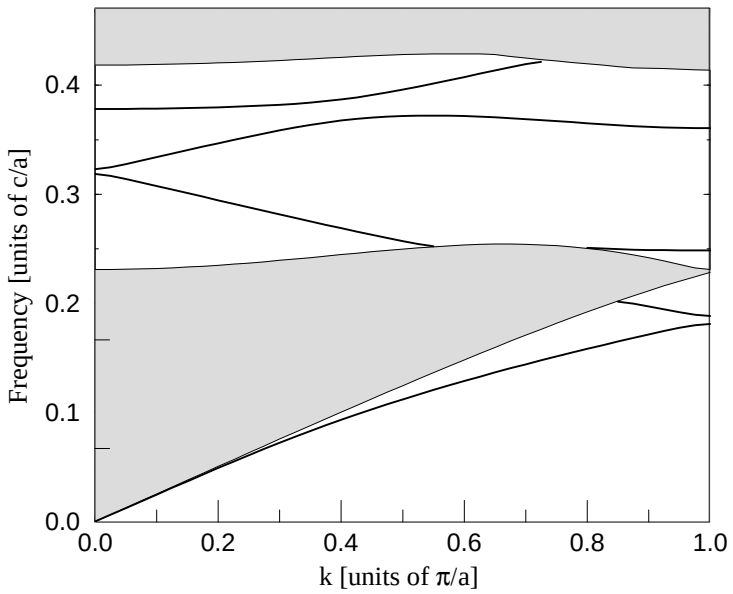

Figure 1.16 Dispersion relation for the photonic crystal waveguide of Fig. 1.15 with $w = \sqrt{3}a$, $f = 60\%$, and $\epsilon_{\text{diel}} = 11.56$. The gray area is the projected band structure of the bulk photonic crystal. The solid lines correspond to guided H-modes that are spatially even with respect to the waveguide axis.

also that the fundamental guided mode lies below the bulk modes, because the field is confined where the dielectric function is higher than the effective dielectric constant of the bulk crystal. After that the fundamental mode is folded at the edge of the Brillouin zone ($\omega a/2\pi c = a/\lambda \simeq 0.17$), it crosses and anti-crosses with the bulk states until it reaches the photonic band gap. The fundamental mode is folded once again at $a/\lambda \simeq 0.32$ and it proceeds towards higher frequencies, where it anti-crosses with the higher order mode at $a/\lambda \simeq 0.37$. While the fundamental guided mode has dispersion similar to modes of conventional dielectric waveguides, the higher order mode resembles those of narrow metallic waveguides. Indeed, the fundamental guided mode originates from conventional index confinement, due to the dielectric path embedded in the photonic crystal. On the contrary, the higher order mode can exist only thanks to the photonic band gap, which acts similarly to perfect metallic mirror. In general, the guided modes of WN linear defects are of two types: dielectric modes and photonic-band-gap modes. This is a peculiarity of photonic crystal waveguides created

by adding dielectric material to the bulk crystal [Joannopoulos, J. D., *et al.* (1995); Johnson, S. G., *et al.* (2000)]. The coexistence of dielectric and photonic-bang-gap guided modes favors the occurrence of multi-mode frequency regions, for instance in the proximity of the anti-crossing between the fundamental and the higher order mode, as shown in Fig. 1.16. Such feature, and its implications, will be extensively discussed in Chapter 3.

The Mini-Stop Band

Another interesting aspect of WN waveguides is the concept of mini-stop band. In the dispersion relation of Fig. 1.16, the fundamental guided mode exhibits gaps at the edges of the Brillouin zone and anti-crossing with the higher order mode. The phenomenon can be easily explained by noting that the walls of the dielectric channel are corrugated by rows of air holes. Such corrugation acts like a one-dimensional periodic potential on the guided modes. Therefore, when the guided mode reaches the edge of the Brillouin zone, the potential opens a mini-gap in the dispersion relation, through the same mechanism described for a one-dimensional photonic crystal in Sec. 1.2.3 [Mekis, A., *et al.* (1998)]. The same happens also for two guided modes of different order, when they become degenerate and have the same symmetry: the periodic potential couples the modes and causes anti-crossing in the dispersion relation [Agio, M., *et al.* (2001)]. Both mini-gap and anti-crossing of guided modes are called mini-stop bands.

CHAPTER 2. OPTICAL PROPERTIES

Measuring the photonic band structure represents one of the major efforts in the study of photonic band gap materials and, since the discovery of photonic crystals, various methods have been proposed [Yablonovitch, E., *et al.* (1989); Robertson, W. M., *et al.* A (1993); Labilloy, D., *et al.* A (1997); Astratov, V. N., *et al.* A (1999)]. Recently, Astratov, V. N., *et al.* A (1999) have reported on a very efficient technique for measuring the quasi-guided modes of photonic-crystal slabs: the so-called *variable-angle reflectance*. This chapter will discuss the determination of photonic bands for representative systems, by means of the above method. Many of the results that are presented have been obtained within a collaboration between experimentalists and theorists at the Department of Physics "A. Volta", Università degli Studi di Pavia, Italy. For a more comprehensive insight, experimental data will be also shown and compared to theory. In particular, reflectance, transmittance and diffraction are calculated ab-initio with the scattering matrix method [Whittaker, D. M., *et al.* (1999)], so that a direct comparison with the measured spectra is possible. Since probing the photonic band structure implies that an incident wave couples to the modes of the system, i.e. an optical response to an external excitation, a correct interpretation of variable-angle reflectance spectra has to account for the *optical properties* of photonic crystals. Indeed, in analogy to the optical properties of solids, selection rules are found to make quasi-guided modes visible or invisible to an external probe. For the above reasons, the measurement of photonic bands is accomplished with a study of the optical properties of photonic crystals, which is based on the group-theory analysis performed in the previous chapter, in Sec. 1.3.2.

Lastly, besides determining the frequency of quasi-guided modes, one would like to quantify their width, which is related to propagation losses. Such information is very important for assessing the guiding properties of such modes. In fact, that would really complete the characterization of a photonic crystal, i.e. measuring both real and imaginary part of the spectrum. Since variable-

angle reflectance relies on the coupling of the external radiation to quasi-guided modes, the method may also attempt to investigate propagation losses and give qualitative trends as a function of the geometry of the patterned waveguide.

The first section is devoted to a brief historical overview of the principal works that brought to the determination of photonic bands, from the microwave regime up to the near-infrared domain, in micron-size photonic crystals. The review points to the optical properties and, in particular, to the assessment of out-of-plane losses of quasi-guided modes in photonic-crystal slabs, which has already been reviewed in Sec. 1.1. Such discussion serves as an helpful background for a better understanding of the results presented in the following sections. Section 2.2 introduces the variable-angle reflectance technique as a method for measuring the photonic band structure and for probing the optical properties of photonic crystals. The above procedure is implemented by means of the scattering matrix method, which is the theoretical counterpart of a variable-angle reflectance experiment. Section 2.3 is dedicated to the study of two-dimensional photonic crystals. The photonic band structure of macro-porous silicon photonic crystals is extracted from variable-angle reflectance spectra. Furthermore, it is shown that the optical properties obey to selection rules for coupling the external field to quasi-guided modes; such rules, which stem from the symmetry properties of the system, can be also inferred from the analysis of reflectance spectra. After dealing with deep two-dimensional photonic crystals, the same study is applied to photonic-crystal slabs. Section 2.4 reports on the determination of the photonic band structure for the air-bridge system and for GaAs/AlGaAs patterned waveguides. The interpretation of reflectance spectra follows the same selection rules discussed in the previous section. A comparison between two GaAs-based samples with different air fraction shows that the width of the resonances, which is proportional to out-of-plane losses, increases with the air fraction. Indeed, a careful analysis of reflectance is also adequate to give insight on the issue of propagation losses in photonic-crystal slabs. To this purpose, Section 2.5 contains a systematic study of the resonant features in reflectance, as a function of various structure parameters, like waveguide thickness, hole radius and etch depth. By looking at the width of a sample resonance, various trends for out-plane losses are presented. Though being far from a direct determination of propagation losses, the study gives important hints for achieving an optimal structure design.

2.1 History

The experimental investigation of photonic bands followed soon the theoretical proposals of Yablonovitch, E. (1987) and John, S. (1987) [Yablonovitch, E., *et al.* (1989); Robertson, W. M., *et al.* A (1993); Gourley, P. L., *et al.* (1994)]. Thanks to the scaling properties of Maxwell's equations the dispersion properties of photonic crystals could be easily tackled by working with "macroscopic" systems, like two-dimensional photonic crystals made of an ordered arrangement of centimeter-size alumina rods. While the measurement of the photonic band gap (frequency range and power attenuation) was not particularly difficult in the microwave regime, a complete determination of the photonic band structure was challenging because of the required knowledge of both frequency and wave-vector of the Bloch states. To this purpose, Robertson, W. M., *et al.* A (1993) conducted experiments on two-dimensional photonic crystals using a phase-sensitive setup: by sending a plane-wave through the sample, the apparatus yields both amplitude and phase of the transmitted field. These information can be then recast to build the photonic band structure. Much more demanding is to transfer the same kind of experiments to the infrared and optical regimes. One could say that the measurement of photonic bands in the infrared domain is not necessary if one exploits the above mentioned scaling properties. Nevertheless, the characterization of micron-size samples was of primarily importance for the advancement of the physics of photonic crystals. The difficulties were double: lack of high quality samples and the need of refined spectroscopic techniques. Finally, a quantitative measurement of transmission, reflection and diffraction in photonic crystals operating at near-infrared wavelengths was reported by Labilloy, D., *et al.* A (1997), who took advantage of high-quality GaAs-based samples [Krauss T. F., *et al.* (1996)] and devised a novel methodology for probing the optical properties of waveguide-embedded two-dimensional photonic crystals [Labilloy, D., *et al.* A (1997); Labilloy, D., *et al.* B (1997)]: the so-called internal light-source method. Using the same technique, a couple of years later, Labilloy, D., *et al.* (1999) were able to the determine the photonic band structure by extracting the Bloch wave-vector from finely resolved transmission spectra: the fine interference pattern is due to the Bloch waves reflected at the cleaved edges of the sample. Later on, similar experiments were performed on other semiconductor-based two-dimensional photonic crystals, like silicon-on-insulator, GaN and InP heterostructures, and

GaAs/Alox [Astratov, V. N., *et al.* A (1999); Lončar, M., *et al.* B (2000); Pacradouni, V., *et al.* (2000); Chow, E., *et al.* (2000); Baba, T., *et al.* (2001); Kawai, N., *et al.* (2001); Lončar, M., *et al.* (2002); Ferrini, R., *et al.* (2002); Coquillat, D., *et al.* (2001); Galli, M., *et al.* B (2002); Patrini, M., *et al.* A (2002)]. These works can be grouped into three main techniques: the internal source method, the end-fire method and the variable-angle-reflectance method. The latter, proposed by Astratov, V. N., *et al.* A (1999), is very attracting for its relative simplicity with respect to the other methods and for being appropriate for a direct measurement of the dispersion of quasi-guided modes. Furthermore, while the other setups might depend on the type of sample, because of the issue of in-plane coupling the external field to the Bloch states or because of the necessity of appropriate internal sources, the variable-angle-reflectance can be performed in general on any semiconductor-based system without major difficulties, as it will be understood from the following sections. However, its flaw derives from the fact that it is limited to quasi-guided modes. Thus, all techniques have their importance.

These efforts, besides aiming to the assessment of the photonic band gap and/or the photonic band structure, sought for a more complete characterization of photonic crystals, namely the measurement of propagation losses. Indeed, this aspects is a fundamental indicator for the feasibility of photonic-crystal integrated circuits. A brief historical overview on this subject has already been provided in the previous chapter (Sec. 1.1). Further and updated reference can be found in the feature issue *IEEE J. Quantum Electronics, 38* (7).

2.2 The Variable-Angle Reflectance

The variable-angle reflectance (VAR) represents a powerful method for measuring the photonic band structure of quasi-guided modes [Astratov, V. N., *et al.* A (1999)]. The technique is based on the coupling of the external field to photonic modes, which yields a resonant feature in an otherwise smooth reflectance spectrum. The process is similar to probing elementary excitations in solids, by measuring the optical properties of the system [Bassani, F., *et al.* (1975)]. The VAR of patterned dielectric slabs can be also obtained with ab-initio methods, so that the calculated spectra can be compared to the experimental ones. The scattering matrix method, developed by Whittaker,

D. M., *et al.* (1999), was indeed proposed for interpreting the VAR measurements by Astratov, V. N., *et al.* A (1999). The availability of exact results is certainly helpful in understanding the reflectance curves, in order to extract the photonic bands.

Since the width of the resonances seen in reflectance is related to the imaginary part of the mode energy, the VAR can be also employed to assess the propagation losses of quasi-guided modes, as discussed in Sec. 2.5. Such information is of primary importance for designing waveguide-embedded photonic crystals, specially for what concerns low-index contrast waveguides, where most of the modes lie above the light line. The same study can be performed on defect states, to infer the band dispersion and the attenuation length of guided modes in channel photonic-crystal waveguides, like the W*N* system introduced in Sec. 1.5. In this case, the VAR experiment has to be performed on arrays of linear defects designed on a single sample. Lastly, VAR is also suitable for studying the diffraction properties of photonic-crystals, which may contain important information on the symmetry of the excited state.

After exposing the basic ideas of the VAR technique, the discussion moves to the introduction of the scattering matrix method, which represents the numerical realization of a VAR experiment. Then, a few examples of reflection, transmission and diffraction spectra are given, in order to provide a more complete understanding of the processes involved in the surface excitation of quasi-guided modes, although the rest of the work will be limited to reflectance studies.

2.2.1 Basic Ideas

The resonant anomalies seen in reflectance correspond to coupling to the external field by grating effect. In fact, the in-plane momentum conservation law that forbids the guided mode from coupling to external photons ceases to be valid as a result of the patterning: a mode with in-plane momentum $\mathbf{k}$ can couple to external modes provided that $\mathbf{k}$ is conserved within a reciprocal lattice vector $\mathbf{G}$. In other words, a mode with Bloch vector $\mathbf{k}$ and frequency ω couples, in principle, to all radiative modes with in-plane momentum $\mathbf{k}+\mathbf{G}$ and frequency ω, provided that $\epsilon\omega^2-(\mathbf{k}+\mathbf{G})^2>0$, where ϵ is the dielectric constant of the external medium (air). The latter condition represents the so-called *light line problem*, which discriminates between guided modes and quasi-guided modes. Out-of-plane diffraction losses are thus a natural consequence of the photonic-crystal pattern (that is why

they are also named *intrinsic*). The coupling strength is related to the off-diagonal components of the dielectric tensor $[\![\epsilon]\!]$.

Now, the reciprocal process is an external wave that couples to the quasi-guided mode. The incident wave, with frequency ω and momentum $(\mathbf{k}, q)$, where $\mathbf{k}$ is the in-plane momentum and q is the vertical wave-vector component along z, impinges the surface of the patterned waveguide. The external wave excites the quasi-guided modes of the system before being reflected and transmitted. The anomaly in reflectance (and transmittance) occurs when the incident wave is resonant to a quasi-guided mode, namely, when energy and in-plane momentum match those of a quasi-guided mode. Furthermore, the quasi-guided mode radiates also into diffraction channels whenever $\epsilon\omega^2 - (\mathbf{k} + \mathbf{G})^2 > 0$.

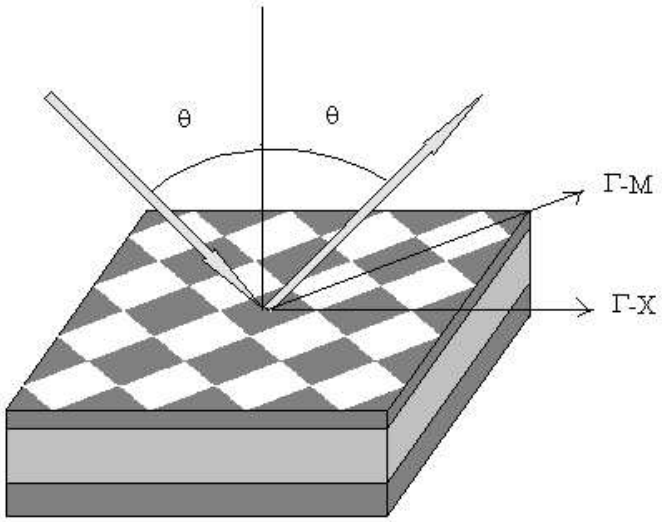

Figure 2.1 Description of the Variable-Angle Reflectance technique. Polarized monochromatic light impinges the surface of a 2D photonic crystal with an angle θ. The reflected beam contains information on the photonic modes of the system. The azimuth is chosen in order to sample the symmetry lines of the 2D Brillouin zone (the example regards a square lattice).

Once understood the mechanism that causes the anomalies in reflectance, how to extract the corresponding photonic band structure? Consider a plane wave of frequency ω that impinges the surface of a photonic-crystal slab with an angle θ, with respect to the normal to the surface (z axis), and with an angle ϕ with respect to a reference in-plane direction (x axis); usually, the x axis

is oriented along a symmetry line of the Brillouin zone, see Fig. 2.1. The wave-vector is determined by the kinematics of the process: $\mathbf{k} = (\omega\sqrt{\epsilon}/c)\sin\theta(\hat{\mathbf{x}}\cos\phi + \hat{\mathbf{y}}\sin\phi)$, for the in-plane wave-vector, and $q = (\omega\sqrt{\epsilon}/c)\cos\theta$, for the vertical component. The in-plane momentum is thus related to the frequency ω and to the incidence angles (θ, ϕ) of the external plane wave. By varying ω, θ and ϕ, one samples the whole photonic band structure that lies above the light line: from the energy position of the anomalies in reflectance and the knowledge of the incidence angles, one goes back to the point of the Brillouin zone that corresponds to the in-plane wave-vector of the incident wave. By reporting the collected data into the dispersion diagram $(\omega, \mathbf{k})$, the photonic band structure is readily obtained. It is often convenient to fix the angle ϕ, so that the plane of incidence is aligned to the desired crystal orientation: $\Gamma - K$ or $\Gamma - M$ for a triangular lattice, $\Gamma - X$ or $\Gamma - M$ for a square lattice. This allows to exploit the polarization of the incident light to separately sample the modes with opposite parity with respect to plane of incidence: transverse electric (TE) or transverse magnetic (TM) polarization couples to odd or even quasi-guided modes, respectively. Thereafter, the angle θ is varied from $0°$ to $\sim 60 - 80°$ in steps of $2.5°$ or $5°$ and, for each value of θ, the frequency of the incident wave spans a certain range to map the desired portion of the dispersion diagram.

Experiment

Fig. 2.2 displays a typical experimental setup for performing VAR on photonic-crystals. A broadband incident beam is selected into TE or TM polarizations, by a calcite Glann-Taylor polarizer, before reaching an elliptical mirror, which allows to select the angle of incidence θ. The beam is collimated and focussed onto the sample surface with a spread angle of $\pm 1°$, where the sample surface is perpendicular to the plane of incidence. The reflected beam is then filtered by another polarizer to assure that the measured light has the desired initial polarization. The light exiting the slit is detected by a liquid-nitrogen-cooled InSb photodiode and a silver mirror is used as absolute reflectance reference. A Fourier transform spectrometer (Bruker IFS-66) yields the reflectance spectrum at a spectral resolution of 1meV.

The experimental data that will be shown in the next sections have been obtained with the above setup by Galli, M., *et al.* A (2002) at "Laboratorio di Spettroscopia Ottica", Università degli

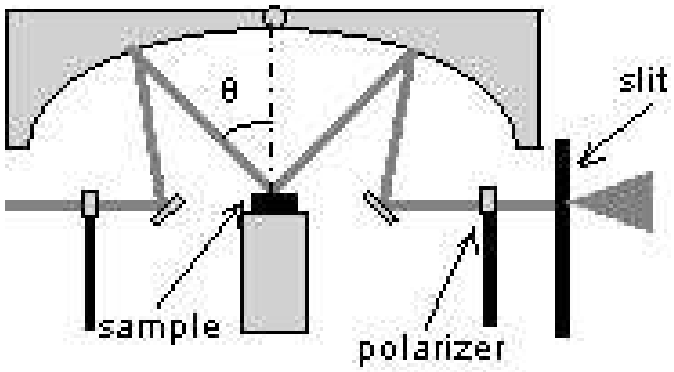

Figure 2.2 Experimental realization of the Variable-Angle Reflectance technique. The elliptical mirror allows to vary the angle of incidence θ. Courtesy of Galli, M., Università degli Studi di Pavia, Italy.

Studi di Pavia, Italy.

2.2.2 The Scattering Matrix Method

The scattering matrix method (SMM) has been developed by Whittaker, D. M., *et al.* (1999) in order to interpret variable-angle-reflectance experiments, conducted by Astratov, V. N., *et al.* A (1999) on GaAs-based two-dimensional photonic crystals. This numerical technique allows to calculate reflection, transmission and diffraction for any layered structure having a one- or two-dimensional pattern. The method is based on the idea of expanding the electromagnetic field in each layer by standard two-dimensional plane-wave expansion and propagating the set of amplitudes through the layers by means of the scattering matrix, instead of the usual transfer matrix. Indeed, in patterned multilayers, for each wave with in-plane wave-vector $\mathbf{k}$ there exists an infinite set of amplitudes corresponding to reciprocal lattice vectors $\mathbf{G}$. Wave components with large in-plane $\mathbf{k}+\mathbf{G}$ vectors are strongly evanescent in the perpendicular z direction; transferring rapidly evanescent amplitudes leads to numerical overflow. From a computational point of view, it is better to work with the corresponding scattering matrix [Ko, D. Y. K., *et al.* (1988)], which relates the amplitudes of the ingoing fields to those of the outgoing fields, with respect to a dielectric interface, instead of linking the left-side fields to the right-side field, as the transfer matrix does.

Even though a detailed description of the SSM can be found in *Phys. Rev. B*, **60**(4) 2610–2618,

which is the original paper by Whittaker, D. M., *et al.* (1999), it is worth to recall the major steps of the derivation, so to give more insight on its theoretical foundation and provide a more complete framework on the interpretation of variable-angle-reflectance spectra. The outline of the numerical scheme is as follows: the electromagnetic field is expanded on a plane-waves basis in each layer; the band structure is solved in each layer yielding a set of states that propagate in the vertical z direction as simple plane waves $\exp(\imath qz)$; a general expression of the electromagnetic field is obtained by superposition of backward and forward Bloch states; the scattering matrix is constructed; finally, reflection, transmission and diffraction are calculated by assuming an incident plane wave as initial condition.

Consider Maxwell's equations in the form of Eqs. (1.3a) and (1.3b). Assuming harmonic time dependence, see Eq. (1.4), and rescaling $\omega/c \to \omega$ and $\omega\mathbf{E} \to \mathbf{E}$, the curl equations become

$$\nabla \times \mathbf{H}(\mathbf{r}) = -\imath\epsilon(\mathbf{r})\mathbf{E}(\mathbf{r})\,, \qquad\qquad \nabla \times \mathbf{E}(\mathbf{r}) = \imath\omega^2\mathbf{H}(\mathbf{r})\,. \tag{2.1}$$

Notice that, for harmonic fields, the divergence equation for the electric field is automatically implied by Ampere's law. The divergence equation for the magnetic field can be satisfied by using basis states with zero divergence. The dielectric function $\epsilon(\mathbf{r})$ is written as $\epsilon_j(\mathbf{x})$, where j labels the j-th layer and $\mathbf{x} = (x, y)$ represents the in-plane coordinates.

Focus on the j-th layer and expand the magnetic field on a zero-divergence plane-wave basis:

$$\begin{aligned}\mathbf{H}_{\mathbf{k},q}(\mathbf{x}, z) = \sum_{\mathbf{G}} \Bigg(& c_x(\mathbf{k}+\mathbf{G}, q)\left[\hat{\mathbf{x}} - \frac{1}{q}(k_x + G_x)\hat{\mathbf{z}}\right] + \\ & + c_y(\mathbf{k}+\mathbf{G}, q)\left[\hat{\mathbf{y}} - \frac{1}{q}(k_y + G_y)\hat{\mathbf{z}}\right]\Bigg) e^{\imath(\mathbf{k}+\mathbf{G})\cdot\mathbf{x} + \imath qz}\,,\end{aligned} \tag{2.2}$$

where $\mathbf{k}$ is the in-plane Bloch vector, q is the wave-vector along the vertical direction, $\mathbf{G}$ is a reciprocal vector and c_x, c_y are the expansion coefficients; $\hat{\mathbf{x}}, \hat{\mathbf{y}}, \hat{\mathbf{z}}$ are the axes unit vectors. It is apparent that $\nabla \cdot \mathbf{H}_{\mathbf{k},q}(\mathbf{x}, z) = 0$. Eq. (2.2) can be rewritten in a more compact form as

$$\mathbf{H}_{\mathbf{k},q}(\mathbf{x}, z) = \sum_{\mathbf{G}} \mathbf{h}(\mathbf{k}+\mathbf{G}, q; z) e^{\imath(\mathbf{k}+\mathbf{G})\cdot\mathbf{x}}\,, \tag{2.3}$$

with $\mathbf{h}(\mathbf{k}+\mathbf{G}, q; z)$ representing the quantities into the round brackets multiplied by the phase $\exp(\imath qz)$. By substituting Eq. (2.3) into the magnetic-field curl equation, one finds the correspond-

ing Fourier coefficients for the electric field

$$\begin{aligned}\mathbf{e}(\mathbf{k}+\mathbf{G},q;z) =& \frac{1}{q}e^{\imath qz}\sum_{\mathbf{G}'}\eta_{\mathbf{G},\mathbf{G}'}\times \\ & \left\{\left[(k_y+G'_y)(k_x+G'_x)c_x(\mathbf{k}+\mathbf{G}',q)+\left(q^2+(k_y+G'_y)^2\right)c_y(\mathbf{k}+\mathbf{G}',q)\right]\hat{\mathbf{x}}+\right. \\ & -\left[(k_x+G'_x)(k_y+G'_y)c_y(\mathbf{k}+\mathbf{G}',q)+\left(q^2+(k_x+G'_x)^2\right)c_x(\mathbf{k}+\mathbf{G}',q)\right]\hat{\mathbf{y}}+ \\ & \left.+q\left[(k_y+G'_y)c_x(\mathbf{k}+\mathbf{G}',q)-(k_x+G'_x)c_y(\mathbf{k}+\mathbf{G}',q)\right]\hat{\mathbf{z}}\right\}\,,\end{aligned} \tag{2.4}$$

where $[\![\eta]\!]_{\mathbf{G},\mathbf{G}'}=\eta_{\mathbf{G},\mathbf{G}'}$ is the usual notation for the inverse matrix of the dielectric function in Fourier space. The full expression for the electric field reads

$$\mathbf{E}_{\mathbf{k},q}(\mathbf{x},z)=\sum_{\mathbf{G}}\mathbf{e}(\mathbf{k}+\mathbf{G},q;z)e^{\imath(\mathbf{k}+\mathbf{G})\cdot\mathbf{x}}\,. \tag{2.5}$$

By substituting $\mathbf{e}(\mathbf{k}+\mathbf{G},q;z)$ and $\mathbf{h}(\mathbf{k}+\mathbf{G},q;z)$ into the second curl equation (2.1), one obtains three identities, corresponding to each field component, x,y,z; however, one identity is linearly dependent on the other two. It is convenient to work with the identities related to the in-plane components. Using the matrix notation $[\![k_i]\!]_{G_i,G'_i}=(k_i+G_i)\delta_{G_i,G'_i}$ and $[\![c_i]\!]_{\mathbf{G}}=c_i(\mathbf{k}+\mathbf{G},q)$, with i being either x either y, the identities are gathered in a single matrix equation

$$\begin{aligned}&\left\{\begin{pmatrix}[\![\eta]\!] & 0\\ 0 & [\![\eta]\!]\end{pmatrix}\left[q^2+\begin{pmatrix}[\![k_x]\!][\![k_x]\!] & [\![k_x]\!][\![k_y]\!]\\ [\![k_y]\!][\![k_x]\!] & [\![k_y]\!][\![k_y]\!]\end{pmatrix}\right]+\right. \\ &\qquad\left.+\begin{pmatrix}[\![k_y]\!][\![\eta]\!][\![k_y]\!] & -[\![k_y]\!][\![\eta]\!][\![k_x]\!]\\ -[\![k_x]\!][\![\eta]\!][\![k_y]\!] & [\![k_x]\!][\![\eta]\!][\![k_x]\!]\end{pmatrix}\right\}\begin{pmatrix}[\![c_x]\!]\\ [\![c_y]\!]\end{pmatrix}=\omega^2\begin{pmatrix}[\![c_x]\!]\\ [\![c_y]\!]\end{pmatrix}\end{aligned} \tag{2.6}$$

The notation can be even more compact if the 2×2 block matrices are written as $[\![\mathcal{E}]\!]^{-1}$, $[\![\mathbf{K}]\!]$ and $[\![\mathcal{K}]\!]$, and the coefficients are grouped in the vector $[\![\mathbf{C}]\!]=([\![c_x]\!],[\![c_y]\!])^T$:

$$\left[[\![\mathcal{E}]\!]^{-1}\left(q^2+[\![\mathbf{K}]\!]\right)+[\![\mathcal{K}]\!]\right][\![\mathbf{C}]\!]=\omega^2[\![\mathbf{C}]\!]\,. \tag{2.7}$$

Now, ω and $\mathbf{k}$ are good "quantum numbers" and are given as initial condition. On the contrary, q is not conserved in the process, because of the absence of any translational symmetry in the vertical direction. Thus, the general solution must be a linear combination of states (2.3) or (2.5) for different q. That is why, Eq. (2.7) must be recast as an eigenvalue problem for q, not for ω. To this purpose, one simply multiplies the above expression by $[\![\mathcal{E}]\!]$, obtaining

$$\left[[\![\mathcal{E}]\!]\left(\omega^2-[\![\mathcal{K}]\!]\right)+[\![\mathbf{K}]\!]\right][\![\mathbf{C}]\!]=q^2[\![\mathbf{C}]\!]\,. \tag{2.8}$$

Eq. (2.8) is an asymmetric eigenvalue problem, which can be even complex, if $\epsilon(\mathbf{r})$ has an imaginary part. The fact that the eigenvalue problem is not symmetric, implies that the corresponding eigenvalues q^2 can be complex even for real $\epsilon(\mathbf{r})$. A complex or negative q^2 belongs to waves that are evanescent in the vertical direction, the ones responsible for numerical overflow in the transfer matrix method. A useful orthogonality property can be derived by recasting Eq. (2.8) into a not-positive-definite generalized symmetric eigenvalue problem. It follows that eigenvectors $[\![\mathbf{C}]\!]_n$ and $[\![\mathbf{C}]\!]_{n'}$, corresponding to eigenvalues q_n and $q_{n'}$ obey the condition

$$[\![\mathbf{C}]\!]_n^T \left(\omega^2 - [\![\mathcal{K}]\!]\right) [\![\mathbf{C}]\!]_{n'} = \delta_{n,n'} \,, \tag{2.9}$$

with n and n' varying between 1 and $2N$. This relationship will be useful to express the scattering matrix in terms of the expansion coefficients. Eq. (2.8) can be numerically solved by truncating the expansion to a wave-vector cut-off $K : |\mathbf{G}| < K$ and using standard routines for the diagonalization of a general matrix, be real or complex depending on $\epsilon(\mathbf{r})$. If N is the number of reciprocal vectors used in the expansion, the "hamiltonian" matrix has dimensions $2N \times 2N$. Notice that the eigenvectors have also to be computed, because they will be used in the construction of the scattering matrix.

The computed eigenvectors must satisfy the orthogonality relationship (2.9). For degenerate eigenvalues, the corresponding eigenvectors can be orthogonalized using a generalized Gram-Schimdt procedure. Otherwise, when the eigenvalues are not degenerate, the eigenvectors should be already orthogonal, as they are computed by the routine. Since the diagonalization process is often a black box, the orthogonality of non degenerate eigenvectors is practically left to the routine "goodness". `Lapack 3.0` routines have been found to comply with this requirement. However, it is likely to happen that nearly-degenerate eigenvectors do not satisfy Eq. (2.9) and, very often, none are written as exactly degenerate, unless the layer be unpatterned[1].Therefore, it is up to the programmer to decide whether two eigenvalues are degenerate or not, according to the following criterion: the eigenvalues differing by a quantity below a cut-off will undergo the Gram-Schimdt procedure that imposes the orthogonality relationship, if not already satisfied. In brief, there are two extremes: if the cut-off is

[1]If the layer is unpatterned, eigenvalues and eigenvectors are easily found by analytical derivation. This does not hold any more if the layer is patterned. It could happen that degenerate states are computed with a tiny splitting, because of numerical accuracy and truncation of the plane-wave expansion.

chosen too small, there will be non degenerate eigenvectors that do not satisfy Eq. (2.9), without the possibility of applying the Gram-Schmidt orthogonalization. On the other hand, if the cut-off is too large, the Gram-Schmidt procedure could mix states that are not truly degenerate. Since the scattering matrix is built using the eigenvectors, the above errors will propagate to the scattering matrix, with eventual numerical failure. Evidently, even the SMM has its weakness somewhere. Nevertheless, after accurate tuning of the cut-off, the method is found to be stable and accurate. After such important clarification, there are other major steps before completing the derivation of the SMM.

As already mentioned, the fields can be expressed as a combination of backward and forward waves, with vertical wave-vector q_n and complex amplitudes a_n and b_n. These amplitudes have to be determined by applying the boundary conditions at each dielectric interface, plus an initial condition. Since the boundary conditions are easily worked-out on the in-plane field components, it is convenient to find the relationship between the latter and the amplitudes a_n and b_n. Using the following matrix notation for the in-plane field components $[\![\mathbf{h}_\parallel(z)]\!]_{\mathbf{G}} = (h_x(\mathbf{k}+\mathbf{G};z), h_y(\mathbf{k}+\mathbf{G};z))^T$ and $[\![\mathbf{e}_\parallel(z)]\!]_{\mathbf{G}} = (-e_y(\mathbf{k}+\mathbf{G};z), e_x(\mathbf{k}+\mathbf{G};z))^T$ (note the skew), where the q dependence has been dropped[2], the linear combination reads

$$[\![\mathbf{h}_\parallel(z)]\!] = \sum_n [\![\mathbf{C}]\!]_n \left(e^{\imath q_n z} a_n + e^{\imath q_n (d-z)} b_n \right) , \tag{2.10}$$

where d is the thickness of the layer and $0 \leq z \leq d$. If the arbitrary sing in $\sqrt{q_n^2}$ is chosen to make $\mathrm{Im}\{q_n\} > 0$, a_n and b_n are the maximum amplitudes of each wave in the layer. An expression similar to Eq. (2.10) holds for the electric field components. For the sake of compactness, define once again a matrix notation, $[\![q]\!]_{n,n'} = q_n \delta_{n,n'}$, $[\![f(z)]\!]_{n,n'} = e^{\imath q_n z}\delta_{n,n'}$, $[\![a]\!]_n = a_n$, $[\![b]\!]_n = b_n$ and define $[\![\mathrm{C}]\!]$ as the matrix, whose column vectors are $[\![\mathbf{C}]\!]_n$. A few further steps yield to the following equation, where the field components are expressed in terms of the amplitudes:

$$\begin{pmatrix} [\![\mathbf{e}_\parallel(z)]\!] \\ [\![\mathbf{h}_\parallel(z)]\!] \end{pmatrix} = \underbrace{\begin{pmatrix} \left(\omega^2 - [\![\mathcal{K}]\!]\right) [\![\mathrm{C}]\!] [\![q]\!]^{-1} & -\left(\omega^2 - [\![\mathcal{K}]\!]\right) [\![\mathrm{C}]\!] [\![q]\!]^{-1} \\ [\![\mathrm{C}]\!] & [\![\mathrm{C}]\!] \end{pmatrix}}_{[\![M]\!]} \begin{pmatrix} [\![f(z)]\!][\![a]\!] \\ [\![f(d-z)]\!][\![b]\!] \end{pmatrix} . \tag{2.11}$$

[2]In the linear combination, the dependence on the vertical wave-vector q is dropped, because it is not a good "quantum number" any more. Notice also that in other expressions, like $[\![c_i]\!]_{\mathbf{G}} = c_i(\mathbf{k}+\mathbf{G}, q)$, the q-dependence has been replaced by n, the label for the eigenvalues.

By exploiting the orthogonality relationship (2.9), the inverse of $[\![M]\!]$ is

$$[\![M]\!]^{-1} = \frac{1}{2}\begin{pmatrix} [\![q]\!][\![\mathrm{C}]\!]^T & [\![\mathrm{C}]\!]^T\left(\omega^2 - [\![\mathcal{K}]\!]\right) \\ -[\![q]\!][\![\mathrm{C}]\!] & [\![\mathrm{C}]\!]^T\left(\omega^2 - [\![\mathcal{K}]\!]\right) \end{pmatrix}. \tag{2.12}$$

With $[\![M]\!]$ and its inverse one can obtain the in-plane field components from the amplitudes and vice versa. Note that, if the plane-wave expansion has dimension N, $[\![M]\!]$ is a $4N \times 4N$ matrix. These quantities are used to construct the scattering matrix of the whole structure.

The scattering matrix relates the amplitudes of forward and backward waves in different layers of the structure. More precisely, the amplitudes of the ingoing waves are found in terms of those of the outgoing ones. Since the amplitudes are vectors of dimension $2N$, the scattering matrix $[\![S]\!]$ must have dimensions $4N \times 4N$:

$$\begin{pmatrix} [\![a]\!]_j \\ [\![b]\!]_{j'} \end{pmatrix} = [\![S(j',j)]\!] \begin{pmatrix} [\![a]\!]_{j'} \\ [\![b]\!]_j \end{pmatrix} = \begin{pmatrix} [\![S]\!]_{11} & [\![S]\!]_{12} \\ [\![S]\!]_{21} & [\![S]\!]_{22} \end{pmatrix} \begin{pmatrix} [\![a]\!]_{j'} \\ [\![b]\!]_j \end{pmatrix}. \tag{2.13}$$

where j and j' represent two layers and $[\![S]\!]_{il}$ are $2N \times 2N$ matrix blocks of the scattering matrix. The amplitudes in two adjacent layers are related by the so-called interface matrix $[\![I(j,j+1)]\!]$, which is defined by

$$\begin{pmatrix} [\![f]\!]_j[\![a]\!]_j \\ [\![b]\!]_j \end{pmatrix} = [\![I(j,j+1)]\!] \begin{pmatrix} [\![a]\!]_{j+1} \\ [\![f]\!]_{j+1}[\![b]\!]_{j+1} \end{pmatrix} = \begin{pmatrix} [\![I]\!]_{11} & [\![I]\!]_{12} \\ [\![I]\!]_{21} & [\![I]\!]_{22} \end{pmatrix} \begin{pmatrix} [\![a]\!]_{j+1} \\ [\![f]\!]_{j+1}[\![b]\!]_{j+1} \end{pmatrix}, \tag{2.14}$$

where $[\![f]\!]_j = [\![f(d_j)]\!]_j$. The interface matrix contains the electromagnetic boundary conditions, i.e. continuity of the in-plane field components of $\mathbf{E}$ and $\mathbf{H}$. Such condition is satisfied by applying Eq. (2.11) in the $(j+1)$-th layer, using $z = 0$. This gives the in-plane components at the right-side of the interface, in terms of the amplitudes in the $(j+1)$-th layer. Thereafter, the in-plane components of the left-side (equal to those of the right-side) are transformed into the amplitudes of the j-th layer, by application of the inverse equation (2.12), for the j-th layer and $z = d_j$. In other words, the interface matrix is simply given by

$$[\![I(j,j+1)]\!] = [\![M]\!]_j^{-1}[\![M]\!]_{j+1}. \tag{2.15}$$

Once that the interface matrix is known, the scattering matrix is computed layer-by-layer by recasting Eq. (2.14) into Eq. (2.13). If $[\![S(j',j)]\!]$ is the scattering matrix between the j'-th and the

j-th layers, the scattering matrix between the j'-th and the $(j+1)$-th layers follows the recipe

$$[\![S(j',j+1)]\!]_{11} = \left([\![I]\!]_{11} - [\![f]\!]_j [\![S(j',j)]\!]_{12} [\![I]\!]_{21}\right)^{-1} [\![f]\!]_j [\![S(j',j)]\!]_{11}\,; \tag{2.16a}$$

$$[\![S(j',j+1)]\!]_{12} = \left([\![I]\!]_{11} - [\![f]\!]_j [\![S(j',j)]\!]_{12} [\![I]\!]_{21}\right)^{-1} \left([\![f]\!]_j [\![S(j',j)]\!]_{12} [\![I]\!]_{22} - [\![I]\!]_{12}\right) [\![f]\!]_{j+1}\,; \tag{2.16b}$$

$$[\![S(j',j+1)]\!]_{21} = [\![S(j',j)]\!]_{22} [\![I]\!]_{21} [\![S(j',j+1)]\!]_{11} + [\![S(j',j)]\!]_{21}\,; \tag{2.16c}$$

$$[\![S(j',j+1)]\!]_{22} = [\![S(j',j)]\!]_{22} [\![I]\!]_{21} [\![S(j',j+1)]\!]_{12} + [\![S(j',j)]\!]_{22} [\![I]\!]_{22} [\![f]\!]_{j+1}\,; \tag{2.16d}$$

where $[\![I]\!]_{il} = [\![I(j,j+1)]\!]_{il}$. Using Eqs. (2.16a-d), plus the initial condition that $[\![S(j',j')]\!] = [\![1]\!]$, the scattering matrix of the whole heterostructure is built up one layer at a time. The stability of the SMM relies on the fact that all the elements of $[\![f]\!]$ have absolute value less than unity, because of $\mathrm{Im}\{q_n\} > 0$. Therefore, the matrix inversion of Eqs. (2.16a-b) is dominated by the non-singular matrix $[\![I]\!]_{11}$. It is worth to remark, however, that the orthogonality of the eigenvectors is important not only in the analytical derivation of $[\![M]\!]^{-1}$, but also for a well behaved numerical inversion of the matrices in Eqs. (2.16a-b). Indeed, it has been found that the order of magnitude of the accuracy in defining two eigenvectors orthogonal propagates to the accuracy in computing the inverse of $([\![I]\!]_{11} - [\![f]\!]_j [\![S(j',j)]\!]_{12} [\![I]\!]_{21})$. In order to calculated reflection, transmission and diffraction, one needs the scattering matrix of the whole structure, i.e. $[\![S(0,N)]\!]$, if $j = 0$ labels the surface and $j = N$ the substrate.

In a reflectance calculation, the initial condition is an incident plane wave impinging the surface of the heterostructure; namely $[\![a]\!]_0$ is determined by the incident geometry and $[\![b]\!]_N = 0$. Then, $[\![b]\!]_0$ refers to reflected and diffracted waves at the surface, while $[\![a]\!]_N$ is for transmitted and diffracted waves in the substrate. The relationship between these amplitudes is given they the scattering matrix:

$$[\![b]\!]_0 = [\![S(0,N)]\!]_{21} [\![a]\!]_0 \qquad\qquad [\![a]\!]_N = [\![S(0,N)]\!]_{11} [\![a]\!]_0\,. \tag{2.17}$$

What remains is to write the amplitudes in terms of the external plane waves. Eqs. (2.11) and (2.12) provide the required expressions to pass from one quantity to the other one, and vice versa. Define the incident plane wave (i) of frequency ω, with its polarization and direction of propagation, by means of the polar coordinates (θ, ϕ), see Fig. 2.3. If ϵ is the dielectric constant of the external

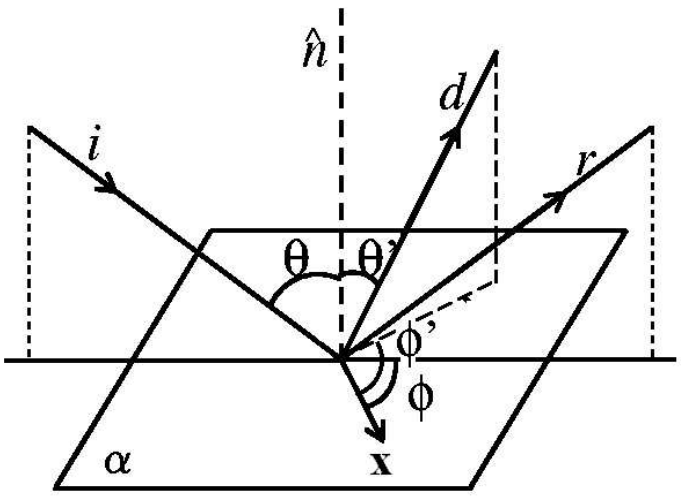

Figure 2.3 Kinematics of reflection r and diffraction d in air. The diffraction angles, θ' and ϕ', are determined by energy and momentum conservation. i is the incident beam with polar angles (θ, ϕ) and $\hat{\mathbf{n}}$ is the normal to the surface α.

medium (usually air), the associated in-plane wave-vector is written as

$$\mathbf{k} = \omega\sqrt{\epsilon}\sin\theta\,(\hat{\mathbf{x}}\cos\phi + \hat{\mathbf{y}}\sin\phi)\ , \tag{2.18}$$

(remember that $\omega/c \to \omega$). Then, the plane wave is classified according to parity with respect to the plane of incident. The TE (odd) and TM (even) waves have field components

$$\begin{aligned}\mathbf{E}_{\mathrm{TE}} =& \frac{4\pi\omega}{c} Z^{1/2}\,(\hat{\mathbf{x}}\sin\phi - \hat{\mathbf{y}}\cos\phi)\ , \\ \mathbf{H}_{\mathrm{TE}} =& Z^{-1/2}\,(\hat{\mathbf{x}}\cos\theta\cos\phi + \hat{\mathbf{y}}\cos\theta\sin\phi - \hat{\mathbf{z}}\sin\theta)\ ,\end{aligned} \tag{2.19a}$$

$$\begin{aligned}\mathbf{E}_{\mathrm{TM}} =& \frac{4\pi\omega}{c} Z^{1/2}\,(\hat{\mathbf{x}}\cos\theta\cos\phi + \hat{\mathbf{y}}\cos\theta\sin\phi - \hat{\mathbf{z}}\sin\theta)\ , \\ \mathbf{H}_{\mathrm{TM}} =& -\,Z^{-1/2}\,(\hat{\mathbf{x}}\sin\phi - \hat{\mathbf{y}}\cos\phi)\ ,\end{aligned} \tag{2.19b}$$

multiplied by the phase factor $\exp(\imath\mathbf{k}\cdot\mathbf{x} + \imath qz)$. Z is the intrinsic impedance of the external medium. The normalization is chosen so that the true Poynting vector $P = c/(4\pi\omega)\mathbf{E}\times\mathbf{H}$ has unit magnitude. The incident TE or TM plane wave has to be translated into the amplitude $[\![a]\!]_0$. If the lattice period is sufficiently short that the in-plane wave-vector lies within the Brillouin zone, the fields of Eq. (2.19a) or Eq. (2.19b) correspond to the $\mathbf{G} = \mathbf{0}$ components of the in-plane fields

$[\![\mathbf{e}_\parallel]\!]$ and $[\![\mathbf{h}_\parallel]\!]$ and the others ($\mathbf{G} \neq 0$) are all zero. The reflected wave (r) is obtained from the $\mathbf{G} = 0$ component of the amplitude $[\![b]\!]_0$, which is then resolved into TE-TM polarization using the polarization projector operators. The reflection coefficient R is simply the Poynting vector of the reflected wave. All the $\mathbf{G} \neq \mathbf{0}$ components of $[\![b]\!]_0$ correspond to evanescent waves and contribute to the near field.

When the in-plane wave-vector of the incident wave is sufficiently large to lie outside the Brillouin zone, diffraction takes place. If $\mathbf{G}$ is the reciprocal vector that brings the wave-vector inside the Brillouin zone, the incident wave provides the $\mathbf{G}$-th components to $[\![\mathbf{e}_\parallel]\!]$ and $[\![\mathbf{h}_\parallel]\!]$, while all others are zero. The reflected wave is obtained by taking the same $\mathbf{G}$-th components of the fields calculated from $[\![b]\!]_0$. All the other components corresponding to non evanescent waves will contribute to diffraction (d). The same rule apply for transmission and diffraction in the substrate.

The whole procedure can be represented by the following scheme

$$\begin{array}{c}\text{TE or TM}\\ \text{incident wave } (i) \Rightarrow \\ (\omega,\theta,\phi)\end{array} \quad \begin{array}{c}[\![a]\!]_0\\ \mathbf{G}\text{-th comp.}\end{array} \quad \Rightarrow [\![S(0,N)]\!] \Rightarrow \begin{cases} [\![b]\!]_0 \Rightarrow & \begin{cases} \text{reflection } (r), & \text{if } \mathbf{G}' = \mathbf{G}; \\ \quad (\omega,\theta,\phi) & \\ \text{diffraction } (d), & \text{if } \mathbf{G}' \neq \mathbf{G} \text{ and } ; \\ \quad (\omega,\theta',\phi') & \omega^2\epsilon > (\mathbf{k}+\mathbf{G}')^{\mathbf{2}} \end{cases} \\ [\![a]\!]_N \Rightarrow & \begin{cases} \text{transmission } (t), & \text{if } \mathbf{G}' = \mathbf{G}; \\ \quad (\omega,\theta'',\phi) & \\ \text{diffraction } (d), & \text{if } \mathbf{G}' \neq \mathbf{G} \text{ and } ; \\ \quad (\omega,\theta',\phi') & \omega^2\epsilon_{\rm s} > (\mathbf{k}+\mathbf{G}')^{\mathbf{2}} \end{cases} \end{cases}$$

where θ'' obeys Snell's law: $\sin\theta'' = \sqrt{\epsilon_{\rm s}/\epsilon}\sin\theta$, with $\epsilon_{\rm s}$ as the substrate dielectric function. The angles of the diffracted waves (θ',ϕ') are found by imposing the constraints of energy and in-plane momentum conservation. Eventually, the reflected, transmitted and diffracted waves are resolved into TE and TM polarization, before that the corresponding Poynting vectors are calculated. Since the incident power is normalized to unity, the final expressions for reflection (R), transmission (T) and diffraction (D) coefficients are:

$$R = P(r)\,, \qquad T = P(t)\frac{\cos\theta''}{\cos\theta}\,, \qquad D = P(d)\frac{\cos\theta'}{\cos\theta} + P^{(s)}(d)\frac{\cos\theta'^{(s)}}{\cos\theta}\,,$$

where $P(r,t,d)$ are the respective Poynting vectors and (s) means substrate. Notice that the

diffraction coefficient accounts for diffraction in both sides of the structure. If all media are lossless, then $(T+R+D)^{(\mathrm{TE})}+(T+R+D)^{(\mathrm{TM})}=1$. On the contrary, in the presence of absorption, the sign $=$ must be replaced by $<$.

In conclusion, the numerical operations required by the SMM are: inversion of the $N \times N$ dielectric matrix, diagonalization of the $2N \times 2N$ "hamiltonian" general real or complex matrix, Gram-Schmidt's orthogonalization for degenerate eigenvectors, and inversion of a general $2N \times 2N$ complex matrix. It is apparent that the method is much more demanding than the standard plane-wave expansion used for computing the band structure of two-dimensional photonic crystals. That is why convergence tests are fundamental for determining the best trade-off between accuracy and speed [Whittaker, D. M., *et al.* (1999)]. For typical layered semiconductors, calculations performed with 61-109 plane waves are satisfactorily accurate, if the inversion of the dielectric matrix is performed using the inverse rule [Li, L. (1996)].

As a last remark, it is noticeable that the SMM is particularly suitable for modelling realistic conditions, because the calculation can be performed including either any material dispersion $\epsilon(\omega)$, either absorption $\mathrm{Im}\{\epsilon\} \neq 0$. Not to mention that the freedom in choosing a certain one- or two-dimensional pattern, or choosing the vertical profile of the heterostructure, as well as the number of layers, is practically no-limits. Furthermore, the method can also treat uniaxial media, after minor changes to the code. Some more work is needed instead, if one wants to use the SMM for the calculation of emission spectra [Whittaker, D. M., *et al.* (1999)]. In this context, the method will be used only for computing reflection, transmission and diffraction of semiconductor-based photonic crystals. In specific cases, material dispersion and absorption are included to fit the experimental reflectance, but, most of the times, the dielectric function is chosen to be a constant.

2.2.3 Reflection, Transmission and Diffraction

To better understand the optical properties of photonic crystals, consider for a moment the simplest case: a suspended dielectric membrane with a one-dimensional pattern, like the system discussed in Sec. 1.4.2: core dielectric constant $\epsilon = 12$, waveguide thickness $d = 0.5a$ and air filling ratio $f = 30\%$. The incidence angles θ and ϕ are chosen to be 50° and 0°, respectively, where ϕ is with respect to the axis aligned with the direction of periodicity. A TM-polarized

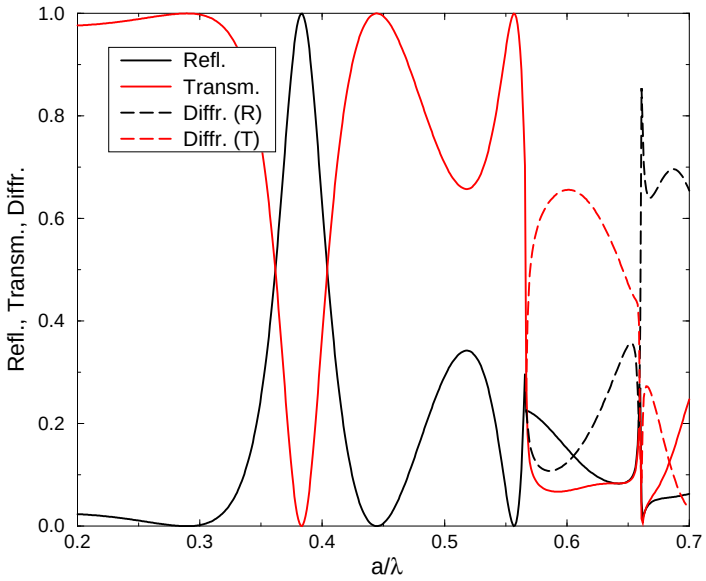

Figure 2.4 TM-polarized transmission, reflection and diffraction for the air bridge one-dimensional photonic crystal of Fig. 1.10. Parameters: $\epsilon = 12$, $d = 0.5a$, and $f = 30\%$. Incident wave: $\theta = 50°$, $\phi = 0°$ and TM-polarization. Diffr. (R) and Diffr. (T) mean diffraction above and below the membrane, respectively.

incident beam samples the photonic states that lie above the light line: reflection, transmission and diffraction are calculated for $a/\lambda = \omega a/2\pi c$ from 0.2 to 0.7. Because the plane of incidence is a mirror plane for the system, the whole process preserves the initial polarization, so that the TM $\rightarrow$ TE conversion is zero. For the same reason, the external wave couples only to photon states that have the same symmetry with respect to the plane of incidence. Then, the incident beam is reflected and transmitted. Moreover, if the frequency is high enough to be above the folded light line $\omega/c = |\mathbf{k} + \mathbf{G}|$, diffraction occurs too. Notice that the polarization is conserved also in the diffraction process, because the diffracted beams lie in the plane of incidence. There are infinite diffraction cut-offs ω_c, which are determined by imposing that $\omega_c/c = |\mathbf{k} + \mathbf{G}|$. The cut-off frequencies can be expressed in terms of the incidence angles by the formulae (2.20): the first one is for $\phi = 0$, whereas the second one is for the general case. $n \in \mathbb{N}$ represents the diffraction order and corresponds to $G = n2\pi/a$.

$$\frac{\omega_c a}{2\pi c} = \frac{n}{1+\sin\theta}\,, \qquad \frac{\omega_c a}{2\pi c} = \frac{n}{\sqrt{1-\sin^2\phi\sin^2\theta}+\cos\phi\sin\theta}\,. \tag{2.20}$$

Fig. 2.4 shows reflection, transmission and diffraction for the above mentioned initial conditions. Since the pattern is one-dimensional, the curves have been calculated employing only 31 plane waves. Diffr.(R) represents diffraction in the top cladding, while Diffr.(T) is for diffraction in the bottom cladding. They exhibit the same cut-off ($a/\lambda_c = 0.566$), because both external media are air. Notice that $T + R + D$ is equal to one below and above the diffraction cut-off, as it has to be. The anomalies in either reflection, transmission or diffraction correspond to the excitation of quasi-guided modes of the photonic-crystal slab; see for example the sharp resonance at $a/\lambda \simeq 0.66$, which matches a mode visible in Fig. 1.10. Notice also that diffraction is the dominant process above its cut-off.

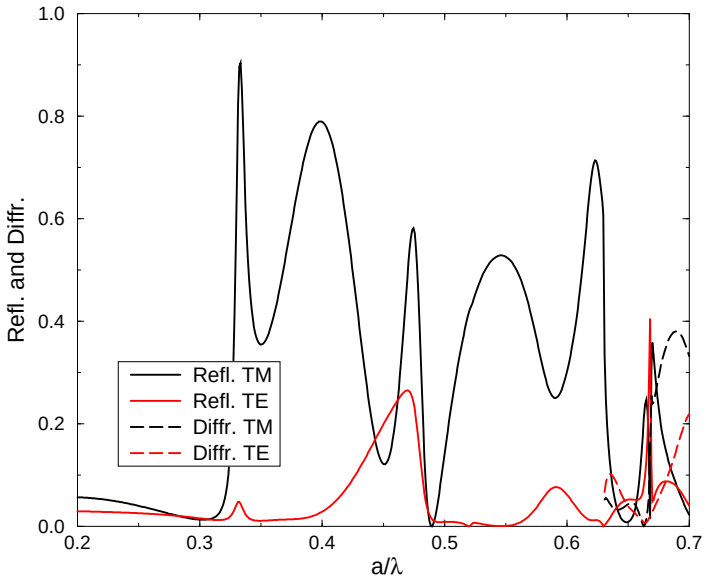

Figure 2.5 Reflection and diffraction for the air bridge one-dimensional photonic crystal of Fig. 1.10. Parameters: $\epsilon = 12$, $d = 0.5a$, and $f = 30\%$. Incident wave: $\theta = 50°$, $\phi = 30°$ and TM-polarized.

Fig. 2.5 shows the TM $\rightarrow$ TE conversion in reflection and diffraction for the same air bridge system, when the TM-polarized incident wave impinges with angles $\theta = 50°$ and $\phi = 30°$. Now, the plane of incidence does not represent a mirror plane any more. Furthermore, as the incidence

angles have changed, the diffraction cut-off is different from the previous case. Using Eq. 2.20, the cut-off is found to be $a/\lambda_c = 0.63$. The polarization conversion is rather relevant for certain frequency values. This is due to the strong anisotropy induced by the one-dimensional pattern; for a two-dimensional photonic crystal, the polarization conversion is overall weaker.
For two-dimensional photonic crystals, the study of diffraction is more complicated, of course, but it is conceptually identical to the one-dimensional case: the cut-offs are always given by $\omega_c/c = |\mathbf{k} + \mathbf{G}|$, where now $\mathbf{G}$ spans two dimensions. Again, the polarization conversion is null if the plane of incidence corresponds to a mirror plane of the photonic crystal.

The SMM is now applied to two-dimensional photonic crystals and photonic-crystal slabs to study their optical properties and extracting information on the photonic band dispersion. Moreover, for photonic-crystal slabs only, the method is also used to evaluate the propagation losses of the guided resonances.

2.3 Two-Dimensional Photonic Crystals

For in-plane propagation, two-dimensional photonic crystals have been shown to have Bloch modes with well defined polarization states, according to parity with respect to the plane of periodicity, called H-modes (even) and E-modes (odd). Furthermore, each state can be specified by association to a certain irreducible representation of the corresponding small point group. In Sec. 1.3.2, the group theory analysis has been helpful in understanding the formation of photonic bands, with emphasis on the removal of degeneracy and on the photonic band gap. The present objective is to study how symmetry properties affect the determination of the band structure carried out with the VAR technique; in other words, how the external field couples to photonic-crystal modes. Also, the aim is to show that the method is suitable for obtaining the dispersion relation of two-dimensional photonic crystals, without need of embedding the system in a waveguide configuration. This is a remarkable feature, because it goes beyond to the original argument, borrowed from grating theory, that the sharp resonances in the reflectance curve correspond to the excitation of guided resonances in a photonic-crystal slab [Astratov, V. N., *et al.* A (1999)]. More generally,

the anomalies in reflectance of two-dimensional photonic crystals are due to matching of the external field with a Bloch state, which behaves like a one-dimensional critical point, whose density of state is given by photon dispersion in the vertical direction only, whereas the in-plane momentum is conserved.

For what concerns the theoretical implementation of a VAR study on two-dimensional photonic crystals, the calculation is easily accomplished by applying the SMM to a system composed by two semi-infinite layers, air and two-dimensional photonic crystal, with a common interface. The presence of the interface breaks the symmetry with respect to the plane of periodicity, so that the classification into H-modes E-modes is not rigorously valid anymore. Nevertheless, the bulk dispersion relation is not modified at all by the surface and the SMM samples a truly two-dimensional photonic band structure.

As regards an experimental realization of the above analysis, if one wants to measure bands in the near-infrared frequency regime, macro-porous silicon is the unique system that provides high aspect ratios for obtaining a two-dimensional photonic crystal. Therefore, the possibility of a direct comparison with experimental curves and theory makes macro-porous silicon the preferable system for studying the optical properties of two-dimensional photonic crystals.

2.3.1 Macro-Porous Silicon Photonic Crystals

Macro-porous silicon photonic crystals are obtained by electrochemical etching of n-type bulk silicon samples [Lehmann, V., *et al.* (1990); Grüning, U., *et al.* (1996)]. The resulting pores have regular shape and are organized according to a two-dimensional lattice, which provides a periodic modulation of the dielectric function in the plane parallel to the sample surface. Unlike waveguide-based photonic crystals, macro-porous silicon can be considered as homogenous along the hole axes, since pores of $50 - 100\mu$m depth can be achieved, while the lattice constant can be of the order of $1 - 2\mu$m [Birner, A., *et al.* (1998); Rowson, S., *et al.* (1999)] or even less. The above features show that macro-porous silicon is an ideal system for studying the optical properties of two-dimensional photonic crystals from mid-infrared (10μm) to telecommunication wavelengths ($1.3, 1.5\mu$m). It is worth to mention that recent studies have also investigated defect states created in macro-porous silicon, namely waveguides [Leonard, S. W., *et al.* (2000)] and micro-resonators [Kramper, P., *et*

al. (2001)], but not in the spirit of the VAR technique. It is worth to mention that there are also attempts to attain vertical confinement in macro-porous silicon [Schilling J., *et al.* A (2001)].

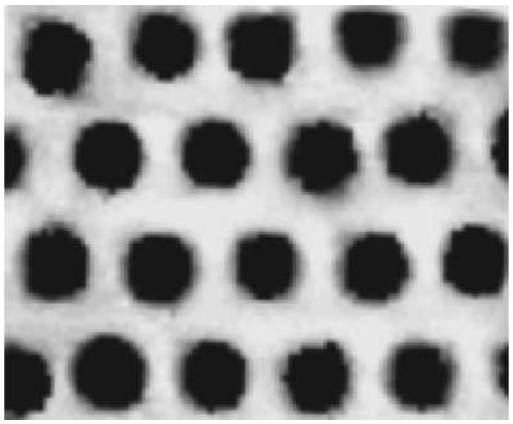

Figure 2.6 AFM image of a macro-porous silicon photonic crystal (dimensions: $10 \times 8.4\mu$m). The lattice constant is $a = 2\mu$m and the hole radius is $r = 0.24a$. Courtesy of Patrini, M., Università degli Studi di Pavia, Italy, and Bettotti, P., Università degli Studi di Trento, Italy.

Fabrication Method

As already mentioned, macro-porous samples are prepared by electrochemical etching of a pre-patterned substrate. More precisely, a two-dimensional lattice is defined by standard lithography on a silicon substrate with $\langle 100 \rangle$ orientation and the initial etch pits are transferred to the substrate by a hot KOH treatment (alkaline etching). The resulting inverted pyramids act like initial pores. The next step consists of etching deep and regular holes through an electrochemical process. Substrates with n-type or p-type doping can be used, though the original method was developed on n-type silicon [Lehmann, V., *et al.* (1990)]. For n-type substrates, deep pores are etched under anodic bias and stabilized backside illumination in hydrofluoric acid. The pore formation relies on the dissolution of silicon, promoted by the electrons generated by the backside illumination and diffused by the anodic bias. The presence of the initial pits attracts the diffused electrons, so that silicon is dissolved much faster than elsewhere. Stabilized illumination is necessary for obtaining a constant diameter as the etching process advances. While the two-dimensional lattice is defined by

lithography, the hole diameter (air filling ratio) is controlled by the illumination intensity. After the etching process, variations of the hole shape both with depth and with the neighboring holes can be very small. The etch pits are then removed by polishing with diamond powder. Sometimes, a subsequent oxidation/etching step is used to increase the hole diameter and correct possible irregularities.

The sample under investigation has a triangular lattice with circular pores having a center-to-center distance $a = 2\mu$m and hole radius $r = 0.24a$. An atomic force microscopy (AFM) image of the sample is shown in Fig. 2.6. In the next section, the photonic bands are extracted from VAR curves calculated with the SMM and compared to experimental data. A symmetry analysis will explain the selection rules of the process. Arguments on the line-shape of the anomalies seen in reflectance curves are also given. For a more detailed study of this sample, please refer to Galli, M., *et al.* A (2002).

2.3.2 Reflectance and Selection Rules

VAR from the sample surface is calculated by means of the SMM along the $\Gamma - K$ and $\Gamma - M$ crystal orientations, for both TE and TM polarizations, employing 151 plane waves. The material dielectric function is assumed to have a small dispersion, from 11.7 at 0.15eV up to 11.8 at 0.5eV, and no absorption. Fig. 2.7 shows the calculated reflectance for TE-polarized light incident along the $\Gamma - K$ orientation; Fig. 2.8 compares the measured and calculated reflectance along $\Gamma - K$ for TE and TM polarizations. Experimental data are courtesy of Galli, M., Università degli Studi di Pavia, Italy. The reflectance curves of the macro-porous silicon sample display prominent features with a well defined dispersion as a function of incidence angle. There is a good overall agreement between the experimental and calculated spectra as regards to the number of structures in reflectance and their dispersion, although the experimental line-shape is more complex than the theoretical one. The spectral strength of the structure depends on the angle θ. Most features become vanishingly weak at $\theta = 5°$, where only one strong structure at 0.29eV is observed.

The results of Figs. 2.7 and 2.8 (and the analogous ones for reflectance along $\Gamma - M$, not shown here) are interpreted in the following way. When the frequency ω and the in-plane wave-vector $\mathbf{k}$ match those of a photonic mode propagating in the plane, a diffracted beam is created in the material and

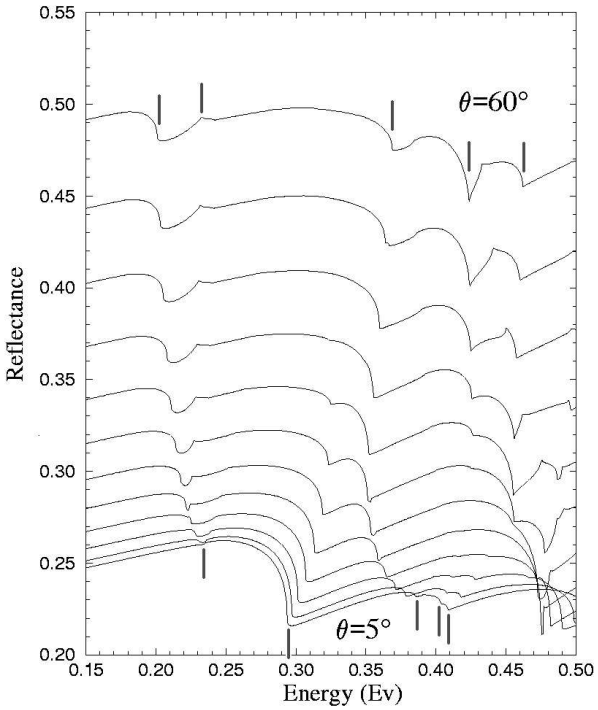

Figure 2.7 Calculated reflectance for the macro-porous silicon sample of Fig. 2.6 with TE polarized light incident along the $\Gamma - K$ orientation. The angle of incidence is varied from 5° to 60° with a step of 5°. Vertical bars mark the positions of 2D photonic modes for 5° and 60°.

a corresponding structure appears in reflectance. This is very clear in the calculation, where the onset of a diffracted beam corresponds to a complex wave-vector component q that goes through zero and becomes real. In the work by Astratov, V. N., *et al.* A (1999), a similar approach was used for patterned GaAs-based waveguides. However, in the present case, there is no waveguide and a structure in reflectance marks the *onset* of a photonic mode, which is excited and remains propagating also for higher frequencies.

While most features in the experimental curves show a typical dispersive shape, the calculated curves exhibit a discontinuous derivative in correspondence of the onset of a photonic mode, such as for critical-point transitions [Bassani, F., *et al.* (1975); Cardona, M., *et al.* (1996)]. This "universal" line-shape is broadened in the experiments, probably because of sample inhomogeneity. Each critical point in reflectance is related to a singularity in the diffracted intensity $D(\omega)$, which may be calculated by interpreting the excitation of a photonic mode as an "absorption" process

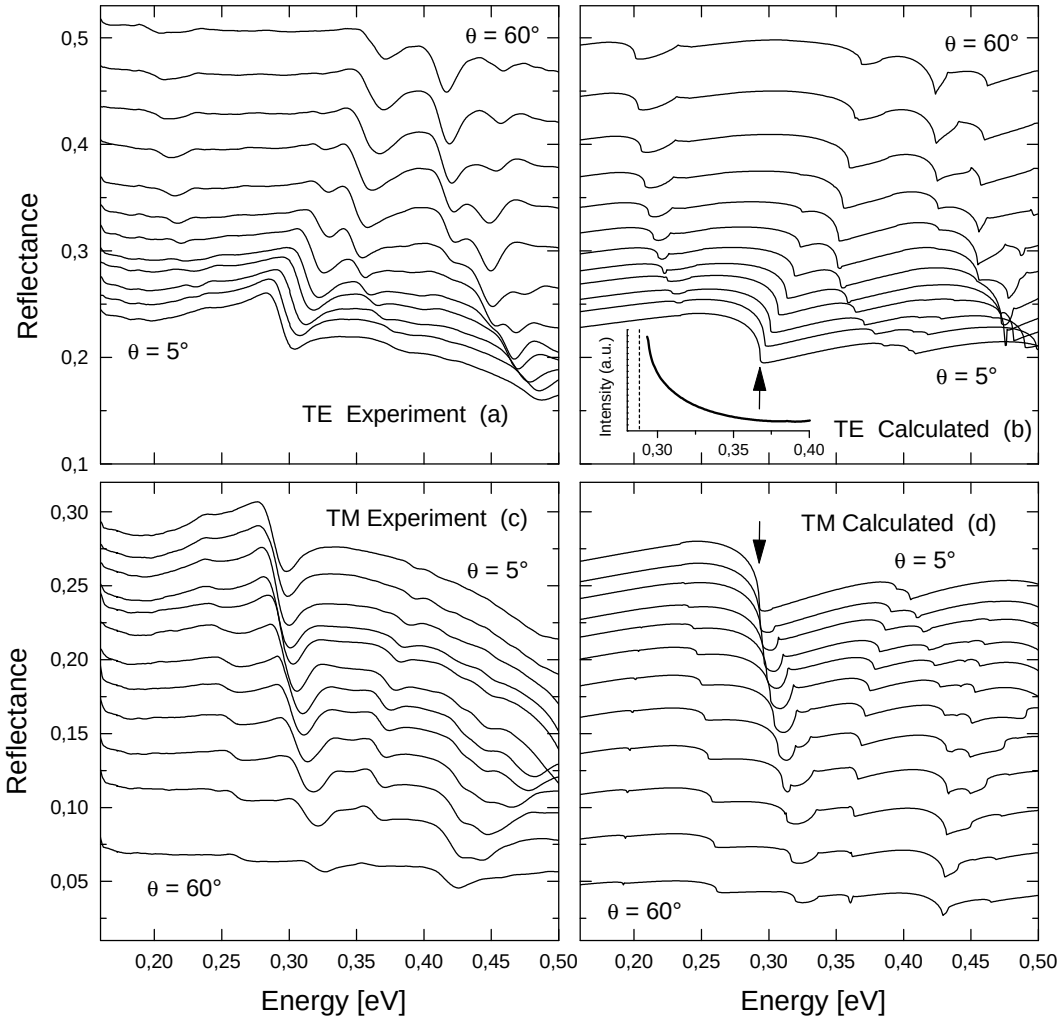

Figure 2.8 (a),(c): experimental reflectance of the sample of Fig. 2.6 for light incident along the $\Gamma - K$ orientation, for TE and TM polarizations; courtesy of Galli, M., Università degli Studi di Pavia, Italy. (b),(d): calculated reflectance. The angle of incidence is varied from 5° to 60° with a step of 5°. The curves at 5°, 10° and 15° are slightly off-set for clarity. Inset to (b): diffracted intensity corresponding to the allowed mode at $\theta = 5°$ (onset marked by arrows).

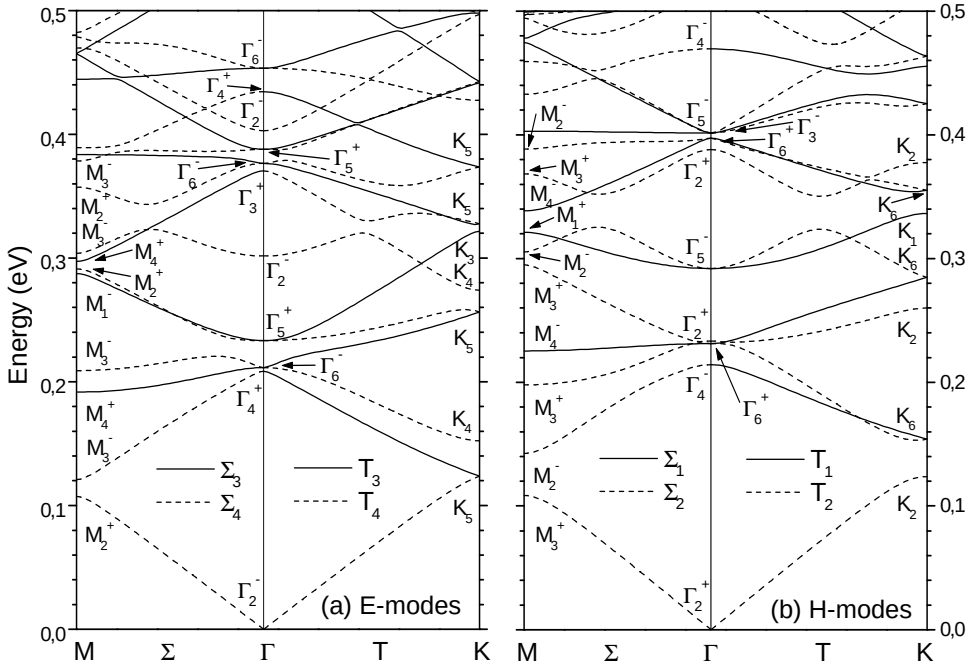

Figure 2.9 Top panels: photonic bands of a triangular lattice of air holes in silicon with $a = 2\mu$m, $r = 0.24a$; (a) E-modes, (b) H-modes.

(the intensity of the diffracted beam is removed from specular reflectance and transmittance): thus $D(\omega)$ may be expressed as

$$D(\omega) \propto \int \mathrm{d}\mathbf{k}' \int \mathrm{d}q \, \delta_{\mathbf{k}',\mathbf{k}} \delta(\hbar\omega - E(\mathbf{k}', q)) \,, \tag{2.21}$$

where $|\mathbf{k}| = (\omega/c)\sin\theta$. The parallel wave-vector $\mathbf{k}$ is conserved and the out-of-plane dispersion of all bands (except close to the special point $\omega = 0$) is quadratic in q, around $q = 0$ [Joannopoulos, J. D., *et al.* (1995)], with a threshold $E(\mathbf{k}, 0) \equiv E_0$. Thus Eq. (2.21) yields $D(\omega) \propto (\hbar\omega - E_0)^{-1/2}$, like for a one-dimensional density of states. The inset of Fig. 2.8b shows the calculated diffracted intensity of the allowed mode at near-normal incidence, which indeed has the form of an inverse square root close to the threshold E_0=0.29eV. A similar behavior is found for all diffracted rays, proving that each spectral feature in reflectance corresponds to a one-dimensional critical point.

The selection rules for specular reflectance are discussed starting from the symmetry properties of the system. The photonic band structure of the photonic crystal under investigation, for in-plane propagation, is classified into H-modes and E-modes, as displayed in Fig. 2.9. Recall that

the point group of the triangular lattice is D_{6h}, view as direct product of C_{6v} and C_s. The small point group is C_{2v} for the $\Gamma - M$, $\Gamma - K$ and $M - K$ directions, though the twofold axis of C_{2v} differs in the three cases. Recall also that the twofold degenerate levels at Γ can have Γ_5^+ or Γ_6^- symmetry for E-modes and Γ_5^- or Γ_6^+ for H-modes; Γ_5^+ (Γ_5^-) is the symmetry of the xy component of a pseudovector (vector), see Sec. 1.3.2. The surface of the crystal breaks mirror symmetry with respect to the $x - y$ plane, so that the reflection σ_{xy} is not a symmetry operation anymore. The photonic modes should then be classified according to the subgroup C_{6v} of the point group at Γ and the corresponding subgroups at other $\mathbf{k}$ points. Along the $\Gamma - M$ and $\Gamma - K$ directions the small point group becomes C_s, i.e. specular reflection with respect to the plane of incidence is the only symmetry operation besides the identity.

The general selection rule can be stated as follows: *a photonic band can appear in reflectance only if it has the same symmetry of the incident electromagnetic field.* At normal incidence, the electric field (E_x, E_y) as well as the magnetic field (H_x, H_y) transform similar to the twofold degenerate representation Γ_5 of C_{6v}. The irreducible representations of D_{6h} that reduce to this representation are Γ_5^+ and Γ_5^-, which implies that only states with symmetries $\Gamma_5^\pm$ can appear in reflectance. Such selection rule is obeyed in reflectivity curves of Figs. 2.7 and 2.8; in particular, the strong structure around 0.29eV at $\theta = 5^\circ$ corresponds to the allowed band with symmetry Γ_5^-, see Fig. 2.9.

Concerning now selection rules along $\Gamma - M$ and $\Gamma - K$, notice that these are the only orientations for which the plane of incidence is also a mirror plane of the structure: the photonic bands can be classified as even or odd with respect to this mirror symmetry. A TE wave is odd for specular reflection with respect to the plane of incidence, while a TM wave is even. Therefore, a TE-polarized wave interacts with photonic bands that are odd for specular reflection in the vertical mirror plane, while a TM-polarized wave interacts only with even bands. Odd photonic bands correspond to Σ_3 and Σ_2 representations of C_{2v} for $\Gamma - M$ (T_3 and T_2 for $\Gamma - K$), while even bands correspond to Σ_1 and Σ_4 for $\Gamma - M$ (T_1 and T_4 for $\Gamma - K$).

Notice that an incident plane wave can interact with both $E-$ and H-modes of the photonic structure. For this reason, it is appropriate to compare the photonic bands extracted from a reflectivity experiment not with those of E- and H-modes, but rather with those of the same parity with respect to a specular reflection in the plane of incidence. Such comparison is shown in Fig. 2.10.

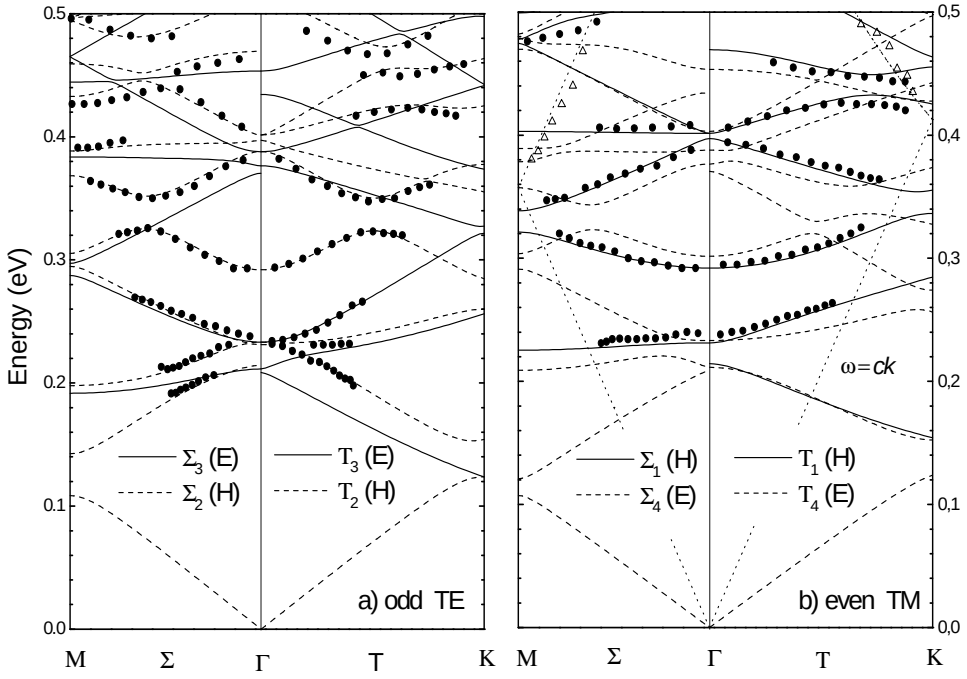

Figure 2.10 Measured dispersion of the photonic bands (points), derived from the structures in reflectance curves; the solid and dashed lines are the same photonic bands of Fig. 2.9, separated according to parity with respect to the plane of incidence: (a) TE polarization, odd modes, (b) TM polarization, even modes. The open triangles in (b) represent diffraction in air and must be compared with the folded free-photons dispersion (dotted lines).

It can be seen that some non degenerate bands "stop" at the Γ point for a given polarization and "restart" in the other polarization: this peculiar behavior is due to the fact that the mirror plane changes when turning from the $\Gamma - M$ to the $\Gamma - K$ direction. The experimental points agree very well with the calculated photonic bands of the proper parity. Anti-crossings are seen to occur between bands of the same symmetry, e.g. between two Σ_2 states and between two T_2 states around 0.3-0.36eV.

Not all bands that are allowed by symmetry appear in reflectance curves. This is not in contrast with the selection rule: an allowed band may have a nonzero, yet very weak, spectral strength. Indeed, theoretical simulations with a very fine mesh indicate that weaker structures are present, which in the experiments fall below the signal-to-noise ratio. It is interesting to remark that most

measured photonic bands correspond to H-modes. This may be understood since, at normal incidence, the Γ_5^- mode at 0.29eV is much more intense than Γ_5^+. At oblique incidence, the photonic bands that are forbidden at $\mathbf{k} = 0$ gain spectral strength by mixing with allowed bands: since only one strong feature Γ_5^- is present below 0.5eV, most photonic bands that appear in reflectance in this energy range have H-mode character.

The experimental points, marked by open triangles in Fig. 2.10b, have a steep dispersion and do not match any photonic band of the silicon material. However, they match the dispersion of light in air, folded in the Brillouin zone: the corresponding structures in reflectance mark the onset of diffraction in air. These structures depend only on the Bravais lattice (not on the pore shape or depth) and would be present also for a shallow grating [Wood, R. W. (1902)]. In the present context, these "Wood anomalies" represent photonic bands in the upper half-space and are intermixed with photonic bands of the macro-porous silicon crystal.

In conclusion, the photonic bands of a two-dimensional photonic crystal can be determined by variable-angle reflectance: the spectral features, which yield the energy position of a photonic mode at $q = 0$, are interpreted as one-dimensional critical points. Only bands with the same symmetry of the incident electromagnetic field can appear in reflectance. The selection rules derived from symmetry show that the photonic modes behave similar to other elementary excitations in solids. The same analysis is now applied to two-dimensional photonic-crystal slabs.

2.4 Two-Dimensional Photonic-Crystal Slabs

As already mentioned, the VAR technique has been first performed on weak index-contrast photonic crystal slabs [Astratov, V. N., *et al.* A (1999)]. Both theory and experiment can be conducted very much the same as shown for two-dimensional photonic crystals. The SMM has now to deal with two semi-infinite layers (air and substrate) separated by a certain number of finite-thickness layers, which form the desired planar waveguide. Then, each layer has to be patterned, completely or partially, to obtain the photonic crystal structure. It is intuitive that the core layer must be completely perforated in order to attain well defined resonances; a more detailed study on

that will be reported in Sec. 2.5. As discussed in Sec. 1.4, there is too much freedom in choosing the structure parameters, for thinking of a systematic and comprehensive study of all possible heterostructure geometries. That is why, the idea is again to group several systems into classes that exhibit similar features and restrict the study to representative cases only. Moreover, while in Sec. 1.4 the study has been focussed on photonic-crystal slabs characterized by infinite etch-depth, with the SMM it is possible to extend the study to more realistic systems, with finite etch-depth and also material dispersion and/or absorption.

In the present section, two cases will be shown: the air bridge system, corresponding to a high-index-contrast photonic-crystal slab, and a GaAs-based photonic crystal, which is for the weak-index contrast case. The SMM is used to extract the photonic band structure existing above the light line, as seen for macro-porous silicon photonic crystals. The aim is also to show that the band-structure picture is meaningful for interpreting the guided resonances, or quasi-guided modes, as stated in Sec. 1.4.2, and that the numerical method by Andreani, L. C. (2002) gives quantitative results also for modes above the light line. Furthermore, from the analysis of reflectance spectra, one finds again the selection rules described in the previous section for two-dimensional photonic crystals. Indeed, the symmetries involved in the coupling process to the external field depend only on the two-dimensional pattern, whereas the coupling strength may depend on the vertical geometry and on the hole etch-depth too.

As a final remark, while for a two-dimensional photonic crystal each mode retains a dispersion in the vertical direction, thus providing a behavior typical of a one-dimensional critical point in the reflectance structures, for a two-dimensional photonic-crystal waveguide, the modes have only in-plane dispersion, so that coupling to the external field appears as a resonant process, where ω and $\mathbf{k}$ of the incident wave match those of a guided-resonance. This results in a typical dispersion-like line-shape [Fan, S., *et al.* (2002)], in contrast to the "absorption-like" line-shape described in Sec. 2.3.2.

2.4.1 The Air Bridge

The air-bridge system represents the simplest two-dimensional photonic-crystal slab, being made of a single dielectric membrane suspended in air. Indeed, it is one of the few systems for which

photonic bands and out-of-plane losses have been computed using ab-initio methods [Johnson, S. G., *et al.* (1999); Ochiai, T., *et al.* A (2001); Sakoda, K. (2001)], except the SMM. For this reason, the air bridge is particularly suitable for testing the numerical method introduced in Sec. 1.4.1. Here, the photonic bands are extracted from the reflectance curves and are compared with those calculated by expansion on the guided modes of the effective waveguide.

Fig. 2.11a shows the reflectance for a TM-polarized plane wave incident along the $\Gamma - K$ orientation on the surface of an air-bridge photonic crystal slab, see Fig. 1.9d, made of a triangular lattice of air holes, with radius $r = 0.24a$, and having a waveguide thickness $d = 0.3a$. The curves are shifted for clarity. Sharp resonance features are readily apparent on the reflectance curves and may have the form of maxima, minima, or often, of dispersive line-shapes. Fig. 2.11b displays the photonic band dispersion determined from the curves of Fig. 2.11a (and the analogous ones for other orientations and polarization, not shown) by taking the approximate central position of each resonance. Solid (open) circles represent the points extracted from the reflectance curves for TM (TE) polarization with respect to the plane of incidence. They are compared with the photonic bands of the air bridge, which were already given in Fig. 1.11a, but, for the $\Gamma - M$ and $\Gamma - K$ directions, they are now classified in terms of parity with respect to specular reflection $\sigma_{\mathbf{k}z}$: the vertical plane coincides with the plane of incidence. As found for two-dimensional photonic crystals, modes that are even with respect to $\sigma_{\mathbf{k}z}$ (indicated by solid lines) couple only to TM-polarized incident light, while odd modes with respect to $\sigma_{\mathbf{k}z}$ (dashed lines) couple to TE-polarized light. Notice that a linearly polarized plane wave incident from the surface couples to both even and odd modes with respect to σ_{xy} (H-modes and E-modes for a two-dimensional photonic crystal). Indeed, though the air-bridge be still symmetric with respect to the xy plane, the initial condition of a plane wave incident from the top surface breaks the symmetry in Maxwell's equations and makes the wave couple to modes of both parity. The same holds for macro-porous silicon, where the system is already asymmetric because of the interface with air.

There is a very good agreement between the photonic bands calculated by the method of Andreani, L. C. (2002) and those deduced from reflectance, when the proper parity with respect to $\sigma_{\mathbf{k}z}$ is taken into account. This shows that the expansion in waveguide modes of the effective slab is a reliable method for calculating the energies of quasi-guided modes and that the choice of the

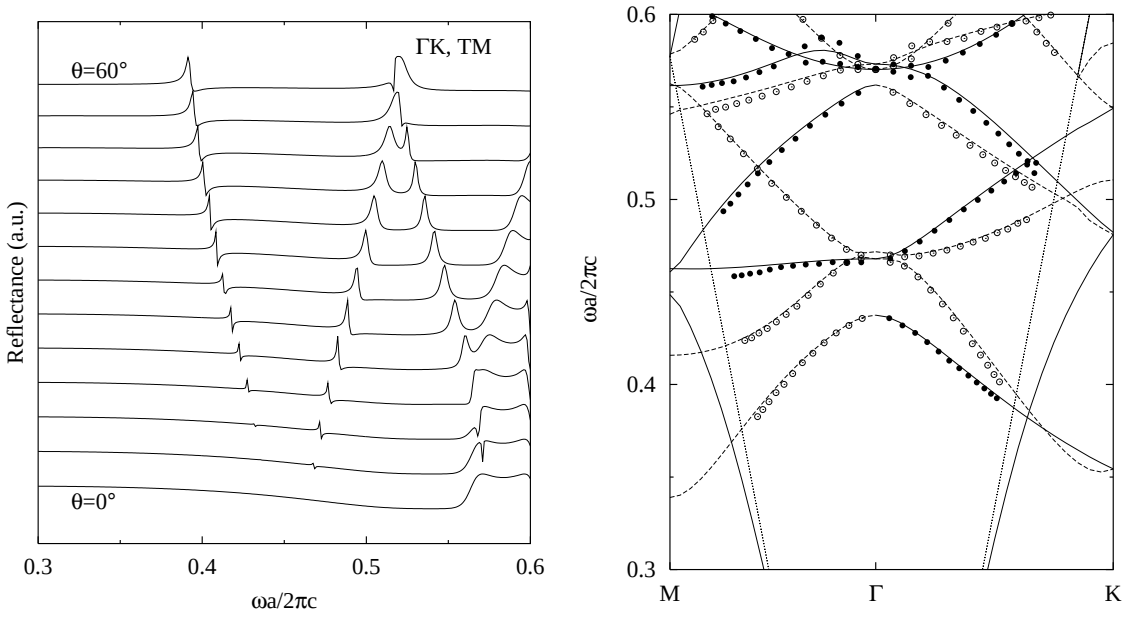

(a) (b)

Figure 2.11 Reflectance and photonic bands of the air bridge system of Fig. 1.9d, with thickness $d = 0.3a$ and hole radius $d = 0.24a$. (a) Calculated surface reflectance for a TM-polarized plane wave incident along the Γ-K orientation of the two-dimensional lattice. The angle of incidence is varied from $\theta = 0^\circ$ to $\theta = 60^\circ$ with a step of 5°. (b) Photonic bands. Lines represent the bands calculated from the expansion in waveguide modes, while points are extracted from the calculated reflectance. Solid lines and closed circles: even modes with respect to a vertical mirror plane $(\mathbf{k}, z)$, probed by TM-polarized light. Dashed lines and open circles: odd modes with respect to a vertical mirror plane $(\mathbf{k}, z)$, probed by TE-polarized light. The dotted line represents the dispersion of light in air. Both reflectance and photonic bands have been calculated employing 109 plane waves.

effective dielectric constant, as the spatial average of $\epsilon_j(\mathbf{x})$ in the j-th layer, is appropriate.

Other symmetry aspects of the reflectance calculation and of the photonic bands recall the discussion made in Secs. 1.4.4 and 2.3.2. First, notice that there are a few bands, even with respect to $\sigma_{\mathbf{k}z}$ along the $\Gamma - M$ direction, which become odd along the $\Gamma - K$ direction, or vice versa. They correspond to photonic states that have a threefold, but not sixfold, symmetry at the Γ point. Secondly, most resonance features in reflectance become vanishingly small at normal incidence, except for a structure at $\omega a/2\pi c \simeq 0.57$, which remains strong at $\theta = 0°$ and splits into two at oblique incidence. The explanation for that has already been given in Sec. 2.3.2: since the only photonic modes, which can be excited, are those having the same symmetry of the incident electromagnetic field and the latter belongs to a twofold degenerate representation of the point group at Γ, non degenerate bands must be optically forbidden at $\theta = 0°$. The twofold degenerate photonic mode at $\omega a/2\pi c = 0.57$ is optically allowed and its energy can be determined from normal-incidence reflectance. The same argument implies that non degenerate bands have zero radiative line-width at $\mathbf{k} = 0$ [Ochiai, T., *et al.* A (2001)]. Nevertheless, if these photonic states lie above the folded light line, they can couple to the diffracted field in air, which is not twofold degenerate, being $\theta \neq 0°$. For this reason, such modes acquire a finite radiative line-width: even though the diffraction process of zero-th order is optically forbidden, coupling to the external field is provided by the diffraction processes of higher order [Andreani, L. C., *et al.* B (2002)].

2.4.2 GaAs-based Photonic Crystals

Contrary to the air bridge, which supports both guided and quasi-guided modes, low index contrast waveguides like the GaAs/AlGaAs heterostructure have only quasi-guided modes in the whole energy spectrum, see Sec. 1.4. Nevertheless, as already shown for the air bridge system, the guided resonances are well defined modes, though with an attenuation length, whose dispersion resembles that of two-dimensional photonic crystals, apart some vertical confinement effects. In this sense, due to the low index contrast of the planar waveguide, GaAs-based photonic crystals exhibit a photonic band structure that differs not much from a pure two-dimensional system, as shown in Sec. 1.4.3. This feature makes GaAs-based photonic crystal particularly interesting, because the dispersion and the band gap properties studied for two-dimensional photonic crystals can be

transferred to a realistic system, with the advantage of vertical confinement, but also with the unavoidable price of intrinsic propagation losses. However, the GaAs/AlGaAs system discussed in Sec. 1.4.3 is not realistic, because it is not possible to attain an infinite etch depth, besides the impossibility of growing semi-infinite cladding and substrate. The common waveguide configuration for GaAs-based photonic crystals consists of a core layer of GaAs, capped with a thin layer of AlGaAs, before the interface with air, and clad with another layer of AlGaAs, to separate the core layer from the GaAs substrate. The pattern must be deep enough to reach the bottom cladding. Since the top cladding is not strictly necessary (it just makes the waveguide more symmetric), sometimes the core layer is directly interfaced with air, see Fig. 2.12. Even though the resulting structure has a strong asymmetry, the absence of the top cladding allows to etch deeper holes in the bottom cladding, where the control of out-of-plane losses is more critical, due to the presence of a high index substrate.

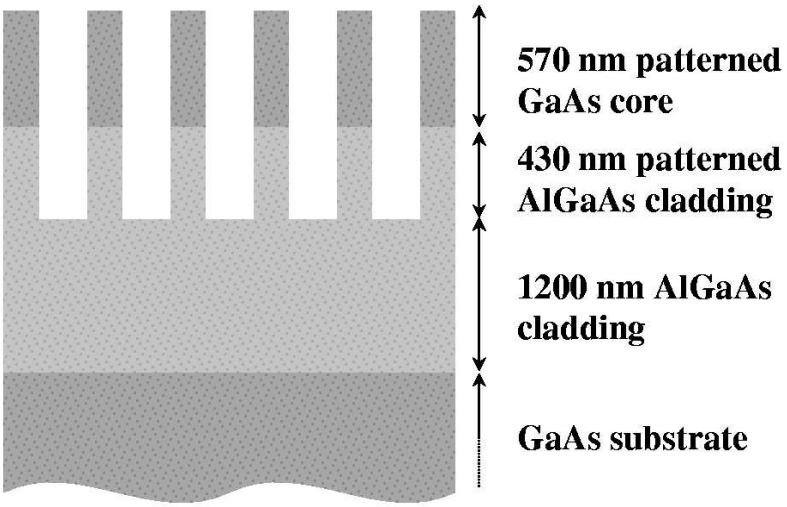

Figure 2.12 Cross-section of a typical GaAs-based photonic crystal.

Measurements of the dispersion of quasi-guided modes have been performed on GaAs-based photonic crystals patterned with a triangular lattice of holes [Astratov, V. N., *et al.* A (1999)], as this structure is the "conventional" one for obtaining a polarization-sensitive band gap at relatively small air fractions, or with a one-dimensional lattice of stripes [Astratov, V. N., *et al.* (2000)]. Similar measurements have been performed on GaN/sapphire waveguides, also patterned with a triangular lattice of holes [Coquillat, D., *et al.* (2001)]. The study of the photonic bands of different

lattices is interesting in order to investigate the dependence of the photonic band dispersion and band gaps on the lattice symmetry and on the basis. Various kinds of "non-conventional" lattices and symmetry reduction have been theoretically studied for the two-dimensional case [Villeneuve, P. R., *et al.* (1992); Padjen, R., *et al.* (1994); Anderson, C. M., *et al.* (1997); Wang, X.-H., *et al.* (1999); Agio, M., *et al.* A (2000)]; however, there are only a few cases that have been studied in a waveguide configuration. Thus, since there is much literature on the determination of the photonic band structure of photonic-crystal slabs with a triangular lattice, it is worth to live the mainstream for a while and focus the attention on a different kind of pattern, which has been shown to exhibit a complete band gap in a range of filling factors near to the close-packing condition [Wang, X.-H., *et al.* (1999); Agio, M., *et al.* A (2000)] and has also been studied by means of the VAR technique [Galli, M., *et al.* B (2002)]. It is about the so-called chessboard lattice.

The Chessboard Lattice

The chessboard lattice consists of square columns of either dielectric or air rotated by 45° with respect to the square axes of the lattice, see Fig. 2.13a-c. The structure is characterized by the filling factor f of the dielectric, which is related to the lattice constant a and the column diagonal b by $f = b^2/2a^2$, in the case of dielectric columns [Fig. 2.13a], or $f = 1 - b^2/2a^2$, for air columns [Fig. 2.13b]. For the close-packed condition $b = a$, or $f = 0.5$, the two cases become equivalent and the structure resembles a chessboard. For convenience, refer to the structure of Fig. 2.13 as "chessboard" lattice for every value of f. Fig. 2.13c represents the Brillouin zone for a square lattice, with symmetry points.

The photonic band structure is calculated by means of the plane wave expansion method, where the Fourier transform of the dielectric constant $\epsilon_{\mathbf{G}',\mathbf{G}''} = \epsilon(\mathbf{G}' - \mathbf{G}'') = \epsilon_{\mathbf{G}} \to \epsilon_{G_x,G_y}$ reads

$$\epsilon_{G_x,G_y} = \begin{cases} f\epsilon_{\text{diel}} + (1-f), & \mathbf{G} = \mathbf{0}; \\ 4(\epsilon_{\text{diel}} - 1)\dfrac{\cos(G_y b/2) - \cos(G_x b/2)}{a^2(G_x^2 - G_y^2)}, & \mathbf{G} \neq \mathbf{0}; \\ (\epsilon_{\text{diel}} - 1)b\dfrac{\sin(G_x b/2)}{a^2 G_x}, & \mathbf{G} \neq \mathbf{0} \text{ and } G_y = \pm G_x. \end{cases} \tag{2.22}$$

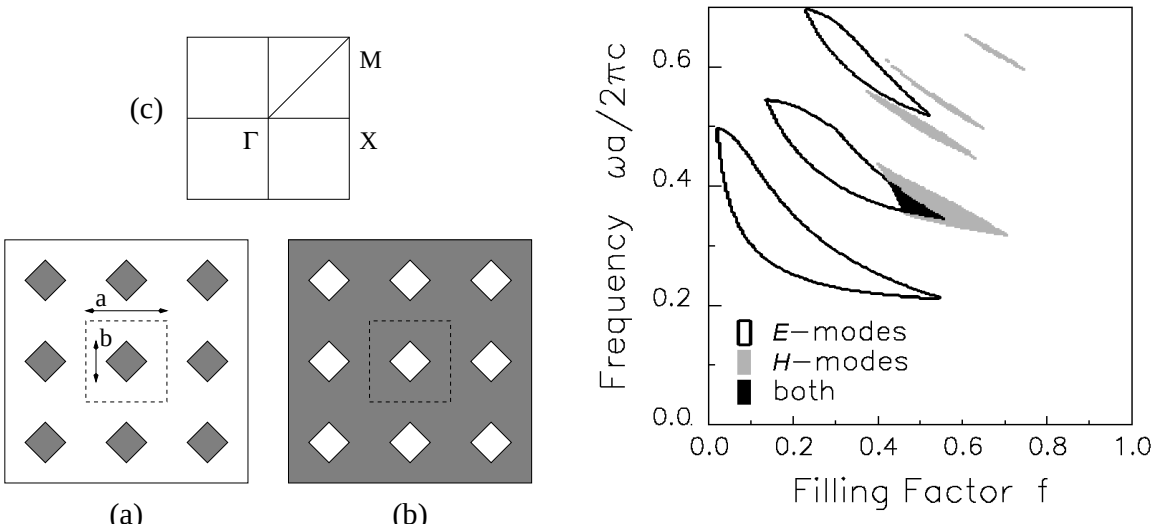

Figure 2.13 (Left panels) The chessboard lattice: (a) dielectric rods in air, (b) air rods in dielectric. The dashed lines mark the unit cell, a is the lattice constant and b is the rod diagonal; (c) the Brillouin zone with symmetry points, Γ, X, M. (Right panel) Gap map for the chessboard-lattice two-dimensional photonic crystal for a background dielectric constant $\epsilon_{\text{diel}} = 12$. A black spot corresponds to the existence of a band gap for both polarizations.

Choosing $\epsilon_{\text{diel}} = 12$ as the material dielectric constant, the chessboard lattice is found to have a complete photonic band gap, see Fig. 2.13, arising from overlap of the second E-polarized gap with the first H-polarized gap. The full band gap exists for a range of filling factors around the close-packing condition $f = 0.5$. The gap map shows that E-polarized gaps are favored for the case of non overlapping dielectric columns ($f < 0.5$), while H-polarized gaps are favored in the case of air columns ($f > 0.5$). Although the overlap of E- and H-polarized gaps does not follow a simple rule, the existence of a complete band gap is related to the fact that the chessboard lattice, near the close-packing condition, has both dielectric columns and connected dielectric regions. The chessboard lattice has the same symmetry and simplicity of the conventional square lattice.

Fabrication Method

In order to fabricate samples with the above pattern, the first step is to define a mask by e-beam lithography, see Fig. 2.14a, which is used to write the photonic-crystal design on to the

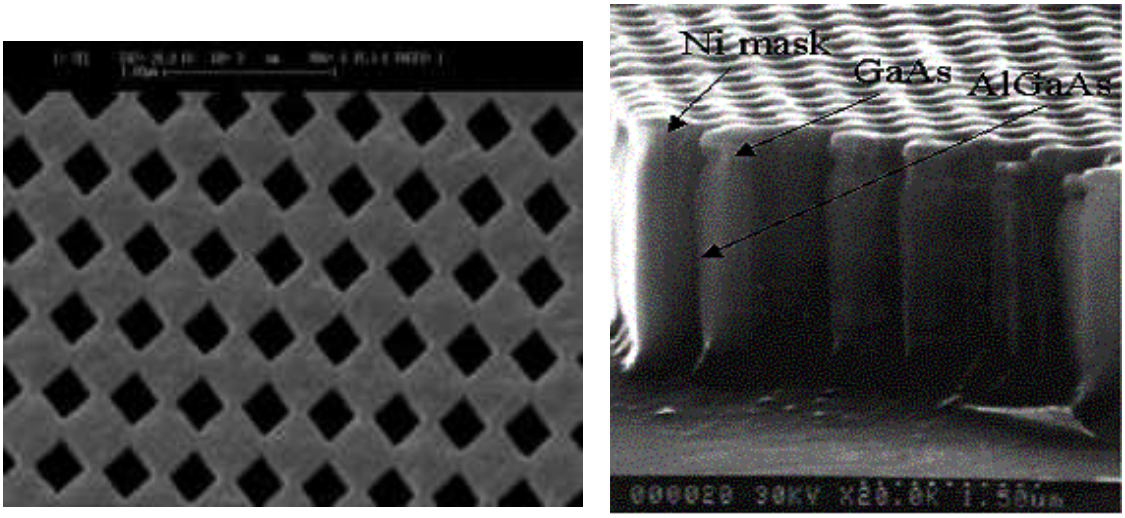

(a) (b)

Figure 2.14 (a) SEM image of the chessboard lattice X-ray mask, with $a = 564$nm. (b) Detailed SEM image of the epitaxial AlGaAs slab after the etching process. Courtesy of Romanato, F. *et al.*, NNL - INFM, Italy.

GaAs/AlGaAs heterostructure surface. The mask consists of a chessboard lattice of squares with 282nm side, spaced by a lattice constant of 500nm. The GaAs/AlGaAs layers are grown by low pressure metal organic chemical vapor deposition (LP-MOCVD), on $\langle 100 \rangle$-oriented semi-insulating GaAs substrates. The resulting heterostructure consists of a 200nm GaAs buffer layer, followed by 1630nm of $Al_{0.25}Ga_{0.75}As$ and 570nm of GaAs as core layer, see Fig. 2.12. Proximity X-ray lithography has been used to transfer the patterning to the samples. In fact, if the gap between the e-beam mask and the heterostructure can be controlled at a micrometer level, one can exploit diffraction effects to generate superstructure not found in the pattern of the original mask. Thus, the interest in using X-ray lithography is that several two-dimensional patterns can be obtained from a single mask [Romanato, F., *et al.* (2002)]. A pre-exposure process step requires the spinning of resists on the sample surface: they are chosen of both tones (PMMA 1.07 and SAL 601), in order to have positive and negative transfer of the mask patterning. Indeed, also the resist contribute to obtaining different two-dimensional patterns, in combination with the X-ray diffraction control. Then, a lift-off process has been performed by evaporating 10nm of nickel and stripping the resid-

ual resist. Nickel indeed exhibits an extremely high selectivity to the reactive ion etching (RIE) performed by an induced coupled plasma (ICP) RIE reactor in an atmosphere of 95% $SiCl_4$ and 5% of Ar, and biasing the cathode at 230eV. The etching time was 5 minutes, leading to an etch depth of about 1μm in the heterostructure, see Fig. 2.14b. More details on fabrication are given in the paper by Romanato, F., *et al.* (2002).

Two samples have been studied under the VAR technique by Galli, M., *et al.* B (2002). The first sample, called L2, has been patterned on PMMA resist and consists of air rings with an air fraction of 12%: the shape of the rings reflects the tilted squares of the mask. The two-dimensional pattern of the second sample, called RUN3, which has been obtained by exposing a SAL601 resist film, is made of dielectric squares, also tilted by 45°; the dielectric fraction is close to 28%.

The Sample L2

Fig. 2.15 shows a SEM image of the sample L2 and a sketch of its unit cell. The calculation of both reflectance and photonic bands requires the knowledge of the dielectric constant in Fourier space. However, the unit cell of Fig. 2.15 looks rather different (and more complicated) from the original chessboard cell of Fig. 2.13. Now, the diagonal part of $\epsilon_{\mathbf{G},\mathbf{G}'}$ is simply $f + (1-f)\epsilon_{\text{diel}}$, where f is the air fraction of L2. The off-diagonal components of the Fourier transform of $\epsilon(\mathbf{x})$ can be easily obtained from the expression of Eq. (2.22), by exploiting the following trick. Think that the sample L2 is made of a chessboard lattice with air columns with side $l_1 = 0.47a$ ($\epsilon_1(\mathbf{x})$), plus a chessboard lattice of dielectric columns with side $l_2 = 0.32a$ ($\epsilon_2(\mathbf{x})$), minus an homogenous medium with $\epsilon = 1$; i.e. $\epsilon(\mathbf{x}) = \epsilon_1(\mathbf{x}) + \epsilon_2(\mathbf{x}) - 1$. Plugging the above expression into Eq. (1.23) and using Eq. (2.22) for $\epsilon_1(\mathbf{x})$ and $\epsilon_2(\mathbf{x})$, the final formula for $\epsilon_{\mathbf{G},\mathbf{G}'}$ is

$$\epsilon_{G_x,G_y} = \begin{cases} f + (1-f)\epsilon_{\text{diel}}, & \mathbf{G} = \mathbf{0}; \\ 4(\epsilon_{\text{diel}} - 1)\left[\dfrac{\cos(G_y b_2/2) - \cos(G_x b_2/2)}{a^2(G_x^2 - G_y^2)} - \dfrac{\cos(G_y b_1/2) - \cos(G_x b_1/2)}{a^2(G_x^2 - G_y^2)}\right], & \mathbf{G} \neq \mathbf{0}; \\ (\epsilon_{\text{diel}} - 1)\left[b_2 \dfrac{\sin(G_x b_2/2)}{a^2 G_x} - b_1 \dfrac{\sin(G_x b_1/2)}{a^2 G_x}\right], & \mathbf{G} \neq \mathbf{0} \text{ and}; \\ & G_y = \pm G_x \end{cases} \tag{2.23}$$

where $b_1 = \sqrt{2}l_1$ and $b_2 = \sqrt{2}l_2$. Notice that the homogenous contribution "-1" does not influence the off-diagonal components of $\epsilon_{\mathbf{G},\mathbf{G}'}$.

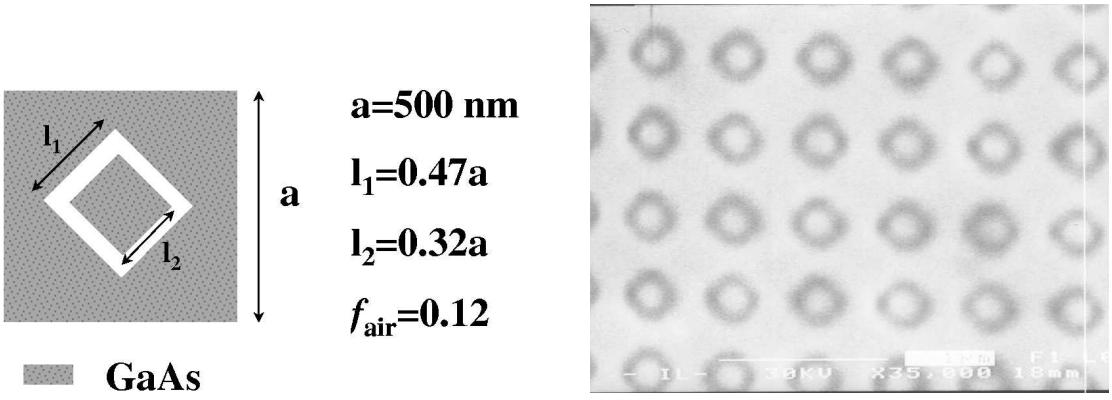

Figure 2.15 Sample L2: unit cell (left) and SEM image (right). Courtesy of Romanato, F. *et al.*, NNL - INFM, Italy.

The symmetry properties and selection rules of the sample L2 recall in part those of the air bridge and of macro-porous silicon. For a wave-vector $\mathbf{k}$ along a lattice direction (the $\Gamma - X$ and the $\Gamma - M$ directions), specular reflection with respect to a vertical plane $\mathbf{k} - z$ is a symmetry operation and the TE or TM polarization of the incident wave is maintained in reflectance. Correspondingly, the photonic bands can be classified as even or odd with respect to vertical mirror symmetry. They are probed by a polarized incident wave as follows: a TM-polarized wave couples to even bands, a TE-polarized wave couples to odd bands. Note that for the present asymmetric air/GaAs/AlGaAs structure there is no mirror symmetry with respect to the waveguide plane (unlike in the air bridge and in homogeneous two-dimensional photonic crystals).

As regards the calculations, the two-dimensional dielectric pattern, displayed in Fig. 2.16, is expressed by Eq. 2.23. The thicknesses of core and cladding are taken from ellipsometry results: air (semi-infinite), GaAs oxide 0.0029μm, GaAs 0.5764μm, AlGaAs 1.6386μm, GaAs substrate (semi-infinite). For the calculation of photonic bands only the thickness of the core layer is used, since the patterned lower cladding is assumed to be of semi-infinite extent. For the reflectance calculations, instead, the etch depth is also included: this is taken to be 1μm. The values are close to those estimated from etching rates and they have been slightly adjusted in order to reproduce the interference fringes in the reflectance spectra. Moreover, the reflectance calculation accounts for the frequency-dependent dielectric constants of GaAs and AlGaAs [Palik, E. D. (1985)]. 109 plane waves have been employed in the calculations.

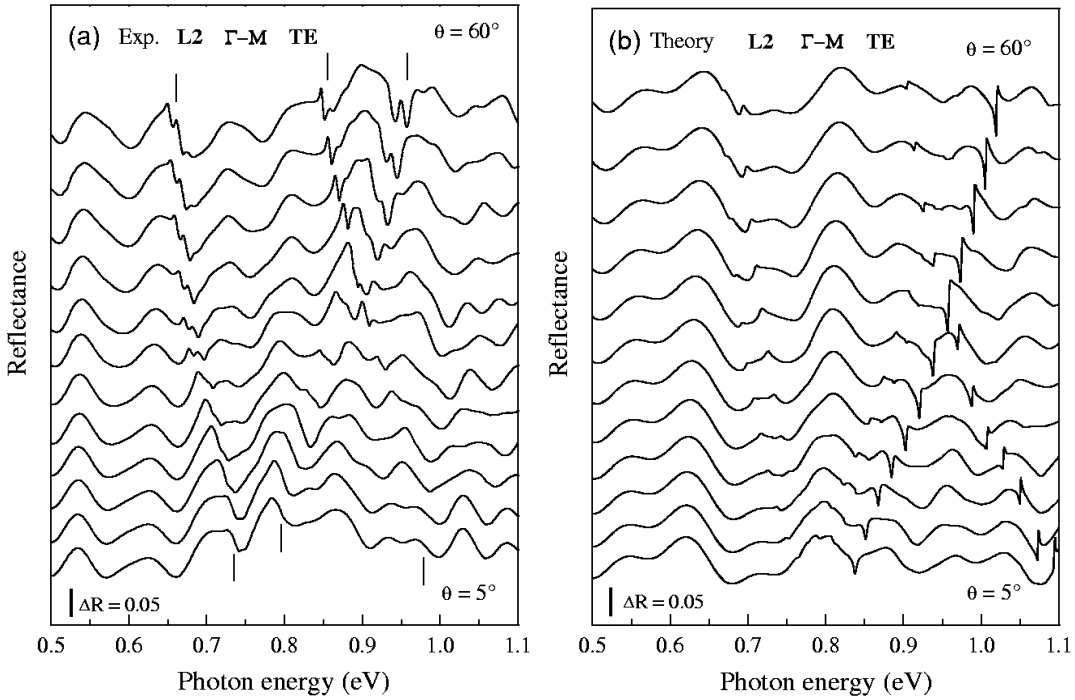

Figure 2.16 Experimental (a) and calculated (b) variable angle reflectance for TE-polarized light incident along the $\Gamma - M$ direction. The angle of incidence is varied in steps of 5°. The different curves are vertically shifted for clarity. Experimental data courtesy of Galli, M., Università degli Studi di Pavia, Italy.

The VAR spectra are presented in Fig. 2.16a for TE polarized light incident along the $\Gamma - M$ direction of the two-dimensional Brillouin zone. The corresponding calculated spectra are shown in Fig. 2.16b. Similar results are obtained for light incident along the $\Gamma - K$ orientation and for TM-polarization (not shown here). The angle of incidence θ ranges from 5° to 60° in steps of 5° and each curve corresponding to a different θ value has been vertically shifted by a constant quantity in order to better appreciate the angular evolution of reflectance.

What can first be noticed in reflectance spectra are pronounced interference oscillations arising from the multilayer structure of the system. The oscillations result from a combination of two different interference patterns: one with a slowly-varying long-period one ad another one with fast-varying short-period. These are related to the core layer and the core + cladding layers of the waveguide. However, the period of the oscillations slightly changes upon increasing frequency. This effect could be explained by considering that on increasing frequency the electromagnetic field gets more con-

fined within the dielectric regions of the patterned waveguide [Joannopoulos, J. D., *et al.* (1995)]. This, in turns, leads to an effective refractive index, experienced by the incident radiation, that increases with frequency and, therefore, changes the period of the interference. The interference pattern is well reproduced by the calculation with the etch depth of 1μm. Besides the complex interference background, several narrow structures (indicated by vertical bars in Fig. 2.16a for $\theta = 5°$ and $\theta = 60°$) are clearly observed. By increasing the angle of incidence, the energy positions of these sharp features display a well-defined dispersion.

Once again, these narrow structures are ascribed to resonant coupling of the incident external radiation to quasi-guided modes of the patterned waveguide, occurring whenever phase-matching conditions are fulfilled. Upon varying the incidence angle, the in-plane wave-vector changes accordingly and the different matching conditions lead to smooth energy dispersion of the resonances. There is an overall good agreement between experimental spectra and calculated ones: both the multiple interference pattern and the observed resonances are well accounted for by calculations. Notice that the intensity and shape of the structures change markedly with angle, showing a variety of maxima, minima and dispersive-like line-shapes. However, they remain relatively narrow and well defined even for high θ values, exhibiting a FWHM of the order of 10^{-2}eV. While the amplitude of the resonances is related to the coupling strength to guided modes, their width is mainly determined by radiative and dissipative losses, which are expected to be low for patterned waveguides with a low air fraction [Benisty, H., *et al.* (2000); Kawai, N., *et al.* (2001)]. In fact, despite some surface inhomogeneity possibly coming from the etching process, the observation of relatively narrow features can be considered as an indication of good guiding properties. This suggests that samples with low air fraction may be useful for achieving low-loss propagation, although the relatively weak coupling strength imposes stringent matching-conditions for the excitation of quasi-guided modes.

As already pointed out, the dispersion of photonic bands that lie above the light line can be conveniently extracted from the energy position of the resonances *versus* the in-plane wave-vector $\mathbf{k}$ that spans the Brillouin zone upon varying the angle θ. Since most structures in reflectance spectra exhibit a dispersive-like shape, the inflection point is chosen as the energy position for the propagating mode. This analysis is reported in Fig. 2.17, where measured bands (left panel) are

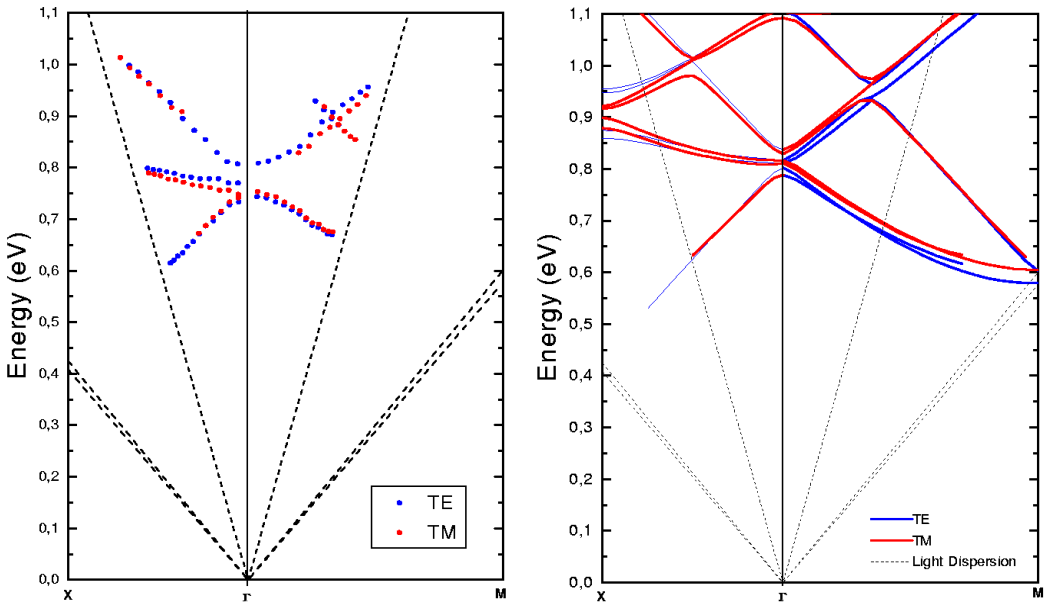

Figure 2.17 Experimental (left panel) and calculated (right panel) photonic modes for different polarizations with respect to the plane of incidence: TE (blue), TM (red). The dotted lines represent the dispersion of light in air, in the core and cladding.

compared with the calculated ones (right panel). Photonic bands are separated in TE and TM modes, according to parity with respect to the plane of incidence $\mathbf{k} - z$. The frequency dispersion of the dielectric functions of GaAs and AlGaAs are taken into account in an approximate way by calculating each group of nearby bands with $\epsilon(\omega)$ chosen at an average frequency. Dotted lines represent the dispersion of photons in GaAs, AlGaAs and in air.

Most of the calculated bands in the investigated range can be identified in the experimental spectra, and a rather good agreement for dispersion and energy values is obtained both for TM and TE modes. Particularly, an anti-crossing of two bands can be clearly observed around 0.9eV, in the experimental and calculated spectra along the $\Gamma - M$ direction. Notice that TE and TM bands have very similar dispersion both along the $\Gamma - M$ and $\Gamma - X$ directions, and exhibit rather small energy gaps at the high symmetry points of the Brillouin zone. Actually, due to the quite low air fraction, the system is very close to the ideal *empty lattice* or *free photon* case, where light propagation would be simply governed by an unpatterned slab with the average refractive index [Ochiai, T., *et al.* B (2001)].

The Sample RUN3

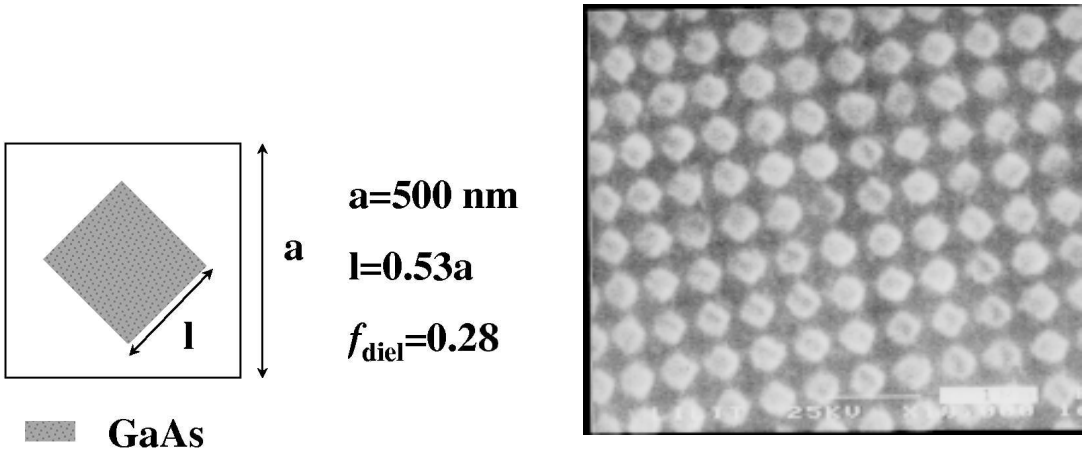

Figure 2.18 Sample RUN3: unit cell (left) and SEM image (right). Courtesy of Romanato, F. *et al.*, NNL - INFM, Italy.

Fig. 2.18 shows a SEM image of the sample RUN3 and a sketch of its unit cell. This time, the two-dimensional pattern results in a chessboard lattice of dielectric rods in air, whose dielectric function Fourier transform is given by Eq. (2.22), where b is taken to be $\sqrt{2}l$, with $l = 0.53a$. The VAR spectra (experimental and calculated) are shown in Fig. 2.19 for TE polarized light incident along the $\Gamma - X$ directions. Similar results are obtained for light incident along the $\Gamma - M$ orientation and for TM polarization (not shown here). Again, the angle of incidence θ is varied from 5° to 60° in steps of 5° and the curves are vertically shifted for clarity.

As can be noticed, interference fringes from the waveguide structure still characterize the reflectance spectra. The period of the interference is now much longer, due to the considerably higher air fraction and correspondingly lower effective index. The interference pattern is again a complex superposition of core and core + cladding contributions and is well reproduced by theory with an etch depth of 0.95μm. The layer thicknesses are taken from the same ellipsometry values found for the sample L2. A large air fraction causes also that the angular dependent resonant structures are considerably broader than in sample L2. As mentioned before, broader resonances imply a larger coupling to leaky waveguide modes and, therefore, an increase of out-of-plane diffraction losses. Good agreement is found between calculated and experimental curves, even though in this case the

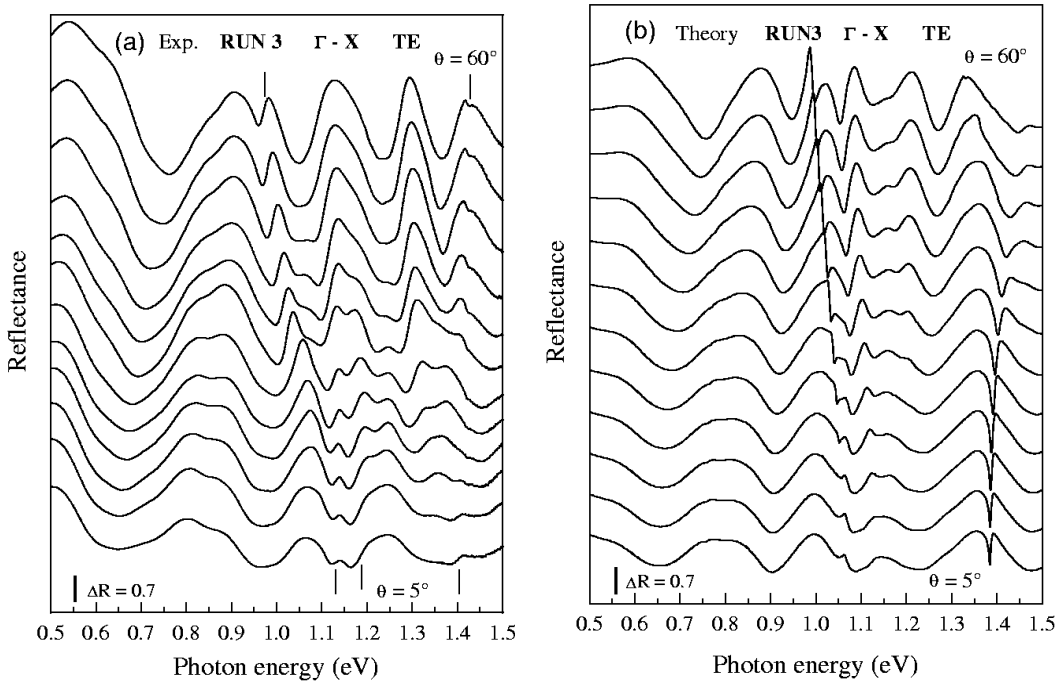

Figure 2.19 Experimental (a) and calculated (b) variable angle reflectance for TE polarized light incident along the $\Gamma - X$ direction. The angle of incidence is varied in steps of 5°. The different curves are vertically shifted for clarity. Experimental data courtesy of Galli, M., Università degli Studi di Pavia, Italy.

calculated resonances appear to be slightly sharper than the experimental ones. This is probably due to some disorder effect in the sample.

The photonic bands of the sample RUN3 are reported in Fig. 2.20, where experimental bands (left panel) are compared to the calculated ones (right panel). The criteria adopted for the analysis of the experimental spectra and the methods of calculation are the same as for sample L2. The overall situation is rather different, compared to the results obtained for sample L2. The whole band diagram is shifted to higher energies, and TE and TM bands are now well separated and show a fairly dissimilar dispersion: both features follow from the large air fraction. Notice that truly guided modes exists for both TE and TM polarizations. However, as results from the band diagrams, the lowest bands in the guided mode region have a finite cut-off wavelength imposed by the thickness of the asymmetric waveguide. The guided modes go over smoothly into the radiative region, when crossing the light line, and should be viewed as quasi-guided modes thereafter. The

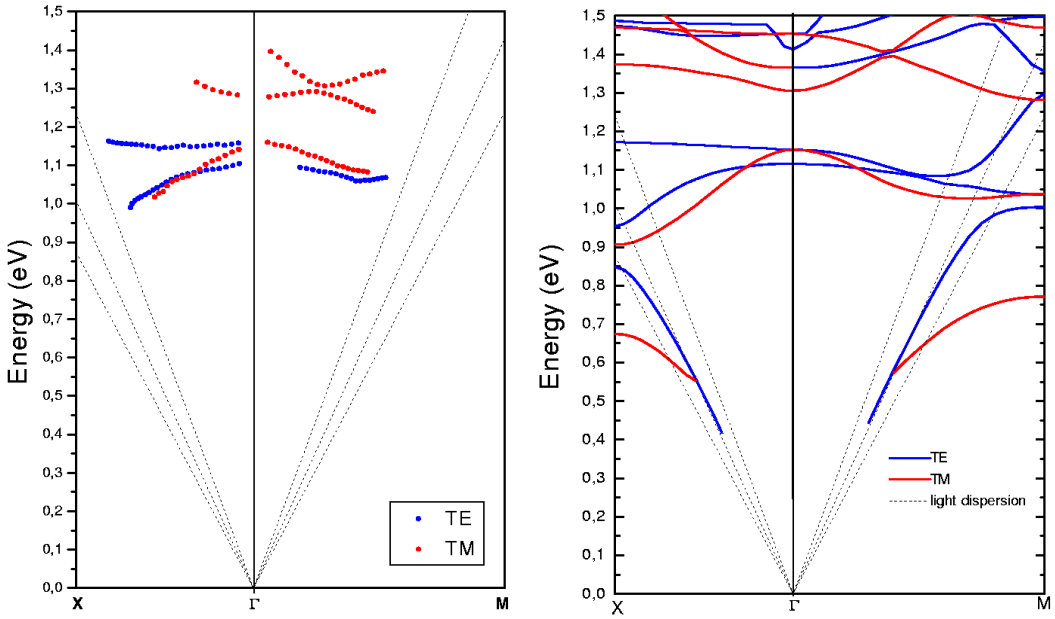

Figure 2.20 Experimental (left panel) and calculated (right panel) photonic modes for different polarizations with respect to the plane of incidence: TE (blue), TM (red). The dotted lines represent the dispersion of light in air, in the core and cladding.

first order waveguide mode folded in the radiative region has gaps at the center zone and edge. Since the waveguide is asymmetric, there is no parity distinction between first and second-order modes and their energy dispersions anti-cross with very small gaps. Good overall agreement if found between the bands extracted from reflectance and the calculated ones. It is remarkable that a gap around 1.2eV opens for both polarizations over most of the Brillouin zone: the gap is large close to Γ and closes only very near to the zone boundary. The photonic density of states is expected to be very low in the energy region 1.15-1.25eV, which can be called a *pseudo-gap*. Linear defects in the two-dimensional lattice would act as channel waveguides and would support propagating modes in this pseudo-gap.

In summary, the sample L2, with a basis of air rings and an air fraction of 12%, exhibits narrow resonant structures, indicating good guiding properties for the photonic quasi-guided modes. All qualitative features of reflectance and photonic bands are well reproduced by theory, including anti-crossings of the states along the $\Gamma - M$ direction. The dispersion of photonic modes is similar

for TE and TM polarizations and is close to that of free photons in an effective waveguide. The sample RUN3, with a basis of tilted dielectric squares and an air fraction of 72%, shows broader spectra features, related to the higher radiative width and diffraction losses of quasi-guided modes. The photonic dispersion of photonic modes is strongly different for the two polarizations and a pseudo-gap occurs around 1.2eV, where the photonic density of states is expected to be very low.

The VAR spectra of the air bridge system and of the GaAs/AlGaAs patterned heterostructure exhibit sharp features that correspond to the excitation of quasi-guided modes in the waveguide structure. The spectra are calculated using a scattering matrix approach, which allows an exact solution of Maxwell's equation, apart a wave-vector cut-off. The photonic bands can be thus extracted from reflectance curves and compared to the ones calculated with the method based on the expansion on waveguide modes. Good agreement is found between the two methods, and also with experimental data. This shows that the photonic band picture is valid also above the light line, where a continuous spectrum is arranged in guided resonances or quasi-guided modes, and that the VAR is adequate for measuring the photonic band structure. The present study is also a test of the expansion method implemented for calculating the photon dispersion in photonic-crystal slabs, whose approximation consists of neglecting coupling to leaky modes: the method is found to be reliable for obtaining the band structure of both strong and weak index confinement structures. The coupling of the external field to quasi-guided modes obeys to selection rules that can be inferred from a symmetry analysis of the two-dimensional pattern: the incident plane wave must have the same symmetry of the quasi-guided mode, besides matching ω and $\mathbf{k}$, in order to have coupling. When the VAR is calculated along the symmetry lines of the Brillouin zone, the plane of incidence represents a mirror plane for the crystal: using TE (TM) polarized light, one probes the states that are odd (even) with respect to the plane of incidence. The symmetry brought by the vertical profile of the planar waveguide does not influence the selection rules for the VAR. Nevertheless, a symmetric structure with respect to the waveguide plane exhibits band crossings [Fig. 2.11], while an asymmetric structure shows band anti-crossings [Figs. 2.16 and 2.17].

The VAR spectra obtained for the samples L2 and RUN3 show that the system with a larger air fraction is characterized by broader resonances. Such trend is in agreement with the phenomenolog-

ical model developed by Benisty, H., *et al.* (2000) and with the exact numerical result that broad resonances correspond to large propagation losses and vice versa [Ochiai, T., *et al.* A (2001)]. That is why the sample L2 is expected to have better guiding properties than the sample RUN3. Since the determination of out-of-plane losses is fundamental for designing photonic-crystal slabs, one would use the VAR technique to infer such information, at least qualitatively, by looking at the width of the resonances. The purpose is to complete the comparison between high- and low-index confinement structures, which started in Sec. 1.4.3 about the photonic band structure, and, more generally, to understand the dependence of out-of-plane losses on various structure parameters. The assessment of propagation losses will help in finding which are the main guidelines for designing an efficient photonic-band-gap material.

2.5 Out-of-Plane Losses

The SMM is here exploited to provide some trends of out-of-plane losses as a function of various structure parameters. The systems under study are once again the air bridge and the GaAs-based photonic crystals. For simplicity, frequency and incidence angles are tuned to match a photonic mode that is rather distant from the other resonances. The idea is to isolate a well defined resonance that exhibits a clear dispersive line shape, and concentrate only on this one. It is clear that such approach is by no means complete, because it focusses on a single mode at a single Bloch vector, but it is already sufficient to give a flavor of what are the dependencies on the dielectric contrast, the core thickness, the hole radius and, finally, the etch depth. In fact, out-of-plane losses depend both on the Bloch vector and on the band index [Ochiai, T., *et al.* A (2001); Lončar, M., *et al.* (2002)]. However, it is given for granted that the following trends are qualitatively correct, as long as they track the evolution of the same state.

Consider the air bridge system studied in Sec. 1.4.3 for core thickness $d = 0.3a$ and focus the attention on the band around $a/\lambda \simeq 0.4$ along $\Gamma - K$, which is optically active to a TM-polarized probe, see Fig. 2.11. This is the quasi-guided mode chosen to represent out-of-plane losses in a strong confinement photonic-crystal slab. As to the weak confinement system, consider a GaAs-based photonic crystal with the following structure: AlGaAs ($\epsilon = 11$ and layer thickness $d = 0.5a$),

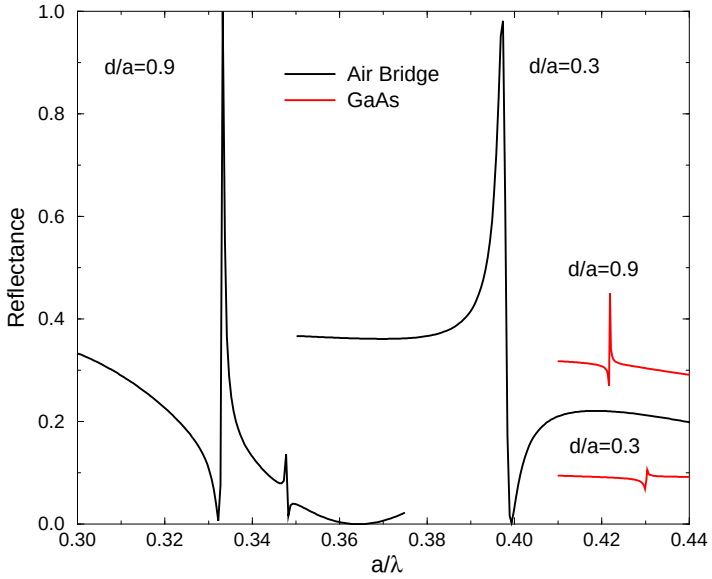

Figure 2.21 TM-polarized reflectance for a GaAs-based photonic crystal and a patterned air bridge. Both the air bridge and the GaAs/AlGaAs heterostructure are patterned with a triangular lattice of air holes, with $r = 0.24a$. Air bridge: air (semi-infinite), patterned core ($\epsilon = 12$, $d = 0.3a, 0.9a$), air (semi-infinite). GaAs/AlGaAs heterostructure: air (semi-infinite), patterned AlGaAs ($\epsilon = 11$, $d = 0.5a$), patterned GaAs ($\epsilon = 12$, $d = 0.3a, 0.9a$), patterned AlGaAs ($\epsilon = 11$, semi-infinite). Incident wave: $\theta = 50°$, $\phi = 0°$ and TM-polarized. For clarity, the curve corresponding to the $0.9a$-thick GaAs has been shifted upwards by 0.2.

GaAs ($\epsilon = 12$ and $d = 0.3a$) and AlGaAs (semi-infinite) as substrate. All layers are patterned with a triangular lattice of air holes, whose radius is $r = 0.24a$, like for the air bridge. Also for this case, the quasi-guided mode that represents out-of-plane losses is a state close to $a/\lambda \simeq 0.43$ along $\Gamma - K$, which couples to TM-polarized waves, see Fig. 1.12a[3]. Both modes, for the air bridge and the GaAs/AlGaAs, are sampled by TM-polarized light with incidence angles $\theta = 50°$ and $\phi = 0°$. The calculations are always performed using 109 plane waves.

Fig. 2.21 shows the respective dispersive line shapes associated to the above modes. First of all,

[3]It is the band (solid line) along $\Gamma - K$ with negative dispersion, around $\omega a/2\pi c \simeq 0.4$. Notice that, in the present system, the bands are slightly blue-shifted, because the outmost top cladding is air, instead of being AlGaAs.

the amplitude of the resonances relative to the air bridge is larger than for the GaAs/AlGaAs system: this has to do with a different coupling strength to external radiation. As regards the width of the resonances, the one belonging to the GaAs/AlGaAs photonic crystal is roughly one order of magnitude smaller than the one shown by the air bridge; thus one is led to conclude that propagation losses are ten times smaller in weak confinement photonic crystals.
When the core thickness is increased to $d = 0.9a$, the width of the resonances diminishes for both systems. However, while for the GaAs/AlGaAs patterned waveguide the energy position of the quasi-guided mode does not depend much on the core thickness, for the air bridge, the blue-shift is considerably reduced.

2.5.1 Vertical Confinement Effects

For a deeper insight on vertical confinement effects, the above weak- and strong-confinement photonic-crystal slabs are now studied for different core thicknesses d/a; all the other parameters are left unchanged. Fig. 2.22 displays the evolution of the resonances as a function of d/a, for the air bridge (top) and for the GaAs/AlGaAs heterostructure (bottom). As already noticed in Fig. 2.21, the width of the resonances gets narrower, as d/a increases, and the blue-shift is also reduced: $\Delta(a/\lambda) \simeq 0.06$ for the air bridge and $\Delta(a/\lambda) \simeq 0.008$ over the same d/a range. Moreover, the amplitude of the resonances is always much smaller in the weak-confinement case (notice that the reflectance curves are vertically shifted by 1.0 for the air bridge and by 0.1 for the GaAs/AlGaAs waveguide, so that they appear deceptively similar). Though out-of-plane losses may diminish to a "reasonable" value, the air bridge cannot be too thick, because the onset of higher-order waveguide modes will close the photonic band gap [Johnson, S. G., *et al.* (1999); Andreani, L. C. (2002)], disrupting the guiding properties of linear defects and precluding any further application. On the contrary, it is more convenient to work with relatively thick weak-confinement structures: out-of-plane losses are smaller than for thin cores, the modes are closer the the ideal two-dimensional case and higher-order waveguide modes occur at higher frequencies, well above the first band gap. Furthermore, the small dielectric contrast provides a good tolerance of the photonic band structure with respect to the layer thicknesses. Nevertheless, the other alternative would be to use the truly guided modes of a thin air bridge system. However, the presence of any defect that breaks the

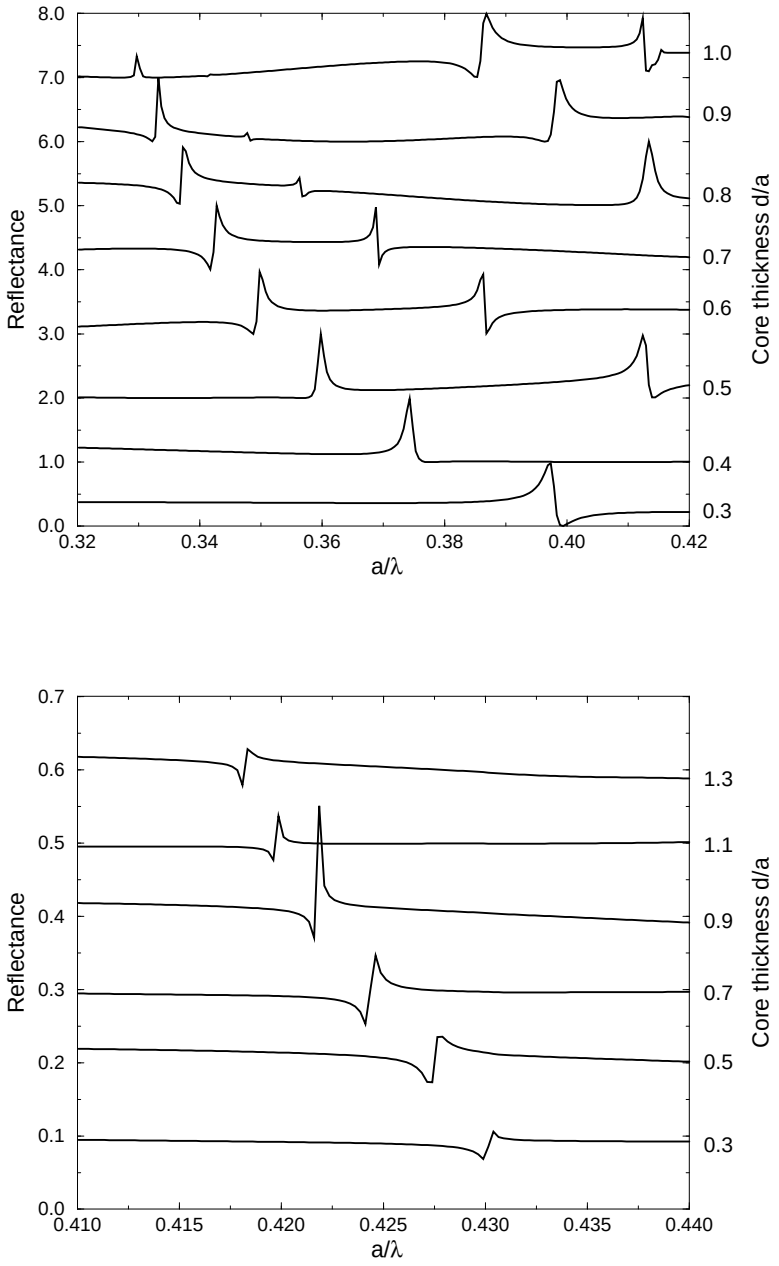

Figure 2.22 TM-polarized reflectance as a function of the core thickness d/a for the air bridge and the GaAs/AlGaAs heterostructure described in the caption of Fig. 2.21: (top panel) air bridge, (bottom panel) GaAs/AlGaAs. For clarity, the curves for the air bridge are vertically shifted by 1.0 and those for the GaAs/AlGaAs waveguide by 0.1. Incident wave: $\theta = 50°$, $\phi = 0°$ and TM-polarized.

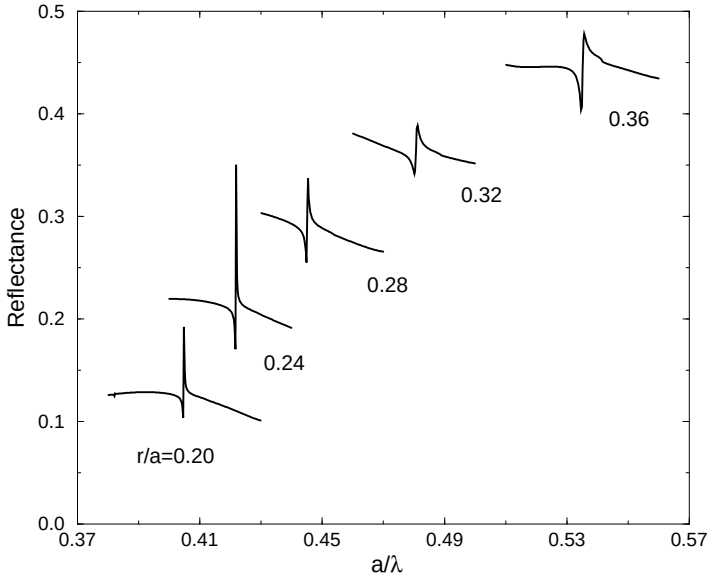

Figure 2.23 TM-polarized reflectance as a function of the hole radius r/a for the GaAs/AlGaAs heterostructure described in the caption of Fig. 2.21, where the GaAs core layer has now thickness $d = 0.9a$. For clarity, the reflectance curves are vertically shifted by 0.1. Incident wave: $\theta = 50°$, $\phi = 0°$ and TM-polarized.

translational symmetry (bends, resonant cavities, etc.), will cause much larger losses than the same defect embedded in a weak-confinement waveguide, in accordance to what is found for the quasi-guided modes of Fig. 2.21. Since defects are necessary elements of a photonic-crystal integrated circuit, these results suggest that it is more advantageous to employ the quasi-guided modes of thick weak-confinement waveguides rather than the guided modes of a thin air bridge or similar strong-confinement structures.

2.5.2 Dependence on the Filling Factor

The above considerations lead to choose a GaAs-based photonic-crystal slab with core thickness $d = 0.9a$. However, for $r = 0.24a$, such system exhibits an H-like band gap[4] that is a little too narrow to be suitable for applications. This can be easily overcome by increasing the hole radius

[4]In fact, the small waveguide asymmetry guarantees that the distinction into E-like and H-like modes is a good approximation.

to obtain a larger band gap, as shown in Fig. 1.14c. However, as suggested by Benisty, H., *et al.* (2000), out-of-plane losses increase with the filling ratio, so that one has to find a compromise between having a larger band gap and larger out-of-plane losses.

Fig. 2.23 shows the dependence of the resonance with respect to the hole radius, from $r = 0.20a$ to $r = 0.36a$. Indeed, the width found for $r = 0.36a$ is much larger than the one corresponding to $r = 0.20a$ and the same holds for out-of-plane losses. By looking at Fig. 2.23 and Fig. 1.14c, the best trade-off seems to occur for a hole radius within the range of $0.28a - 0.32a$, which corresponds to a filling ration of $\sim 30\%$-35%.

2.5.3 Dependence on the Etch Depth

Although these parameters are optimal in theory, in practice one has to face the issue of having a finite etch depth for the air holes. The etch depth depends on the materials (GaAs, AlGaAs, InP, Si) and on their respective etching techniques. Moreover, the etch depth depends also on the hole radius: the etching process is indeed more demanding for small radii. That is why it is interesting to see how out-of-plane losses vary with the etch depth [Benisty, H., *et al.* A (2002)]. In this case, the GaAs/AlGaAs waveguide is patterned with air holes having radius $r = 0.32a$. The top AlGaAs cladding ($d = 0.5a$) and the GaAs core ($d = 0.9a$) are completely etched, while the AlGaAs substrate is etched up to a depth between $0.5a$ and $3.0a$. The results are shown in Fig. 2.24. From the reflectance curves, it is apparent that the energy position of the resonances does not depend on the etch depth. This is good news, since some tolerance is allowed in the etch depth, without effects on the photonic band structure. However, as the etch depth goes from infinity to $0.5a$, the corresponding resonances get broadened. Following the trend, it is found that the width of the resonances reaches the intrinsic value (represented by infinite etch depth), when the etch depth is larger than a critical value $h_c \sim 3.0a$. This is because, as the etch depth increases, the guiding properties of the heterostructure approach those of the intrinsic case; i.e. the critical etch depth h_c corresponds to a point, where the vertical profile of the quasi-guided mode is negligibly different from the intrinsic case. In practice, for a lattice constant $a = 400$nm, the total etch depth as to be $0.5a + 0.9a + 3.0a = 4.4a \Rightarrow h_c = 1760$nm, while for $a = 500$nm the value is $h_c = 2200$nm. Such depths are already attainable for GaAs-based photonic crystals, by

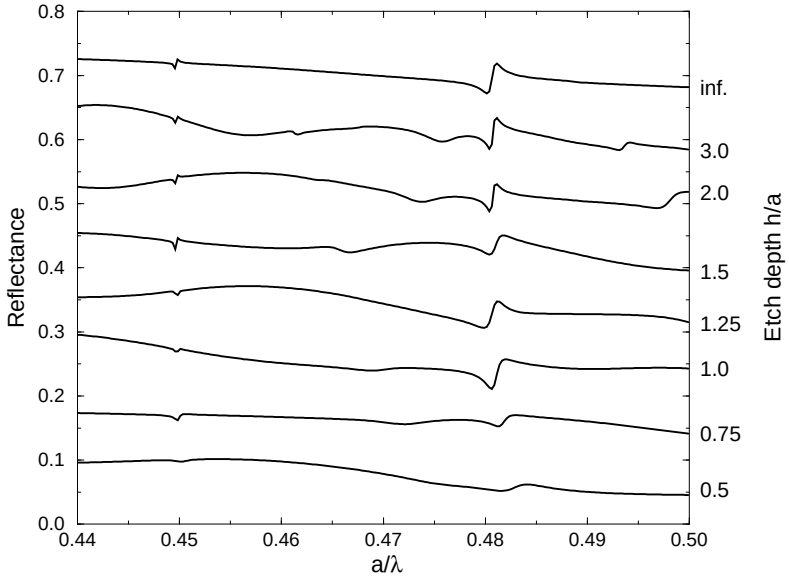

Figure 2.24 TM-polarized reflectance as a function of the etch depth h/a for a GaAs/AlGaAs heterostructure: air (semi-infinite), patterned AlGaAs ($\epsilon = 11$, $d = 0.5a$), patterend GaAs ($\epsilon = 12$, $d = 0.9a$), patterned AlGaAs ($\epsilon = 11$, $h/a = 0.5 - \infty$) and AlGaAs substrate ($\epsilon = 11$, semi-infinite). All patterned layers have air holes with radius $r = 0.32a$. For clarity, the reflectance curves are vertically shifted by 0.09. Incident wave: $\theta = 50°$, $\phi = 0°$ and TM-polarized.

means of state of the art technology. However, this is not the case for any heterostructure, where material-related technological issues might make this goal more challenging, besides considering that the critical etch depth depends on several structure parameters, like the hole radius, the layer thicknesses and the dielectric contrast, for instance.

In conclusion, weak-confinement photonic-crystal slabs exhibit low propagation losses for relatively thick cores, small air filling ratios and sufficient etch depth. If these conditions are fulfilled, these systems can be promising candidates for the realization of photonic-crystal integrated circuits.

CHAPTER 3. WAVE PROPAGATION

After studying the photonic band structure and the optical properties of semiconductor-based two-dimensional photonic crystals, the discussion moves to wave propagation. Wave propagation concerns the in-plane transmission properties of bulk two-dimensional photonic crystals, linear defects and more complex structures. The subject is, of course, of great interest for technological applications. That is why the work is intended to start from simple systems and, step by step, to build up a photonic-crystal device, namely a combiner for an integrated multi-wavelength laser source. This result is part of the European Union Information Societies Technology program, called Photonic Crystal Integrated Circuits (PCIC), and has been developed in collaboration within the research consortium. Such example is just one of the possible applications and, actually, it can be still considered a building block, rather than a photonic-crystal device. Nevertheless, it already possesses a degree of complexity that allows to gather a collection of important concepts, which are with wave propagation. The PCIC consortium has chosen to work with weak index confinement two-dimensional photonic-crystal slabs, in particular GaAs and InP systems. The AlGaAs/GaAs/AlGaAs configuration has been used as a reference, thanks to the expertise reached in its fabrication and characterization. Instead, the InP/GaInAsP/InP system has been aimed to be the novel structure for fabrication of photonic-crystal devices, operating at 1.5μm.

From the point of view of theory, the purpose is to make use of modelling tools for designing the desired functionality, be a waveguide, a resonant cavity or a more complex structure. The Finite-Difference Time-Domain (FDTD) method appears to be the proper one, for its flexibility in treating almost any photonic-crystal geometry.

As already mentioned, photonic crystals based on low-index-contrast planar waveguides do not support truly guided modes, but resonances, which imply propagation losses. This issues, plus other important ones like bending of light, modal mixing and mono-mode transmission, will be

discussed inside this chapter and possible solutions will be proposed.

The discussion begins with an historical overview of the subject, with emphasis on low-index-contrast systems. Then, the two-dimensional FDTD method is explained in detail, with the necessary implementations and extensions for calculating transmission spectra of two-dimensional photonic crystals, including propagation losses. Section 3.3 introduces InP-based two-dimensional photonic-crystal slabs, with mention to the fabrication method. The two-dimensional FDTD is compared against the full three-dimensional FDTD method, as a valid approximation for modelling weak-confinement systems; the test is performed on bulk photonic crystals. With Section 3.4 the attention moves to wave propagation in linear defects, translating the general concepts of dispersion relation and of mini-stop band, seen in Sec.1.5, into transmission spectra. Section 3.5 deals with one of the main arguments of this chapter: bends in linear defects. The difference between single-mode (W1) and multi-mode waveguide (W3) is shown, putting in evidence advantages and issues of both cases. Several bend designs are proposed for the W3 waveguide. The objective is to obtain mono-mode transmission in the fundamental guided mode. Comparison with experimental data is also shown. The last section is dedicated to more complicated structures, namely splitters and combiners. The discussion is oriented towards the demonstration of a low-cross-talk combiner for a multi-wavelength-source laser.

3.1 History

As discussed in the last part of Sec. 1.1, besides the intense research on the photonic band structure of bulk photonic crystals, a parallel activity was devoted to the investigation of the defect states created by appropriate design of the dielectric pattern. Such efforts were oriented towards the realization of active and passive components for photonic-crystal integrated circuits, like waveguides, resonators, add/drop filters, lasers and other optical devices. These ideas were founded on the existence of the photonic band gap: by tuning and tailoring defect states within the band gap domain, one wishes to achieve the desired functionality. However, between the proposal by Meade, R. D., *et al.* (1994) of using two-dimensional photonic-crystal slabs to attain a complete control of light and designing non-conventional waveguides and high-Q-factor resonators, and the availability

of appropriate samples [Krauss T. F., *et al.* (1996)], most of the advancement was necessarily in theory, or in experiments performed in the microwave frequency domain [*J. Opt. Soc. Am. B, 10* (2); Joannopoulos, J. D., *et al.* (1995)]. However, later on, much work was successfully conducted also for what concerns the fabrication and characterization of photonic-crystals-based components operating at infrared and optical wavelengths.

As regards the area of micro-cavities, Villeneuve, P. R., *et al.* (1996) theoretically investigated the properties of resonant modes in two- and three-dimensional photonic crystals. They showed how such properties can be controlled by defect engineering. In this context, Foresi, J. S., *et al.* (1997) were the first ones to report on the fabrication and characterization of a photonic-crystal micro-resonator operating at the telecommunication wavelength (1.55μm). The structure was obtained by etching the desired pattern in a silicon-on-insulator waveguide. Though the Q-factor was only 265, the tiny modal volume ($0.0455\mu\text{m}^3$) was very promising for achieving a high degree of integration. Subsequently, Painter, O., *et al.* A (1999) published a numerical study of defect modes of two-dimensional photonic-crystals based on a self-standing dielectric membrane. They calculated a Q-factor of 20,000, whose increase was limited by radiative losses in the vertical direction. The same system was experimentally studied by Pottier, P., *et al.* (1999), who found Q-factors up to 900, but for larger cavities than those considered by Painter, O., *et al.* A (1999). Similar experiments were conducted by Benisty, H., *et al.* (1999) on GaAs-based photonic-crystal slabs. It is worth to mention that there are also studies related to macro-porous silicon photonic-crystals: Kramper, P., *et al.* (2001) performed direct spectroscopy of a deep two-dimensional photonic-crystal micro-resonator identifying two resonances with Q-factors of 640 and 190. Although these values are not very high, the extremely small mode areas result in generalized finesse comparable with the microdisk and the micropillars, respectively. Such high finesse were also achieved in photonic-crystal slabs [Painter, O., *et al.* B (1999)].

Besides micro-resonators, another important element for photonic-integrated circuits is the waveguide. Photonic crystals appeared particularly attracting thanks to the possibility of guiding light through sharp bends without losses, contrary to what happens for dielectric waveguides, and for the possibility of on-chip integration. Mekis, A., *et al.* (1996) numerically demonstrated that 90° sharp bends, designed in a square lattice of dielectric pillars, can have very efficient transmission.

The same structure was experimentally assessed by Lin, S.-Y., *et al.* B (1998) in the micro-wave regime: they indeed found that nearly 100% of light goes though the bend. However, the challenge was to obtain the same nice results for micron-size photonic-crystals. Before working on bent waveguides, wave propagation was studied in straight waveguides: Baba, T., *et al.* (1999) for silicon-on-insulator, Benisty, H., *et al.* (1999) and Talneau, A., *et al.* (2001) for GaAs/AlGAs, and Chow, E., *et al.* (2000) for GaAs/Alox-based photonic crystals. As already mentioned, these studies led to the discovery of mini-gaps in the waveguide transmission spectrum [Mekis, A., *et al.* (1998); Olivier, S., *et al.* A (2001)], the so-called mini-stop band. As far as bent waveguides are concerned, Tokushima, M., *et al.* (2000) measured high transmission through a 120° sharp bends in single-defect waveguides, designed in triangular-lattice photonic crystals based on silicon-on-insulator planar waveguides. Also, Lončar, M., *et al.* A (2000) reported on 60° bends in single-defect waveguides created in etched silicon-on-insulator heterostructures. Chow, E., *et al.* (2001) attained very high efficiency in 60° bends for single-defect waveguides made in GaAs/Alox-based photonic crystals with a triangular lattice of air holes. Similar results were theoretically predicted by Chutinan, A., *et al.* (2000, 2002) for the same designs applied to air bridge systems. However, all these cases regard bends created in single-mode waveguides (the W1 waveguide). Since wider waveguides may yield lower propagation losses, particular attention was put on waveguides made by removing more than one row of holes (WN waveguides). The price to pay was the loss of single-mode transmission. Indeed, even two-row removed waveguides are unavoidably multi-mode. Moosburger, J., *et al.* (2001); Talneau, A., *et al.* A (2002) showed improved transmission in W3 waveguides by smoothing 60° bends adding $\Gamma - M$ sections to the bend corner. Olivier, S., *et al.* B (2001) investigated the idea of using coupled resonators to guide light through sharp bends. However, such designs did not guarantee single-mode transmission, which is a fundamental feature for cascading elements. Very recently, Talneau, A., *et al.* B (2002) proposed a novel bend design based on the concept of adiabatic taper [Lalanne, Ph., *et al.* (2002)]. The idea is to taper a W3 waveguide to a W1 waveguide in the very proximity of the bend, so that single-mode transmission is guaranteed by the narrow channel itself.

Another important element for photonic-crystal integrated circuits is the so-called channel drop filter. The theory and the demonstration of the feasibility of photonic-crystal add/drop filter was

made by Fan, S., *et al.* (1998). However, due its extreme sensitivity to losses, such device has yet to be experimentally tested. Lastly, the passive elements have to be completed by active elements like photonic-crystal lasers for instance. They are interesting because they can be integrated in a photonic-crystal chip and they may exhibit low threshold current and low power consumption. All of that is state-of-the-art research [Painter, O., *et al.* B (1999); Happ, T., *et al.* (2002); Ryu, H.-Y., *et al.* (2002); Shkunov, M. N., *et al.* (2002); Cao, J. R., *et al.* (2002); Imada, M., *et al.* (2002)].

3.2 The Finite-Difference Time-Domain Method

Calculating the transmission properties of photonic crystals is, essentially, the problem of solving Maxwell's equations for finite systems with a periodic dielectric function. The classical transfer matrix method [Pendry, J. B., *et al.* (1992)] allows to obtain several transfer functions for simple structures, like bulk photonic crystals or linear defects, but it is not easily applicable to more complicated geometries, like sharp bends, combiners, channel-drop filters and other multi-port devices. The Finite-Difference Time-Domain (FDTD) method [Tavlove, A. (1995)], instead, is much more flexible as regards the geometry of the system that has to be modelled. This is because while the transfer matrix method expands the electromagnetic field on plane waves, the FDTD method works in direct space on the full fields, defined on a space-time mesh.

The FDTD method dates back to the work of Yee, K. S. (1966), who proposed an algorithm for solving the time-dependent Maxwell's curl equations, which transforms the differential operators in finite differences in space and time. The method has been extensively used mainly in electrical engineering, in antenna's design and in radar science, also for military defense projects, like for the radar-invisible aircraft fighters (radar cross section mitigation). With the advent of photonic crystals, the FDTD method has been found also a powerful technique for studying and designing building blocks for photonic integrated circuits.

3.2.1 Basic Ideas

To introduce the Yee algorithm, consider first the derivative of a one-variable function $f(x)$,

$$\frac{\mathrm{d}f(x)}{\mathrm{d}x} = f'(x) = \lim_{h\to 0^+} \frac{f(x+h) - f(x)}{h}\,. \tag{3.1}$$

Recalling that the value of $f(x+h)$ can be obtained from Taylor expansion of $f(x)$, $f'(x)$ is approximated by the following second-order accurate central difference,

$$f'(x) = \frac{f(x+h) - f(x-h)}{2h} + O[h^2]\,. \tag{3.2}$$

Eq. (3.2) represents the classical technique used in numerical analysis for calculating the first derivative of a function. The Yee algorithm is a little bit more sofisticate, because it works with Maxwell's curl equations. Since the systems under investigation are two-dimensional photonic crystals, the discussion is limited to the two-dimensional FDTD method. For the implementation of the one- and three-dimensional FDTD methods, please refer to Tavlove, A. (1995).

Thus, consider a two-dimensional system and focus the attention on Maxwell's curl equations

$$\nabla \times \mathbf{H}(\mathbf{x},t) - \frac{1}{c}\frac{\partial}{\partial t}\epsilon(\mathbf{x})\mathbf{E}(\mathbf{x},t) = 0\,, \qquad \nabla \times \mathbf{E}(\mathbf{x},t) + \frac{1}{c}\frac{\partial}{\partial t}\mathbf{H}(\mathbf{x},t) = 0\,, \tag{3.3}$$

with $\mathbf{x} = (x,y)$ and the fields H-polarized. Before proceeding, it is convenient to define the following notation for the finite differences. The two-dimensional space is defined on a discrete uniform rectangular mesh $x-y$. Likewise, time is discretized by division in uniform intervals Δt. Denote a space point in the mesh as

$$(i,j) = (i\Delta x, j\Delta y)\,, \tag{3.4}$$

where Δx and Δy are, respectively, the lattice space increments in the x and y coordinate directions, and i,j are integers. Further, denote any function f of space and time evaluated at a discrete point in the grid and at a discrete point in time as

$$f(i\Delta x, j\Delta y, n\Delta t) = f|^n_{i,j}\,. \tag{3.5}$$

Yee made use of central differences for obtaining the finite-difference version of Eq. (3.3). Consider the application of Eq. (3.2) for the evaluation of the first partial space derivative of f in the x direction, at the fixed time $t_n = n\Delta t$:

$$\frac{\partial f}{\partial x}(i\Delta x, j\Delta y, n\Delta t) = \frac{f|^n_{i+1/2,j} - f|^n_{i-1/2,j}}{\Delta x} + O[(\Delta x)^2]\,, \tag{3.6}$$

where the $\pm 1/2$ increment in the i subscript of f represents a space finite-difference over $\pm 1/2\Delta x$. Eq. (3.6) is second-order accurate like Eq. (3.2), but it is apparent that the data used for central

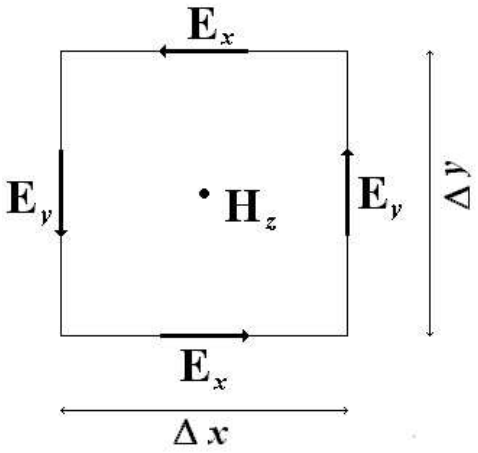

Figure 3.1 Positions of the H-polarized field components for the central-difference derivatives. Each field component is defined on a uniform rectangular mesh with displacements Δx and Δy. Each mesh is shifted by $\Delta x/2$ or $\Delta y/2$ from the others so that if H_z is positioned at the lattice points $(i, i \pm 1, \ldots, i \pm m; j, j \pm 1, \ldots, j \pm n)$, E_x will be at $(i, i \pm 1, \ldots, i \pm m; j + 1/2, j + 1/2 \pm 1, \ldots, j + 1/2 \pm n)$ and E_y at $(i + 1/2, i + 1/2 \pm 1, \ldots, i + 1/2 \pm m; j, j \pm 1, \ldots, j \pm n)$.

differencing are taken to the right and left of the observation point i, j by only $\Delta x/2$, rather than a full Δx. Yee chose this notation because he wished to interleave the **E** and **H** components in the space lattice at intervals of $\Delta x/2$, as shown in Fig. 3.1. Eq. (3.6) provides a numerical approximation of $\partial E_y(\mathbf{x}, t)/\partial x$ at the grid point i, j and at the time coordinate n. In analogy to Eq. (3.6), the other partial derivative $\partial f|^n_{i,j}/\partial y$ can be written simply by incrementing the j subscript of f by $\pm 1/2\Delta y$. A similar expression holds for the partial time derivative, evaluated at the grid point i, j

$$\frac{\partial f}{\partial t}(i\Delta x, j\Delta y, n\Delta t) = \frac{f|^{n+1/2}_{i,j} - f|^{n-1/2}_{i,j}}{\Delta t} + O[(\Delta t)^2]\,, \tag{3.7}$$

where now the finite-difference is over $\pm 1/2\Delta t$. The notation is chosen again to interleave the **E** and **H** components in time at intervals $\pm 1/2\Delta t$ for implementing the so-called "leapfrog" algorithm.

3.2.2 Finite-Difference Expressions for Maxwell's curl equations

The above ideas can be now applied to achieve a numerical approximation of Eq. (3.3). Choose for instance H-modes. By means of Eqs. (3.6) and (3.7), Ampere's law is rewritten as

$$\frac{1}{c}\epsilon_{i,j+1/2}\frac{E_x|_{i,j+1/2}^{n+1/2}-E_x|_{i,j+1/2}^{n-1/2}}{\Delta t}=\frac{H_z|_{i,j+1}^{n}-H_z|_{i,j}^{n}}{\Delta y}\,, \tag{3.8a}$$

$$\frac{1}{c}\epsilon_{i+1/2,j}\frac{E_y|_{i+1/2,j}^{n+1/2}-E_y|_{i+1/2,j}^{n-1/2}}{\Delta t}=-\frac{H_z|_{i+1,j}^{n}-H_z|_{i,j}^{n}}{\Delta x}\,, \tag{3.8b}$$

with $\epsilon_{i,j}=\epsilon(i\Delta x, j\Delta y)$ is the position-dependent dielectric function. In the same manner, Faraday's law reads

$$-\frac{1}{c}\frac{H_z|_{i,j}^{n+1}-H_z|_{i,j}^{n}}{\Delta t}=\left(\frac{E_y|_{i+1/2,j}^{n+1/2}-E_y|_{i-1/2,j}^{n+1/2}}{\Delta x}-\frac{E_x|_{i,j+1/2}^{n+1/2}-E_x|_{i,j-1/2}^{n+1/2}}{\Delta y}\right)\,. \tag{3.8c}$$

Focussing on Eq. (3.8a), note that all field quantities on the right-hand side are evaluated at time step n, while on the left-hand side, the electric field components are evaluated at time step $n\pm 1/2$, as imposed by the leapfrog algorithm. Assuming that the values of the field components for n and $n-1/2$ are stored in the computer memory, the only unknown remains $E_x|_{i,j+1/2}^{n+1/2}$. Rearranging Eq. (3.8a), so that the term $E_x|_{i,j+1/2}^{n+1/2}$ is isolated on the left-hand side, yields

$$E_x|_{i,j+1/2}^{n+1/2}=E_x|_{i,j+1/2}^{n-1/2}+\frac{c\Delta t}{\epsilon_{i,j+1/2}\Delta y}\left(H_z|_{i,j+1}^{n}-H_z|_{i,j}^{n}\right)\,. \tag{3.9a}$$

In a similar manner, finite-difference expressions are derived for the remaining equations

$$E_y|_{i+1/2,j}^{n+1/2}=E_y|_{i+1/2,j}^{n-1/2}-\frac{c\Delta t}{\epsilon_{i+1/2,j}\Delta x}\left(H_z|_{i+1,j}^{n}-H_z|_{i,j}^{n}\right)\,, \tag{3.9b}$$

$$H_z|_{i,j}^{n+1}=H_z|_{i,j}^{n}-\frac{c\Delta t}{\Delta x}\left(E_y|_{i+1/2,j}^{n+1/2}-E_y|_{i-1/2,j}^{n+1/2}\right)+\frac{c\Delta t}{\Delta y}\left(E_x|_{i,j+1/2}^{n+1/2}-E_x|_{i,j-1/2}^{n+1/2}\right)\,. \tag{3.9c}$$

After initializing the fields $\mathbf{H}$ and $\mathbf{E}$ at the time steps 0 and $1/2$, respectively, a loop over Eqs. (3.9a), (3.9b) and (3.9c) allows to update the field until the desired time step. For each time step, another loop has to be performed over the points i,j to update the fields on the grid. In practice, two nested loops simulate the space-time evolution of the electromagnetic field in any dielectric medium defined by $\epsilon_{i,j}$. The computer has to store only the field values on the grid i,j on a defined time step and the position-dependent dielectric function $\epsilon_{i,j}$; at each time step, the updated field values replace the old ones and so on.

Concerning the Maxwell divergence equations, it can be demonstrated that the Yee grid and algorithm enforce the Gauss law relations for the electric and magnetic fields.

Based on the Yee algorithm, the FDTD method seems to be a simple and efficient technique for solving Maxwell's equations. However, there are some important issues and details that must be carefully considered for successful modelling, namely: stability and numerical dispersion, boundary conditions at the grid's edges, simulation of incident pulses, detection of the transmitted field. Numerical stability and dispersion is too much technical for discussion in this context. Here, it is enough to say that the two-dimensional algorithm is stable if

$$\Delta t \leq \frac{1}{c\sqrt{\frac{1}{(\Delta x)^2} + \frac{1}{(\Delta y)^2}}}\,. \tag{3.10}$$

If the above condition is not fulfilled, the field values will exponentially diverge as time increases. The loop over the grid points must be finite for two reasons: storing the field values over an infinite number of points would require infinite computer memory, a `do` loop over infinite lattice points would require infinite CPU time. Assuming that the grid begins at $i = 1, j = 1$ and terminates at $i = M, j = N$, the field components at $(1, j)$, $(i, 1)$ and (M, j), (i, N) cannot be updated, because the required field components at $(1/2, j)$, $(i, 1/2)$ and $(M+1/2, j)$, $(i, N+1/2)$ are not available. On the other hand, one wants a boundary condition that permits reflection-less outward-propagating numerical waves, almost as if the simulation were performed on a computational domain of infinite extent. In the process, the outer boundary condition must suppress spurious reflections of the outgoing waves to an acceptable level, permitting the FDTD solution to remain valid for all time steps. In the present work, the FDTD code implements Liao absorbing boundary conditions [Liao, Z. P., *et al.* (1984)], where the marginal field values are obtained by extrapolation of the field values over a stencil of internal grid points. The method is based on a Newton backward-difference polynomial. Alternatively, if the system is homogenous or periodic in one direction, Bloch boundary conditions can be used in place of Liao's.

Fig. 3.2 shows the computational domain for a finite two-dimensional photonic crystal. The host material is equal to the dielectric medium of the photonic crystal. The modelled structure is surrounded by a buffer of homogenous dielectric, along the direction where transmission has to be

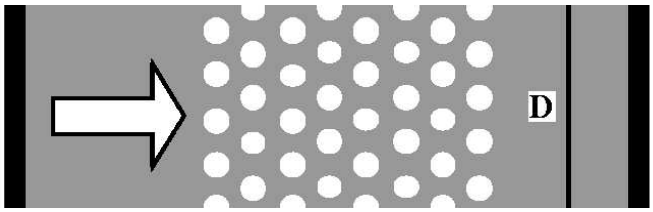

Figure 3.2 FDTD simulation of a simple crystal along the $\Gamma - M$ direction. A plane wave is launched from the left (arrow) and it is collected by a line detector (D) after the photonic crystal. The black-thick edges truncate the computational mesh using Liao absorbing boundary conditions. The other edges use Bloch boundary conditions.

calculated, in this case the $\Gamma - M$ lattice direction. Since the system is finite along $\Gamma - M$, Liao boundary conditions must be used for terminating the two buffers, before and after the photonic crystal. In the $\Gamma - K$ direction, instead, the system is infinitely extended and Bloch boundary conditions can be used.

In order to calculate the transmission, the FDTD method has to implement an incident wave launched from one side of the structure and collect the power at the other side. There are several methods to include a source in the Yee algorithm. For bulk photonic crystals, like the one of Fig. 3.2, a plane wave is chosen as incident source. The source profile is obtained by aligning a set of oscillating dipoles along the desired wave-front. For propagation along the x direction, the dipoles are written as

$$H_z|^{n}_{i_\circ,j}{}^{(s)} = H_\circ \cos(\omega_\circ n\Delta t) e^{-\frac{\sigma^2}{2}(n\Delta t - t_\circ)^2}, \qquad \text{with } j = 1, \ldots, N, \tag{3.11}$$

$i_\circ$ determines the distance of the source from the photonic crystal, $H_\circ$ the amplitude. The dipoles have a Gaussian time profile, so that the incident spectrum is a Gaussian centered at $\omega_\circ$ with standard deviation σ. The time delay $t_\circ$ controls the switch-on of the source. By plugging Eq. (3.11) into Eq. (3.9c), for $i = i_\circ$, the magnetic field finite-difference expression is replaced by

$$\begin{aligned} H_z|^{n+1}_{i,j} = H_z|^{n}_{i,j} - \frac{c\Delta t}{\Delta x}\left(E_y|^{n+1/2}_{i+1/2,j} - E_y|^{n+1/2}_{i-1/2,j}\right) + \\ + \frac{c\Delta t}{\Delta y}\left(E_x|^{n+1/2}_{i,j+1/2} - E_x|^{n+1/2}_{i,j-1/2}\right) + H_z|^{n}_{i_\circ,j}{}^{(s)}. \end{aligned} \tag{3.12}$$

At the beginning of the simulation, the field components are initialized to zero. As time passes, the Gaussian pulse impinges the photonic crystal and the transmitted power exits from the other side.

A line of point detectors, see Fig. 3.2, is positioned at the right-hand side of the photonic crystal. During the simulation, the values of the field components are stored at each detection point. At the end of the time stepping, Fast-Fourier transform of the field components yields the frequency-domain amplitudes. Then, at each point, the Poynting vector component parallel to the desired direction is computed. The total transmitted power is obtained by averaging the Poynting vectors over the line detector. The incident power is calculated by placing the same detector just in front of the photonic crystal, before the source, and running the simulation without photonic crystal to avoid superposition of the incident and reflected waves. The ratio of transmitted power over the incident one yields the transmission coefficient.
The present implementation is used for modelling bulk two-dimensional photonic crystals and one-dimensional cavities. The extension to more complex structures will be described in Sec. 3.4.

The Yee algorithm is second-order accurate. The accuracy can be improved by using smaller and smaller space increments Δx and Δy. In general, having the smallest wavelength twenty times larger than the grid's pitch is enough for converged results. Notice that even if the loop over the grid points is a $O(N^2)$ process, where N is the number of lattice points in one dimension, since the time stepping has to satisfy Eq. (3.10), the whole algorithm is actually a $O(N^3)$ process with three nested `do` loops. For this reason, the three-dimensional version of the FDTD method is very much time consuming, with four nested `do` loops.

3.2.3 Modelling Out-of-Plane Losses

The above implementation of the two-dimensional FDTD method is valid for loss-less media. Benisty, H., *et al.* (2000) proposed that the transmission of weak-confinement two-dimensional photonic-crystal slabs can be calculated, with good approximation, using a two-dimensional model, which accounts for out-of-plane losses by means of a phenomenological parameter. Such approach is very convenient from the modelling point of view, because a two-dimensional method can be employed for designing waveguide-based photonic crystals, in place of *ab initio* techniques. In the transfer matrix method, losses are simply introduced by adding an imaginary part to the holes dielectric function. In the FDTD method, the correct way to implement the Benisty model is to add an artificial electrical conductivity to the air holes. To do that, the Yee algorithm has to be

reformulated starting from Faraday's law with a current

$$\nabla \times \mathbf{H}(\mathbf{x},t) = \frac{4\pi}{c}\mathbf{j}(\mathbf{x},t) + \frac{1}{c}\frac{\partial}{\partial t}\epsilon(\mathbf{x})\mathbf{E}(\mathbf{x},t)\,, \tag{3.13}$$

where $\mathbf{j}(\mathbf{x},t) \neq 0$ only inside the air holes. Using Ohm's law, the above equation is rewritten as

$$\nabla \times \mathbf{H}(\mathbf{x},t) = \frac{4\pi}{c}\sigma(\mathbf{x})\mathbf{E}(\mathbf{x},t) + \frac{1}{c}\frac{\partial}{\partial t}\epsilon(\mathbf{x})\mathbf{E}(\mathbf{x},t)\,, \tag{3.14}$$

A central-difference expression of Eq. (3.14) is obtained in analogy to the previous ones. The conductivity is defined on the grid points as $\sigma_{i,j}$, likewise the dielectric function. For instance, the update equation for the x electric field component reads

$$E_x|^{n+1/2}_{i,j+1/2} = \left(\frac{1-\dfrac{4\pi\sigma_{i,j}\Delta t}{2\epsilon_{i,j+1/2}}}{1+\dfrac{4\pi\sigma_{i,j}\Delta t}{2\epsilon_{i,j+1/2}}}\right) E_x|^{n-1/2}_{i,j+1/2} + \left(\frac{1+\dfrac{4\pi\sigma_{i,j}\Delta t}{2\epsilon_{i,j+1/2}}}{\dfrac{c\Delta t}{\epsilon_{i,j+1/2}\Delta y}}\right)\left(H_z|^{n}_{i,j+1} - H_z|^{n}_{i,j}\right)\,. \tag{3.15}$$

Notice that the central-difference has been obtained by using the *semi-implicit approximation*:

$$E_x|^{n}_{i,j+1/2} = \frac{E_x|^{n+1/2}_{i,j+1/2} + E_x|^{n-1/2}_{i,j+1/2}}{2}\,.$$

The other central-difference expressions are similar to Eq. (3.15).

Defining a conductivity parameter allows to include the effects due to out-of-plane losses. Since the Benisty model deals with the dielectric function ϵ'', sometimes it is better to express the parameter in terms of ϵ'': $\sigma \simeq \omega\epsilon''/4\pi$. Even if σ depends on ω, for narrow spectra it is assumed constant, taking $\omega = \omega_\circ$, and the external loss parameter becomes ϵ''.

The FDTD method is now applied to the systems of interest, namely GaAs-based and InP-based two-dimensional photonic crystals. A similar derivation of the finite-difference equations is easily written also for E-modes. Since these structures are intended to work with polarized light, all simulations are performed for H-modes, if not otherwise stated.

3.3 GaAs- and InP-based Two-Dimensional Photonic Crystals

GaAs- and InP-based two-dimensional photonic crystals are designed in a slightly asymmetric waveguide geometry. Fig. 3.3 shows the lateral profile of the InP heterostructure. The GaInAsP/InP

planar waveguide is grown by metal organic vapor phase epitaxy on n-InP substrates. The core is a 434nm-thick GaInAsP layer, which embeds two strain-compensated quantum wells, emitting at 1.47μm and 1.55μm. The material is lattice matched to InP and possesses a direct band-gap emission wavelength $\lambda_{\mathrm{GAP}} = 1.22\mu$m. The quantum wells are used in characterization experiments based on the internal-probe method [Labilloy, D., *et al.* A (1997); Ferrini, R., *et al.* (2002)]. The top of the core is capped with a 200nm-thick InP layer. At the bottom cladding, a 600nm-thick buffer, made of InP, separates the core from the n-InP substrate. In the spectral region of interest ($\lambda = 1.55\mu$m), the refractive-index values $n_{\mathrm{core}} = 3.35$ and $n_{\mathrm{clad}} = 3.17$ are assumed for GaInAsP and InP, respectively. The resulting structure is a multimode waveguide with three TE guided modes [Saleh, B. E. A., *et al.* (1991)].

The squared field profile $\zeta^2(z)$ of the fundamental guided TE mode and the waveguide step-index profile are displayed in Fig. 3.4. The calculated value of the fundamental mode is $n_{\mathrm{eff}} = 3.23$. Due to material dispersion, n_{eff} is a function of λ: for a photoluminescence beam centered at $\lambda = 1.5\mu$m, the effective index dispersion of the fundamental guided mode is $\partial n/\partial\lambda = -2.5 \times 10^{-4}\mathrm{nm}^{-1}$. Taking into account material dispersion, the corrected values of the effective index range from 3.23 to 3.255. In order to perform FDTD simulations, the effective index is assumed to be 3.24 ($\epsilon_{\mathrm{eff}} = 10.5$), which averages the effects of material dispersion.

The planar waveguide is etched to form a triangular lattice of air holes. In characterization experiments, the lattice constant varies from $\simeq$ 240nm up to $\simeq$ 420nm to sample the whole photonic-band-gap frequency range with the quantum well photoluminescence spectrum. This is the so-called lithographic tuning, which relies on the scaling properties described in Sec. 1.2.3. Even if the waveguide is asymmetric because of the top interface with air, the band gap properties are close to those of symmetric weak-confinement systems, see Fig. 1.14. With the above choices of the lattice constant, the resulting photonic-crystal slabs have a dimensionless thickness d/a larger than 1. For this reason, the photonic resonances will be very close to the photonic bands of a two-dimensional photonic crystal. In order to minimize propagation losses, the filling factor is chosen to be relatively small, 35%, which is enough to build up a band gap for H-like modes. Therefore, theory and experiments are performed with H-polarized light. The small asymmetry of the waveguide assures that the polarization mixing is negligible and that the separation into H-like

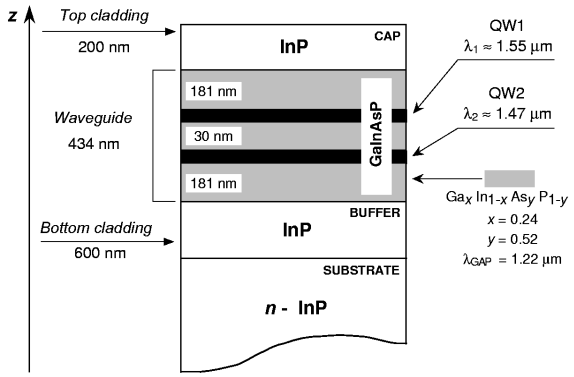

Figure 3.3 InP/GaInAsP waveguide heterostructure. Two strain-compensated GaInAsP quantum wells emitting at two different near-infrared wavelengths are embedded in the core layer. Courtesy of Ferrini, R., EPFL, Switzerland.

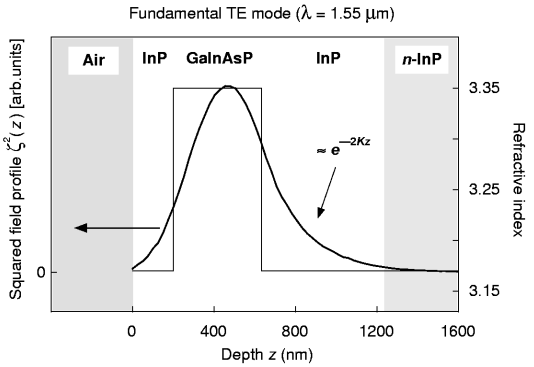

Figure 3.4 Refractive index profile of the InP/GaInAsP waveguide heterostructure of Fig. 3.3 and squared field profile $\zeta^2(z)$ of the fundamental TE mode calculated for $\lambda = 1.55\mu$m. Courtesy of Ferrini, R., EPFL, Switzerland.

modes and E-like modes is valid with good approximation.

These considerations suggest that modelling of the above structures can be done within a two-dimensional approximation, assuming that the system is comparable to an effective two-dimensional photonic crystal, once that the waveguide parameters are fixed. The propagation properties are studied by means of the two-dimensional FDTD method, where the vertical confinement effect is accounted for using the effective index of the fundamental guided mode ($\epsilon_{\text{eff}} = 10.5$), in place of the nominal material values, and out-of-plane losses are included with the *ad hoc* parameter ϵ''. Due to the difficulty of modelling complex structures (bent channel waveguides, splitters,

combiners, add-drop filters) with *ab initio* methods, the two-dimensional approximation represents a balanced trade-off between speed and accuracy in designing photonic-crystal building blocks. Such approximation, however, has to be validated by comparison with a full three-dimensional numerical method and/or by comparison with experiments. First, the method is tested with the three-dimensional FDTD method as regards simple systems, like bulk photonic crystals, again because performing *ad initio* simulations of advanced systems is not easy; secondly, comparison with experimental data will be shown for more complicated structures, like linear defects with bends and Y splitters.

Before testing the two-dimensional approximation against the three-dimensional FDTD method, it is worth to mention some aspects concerning the etching techniques, which may have consequences on out-of-plane losses.

3.3.1 Fabrication Methods and Etch Depth

The photonic crystal structure is etched in the GaInAsP/InP heterostructure by e-beam lithography and chemically assisted ion beam etching (CAIBE). 150nm of SiO_2 sputtered on the sample yields an etch mask suitable for high-resolution patterning. The triangular lattice is written in 500nm spin coated polymethylmethacrylate (PMMA) resist by e-beam exposure. The PMMA is developed in 1:3 methylisobutylketone/propanol and the hole pattern is transferred into the SiO_2 layer using CHF_3/Ar-based reactive ion beam etching (RIE). This two-step writing process provides higher selectivity in the mask patterning.

Since out-of-plane losses strongly depend on the hole morphology [Lalanne, Ph., *et al.* (2001)], optimizing the etching process is of primary importance for obtaining high quality samples. In fact, insufficient hole depth with respect to the vertical extent of the guided mode profile [Benisty, H., *et al.* A (2002)] and/or conical hole shape [Ferrini, R., *et al.* (2002)] increase light scattering into the substrate. In order to minimize out-of-plane losses, the etch depth has to be larger than 1.5μm, with holes as straight as possible. This implies high anisotropy of the etching process and high aspect ratios. CAIBE based on Ar/Cl_2 has been found to yield vertical profiles with high aspect ratios, in comparison to the standard methane-based RIE. For this reason, Ar/Cl_2 CAIBE is used to etch the photonic crystal pattern into the InP-based heterostructure, using the e-beam

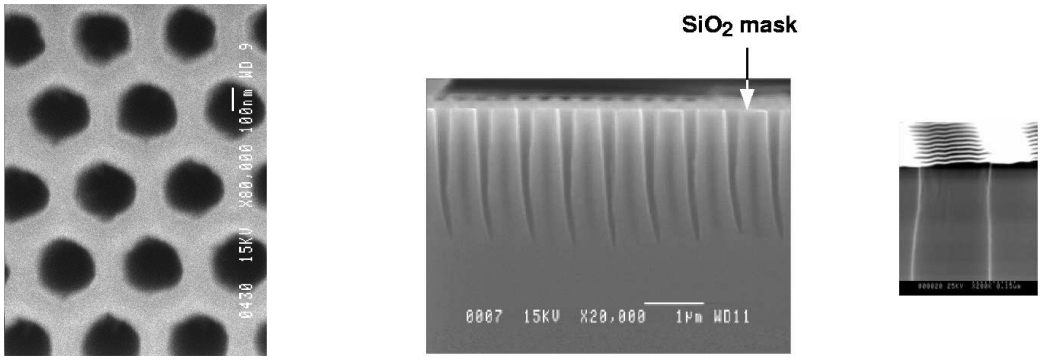

Figure 3.5 SEM micrographs of a photonic crystal with lattice constant a=400nm fabricated using CAIBE etching. The images were taken before the SiO_2 mask removal. Courtesy of Ferrini, R., EPFL, Switzerland, Mulot, M., KTH, Sweden, and Talneau, A., LPN - CNRS, France.

exposed SiO_2 mask. Thus, the sample is sputtered by an energetic argon ion beam with 5sccm flow and 400eV ion energy. At the same time, a chemical attack is generated by a 1sccm chlorine flow. Argon ions sputter phosphorus atoms, whereas chlorine enhances the removal of indium atoms by forming volatile products ($InCl_x$). Since the vapor pressure of $InCl_x$ is quite low at room temperature, the sample needs to be heated to achieve efficient removal of the etch products. Optimal samples are obtained for a temperature of about 200°C and for an etching time of 20min..
Fig. 3.5 shows a selection of scanning electron microscopy (SEM) micrographs of InP-based photonic-crystal test structures. The air holes are conical, with nearly vertical walls close to the surface and strongly tapered at the bottom, resulting in a carrot-like profile. Notice also that the bottom tails are bent with respect to the hole vertical axis. The mechanism responsible for this bending is not well understood yet. The etch depth is about 2.5μm for hole diameters larger than 220nm. However, for smaller diameters, the hole depth decreases with the hole diameter.

Having carrot-like hole shapes is equivalent, with good approximation, to having straight cylindrical holes with reduced etch depth [Ferrini, R., *et al.* (2002)], which results in increased out-of-plane losses. Thus, from the modelling point of view, the effect of conical hole shape is accounted for by simply increasing ϵ''. On the other hand, if losses are too large, several photonic-crystal functionalities are disrupted and the modelling itself becomes nonsense. That is why being able to fabricate high quality samples with low propagation losses is so important not only in view of

applications, but also at the characterization and modelling levels.

State of the art InP-based photonic crystals exhibit out-of-plane losses that can be modelled assuming $\epsilon'' \simeq 0.1$, which is already an acceptable loss level for characterization and modelling purposes. If one wants to have better performances, the fabrication process has to increase the etch depth while keeping the hole shape cylindrical. Once that the etch depth has reached a critical value, which depends on the waveguide and photonic-crystal geometry, the amount of out-of-plane losses becomes equal to the intrinsic loss level, corresponding to infinite etch depth [Benisty, H., *et al.* A (2002)], as highlighted in Sec. 2.5.3. However, one has always to deal with roughness-induced scattering losses, which are unavoidable in real samples. Nevertheless, also this kind of loss mechanism can be included in the two-dimensional approximation through the ϵ'' parameter.

Another efficient etching technique for InP-based photonic crystals is electron cyclotron resonance / reactive ion etching (ECR/RIE), which provides 3.5μm-deep holes with vertical sidewalls over 2μm at lattice constant $a \sim 380$nm. Recently, the application of induced coupled plasma (ICP) etching in the fabrication of InP-based photonic crystals has given very promising results as etch depth and hole shape are concerned. The method is still under optimization within the PCIC collaboration.

As to GaAs-based photonic crystals, literature has been plenty of results since the pioneering works of Krauss T. F., *et al.* (1996) (fabrication) and Labilloy, D., *et al.* A (1997) (characterization). For this reason, a detailed description of the fabrication process is not reported here. It is worth to mention, however, that the waveguide geometry designed in the PCIC project is similar to the InP system, with AlGaAs and GaAs in place of InP and GaInAsP, respectively, and with the quantum well layers replaced by quantum dots. Due to the different index profile of the GaAs waveguide with respect to InP, the effective dielectric constant of the fundamental TE mode is now $\epsilon_{\text{eff}} = 11.56$, instead of 10.5. Therefore, as far as two-dimensional modelling is concerned, moving from InP- to GaAs-based photonic crystals is resolved in changing the effective dielectric constant, and, as necessary, the loss parameter ϵ''. Moreover, since the index contrast between GaAs and AlGaAs is higher than that between GaInAsP and InP, the field is more confined and a smaller etch depth is enough for reaching intrinsic out-of-plane losses.

3.3.2 Validation of the Two-Dimensional Approximation

The validity of the two-dimensional approximation in modelling weak-confinement photonic-crystal slabs (effective dielectric constant plus *ad hoc* loss parameter) is tested here by comparison with the three-dimensional FDTD method, which is the extension of the FDTD method to the full three-dimensional space [Qiu, M. (2002); Kafesaki, M., *et al.* (2002)]. The test is performed on simple crystals, like bulk photonic crystals or one-dimensional cavities embedded in two-dimensional photonic crystals, as sketched in Fig. 3.6.

Fig. 3.7 shows the transmission spectrum along the $\Gamma - K$ direction for a 8-unit-cell-thick bulk

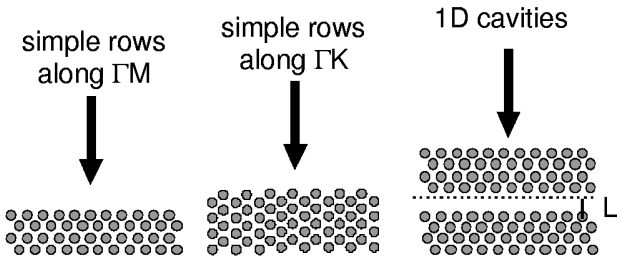

Figure 3.6 Examples of simple two-dimensional photonic crystals.

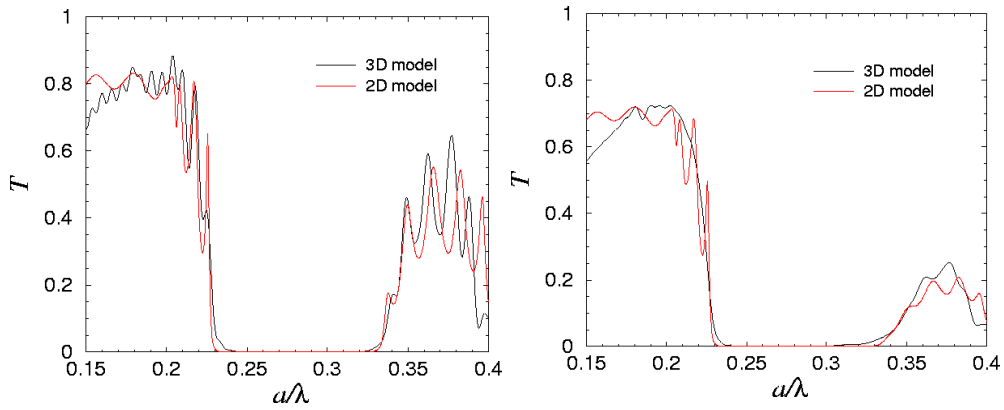

(a) Cylindrical (b) Conical

Figure 3.7 3D vs 2D FDTD simulations. Transmission along the $\Gamma - K$ direction for a 8-unit-cell long photonic crystal; H-polarization. Parameters of the 2D FDTD simulation: $\epsilon = 10.3$, $f = 38\%$ and $\epsilon'' = 0.05$ (0.12) for the cylindrical-hole (conical-hole) case; 3D FDTD simulation: $f = 35\%$, a=420nm, etch-depth=2.5μm and index profile taken from Fig. 3.4. 3D calculations courtesy of Kasesaki, M., IESL - FORTH, Crete, Greece.

photonic crystal, whose layout is displayed in Fig. 3.6, central image. The parameters of the two-dimensional FDTD calculation (red curve) are chosen to fit the three-dimensional FDTD result (black curve). Notice that the position and width of the photonic band gap are well reproduced by the two-dimensional approximation. Also, the interference patterns agree, specially above the air band edge. The discrepancies below the dielectric band edge have to be attributed to some numerical issues encountered in the three-dimensional method, which are not solved yet. The left panel of Fig. 3.7 is for the cylindrical-hole case, while the right panel is for the conical-hole case. By tuning the loss parameter ϵ'', the two-dimensional approximation accounts for the hole morphology: conical holes correspond to increased out-of-plane losses, which agrees with the findings of Benisty, H., *et al.* A (2002). It is noticeable that the conical shape enters the two-dimensional approximation by simply increasing the imaginary dielectric constant.

In order to fit the spectra, the effective dielectric constant has to be 10.3 instead of 10.5. The difference can be attributed to fact that the patterning changes the confinement properties of the planar waveguide. In other words, the field confinement is not independent of the photonic-crystal pattern; therefore, not necessarily the effective dielectric constant of the bare waveguide is the best choice for the two-dimensional approximation. One should homogenize each patterned layer within effective medium theory, then calculate the effective dielectric constant of the fundamental guided mode. Nevertheless, since 10.3 vs. 10.5 is a small correction, it is fine to assume 10.5 as background dielectric constant in two-dimensional simulations.

The fitting filling factor is 38% against a nominal value of 35%, used in the full calculation. The correction is easily explained by recalling that in weak-confinement photonic-crystals the gaps open for smaller filling factors than for the two-dimensional case, see Fig. 1.14. Since for small filling factors the gap increases with the hole radius, the two-dimensional model must increase the nominal filling factor of a few percent.

Overall, the fits of Fig. 3.7 are meant to demonstrate the validity of the two-dimensional approximation, rather than tuning the photonic-crystal parameters, effective dielectric constant, filling factor and imaginary dielectric constant. In the following sections, which are dedicated to the design of basic photonic-crystal functionalities, the parameters are fixed to $\epsilon_{\text{eff}} = 10.5$, $f = 35\%$ and $\epsilon'' = 0.1$, if not otherwise stated. Comparison with experimental data will further strengthen the

two-dimensional approximation.

3.4 W1 and W3 Straight Waveguides

Linear defects in photonic crystals represent the basic passive elements of a photonic integrated circuit. As already explained in Sec. 1.5, making linear defects in two-dimensional photonic crystals allows to guide light along a desired direction, which is, in fact, the analog of copper stripes in printed electrical circuits. Straight waveguides[1] in GaAs- and InP-based photonic crystals are created by simply transferring the desired design to the e-beam mask, used in the lithographic process. Among the all possible choices, a waveguide is obtained by removing a set of adjacent rows of air holes along the $\Gamma - K$ lattice direction, see for instance Fig. 3.8b. As already mentioned in Sec. 1.5, these systems are shortly called WN waveguides, where N stays for the number of removed rows. The choice of using WN waveguides instead of many other possibilities [Johnson, S. G., *et al.* (2000)], is motivated by the fact that this class of linear defects supports index-confined modes, where the field is mainly concentrated in the dielectric channel. These modes suffer smaller propagation losses than the Bloch modes of bulk photonic crystals, because the effect of the patterning is marginal. Since the modes of weak-index confinement photonic crystals have always intrinsic losses, the idea is to minimize propagation losses by using the photonic band gap only where it is strictly necessary, as to form bends or cavities, while straight propagation is guaranteed by conventional index guiding. It is convenient to work with the fundamental guided mode[2], because is the one exhibiting the highest field confinement into the dielectric channel.

Given WN as the basic waveguide design, what is the best choice for the number of rows to remove? A narrow waveguide is likely to be single-mode, but, at the same time, it possesses higher propagation losses with respect to a larger waveguide, which, on the contrary, is likely to be multi-mode. This is because field confinement is more effective in "large" waveguides. The advantage of using single-mode waveguides will be apparent when dealing with transmission through sharp bends. One has to find the right trade-off between the above aspects, also keeping in mind possible

[1] The term waveguide is used either to refer the planar waveguide (heterostructure), either the linear defect created inside the two-dimensional photonic-crystal pattern.

[2] Actually, it would be more correct to say quasi-guided, because of the intrinsic out-of-plane losses. For guided mode is intended the confined state due to the linear defect.

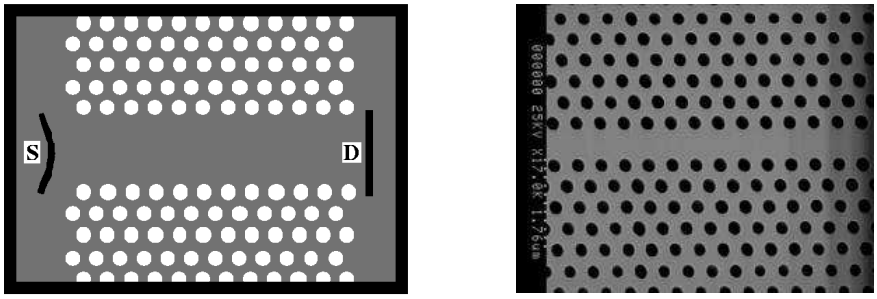

(a) (b)

Figure 3.8 (a) FDTD simulation of a W3 photonic crystal waveguide. The source (S) has a Gaussian profile perpendicular to the waveguide axis. The detector (D) covers the exit of the waveguide. The edges of the computational mesh are terminated with Liao absorbing boundary conditions (black). (b) SEM micrograph of a W1 waveguide; courtesy of Talneau, A., LPN - CNRS, France.

issues as regards performing experiments on these systems.

The W1 waveguide (one row removed) represents the single-mode waveguide, while the W3 waveguide (three holes removed) represent the multi-mode waveguide. Larger waveguides are not considered in detail because they support many modes and the analysis would be too much complicated. The W1 waveguide has already been introduced in Sec. 1.5. Here, the study is completed by calculating and examining the transmission properties, with particular attention to the mini-stop band frequencies. Concerning the W3 waveguide, both dispersion relation and transmission spectrum will be presented.

As far as simulations are concerned, all these structures are modelled within the two-dimensional approximation, using the effective dielectric constant and the loss parameter. In Sec. 3.2.2, the two-dimensional FDTD method has been presented in detail for the case of bulk photonic crystals. For calculating the transmission properties of WN waveguides, a few changes are necessary regarding the FDTD source and the boundary conditions. First of all, since the system is not anymore periodic in the direction perpendicular to propagation, Bloch's boundary conditions are not applicable, but Liao's must be used instead. Since the fundamental mode is the one of interest, the FDTD source

has to optimize the coupling between the incident field and the guided mode, which is not the case for a plane-wave source. Fig. 3.8a sketches the setup for a FDTD simulation of a W3 waveguide. The thick black lines along the perimeter represent the stencils for Liao's boundary conditions. The source (S) is centered with the waveguide and the dipoles are disposed with amplitudes that form a Gaussian profile

$$H_z|^{n}_{i_\circ,j}{}^{(s)} = H_\circ e^{-\frac{1}{2\varsigma^2}(j\Delta y - y_\circ)^2} \cos(\omega_\circ n\Delta t) e^{-\frac{\sigma^2}{2}(n\Delta t - t_\circ)^2}, \qquad \text{with } j = 1, \ldots, N, \tag{3.16}$$

where $y_\circ$ is the y coordinate of the waveguide axis. The width of the source, ς, can be adjusted according to the waveguide: W1 or W3, etc.... The parity of the source selects only guided modes that are spatially even with respect to the waveguide axis. Moreover, the Gaussian profile primarily couples to the fundamental waveguide mode. A detector (D) is positioned at the right end of the waveguide. Also in this case, the width of the detector depends on the waveguide. Notice that a point detector could not be used, because for multi-mode waveguides it would give incorrect transmission results.

3.4.1 The W1 Waveguide

The dispersion relation of a W1 waveguide is reported in Sec. 1.5.2, Fig. 1.16, to discuss an example of WN linear defects in two-dimensional photonic crystals. The system is characterized by a background dielectric constant equal to 11.56, corresponding to the effective dielectric constant of GaAs-based photonic-crystal slabs. The filling factor is 60%, which is larger than the usual values chosen for real samples. In fact, for small filling ratios, the W1 waveguide does not exhibit mini-stop bands in the dispersion relation, being single-mode for almost every frequency in the band gap [Agio, M., *et al.* (2001)]. The choice of $f = 60\%$ is dictated by the intention of studying a guided-mode spectrum with mini-stop bands and higher order modes within the band gap frequencies, which is physically more interesting from a theoretical point of view and is also a completion of the discussion started with Sec. 1.5. For this case only, out-of-plane losses are not included, i.e. $\epsilon'' = 0$. Fig. 3.9 groups the transmission spectra for both bulk two-dimensional photonic crystal and W1 waveguides of different length. The curves are calculated for H-modes that are even with respect to the waveguide axis, by choosing the appropriate FDTD source: Eq. (3.11) for the bulk structure

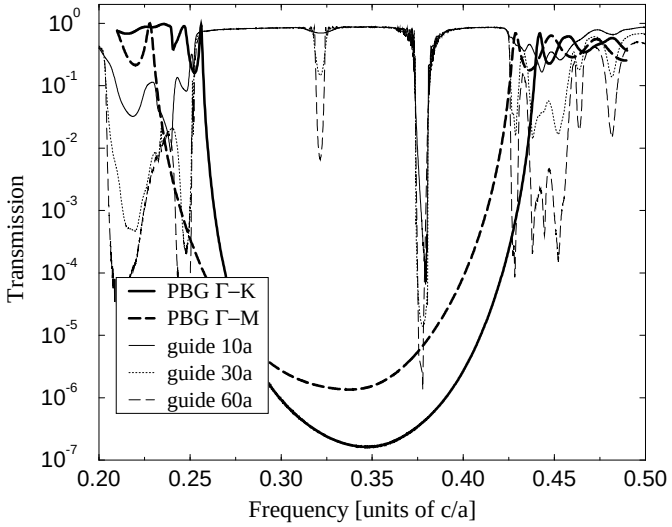

Figure 3.9 Transmission spectra for various lengths of the W1 waveguide described in section 1.5.2: H-polarization, $\epsilon = 11.56$, and $f = 60\%$ (as in Fig. 1.16). The bold solid (dotted) line delimits the $\Gamma - K$ ($\Gamma - M$) H-modes band gap of the bulk photonic crystal. The solid, dotted, and dashed lines correspond to the transmission along the waveguide with length $10a$, $30a$, and $60a$, respectively.

and Eq. (3.16) for the W1 waveguide. The corresponding guided-mode dispersion relation is shown in Fig. 1.16. Inside the photonic band gap, the transmission coefficient of the waveguide is above 80%[3], for almost all frequencies, except for $a/\lambda = \omega a/2\pi c = 0.321$ and $a/\lambda = 0.377$, which correspond to two mini-stop band energies, namely the gap at the edge of the reduced Brillouin zone and the anti-crossing with the higher-order mode, respectively. Notice also that, as the length of the waveguide increases, both drops at the mini-stop bands get larger. On the other hand, for frequencies matching the fundamental guided mode, transmission is independent of the waveguide length.

To better understand the mini-stop bands, the intensity of the electric field $|\mathbf{E}|^2$ for $a/\lambda = 0.321$ and $a/\lambda = 0.377$ is plotted in Fig. 3.10a and Fig. 3.10b, respectively. In Fig. 3.10a, the profile extends all over the waveguide, similar to the pattern of the fundamental guided mode. However,

[3]Because the coupling efficiency of the incident and outgoing waves with the guided mode, the maximum transmission could result less than one. The fact that transmission is independent of the waveguide length confirms that there are no intrinsic losses for $\epsilon'' = 0$ and that reflection occurs at the waveguide interfaces.

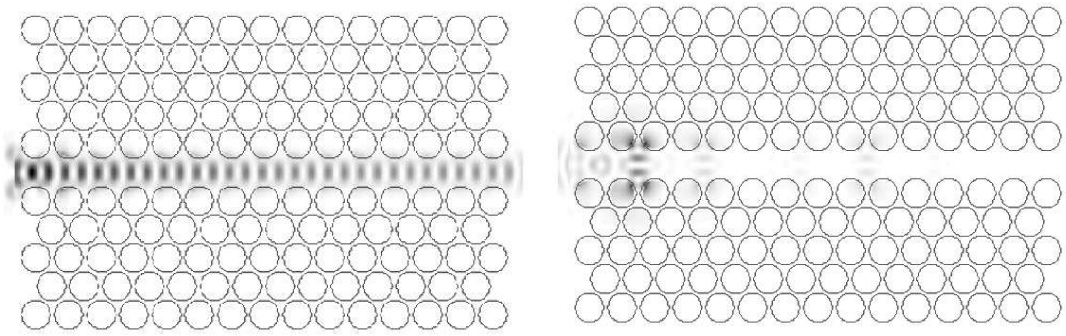

(a) $a/\lambda = 0.321$ (b) $a/\lambda = 0.377$

Figure 3.10 Normalized intensity of the electric field for the frequencies corresponding to the low-frequency mini-stop band (a) and high-frequency mini-stop band (b) of Fig. 3.9.

it slowly decays as the field propagates through the waveguide. Indeed, it corresponds to the gap in the folded fundamental mode for Bloch vector $\mathbf{k} = 0$. The profile shown in Fig. 3.10b is completely different than that of Fig. 3.10a. Due to the anti-crossing between the fundamental mode and the higher-order mode, the field pattern results from a mixing of the two modes. Notice that the field decay is much stronger than for the case of Fig. 3.10a, as it is also apparent in the transmission spectra of Fig. 3.9.

As a last remark, it is worth to briefly discuss the dependence of the mode dispersion with the filling ratio. Since the fundamental mode is almost concentrated in the dielectric channel, its dispersion relation feels the filling factor f mainly through the width of the waveguide ($\mathbf{w} = a(\sqrt{3} - \sqrt{2\sqrt{3}f/\pi})$. On the other hand, the higher-order mode is more extended in the photonic-crystal region and its dispersion relation will be more sensitive to the filling ratio. Indeed, the fundamental mode is guided by the high-refractive-index channel, as for dielectric waveguides, and the the photonic band gap is not important. On the contrary, the higher-order mode does exist because of the photonic band gap. The fact that the filling ratio is not easily controlled by the fabrication process further motivates the choice of working with the fundamental mode of WN waveguides, which exhibits a good dispersion tolerance over Δf. The same is also true as to tolerance with respect to possible local disorder in the hole morphology.

3.4.2 The W3 Waveguide

The W3 waveguide is created by removing three adjacent rows of air holes along $\Gamma - K$, see Fig. 3.8a. The dispersion relation and the transmission spectrum for H-modes, with spatially even parity with respect to the waveguide axis, are reported in Fig. 3.11. The structure parameters correspond to InP-based photonic crystals: $\epsilon = 10.5$, $f = 35\%$ and $\epsilon'' = 0.1$, for the transmission calculation only. The width of the band gap is smaller than for the W1 case, where the filling ratio was chosen to be $f = 60\%$. The waveguide supports both index-guided and band-gap guided modes. The fundamental mode, which is index-guided, anti-crosses with a higher-order mode at $a/\lambda \simeq 0.26$. The latter is characterized by a flat dispersion, typical of band-gap guided modes. Another higher-order mode exists, which also anti-crosses with the flat-dispersion guided mode at $a/\lambda \simeq 0.275$. By considering only H-modes with even parity with respect to the waveguide axis, the waveguide is never single-mode, except a narrow frequency window around $a/\lambda \sim 0.22$.
As to the transmission spectrum, notice that there is a dip in correspondence of the mini-stop band between the fundamental and the flat-dispersion guided modes. The other mini-stop band, located at $a/\lambda = 0.275$, is not seen, because the FDTD source is tuned to excite the fundamental guide mode. In fact, this is also a proof that the FDTD simulation samples the dispersion relation of the fundamental mode. The transmission reaches 90% despite the presence of out-of-plane losses. First of all, the coupling between the incident field and the fundamental guided mode is better than for the W1 waveguide. Secondly, since the fundamental mode is well confined in the dielectric channel, the effect of ϵ'' is small.

By using the same loss parameter ϵ'' and the same filling factor for computing the transmission spectra of W1 and W3 waveguides, it is clear that losses are higher in the narrower waveguide, because the ratio between the field energy in the air holes and in the dielectric channel is inversely proportional to the width of the waveguide and only the field energy in the air holes suffers propagation losses. Moreover, it is easier to couple light into W3 waveguides, than in W1, again because of the width of the dielectric channel.
These considerations advantage the W3 against the W1 waveguide as regards application in photonic-

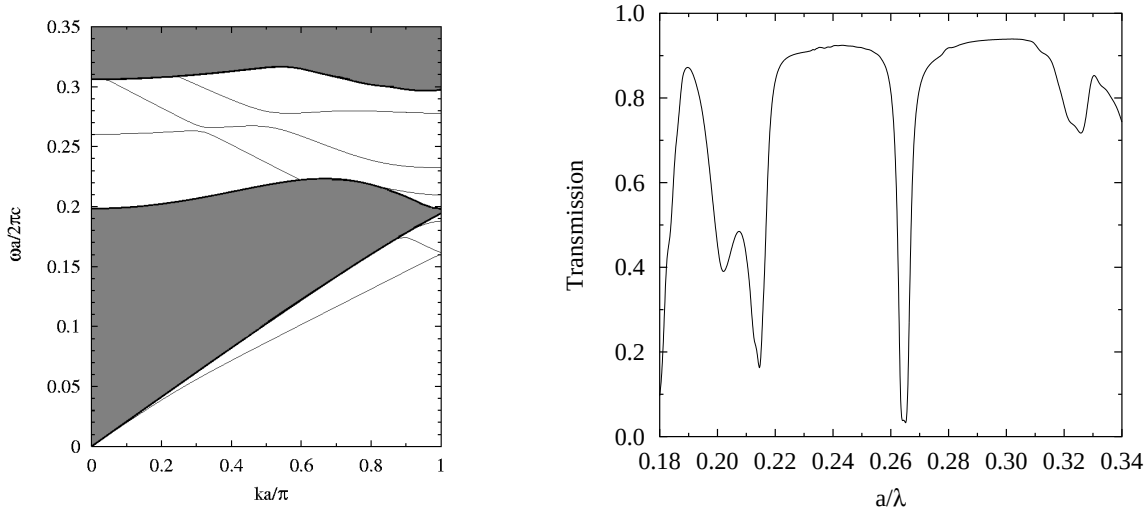

(a) (b)

Figure 3.11 (a) Dispersion relation for a W3 waveguide, with $\epsilon = 10.5$, and $f = 35\%$. The solid lines refer to H-modes that are spatially even with respect to the waveguide axis; the odd modes are not shown. The gray areas are the projected H-modes of the bulk photonic crystal. (b) H-polarized transmission for the same W3 waveguide of length $40a$ and loss parameter $\epsilon'' = 0.1$.

crystal circuits. However, the W3 waveguide is multi-mode, while the W1 is single-mode. Such difference is not much important as long as modal mixing is negligible, like the roughness-induced mixing in straight waveguides. But, when a sharp bend connects two waveguide sections, coupling among the guided modes might not be small and single-mode wave-guiding ceases to exist. Without single-mode wave-guiding, cascading of building blocks is not possible any more. Such issue might preclude the realization of integrated photonic circuitry. In this situation, the solution could be using the W1 waveguide, despite being more lossy than the W3. However, the trade-off might not work if the amount of losses is too large. Scope of the next section is to present all these facts related to the bending of light in W1 and W3 waveguides. By accurate bend design, single-mode guiding is found to be possible also in multi-mode channels.

3.5 Bends in W1 and W3 Waveguides

Designing WN waveguides with sharp bends is easily accomplished by connecting two straight waveguide sections created along different, but equivalent, lattice directions, as displayed in Fig. 3.12. In this sense, the triangular lattice is suitable for making $\pm 60^\circ$ and $\pm 120^\circ$ sharp bends by exploiting the six-fold equivalent $\Gamma - K$ lattice direction [Lončar, M., *et al.* B (2000); Tokushima, M., *et al.* (2000); Chutinan, A., *et al.* (2000); Benisty, H., *et al.* B (2002)]. Notice that it is also possible to make 90° sharp bends by connecting a WN waveguide with another waveguide created along the $\Gamma - M$ direction. However, it is better that the straight sections have always the same wave-guiding properties, if not explicitly necessary. That is why 90° bends are usually avoided in triangular-lattice photonic crystals. Instead, 90° bends are more suitable for square-lattice photonic crystals [Mekis, A., *et al.* (1996); Lin, S.-Y., *et al.* B (1998)].

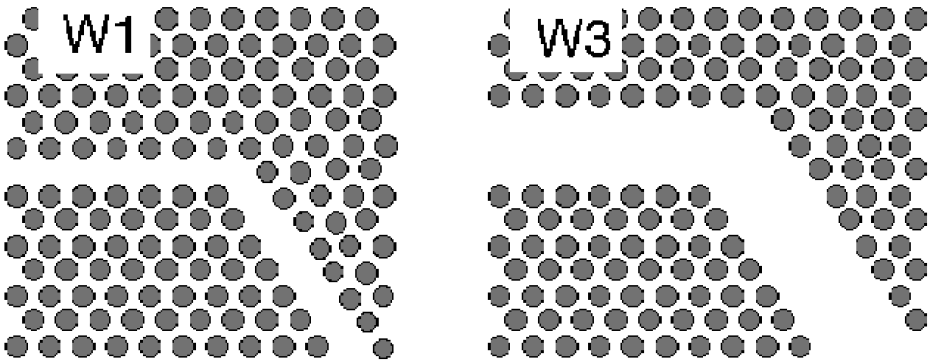

Figure 3.12 Sharp bends in W1 and W3 waveguides.

When a sharp bend is created in a dielectric waveguide, part of the power is lost, because the condition of total internal reflection is not fulfilled at the bend [Espinola, R. L., *et al.* (2001)]. Contrary to dielectric waveguides, the index-guided mode of the WN waveguide does not leak at the bend, thanks to the photonic band gap, which makes the system ideally loss-less. After the bend, the fundamental mode continues to travel under the index-guiding mechanism. The picture index-guiding $\Rightarrow$ band-gap $\Rightarrow$ index-guiding can be explained by considering the bend as a low Q-factor resonant cavity [Mekis, A., *et al.* (1996, 1998)]. The waveguide sections carry the power to the resonant cavity using the index-guided fundamental mode. When a cavity mode is excited, the power flows only along the waveguide sections, because the band gap prevents light

from escaping in other directions. If resonance occurs between the guided mode and the cavity mode, the transmission is expected to be maximum.

Actually, the picture is not so simple if other aspects are considered, like the multi-/single-mode nature of the waveguide and of the resonant cavity or out-of-plane diffraction losses, which can be larger for the resonant cavity. For example, the fundamental guided mode can enter the resonant cavity and exits as a superposition of guided modes (fundamental + higher-order modes). Modal mixing has two consequences: first of all, it prevents the cascading of building blocks, because it modifies the initial conditions (the outgoing field becomes the incident field of the next block), which transmission depends on. Secondly, the power travelling on higher-order modes is rapidly lost, because these modes exhibit more losses than the fundamental guided mode. As to out-of-plane losses, the loss parameter ϵ'' acts on the field while it oscillates in the resonant cavity, upon bouncing against the photonic-crystal walls. The more the field is trapped inside the cavity, the higher are losses. The mechanism qualitatively accounts for losses at the bend. For a more quantitative formulation, three-dimensional models might be required. There are studies performed on double bends in air-bridge systems showing that the two-dimensional FDTD method is in good agreement with three-dimensional FDTD results, even without the loss parameter [Chutinan, A., *et al.* (2000)].

Since the bend breaks the translational symmetry and also the mirror symmetry with respect to the waveguide axis, all the guided modes with defined polarization (H-modes or E-modes) are coupled to each other. Therefore, for studying the bend-induced modal mixing, one has to calculate the dispersion relation irrespective of the parity with respect to the waveguide axis. Concerning wave propagation, the FDTD simulation excites the fundamental guided mode and detects the outgoing field, without any information on the modal mixing that occurred at the bend. Nevertheless, some information can be obtained by looking at the field pattern for selected frequencies, in general those corresponding to maximum transmission. The FDTD detector is always placed perpendicular to the waveguide axis and the photonic crystal is cut along $\Gamma - M$, so that the waveguide is interfaced with the external medium like for the straight-waveguide case. This flexibility is typical of the FDTD method and it explains why it is so extensively used for research in photonic crystals.

3.5.1 The W1 Waveguide

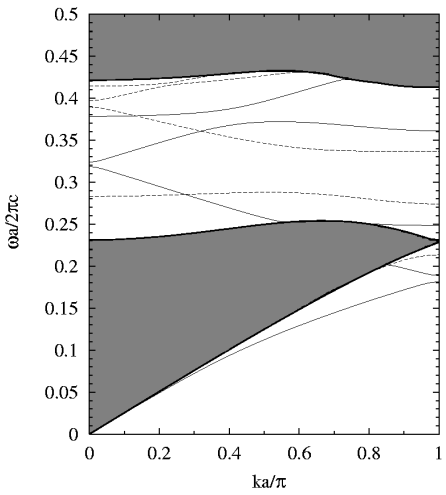

(a)

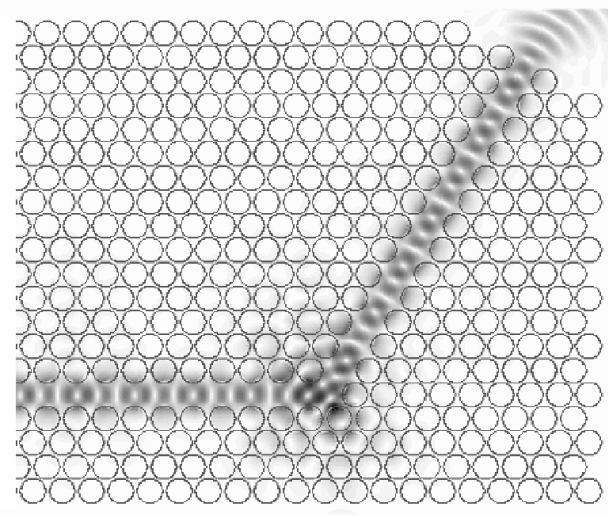

(b)

Figure 3.13 (a) The same dispersion relation of Fig. 1.16. Solid (dotted) lines refer to H-modes that are spatially even (odd) with respect to the waveguide axis. (b) Normalized intensity of the electric field at $a/\lambda = 0.2607$ for a sharp bend in a W1 waveguide. Structure parameters as in Fig. 1.16.

The W1 waveguide presented in the previous sections is characterized by a wide frequency range where the waveguide is single-mode. However, the dispersion relation was calculated only for H-modes with spatially even parity with respect to the waveguide axis. The dispersion relation with all H-modes, even and odd, is shown in Fig. 3.13a. Modes with opposite parity cross, while modes with the same parity anti-cross. Notice that the system supports also odd modes within the band gap frequencies, reducing or cancelling some single-mode regions found for even modes only. In practice, the waveguide is really single-mode in three regions: the first one is located around $a/\lambda \sim 0.26$, between the bulk bands and the first odd mode; the second one, which is also the largest one, occurs for a/λ between $\simeq 0.29$ and $\simeq 0.33$, corresponding to the anti-crossing between the first and second odd mode; the third one is around $a/\lambda \simeq 0.395$ and it is due to the mini-stop band of the odd mode at $\mathbf{k} = 0$. Every single-mode region is characterized by the presence of the sole fundamental guided mode. For achieving single-mode resonant transmission through a sharp

bend, one has to focus on the single-mode frequency regions of the waveguide.

Fig. 3.13b displays the modulus of the electric field $|\mathbf{E}(\mathbf{x})|$ for $a/\lambda = 0.2607$, which belongs to the first single-mode frequency region. In this case, out-of-plane losses are not considered. The field pattern is helpful in understanding the bending mechanism. The fundamental guided mode impinges the bend, where it couples to a resonance, clearly represented by darker tones of gray. Then, the resonance excites the fundamental guided mode in the second waveguide section. The transmission is close to one, as it can be also deduced from the levels of gray in the field plot.

3.5.2 The W3 Waveguide

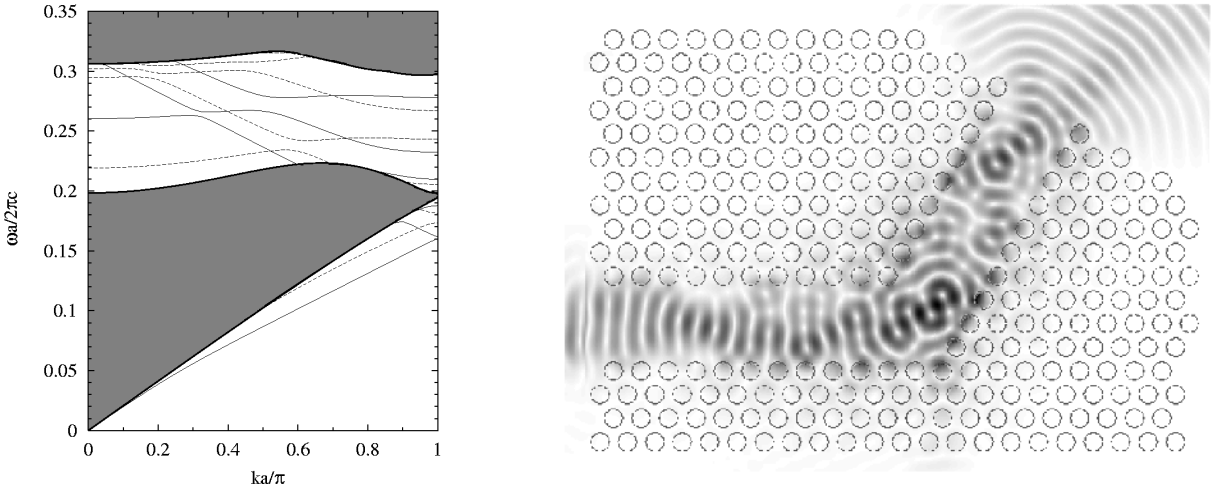

(a) (b)

Figure 3.14 (a) The same dispersion relation of Fig. 3.11a. Solid (dotted) lines refer to H-modes that are spatially even (odd) with respect to the waveguide axis. (b) Normalized intensity of the electric field at $a/\lambda = 0.2297$ for a sharp bend in a W3 waveguide. Structure parameters as in Fig. 3.11. Note: in this case $\epsilon = 11.56$ instead of 10.5.

Likewise for the W1 waveguide, the discussion starts from the dispersion relation for H-modes, represented in Fig. 3.14a. The structure parameters are reported in the figure caption. Since the waveguide is larger than the W1, an index-guided odd mode can exist, in addition to the fundamental guided mode, which is spatially even. The two first index-guided H-modes are easily

recognizable because they appear also outside the band gap; for example, below the bulk bands. Inside the band gap, the two modes run almost parallel to each others and anti-cross with the higher-order modes of the same parity, and cross with those having opposite parity. Inside the band gap, the waveguide is multi-mode everywhere; therefore, since it is likely that the bend will mix the incident fundamental mode with the other ones, single-mode transmission is not expected. To give an idea of the modal mixing occurring at the bend, look at the electric field pattern of Fig. 3.14b. The incident field excites a resonance at the bend, but, this time, the power is redistributed among more guided modes. That is why the field profile shows irregularities, with nodes in the direction perpendicular to the waveguide axis. Notice also that part of the power is reflected and interferes with the incident guided mode. The same happens for every frequency chosen within the band gap. It is clear that this situation is not suitable for cascading other elements, because the bend disrupts single-mode transmission. On the other hand, the bend is a required building block for designing photonic integrated circuits.

In summary, the W1 waveguide allows single-mode transmission through sharp bends, whereas the W3 waveguide, being multi-mode in the whole band-gap region, exhibits modal mixing at each bend insertion. On the contrary, the W1 waveguide is more sensitive to out-of-plane losses than the W3; losses that are unavoidable in weak-confinement photonic-crystal slabs. That is why a large part of the research community has chosen to work with single-mode W1 waveguides created in high-index-contrast photonic-crystal slabs, where the fundamental mode is truly guided below the light line [Baba, T., *et al.* (1999, 2001); Chutinan, A., *et al.* (2000); Lončar, M., *et al.* A (2000); Chow, E., *et al.* (2001), and the feature issue *IEEE J. Quantum Electronics, 38* (7)]. However, the light line restricts the guided-modes region to a narrow interval where the dispersion is rather flat, like for "heavy" photons. This results in a narrow transmission bandwidth and a small group velocity. Furthermore, as soon as the translational symmetry is broken, by inserting bends or resonant cavities, large out-of-plane losses are likely to occur.

By considering all these facts and also the associated fabrication technology, the choice is to embark on a novel proposal: release the single-mode condition over the channel waveguide and choose to work with W3 waveguides created in weak-confinement photonic-crystal slabs, having a moderate

filling factor ($\simeq 35\%$) to minimize out-of-plane losses, and invest on designing efficient sharp bends towards high single-mode transmission. Indeed, modal mixing occurs at the bend, not along the waveguide; in other words, if the bend is designed so that coupling between the fundamental mode and higher-order modes is negligible, single-mode transmission will be achieved.

3.6 Modelling of Bends in W3 Waveguides

Essentially, the modelling of bends in multi-mode waveguides has to tackle the following issues: modal mixing, reflection and out-of-plane losses. The final objective is to achieve single-mode transmission with both minimum reflection and out-of-plane losses. Even if the photonic-crystal parameters and the waveguide width are fixed, there are still too many degrees of freedom in the choice of the proper design. Moreover, since the FDTD method does not provide information on the modal composition of the guided field, it is also difficult to know what are the mode-coupling coefficients associated to a certain bend design. On the other hand, the cut and try design might be long and unfruitful. The choice is to split the problem into specific parts, which allow to decompose the objective into three milestones. The first part (milestone) will deal with increasing the transmission level in the presence of out-of-plane losses, included through ϵ''; modal mixing is not considered at this stage. The second part (milestone) aims to find the conditions for single-mode transmission, irrespective of the transmission level and bandwidth. The final part (milestone) gathers all these information to form the final proposal.

The first milestone is pursued by bend smoothing (Sec. 3.6.1) and adding air slits at the bend

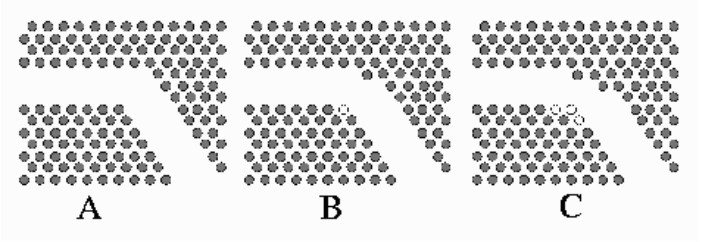

Figure 3.15 Smoothing a bend moving holes at the corner.

corners (Sec. 3.6.4). The second milestone is tackled starting from an extension of the FDTD method, which allows to evaluate the modal mixing of a bend (Sec. 3.6.2). By exploiting the idea

of adiabatic tapering, an implementation of single-mode bend is proposed (Sec. 3.6.3). Finally, tapering, smoothing and slits are put together in a single bend design (Sec. 3.6.4).

3.6.1 Moving holes

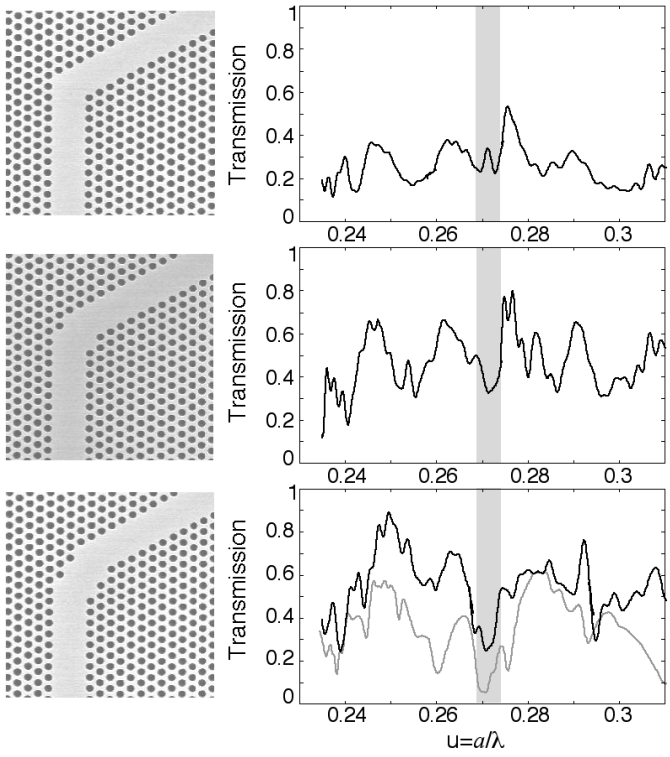

Figure 3.16 Experimental spectra (black curves) and calculated spectra (gray curves) for a corresponding set of bend designs (left panels). From top to bottom: sharp bend, one-hole-moved, three-holes-moved. The gray areas refer to the mini-stop band region. The simulations were performed choosing $\epsilon = 10.5$, $f = 35\%$, and $\epsilon'' = 0.1$. The calculated spectra were slightly stretched to fit the experiments, yielding an effective dielectric function $\epsilon = 10.4$ instead of 10.5. The experimental data are courtesy of Moosburger, J., University of Würzburg, Germany and Olivier, S., EPP, France.

The first attempt to improve the transmission through a bend transition is to introduce a short section at 30°, i.e. along the $\Gamma - M$ direction, by displacing holes from the internal to the external corner, as shown in Fig. 3.15. This is also the idea proposed by Mekis, A., *et al.* (1996) for a 90° bend in a square lattice of dielectric pillars in air. In a very simple picture, the hope is that

the tilted section act like a mirror for the incoming wave, increasing the transmission and reducing the coupling to higher-order modes. In another picture, moving holes can be seen as a way to smooth the bend with increasing length of the $\Gamma - M$ section. The rule for bend smoothing reads $p = n(n+1)/2$, where p is the number of holes moved from the inner to the outer corner and n runs over 0,1,.... For $n = 0$, the design returns to be the sharp bend. The most interesting

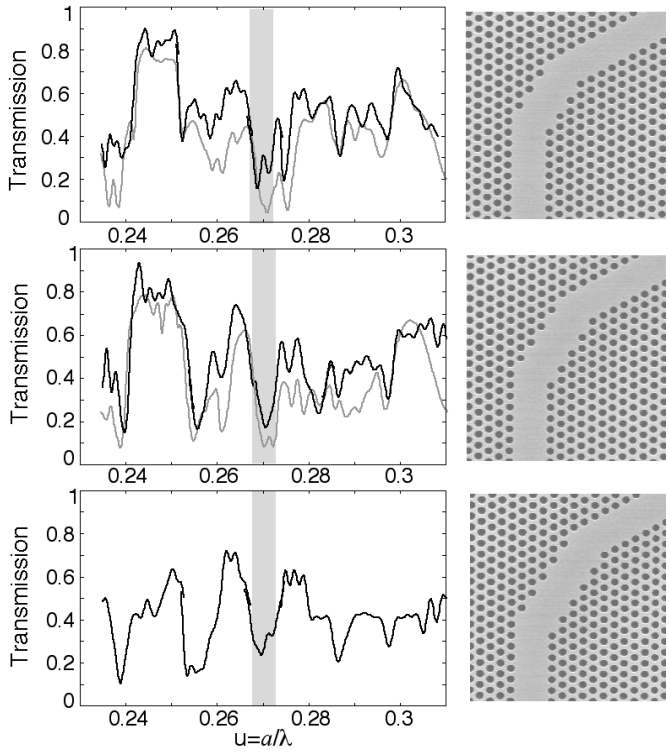

Figure 3.17 Experimental spectra (black curves) and calculated spectra (gray curves) for a corresponding set of bend designs (right panels). From top to bottom: six-holes-moved, ten-holes-moved, fifteen-holes-moved. The gray areas refer to the mini-stop band region. The simulations were performed choosing $\epsilon = 10.5$, $f = 35\%$, and $\epsilon'' = 0.1$. The calculated spectra were slightly stretched to fit the experiments, yielding an effective dielectric function $\epsilon = 10.4$ instead of 10.5. The experimental data are courtesy of Moosburger, J., University of Würzburg, Germany and Olivier, S., EPP, France.

cases are for small p, because, for large p, the $\Gamma - M$ section becomes effectively another waveguide between two bends, rather than a single bend. Figs. 3.16 and 3.17 report the transmission spectra for smoothed bends with $p = 0$ up to $p = 15$. The gray lines represent the calculated spectra, while

the black lines are experimental data obtained within the PCIC collaboration. Notice the good agreement between modelling and experiment, also with respect to fine spectral features. Actually, the calculated spectra have been slightly stretched to better fit the experimental curves. This implies that the optimal modelling parameters are a smaller effective dielectric constant ($\epsilon_{\text{eff}} = 10.4$) and a larger filling factor ($f \sim 40\%$), which conforms with the findings of Sec. 3.7. Despite these small corrections, the experimental data are another proof, besides the comparison with three-dimensional FDTD results, that the two-dimensional approximation is a valid tool for studying wave propagation in weak-confinement photonic crystals.

The corresponding bend design is placed aside of each transmission spectrum. The gray region, around $a/\lambda = 0.27$, refers to the mini-stop band in the fundamental mode. Since the straight waveguide cannot carry power for frequencies within the mini-stop band, it is usual to exclude this region when comparing the transmission levels of different bend designs. It is apparent that the overall transmission increases up to $p = 6, 10$ and decreases for a larger number of displaced holes. In fact, already for $p = 15$, the smoothed bend appears more like two bends connected by a short $\Gamma - M$ waveguide, which involves the transmission properties of the $\Gamma - M$ section itself. For $\epsilon'' = 0.1$ the maximum transmission reaches 80%, which is slightly less than the experimental levels. An explanation for that could derive from an overestimation of out-of-plane losses or from reflection at the interfaces between the waveguide sections and the background medium.

The method of bend smoothing seems to be quite successful as far as overall transmission is concerned. For a more complete analysis, one can refer to the works of Moosburger, J., *et al.* (2001), Talneau, A., *et al.* A (2002) and Benisty, H., *et al.* B (2002). The latter contains a systematic study of bend models based on the idea of smoothing by displacing holes.

For a deeper insight, it would be necessary to look at the various field patterns for several bend designs and frequencies, since the FDTD method does not provide information on the modal mixing occurring at the bend transition. Based on the field profiles seen for the frequencies where the transmission is maximum, none of the above bend designs attained single-mode transmission. Indeed, the field patterns are very similar to the one reported in Fig. 3.14b. For such reason, further design is necessary in view of pursuing the second milestone: conditions for single-mode transmission. To this purpose, it is important to rule out how a bend scrambles the fundamental

guided mode.

3.6.2 The Modal Transmission

The FDTD method is not a modal numerical method, therefore it is difficult to get information on the modal features of the calculated transmission. On the other side, it is as well difficult calculating the transmission of a single bend with modal expansion methods. In the FDTD method, the transmission is calculated detecting the outgoing power along a line perpendicular to the waveguide axis. The power is averaged along that line and divided by the incident power. No modal information is preserved when the power is averaged. In order to retain full information on the modal composition of the outgoing power, one should project the detected fields on the guided modes of the straight waveguides, which implies the knowledge of the profile of all guided modes for all frequencies. This procedure is time consuming and not easy to implement. However, one can avoid to calculate the modal transmission for all modes as long as the main interest concerns the transmission into the fundamental mode. Assume that the incident power is mainly in the fundamental guided mode, that is true for frequencies not in the mini-stop band region. The bend couples the fundamental guided mode to the other modes of the waveguide. After the bend, each mode propagates independently along the straight channel. At the exit one can thus know which modes were excited by the bend. It is important to know how much power is preserved into the fundamental mode and consider the others as lost. For this piece of information it is not necessary to calculate the profile of every mode. The outgoing fields are projected onto their even/odd components with respect to the waveguide axis and the even/odd Poynting vectors are subsequently calculated. In practice, the FDTD source and detector are swapped with respect to each others: the source is place in front of the tilted section and the detector is in front of the waveguide section whose axis is aligned with the x direction. The trick facilitates the decomposition into even and odd fields. Even/odd transmission is the first step to estimate the modal mixing.

The second step is to extract the power of the fundamental guided mode from the even transmission. This part is not yet optimized. At the moment it is only possible to show contour plots of the Poynting vector where the $x - y$ plane represents the frequency and the distance from the waveguide axis. The profile of the Poynting vector provides to some extent details on the modal

composition of the even transmission: a Gaussian profile suggests high transmission into the fundamental guided mode. The projection onto the fundamental guided mode is feasible and will be done in the near future. In summary, with the even/odd decomposition the conversion of the fundamental mode into even and odd modes is calculated. The spectra are normalized with respect to the incident power. Secondly, with the contour plots, one roughly knows how much power goes into the fundamental mode. Here, the Poynting vector, corresponding to spatially even modes, is weighted with a gaussian function $\exp(-(\omega-\omega_\circ)^2/\sigma^2)$, to account for the spectral profile of the incident pulse, and it is normalized to unity.

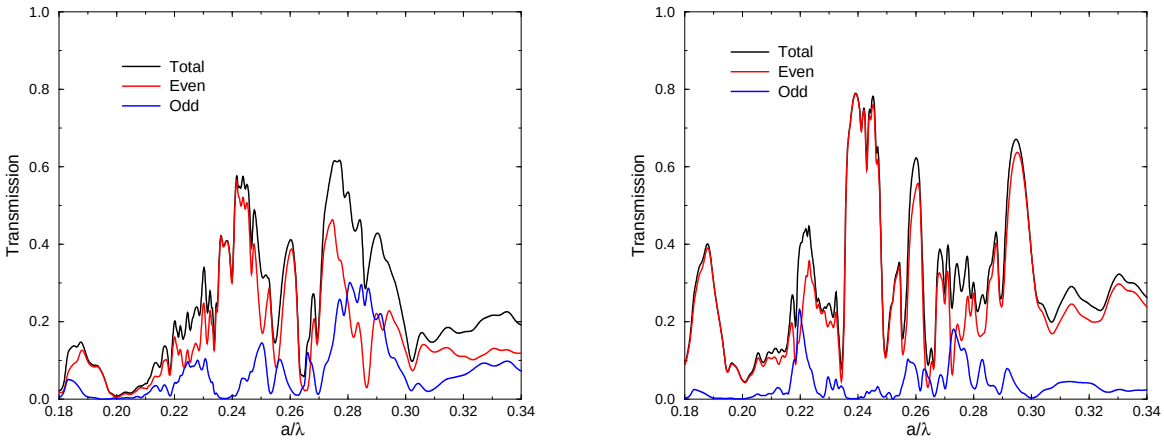

(a) $p = 3$ (b) $p = 10$

Figure 3.18 Modal transmission for a three-holes-moved bend (a) and a ten-holes-moved bend (b). The black line refer to the total transmission. The red (blue) line corresponds to the transmission into spatially even (odd) modes with respect to the waveguide axis. Parameters: $\epsilon = 10.5$, $f = 35\%$, and $\epsilon'' = 0.1$.

Following the above directions, the transmission into even and odd modes has been calculated for the bend designs discussed in the previous section. Two representative cases are shown in Fig. 3.18, where the total transmission (black curves) is also shown[4]. First of all, there are transmission peaks where the contribution of odd modes is important, specially for the case of $p = 3$. These peaks, which are apparently suitable for wave propagation if one looks only at the total transmission,

[4]The spectra are slightly different form those of Figs. 3.16 and 3.17, because they have not been stretched.

must be excluded, because a relevant portion of the power is "lost" into odd modes. In general, the bends with larger p exhibit less coupling with odd modes, as confirmed by a comparison between Fig. 3.18a and Fig. 3.18b. Moreover, for any design, it turns out that the odd transmission is zero for a narrow frequency window close to $a/\lambda = 0.24$. This is not because the bend does not couple the fundamental to the odd modes, but because the W3 waveguide has a mini-stop band in the first odd mode, as displayed in Fig. 3.14a. Therefore, the propagating field cannot have a component into odd modes and transmission may occur into even modes only. The fact that the even transmission is maximum close to this mini-stop band has to be attributed to resonant scattering, rather to the above cited mini-stop band.

Given that the best even transmission is obtained for $a/\lambda \simeq 0.24$, for knowing how much power remains to the fundamental mode, one has to analyze the distribution of the Poynting vector along the linear detector. Fig. 3.19a and Fig. 3.19b show contour and surface plots of the Poynting-

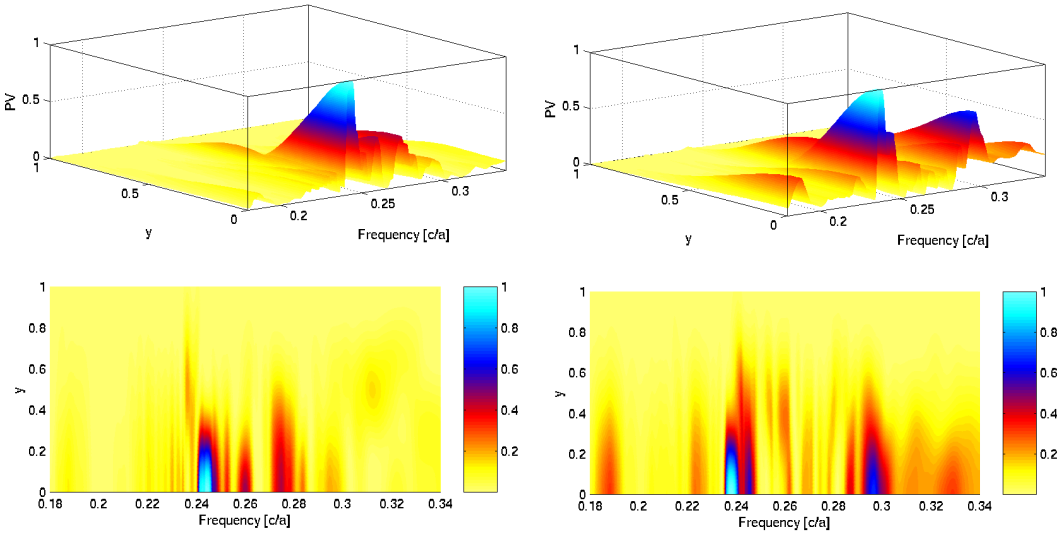

(a) $p = 3$ (b) $p = 10$

Figure 3.19 Poynting vector as a function of frequency and distance from the waveguide axis for the transmission into spatially even modes. y=1 corresponds to $y = 3\sqrt{3}/2a$. (a) three-holes-moved bend; (b) ten-holes-moved bend. Parameters as in Fig. 3.18.

vector profile for the bend designs corresponding to $p = 3$ and $p = 10$, respectively. The x axis refers

to frequency, whereas the y axis represents the distance from the waveguide axis. Both designs are characterized by a main transmission contribution of the fundamental mode for $a/\lambda \sim 0.24$, where the higher-order even mode has a small group velocity. Looking at the whole band gap, notice that the are regions where the transmission goes primarily into higher-order modes.

In conclusion, analyzing the modal transmission provides a better understanding of the mode mixing occurring at the bend transition. In some cases, the presence of mini-stop bands may reduce the number of modes, which necessarily results in a minor mode scrambling, without changing the mode-coupling coefficients associated to a certain bend design. A particularly favorable situation is represented by the mini-stop band between the odd modes at $a/\lambda \simeq 0.235$, which overlaps to a resonant scattering condition for even modes. There, only two even modes remain for guiding light to and from the bend, namely the fundamental and the next higher-order mode. If one could eliminate also this higher-order mode, single-mode transmission would be achieved. In other words, once identified the frequency region where the waveguide supports the smallest number of guided modes, including the fundamental mode, the idea is to work on the bend design to eliminate only those mode-coupling coefficients, which are essential for attaining single-mode transmission. However, even if a few coupling coefficients are involved, it is difficult to know how they depend on the bend geometry.

3.6.3 Taper

A better bend design, for single-mode transmission, can be found by exploiting the concept of adiabatic taper [French Patent 0115057 (2001); Palamaru, M., *et al.* (2001); Lalanne, Ph., *et al.* (2002)]. The principle of operation of an adiabatic taper relies on the fabrication of holes with progressively varying diameter and depth, which synthesizes an artificial material with a gradient effective index. When a certain mode enters the taper, it undergoes a transition towards the mode supported at the other side of the taper. Such smooth transition is devised for optimizing the coupling between two modes travelling under different structures [Mekis, A., *et al.* (2001); Xu, Y., *et al.* (2000)]. For instance, coupling a ridge waveguide to a WN waveguide.

The same idea of taper can be applied to a bent W3 waveguide: an overall optimized transmission may be obtained using the W3 waveguide in the straight sections and a narrower mono-mode

waveguide (W1) at the bend [Talneau, A., *et al.* B (2002)]. In this case, the taper allows reflectionless mode matching between the fundamental modes of the W3 and the W1 waveguides: W3 (straight) ⇒ W1 (bend) ⇒ W3 (straight). With the taper design, one combines both advantages of low propagation losses on a broad W3 multi-mode waveguide and single-mode transmission at the bend based on the W1 waveguide. The taper of interest is displayed in Fig. 3.20a, where it is employed for coupling a ridge waveguide with a W1 waveguide.

By decreasing the radius of the holes that are close to the dielectric channel, it is possible to

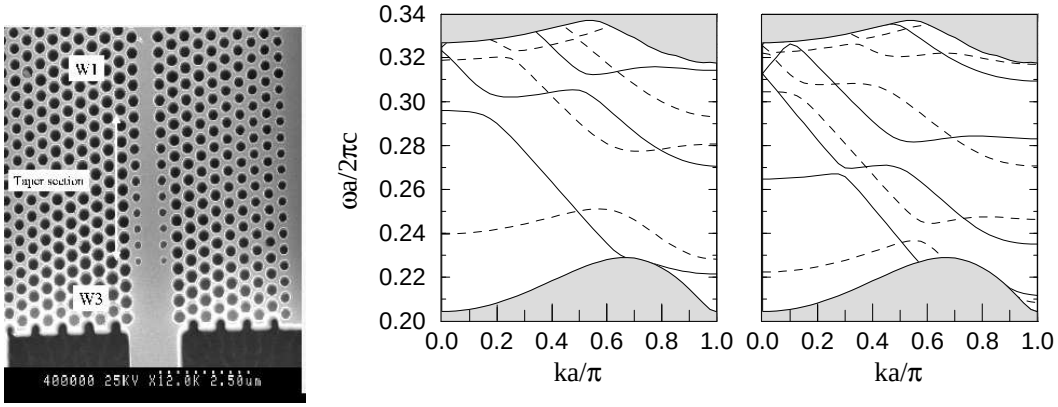

(a) (b)

Figure 3.20 (a) SEM micrograph of a W3 → W1 tapering section; courtesy of Talneau, A., LPN - CNRS, France. (b) Dispersion relation for a W1-30% waveguide (left panel) and a W3 waveguide (right panel). Solid (dashed) lines refer to spatially even (odd) H-modes with respect to the waveguide axis. Photonic-crystal parameters: $\epsilon = 10.5$, $f = 40\%$.

go continuously from a W1 to a W3 waveguide. The W1 dispersion relation changes and more modes appear until the hybrid W1-x waveguide becomes W3. The notation W1-x refers to a hybrid W1 waveguide, where the holes close to the dielectric defect have the radius reduced by $x\%$ of its nominal value; $x = 0\%$ is for the W1 waveguide and $x = 100\%$ for the W3. Fig. 3.20b shows the dispersion relation for W1-30% (left panel) compared to that of a W3 waveguide (right panel). While the W3 waveguide does not exhibit mono-mode regions, W1-30% is mono-mode for frequencies between $a/\lambda = 0.251 - 0.270$. Therefore, it is not necessary to taper down to W1,

as W1-30% is already mono-mode for a sufficiently large bandwidth. In order to design the most compact bend, the straight W1-30% sections have been eliminated, before and after the bend; the resulting design is similar to a W3 bend with a constriction [Mekis, A., *et al.* (1998)]. The novel structure does not guarantee any more single-mode transmission, because the taper is not properly a W1-30% waveguide. Nevertheless, for sufficiently long tapers, the system is expected to attain the mono-mode features of W1-30%.

Two-dimensional FDTD simulations demonstrated that high single-mode transmission ($> 90\%$ for $\epsilon'' = 0$) is achieved on a narrow wavelength domain around $a/\lambda = 0.2515$. The electric field pattern, for the above bend design, is plotted in Fig. 3.21. The tapers are height unit cells long.

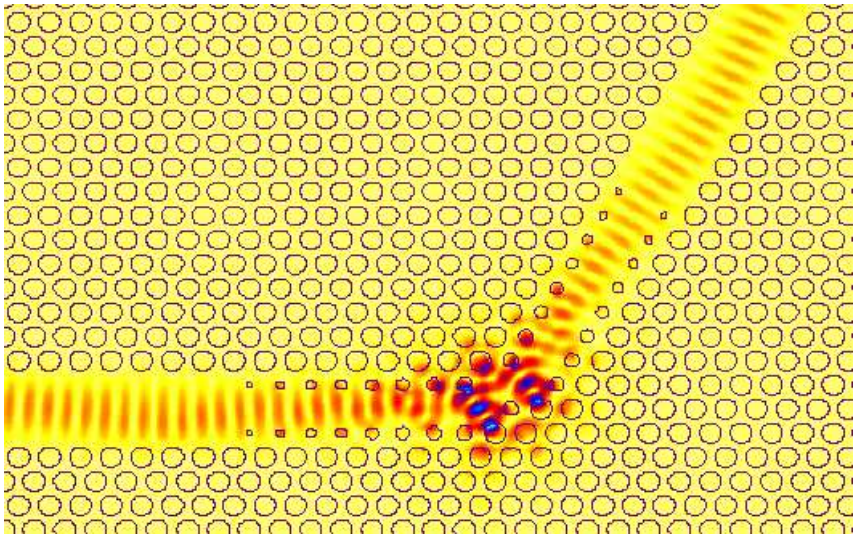

Figure 3.21 Normalized intensity of the electric field through a tapered sharp bend connecting two W3 waveguides. Parameters: $a/\lambda = 0.2515$, $\epsilon = 10.5$, $f = 40\%$ and $\epsilon'' = 0$.

The issue of single-mode transmission has been solved by tapering the W3 waveguide until a mono-mode frequency domain has been obtained in the proximity of the bend. More precisely, the whole system composed by the two tapers and the bend can be seen as a resonant cavity, which couples only with the fundamental guided mode of the W3 waveguide. The fact that the transmission bandwidth is quite narrow suggests that the resonance has a considerable Q-factor with respect to the more naïf hole-displacing design. Therefore, when out-of-plane losses are included,

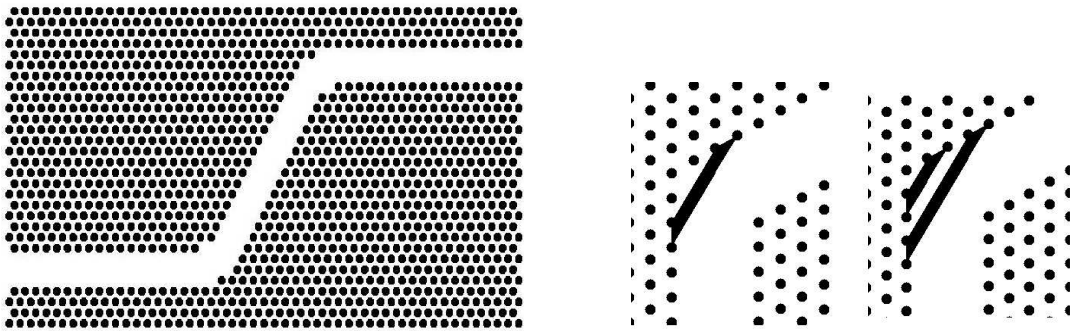

(a) (b)

Figure 3.22 (a) A one-hole-moved double bend in a W3 waveguide. (b) Left panel: one-slit bend design; right panel: two-slits bend design.

the transmission is expected to be strongly reduced, as the field spends more time oscillating inside the resonant cavity. In conclusion, the proposed design is not much suitable for realistic applications, since the transmission bandwidth is too narrow and sensitive to out-of-plane losses. On the other hand, the hole-displacing design provides a broader transmission, which is also more robust against out-of-plane losses, even though it is far from being single-mode.
The idea is to merge the above positive features in a single bend design, which provides single-mode transmission, broad bandwidth and low sensitivity to losses.

3.6.4 Slits

A novel bend design is implemented by replacing the bend corners with air slits [Happ, T., *et al.* (2002)]. In fact, bending of light is obtained by means of the photonic band gap, which guarantees no power escape through the photonic crystal plane. Smoothing the bend with $\Gamma - M$ sections allowed to increase the overall transmission level, even though the photonic crystal boundaries at the bend favor mode coupling and back-reflection. If the $\Gamma - M$ section is replaced by a planar mirror, the bending mechanism can be thought as simple ray reflection, rather than resonant scattering. Assuming that the mirror reflectivity is ideally 100%, a bend design based on ray reflection should exhibit a bandwidth as large as the photonic band gap. Furthermore, if ray reflection takes over the role of the resonant cavity, transmission should be also much more

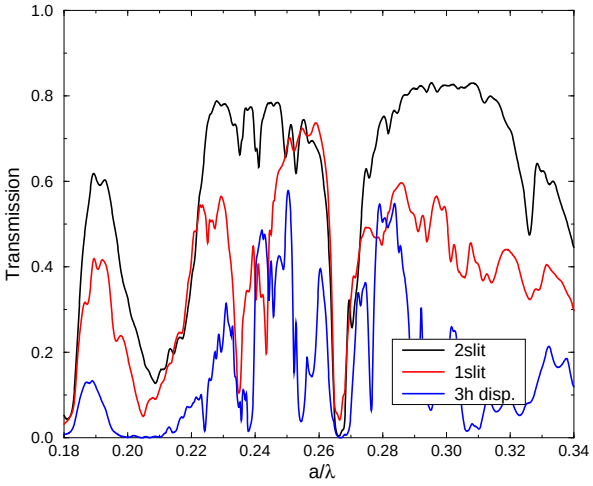

(a)

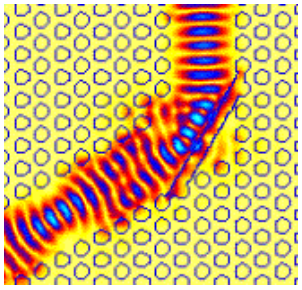

(b)

Figure 3.23 (a) Transmission through a double bend in a W3 waveguide. The black line refers to the two-slits bend design. The red (blue) line corresponds to the one-slit (three-holes-moved) bend design. Parameters: $\epsilon = 10.5$, $f = 38\%$ and $\epsilon'' = 0.1$. (b) Normalized intensity of the electric field at $a/\lambda = 0.2487$ for the one-slit design.

insensitive to out-of-plane losses. An air slit placed at the bend corner operates like a planar mirror. In this case, the reflectivity is not properly 100%, because a single slit is not enough to build up a perfect dielectric mirror, despite of the high dielectric contrast. Better performances are obtained for two slits. In practice, the planar mirror is made of a Bragg reflector embedded inside the two-dimensional photonic crystal; its one-dimensional band gap has to match the two-dimensional band gap of the hosting structure. Also in this case, out-of-plane losses are included by adding ϵ'' to the air slits, besides the holes.

The above ideas are tested on a double-bend system, which is more suitable for putting in evidence the drop of reflection, thanks to the resonant cavity made of the straight sections between the two bends. Indeed, the bend reflectivity affects the modes of the resonant cavity and yields stronger or weaker speckles in the transmission spectrum. Fig. 3.22a shows a double bend implemented with the one-hole-displaced design. The transmission is calculated for three bend designs:

one-hole-displaced (Fig. 3.22), one-slit (Fig. 3.22b, left) and double-slit (Fig. 3.22b, right). The resulting transmission spectrum are reported in Fig. 3.23a. The slit design is clearly much more efficient than the hole-displacing design, in terms of transmission level and bandwidth. Notice also that the one-slit design is still characterized by speckles; on the contrary, the spectrum obtained with the two-slit design is rather flat within the whole band gap, apart the dip due to the mini-stop band. This suggests that one slit is not enough for building up a good mirror, while two slits start to show the benefits of placing a Bragg mirror right at the outer bend corner.

Fig. 3.23b displays the electric field profile for the one-slit bend, with one air hole removed from the inner corner. The field pattern reveals that single-mode transmission is not yet achieved with such bend design.

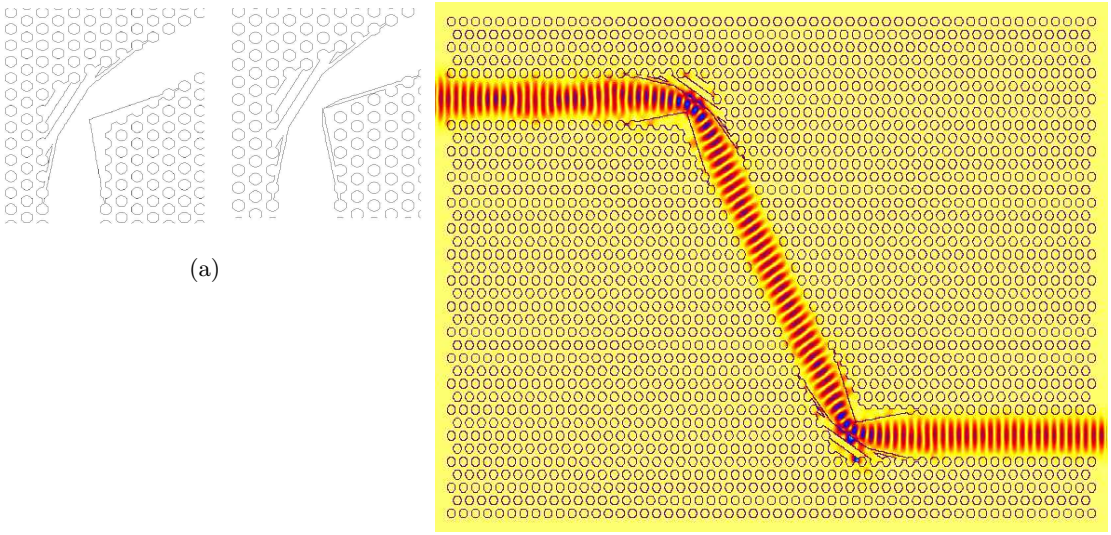

(a)

(b)

Figure 3.24 (a) Slit-taper bend designs. (b) Normalized intensity of the electric field at $a/\lambda = 0.24$ for a slit-taper double bend. Parameters: $\epsilon = 10.5$, $f = 38\%$ and $\epsilon'' = 0.05$.

The slit bend provides high transmission with a large bandwidth, while the taper design yields single-mode transmission in a very narrow frequency domain. By joining both designs into a single one, one expects that the resulting bend achieve single-mode transmission without losing in bandwidth: the bend has to couple with the fundamental guided mode only and, at the same time,

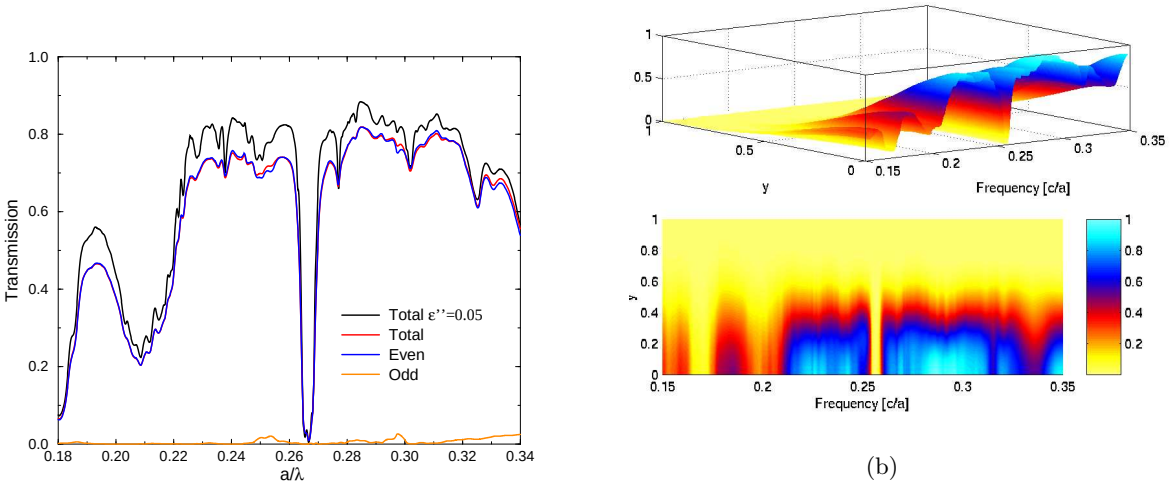

(a) (b)

Figure 3.25 (a) Transmission through a slit-taper double bend in a W3 waveguide. The black (red) line refers to the total transmission for $\epsilon'' = 0.05$ ($\epsilon'' = 0.1$). The blue (orange) line corresponds to the even and odd transmission for $\epsilon'' = 0.1$. (b) Poynting vector as a function of frequency and distance from the waveguide axis for the transmission into spatially even modes. y=1 corresponds to $y = 3\sqrt{3}/2a$. Parameters: $\epsilon = 10.5$, $f = 38\%$ and $\epsilon'' = 0.1$.

the incident wave has to scatter according to the slit mirror.

Fig. 3.24a shows some bend designs, which implement both ideas of taper and slit: the corner is smoothed with a double slit, while the taper is also made of slits, so that its walls are smoother than if variable air holes were used. The field profile reported in Fig. 3.24b, clearly demonstrates that the design allows single-mode transmission. To strengthen this fact, Fig. 3.25 reports the modal transmission for the double slit-taper bend. The complex waveguide exhibits high and broadband transmission that averages to 75% for $\epsilon'' = 0.1$ and 80% for $\epsilon'' = 0.05$. Notice that the transmission is mostly into spatially even modes. Furthermore, the even transmission appears to be mainly in the fundamental guided mode, over a wide frequency range,as it can be inferred from the contour plot of the Poynting vector. Such result is even more impressive if one compares Fig. 3.25 with the hole-displaced designs [Fig. 3.18 and Fig. 3.19].

3.7 Splitters and Combiners

Combiners and splitters represent the upper level fundamental elements for photonic integrated circuits: a splitter is used to channel the incoming light into two or more separate ports; on the contrary, a combiner is used to merge the light coming from two or more ports into a single one. Splitters and combiners are extensively employed for wavelength multiplexing and de-multiplexing in optical communication [Saleh, B. E. A., *et al.* (1991)]. There are several kinds of splitters and combiners, depending on their shape and functionalities. For instance, if the splitter has to redirect light into either one port either the other one, according to the wavelength of the incident beam, it operates as an add/drop filter [Fan, S., *et al.* (1997, 1999)]. Instead, if the splitter divides light irrespectively of the incident frequency, it is much like a conventional beam splitter in ray optics [Manolatou, C., *et al.* (1999)].

For simplicity, consider only three-ports combiners and splitters. In a symmetric splitter the power is equally distributed into the two exit ports, regardless the frequency; in an asymmetric splitter, power is channelled only in one of the two ports, according to the wavelength of the incoming beam. This section deals only with symmetric splitters and combiners obtained by joining three WN waveguide sections, which are separated from each others by an angle of 120° degrees. The same Y geometry can be seen as a combiner or a splitter, depending on which entry port is chosen. Fig. 3.26a shows either a combiner (**A** and **C** as entry ports) either a splitter (**B** as entry port). The cavity created at the junction can be modelled with the same guidelines followed for bends: hole-displacing or slit. The study is conducted mainly on the structure as a combiner, to be used in one of the demonstrators of the PCIC project: a multi-wavelength photonic-crystal laser. The power emitted from the lasers needs to be combined into a single channel, before exiting the device. Such functionality is implemented by an Y combiner, similar to the one reported in Fig. 3.26a.

As to the symmetric splitter, the objective is to attain 50% transmission in both channels without reflection at the junction. The combiner is somehow more complicated: besides back-reflection at the junction, the main issue is represented by the so-called *cross-talk*, i.e. power coming from one entry port that enters the junction and is re-channelled toward the other entry port. The cross-talk may cause interferences between the two entry ports, which is often an unwanted feature.

Furthermore, both devices are also affected by the same issues encountered while studying the bend functionality: mode-mixing and out-of-plane losses. Likewise for bends, the choice is to work with W3 or larger waveguides to reduce as much as possible the amount of out-of-plane losses.

3.7.1 Using W3 Waveguides

The first example of splitter/combiner is made of three W3 waveguide sections connected by a wedge based on the hole-displacing design, see Fig. 3.26a. First consider the system as a splitter: a wave is launched into port **B** and the outgoing power is collected by two detectors placed just in front of ports **A** and **C**. Fig. 3.26b compares the transmission of a splitter with the one of a bend (the corresponding structures are displayed in the right panels). Notice that the transmission of the splitter is multiplied by two, that is the sum of the two exit ports[5]. As done for the bend spectra of Fig. 3.16 and Fig. 3.17, the calculated curves are slightly stretched to fit better with the experimental data. Concerning the splitter, the agreement between experiment and FDTD simulations is not as good as for the bend, specially around $a/\lambda \sim 0.29$. However, the overall behavior is matched. The dip in the center of the spectrum is due once more to the mini-stop band in the W3 waveguide. The transmission level of the splitter is quite good, considering that the loss parameter is $\epsilon'' = 0.1$, and it is maximum in the same frequency domain found for the single bend.

Transmission is always mediated by a cavity resonance, which occurs at the wedge, where three waveguide sections are connected to each others. The basic splitter design is obtained by simply connecting the waveguides at 120° degrees. This yields a cavity with a three-fold symmetry axis. According to the theorem of scattering matrix theory, it is impossible to make a reflectionless Y splitter with three-fold symmetry [Manolatou, C., *et al.* (1999)]. Therefore, to improve transmission, the hole-displacing bend design is applied to the splitter: holes are moved from the outer corners and are gathered between two branches, so to form a wedge with two functions: breaking the three-fold symmetry and smoothing the splitter. The rule reads $p = n(n+1)/2$, like for bends. Fig. 3.27a shows transmission spectra for three designs, corresponding to $p = 3$ (black), $p = 6$ (red)

[5]In the simulations, the power through one port is exactly equal to the power though the other one, because the splitter is symmetric. This is not perfectly true in the experiment, where small asymmetries could take place.

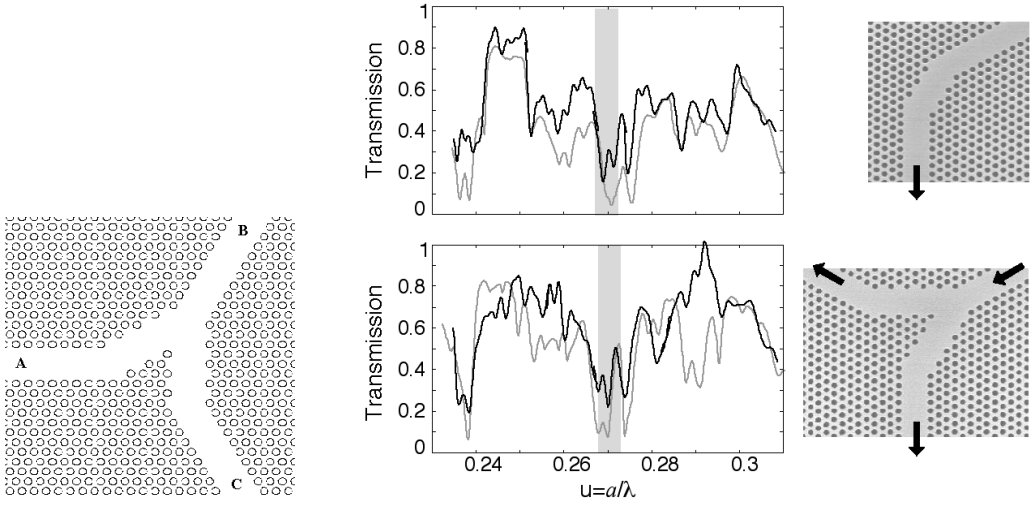

(a) (b)

Figure 3.26 (a) Combiner/splitter with W3 waveguide sections. (b) Experimental spectra (black curves) and calculated spectra (gray curves) for a bend and a splitter respectively (right panels). The transmission for the splitter has been multiplied by a factor of 2. The gray areas refer to the mini-stop band region. The simulations were performed choosing $\epsilon = 10.5$, $f = 35\%$, and $\epsilon'' = 0.1$. The calculated spectra were slightly stretched to fit the experiments, yielding an effective dielectric constant ϵ=10.4 instead of 10.5. The experimental data are courtesy of Moosburger, J., University of Würzburg, Germany and Olivier, S., EPP, France.

and $p = 10$ (blue). The values are multiplied by two to account for both exit ports. The designs with 6 or 10 holes displaced are better than the one with $p = 3$, even though the improvement is not exceptional. For a deeper insight, modal transmission has also been considered: like for bends, the smallest mode-mixing is found around $a/\lambda \simeq 0.24$.

More interesting, in view of the demonstrator, is the combiner configuration: the incident power is launched from port **A** or port **C** and is collected at port **B** and also at port **C** or port **A**, respectively. The reason why only one entry port is selected for each simulation is that the cross-talk would not be detectable otherwise. Moreover, since the system is symmetric with respect to a plane containing the axis of the waveguide corresponding to port **B**, it is enough to choose one entry port

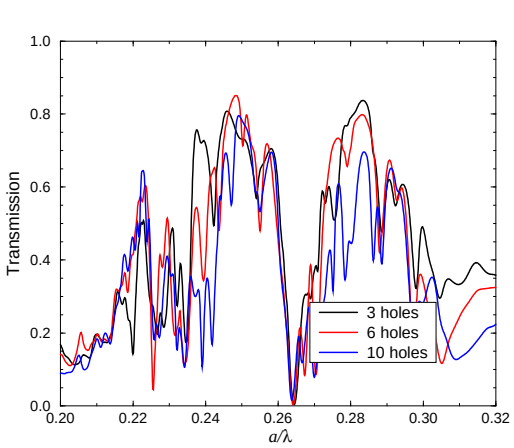

(a) Splitter

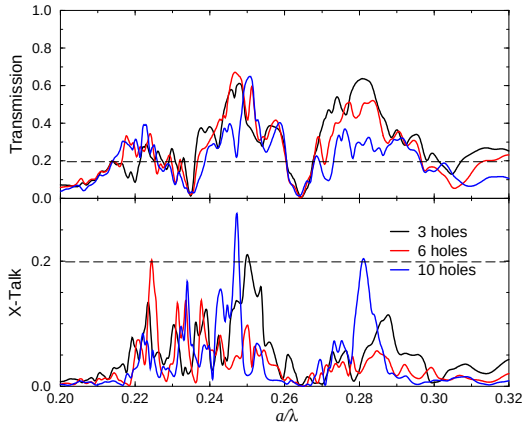

(b) Combiner

Figure 3.27 (a) Splitter transmission for the system of Fig. 3.26a; i.e. $\mathbf{B} \rightarrow \mathbf{A}$ or $\mathbf{B} \rightarrow \mathbf{C}$. The transmission has been multiplied by a factor of 2. (b) Combiner transmission for the system of Fig. 3.26a for three, six and ten holes displaced at the junction. $\mathbf{A} \rightarrow \mathbf{B}$ transmission (top) and $\mathbf{A} \rightarrow \mathbf{C}$ transmission (bottom). Parameters: $\epsilon = 10.5$, $f = 35\%$, and $\epsilon'' = 0.1$.

only, precisely port **A**. The top panel of Fig. 3.27b shows the transmission spectra for the same designs studied in Fig. 3.27a, but, this time, used as combiners. As to the transmission through port **B**, the maximum value ($\simeq 70\%$) is smaller than for the splitter ($\simeq 80\%$), but in the present case, this power is channelled into a single port. In an ideal combiner, one expects that the power is totally transmitted into port **B**; when it does not happen, it means that there is some cross-talk between the channels and/or back reflection. The cross-talk of the above mentioned designs is shown in the bottom panel of Fig. 3.27b. The cross-talk is rather hight, being of the same order of magnitude of transmission. Nevertheless, the best design is obtained for $p = 6$, which exhibit a cross-talk of $\simeq 0.5$ in correspondence of the maximum transmission. It must be given for granted that the transmission is not single-mode.

While the W3 splitters have shown satisfactory performances, which can be easily improved by employing the slit-taper designs, the combiners that have been considered so far exhibit a cross-talk

that is too much large to make the device suitable for any application. That is why it is worth to try other designs, which involve larger waveguides, like W5 or W7. For example, combiners made of two W3 waveguides going into one W5 or W7 waveguide have been studied. In both cases, the cross-talk is much reduced with respect to the original W3 designs, even though, the system with W3 → W7 has been found to have a smaller cross-talk than the one with W3 → W5.

3.7.2 Using W3 and W7 Waveguides

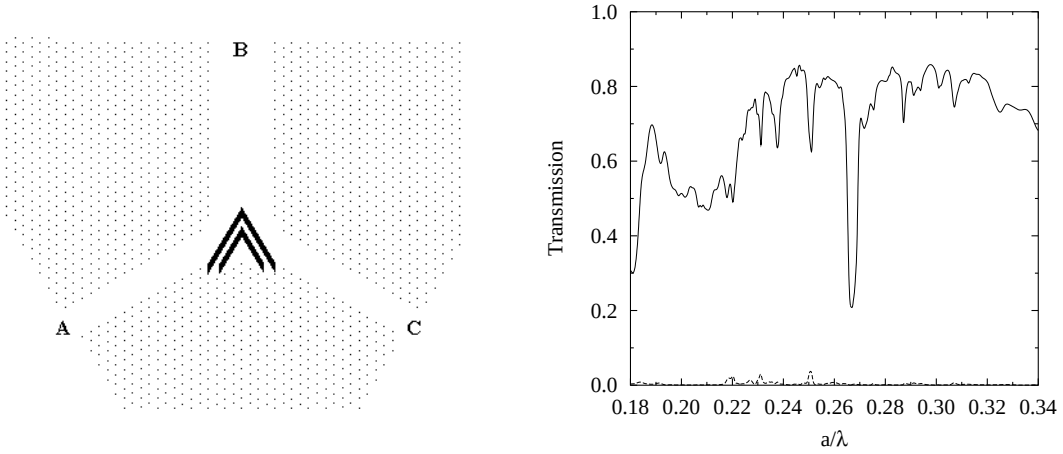

(a) (b)

Figure 3.28 W3 → W7 slit combiner: (a) structure, (b) transmission. The solid (dashed) line correspond to **A** → **B** (**A** → **C**) transmission. Parameters: $\epsilon = 10.5$, $f = 35\%$, and $\epsilon'' = 0.1$.

For the above reasons, the most promising combiner seems to be the one made of two W3 waveguides connected to a W7 waveguide. Instead of using the conventional hole-displacing design, the combiner of Fig. 3.28a is proposed with a slit wedge at the waveguides junction [Happ, T., *et al.* (2002)]. The corresponding transmission and cross-talk are shown in Fig. 3.28b. Notice that the overall transmission is higher than for the W3 designs of Fig. 3.27b, with a maximum around 85%. Also, the curve is rather flat in the whole band gap domain, in accordance to the ray-reflection mechanism discussed in Sec. 3.6.4. The cross-talk is very small, with an average value of -27 dB. With these performances, it is reasonable to think of a photonic-crystal demonstrator that makes

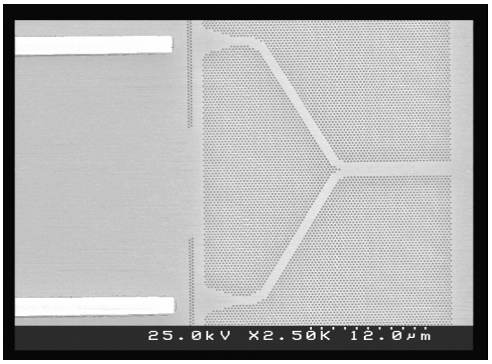

Figure 3.29 SEM micrograph of the combiner used for the multi-wavelength photonic crystal laser; courtesy of Happ, T., University of Würzburg, Germany.

use of such functionality.

3.7.3 Demonstrator

The aim of the demonstrator is to obtain combined operation of two single-mode lasers with a wavelength tunability of 20nm around 1.55μm, with a 100GHz ($\sim$ 0.8nm) channel spacing. Fabrication, characterization and the laser design have been undertaken at the University of Würzburg, one of the PCIC partners, in the group of prof. Forchel A.. In this section, the discussion is limited to the combiner design, which is one of the objectives of the present work. Fig. 3.29 shows a SEM micrographs of one of the combiners used in the first trial designs. At the left, notice the two overgrown ridge waveguides, which form the laser cavity. The cavities are of the order of 650μm long and 30μm far from each others, which is already a critical distance if one considers the thermal cross-talk. Single-mode lasing is achieved for both cavities at a threshold current around 60mA. Between lasers and combiner, a two-row photonic-crystal mirror prevents the power reflected by the combiner from re-entering the laser cavity. The combiner entry ports are tapered to favor coupling with the incident laser light. In the sample shown in Fig. 3.29, the combiner is made of two W3 waveguides connected to a W5 waveguide. The whole system is developed using the InP technology. Of course, modelling the whole structure is too much demanding. At this stage, the simulations have been carried out only on separate parts: the laser cavity or the combiner.
The role of the combiner is to channel two laser sources into a single beam. The major requirements

are thus high transmission, with low sensitivity to out-of-plane losses, low cross-talk and, possibly, single-mode transmission. Several designs are simulated: the W3 → W5 design with hole displaced (the one of Fig. 3.29), a similar one ending with a W7 waveguide. Then the slit-taper designs, again ending with W5 or W7 waveguides and, finally a W3 → W3 designs, which is aimed to achieve single mode transmission. The nomenclature for these designs is reported in Tab. 3.1. For clarity, the designs W3W7s and W3W3s are displayed in Fig. 3.30. Notice the different junction for W3W7s and W3W3s. The W3W5s design is equal to the W3W7s with W5 in place of W7.

Fig. 3.31a compares the transmission performances for the various designs of Tab. 3.1, while

Waveguides	Design	Acronym
W3 → W7	hole displaced	W3W7b
W3 → W5	hole displaced	W3W5b
W3 → W7	slit-taper	W3W7s
W3 → W5	slit-taper	W3W5s
W3 → W3	slit-taper	W3W3s

Table 3.1 Combiner designs for the demonstrator.

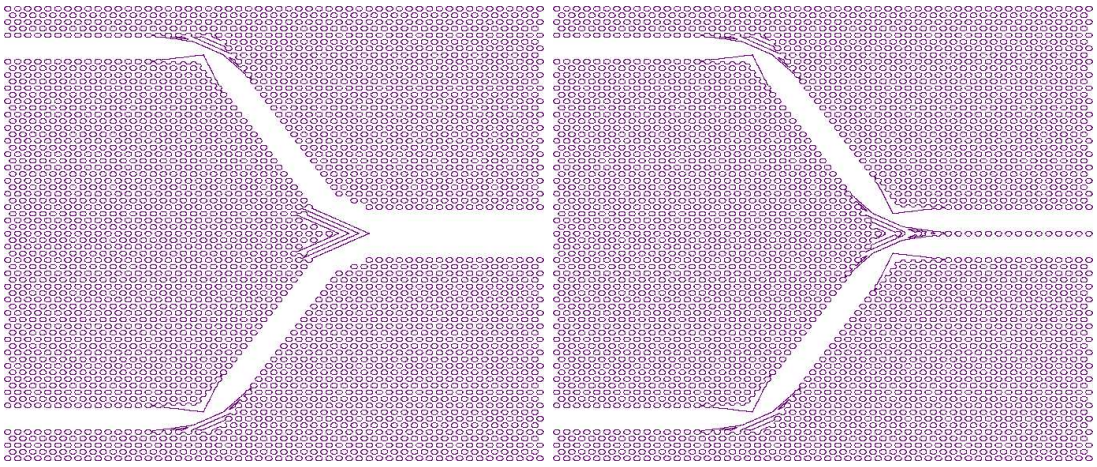

(a) W3→W7 (b) W3→W3

Figure 3.30 Combiner slit designs: (a) W3W7s, (b) W3W3s.

Fig. 3.31b gives the cross-talk in terms of transmission into the wrong port. It is apparent that the best designs are W3W7s and W3W3s. Since the W3W5b combiner, the one employed in the experiment, is not the optimal configuration as far as cross-talk is concerned, it is expected that

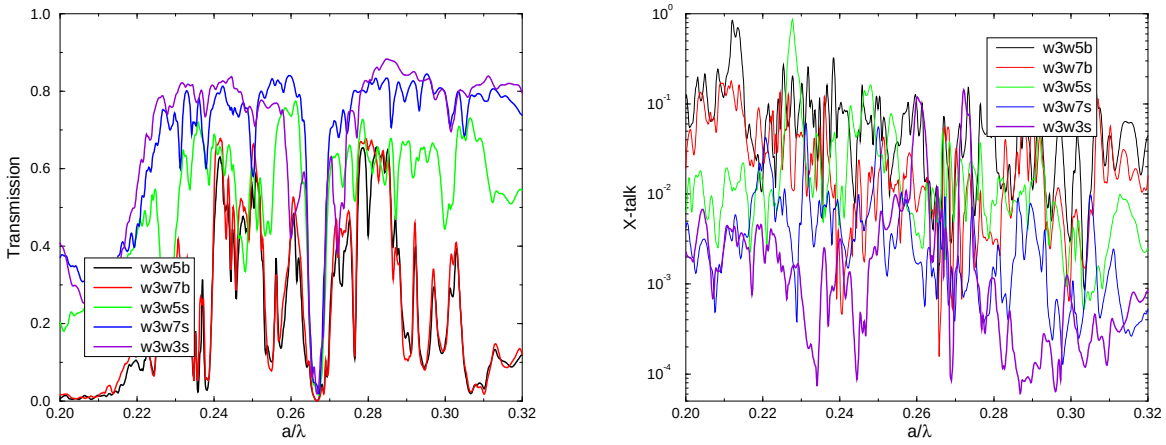

(a) Transmission (b) Cross-talk

Figure 3.31 Transmission (a) and cross-talk (b) for the demonstrator combiners. Parameters: $\epsilon = 10.5$, $f = 38\%$, and $\epsilon'' = 0.1$.

using W3W7s and W3W3s combiners will improve the device performances, as suggested in the previous sections. The transmission spectrum for W3W7s and W3W3s shows a flat profile that averages around 80%. Notice that the slit design has be used for the combiner and for the bends also, see Fig. 3.30. Concerning the cross-talk, while the combiners with displaced holes exhibit a mean value of $\simeq$ -17dB, the ones with slits drops the mean value down to $\simeq$ -27dB. According to laser books, -30dB in the laser cavity is a good starting value. Considering that, above $a/\lambda \simeq 0.27$, there are frequency windows where the cross-talk is below -30dB and that the laser cavity is protected by the photonic-crystal mirror, the present design should guarantee a cross-talk below the -30dB threshold.

If 80% transmission, in the presence of out-of-plane losses, and a -30dB cross-talk represents a fair performance, what about modal transmission? By focussing only on the best designs, W3W7s and W3W3s, the above question can be answered by performing the modal analysis discussed in Sec. 3.6.2. Thanks to the slit-taper design for the bends, transmission is single-mode up to the combiner's junction. Thereafter, for the W3W7s design, the W3 fundamental mode is lost in the cavity and what enters the final W7 branch is a superposition of several guided modes.

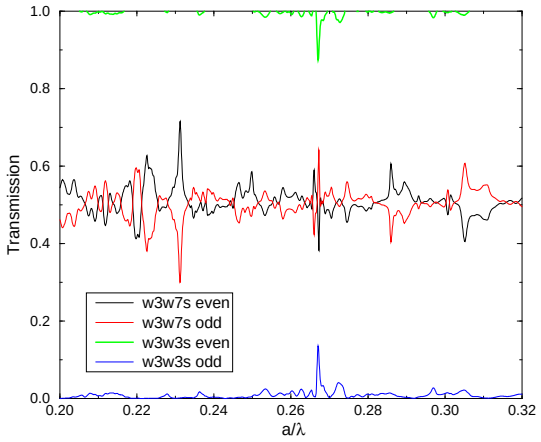

Figure 3.32 W3W3s combiner design: even/odd transmission. Parameters: $\epsilon = 10.5$, $f = 38\%$, and $\epsilon'' = 0.1$.

The consequence is that coupling of the W7 branch to a tapered optical fiber or any other probe device is reduced, proportionally to mode mixing. Such behavior can be guessed by looking at Fig. 3.32, which compares the even/odd transmission for W3W7s and W3W3s. The W3W7s combiner "loses" 50% of the transmitted power into spatially odd modes. However, the objective is to attain transmission only into the fundamental mode. The W3W3s combiner, instead,

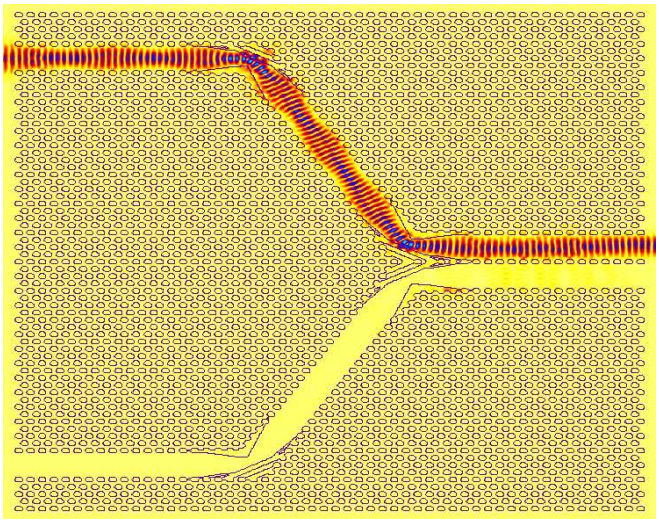

Figure 3.33 W3W3s combiner design: field pattern for $a/\lambda = 0.287$. Parameters: $\epsilon = 10.5$, $f = 38\%$, and $\epsilon'' = 0.1$.

exhibits nearly 100% transmission into spatially even modes, as displayed in Fig. 3.32. Again, this

is due to the slit-taper design at the junction and to the row of air holes that forms two parallel W3 waveguides. The field proceeds very much like as if it were guided in a W3 double bend, like in Fig. 3.24b. Indeed, the field plot, depicted in Fig. 3.33 for $a/\lambda = 0.287$, shows nearly single-mode transmission and small cross-talk. It is expected that the same happens also for other frequencies, since the Poynting vector associated to spatially even modes (not shown here) yields a profile similar to the one of Fig. 3.25b.

It is obvious that more refinements are still necessary, but the present results look promising for realistic application of such device... and this is only one of the possibilities offered by photonic crystals!

CONCLUSIONS AND PERSPECTIVES

The study of semiconductor-based two-dimensional photonic crystals has been organized into three main parts: photonic bands, optical properties and wave propagation. The first part is focussed on the discussion of the photonic eigenstates in photonic-band-gap materials, where the photonic band picture relies on the *periodicity* of the dielectric function and on the *Bloch theorem*. The plane-wave expansion method is introduced as the standard technique for computing the photonic bands of bulk photonic crystals. More insight on the photonic bands is offered by the symmetry analysis of the eigenstates. Indeed, the symmetry properties of photonic crystals can be treated within the group theory formalism: each state is classified according to an irreducible representation of the associated small point group. Furthermore, the use of symmetry may help in reducing the complexity of Maxwell's equations or the computational wave-vector domain; for example, the distinction into E-modes and H-modes in two-dimensional photonic crystals or the determination of the irreducible Brillouin zone.

Two-dimensional photonic-crystal slabs represent a trade-off between the two- and three-dimensional control of light, because the electromagnetic field is vertically confined by means of total-internal reflection, while in-plane confinement relies on the photonic-band-gap property. The states of photonic-crystal slabs can be divided into *guided modes*, below the light line, and into *quasi-guided mode*, or guided resonances, above the light line. Quasi-guided modes are characterized by intrinsic propagation losses due to the patterned dielectric constant that allows coupling to the external field; for this reason, they are also called *out-of-plane diffraction losses*. The existence of guided or quasi-guided modes depends on the waveguide geometry. It is found that strong-confinement waveguides, like the air bridge, support both truly guided and quasi-guided modes. On the contrary, weak-confinement systems, like GaAs-based or InP-based heterostructures, exhibit only quasi-guided modes. For these reasons, there exists a dispute between employing weak-

or strong-confinement waveguides for wave propagation in photonic integrated circuits.

The photon dispersion relation for both guided and quasi-guided modes can be computed by expanding the electromagnetic field on the basis set of the guided modes of an effective waveguide, defined by the spatial average of $\epsilon_j(\mathbf{x})$ in each layer j. This method, proposed by Andreani, L. C. (2002), is particularly interesting for its speed with respect to the super-cell method [Johnson, S. G., *et al.* (1999)] or the three-dimensional finite-difference time-domain method [Chutinan, A., *et al.* (2000)], and for the way guided resonances are treated. It turns out that air-bridge photonic crystals exhibit modes with a strong blue-shift, due to vertical confinement in the dielectric membrane. No complete band gap is found for such system. Moreover, as soon as the width of the membrane d/a is larger than ~ 0.5, the onset of a higher order waveguide mode closes the photonic band gap. As regards weak-confinement photonic-crystal slabs, the band structure is not much different from the ideal two-dimensional case and the cut-off of higher order modes occurs for much larger thicknesses of the core layer than for the air bridge. Thus, the conclusion is that strong-confinement systems must be designed with thin core layers, in order to preserve a wide band gap; on the contrary, weak-confinement photonic crystals have better features for thick ($d/a \simeq 1.0$) core layers, because their band structure approaches the two-dimensional limit, yet providing vertical control of light propagation. However, a comprehensive analysis of these systems requires the study of radiation losses. This is carried out in the second part of this work, where the coupling to the external field is treated within the framework of the variable-angle-reflectance technique [Astratov, V. N., *et al.* A (1999)].

First of all, it is shown that the dispersion relation of quasi-guided modes can be accurately measured by looking at the anomalies in surface reflectance, as first proposed by Astratov, V. N., *et al.* A (1999). The same procedure is numerically implemented with the scattering-matrix method [Whittaker, D. M., *et al.* (1999)]. The variable-angle-reflectance technique has been also applied to deep two-dimensional photonic crystals, namely macro-porous silicon, for extracting the two-dimensional photonic bands. In this case, the anomalies in reflectance show a unique line-shape, due to the onset of diffraction modes in the crystal. Indeed, the discontinuity in reflectance can be related to a one-dimensional critical point in the photonic density of states of the crystal. This is because the modes of two-dimensional photonic crystals retain an off-plane dispersion, while the in-

plane Bloch vector is fixed. Two-dimensional photonic-crystal slabs show anomalies in reflectance that may have complicated line-shapes: minima, maxima and dispersion-like. This fact stems from an interference effect between Lorentzian resonances with a continuum, which can be referred to a Fano resonance [Fano, U., (1961); Fan, S., *et al.* (2002)].

The excitation of a quasi-guided mode, which occurs when its frequency and Bloch vector match those of the incident wave, is found to obey precise *selection rules* that can be directly derived from the symmetry properties of the incident wave and of the photonic state under consideration. To this purpose, a group theory analysis is fundamental for understanding such rules: *a photonic band can appear in reflectance only if it has the same symmetry of the incident electromagnetic field.* In particular, a TE- (TM-) polarized wave couples only to modes that are odd (even) with respect to the plane of incidence, if such plane is also a mirror plane for the crystal. Also, at normal incidence, most of the anomalies vanish, except the ones associated to $\Gamma_5^{\pm}$ states; indeed, Γ_5^{+} (Γ_5^{-}) corresponds to doubly degenerate modes with the symmetry of the xy component of a pseudovector (vector) as for the $\mathbf{H}$ ($\mathbf{E}$) xy components of the incident field, in accordance with the above statement.

The application of the variable-angle-reflectance technique to two samples fabricated starting from GaAs/AlGaAs heterostructures shows that the width of the resonances, which is proportional to the losses, depends on the air fraction of the dielectric pattern. This suggests a systematic analysis of the resonance line-width as a function of the main structure parameters: index contrast, core thickness, hole radius and etch depth. The study is aimed to accomplish the study of the guided resonances in photonic-crystal slabs, with emphasis on sorting out the best waveguide design to attain low-loss propagation. By looking at a sample resonance, it is found that strong-confinement systems exhibit much higher losses than the weak-confinement ones. The same result can be assumed for truly guided modes that impinges a bend or a resonator. Thus, the total balance between guided modes in strong-confinement systems and quasi-guided modes in weak-confinement systems reads: low-losses always for the latter case or high-losses localized at bends and/or resonators for the former? Clearly, the final answer is not easy; see for example the feature issue *J. Opt. Soc. Am. B, 19* (9) for a collection of papers on the subject.

As the core thickness increases, out-of-plane losses decrease for both strong- and weak-confinement photonic-crystal slabs. However, as already mentioned, the band gap in air-bridge-like photonic

crystals is closed by the onset of higher order waveguide modes as soon as the core thickness d/a is greater than ~ 0.5. Moreover, the photonic band structure strongly depends on the core thickness, contrary to what happens for weak-confinement waveguides. These findings favor the choice of weak-confinement heterostructures for the implementation of photonic circuitry. A more complete study of the structure parameters, focussed on GaAs-based photonic crystals, reveals that out-of-plane losses increase with the hole radius and decrease with the etch depth, up to a critical value, where losses equal the intrinsic limit given by infinite etch depth. Putting all these information together, the best design for a low-index-contrast semiconductor-based two-dimensional photonic crystal could be an heterostructure with core thickness $d \simeq a$, patterned with a triangular lattice of holes with radius $r \simeq 0.28a - 0.32a$, up to an etch depth $h \geq 3a$. The resulting structure can be used as the base for devising *building blocks* for photonic integrated circuits. Indeed, the third and last part is devoted to the study of wave propagation in such photonic elements.

The "wafer" structure, employed for designing photonic-crystal building blocks, is either a GaAs-based or an InP-based photonic-crystal slab, both providing weak vertical confinement. This feature allows to treat the problem within a two-dimensional approximation: the vertical confinement effect is accounted for by substituting the nominal dielectric functions with the effective dielectric constant of the fundamental waveguide mode (the material dispersion and the effective constant dispersion are both neglected); out-of-plane losses are included by a phenomenological imaginary dielectric constant [Benisty, H., *et al.* (2000)]. In this framework, wave propagation is numerically studied using a two-dimensional finite-difference time-domain method.

The basic element of a photonic circuit is, of course, the straight channel waveguide. A channel waveguide can be easily obtained by creating a linear defect in the two-dimensional pattern. Among the various possibilities [Johnson, S. G., *et al.* (2000)], the best choice is represented by the so-called WN waveguide, which is obtained by removing N adjacent rows of holes along the $\Gamma - K$ direction of a triangular lattice. The resulting systems support both index-guided and photonic-band-gap-guided modes. The idea is to work with index-guided modes, because they are subject to much smaller propagation losses than band-gap-guided modes and also than bulk Bloch states. Thus, the photonic band gap is necessary only when the guided mode encounters a bend or a resonator, so that losses are as small as possible. It is worth to mention that the corrugated

sides of the linear waveguide cause backward coupling, which is featured by mini-gaps, also known as *mini-stop bands*, in the guided-mode dispersion relation.

Depending on the width of the dielectric channel and on the extent of the photonic band gap, the waveguide can be mono-mode or multi-mode. This property is particularly critical for bent waveguides, where broken symmetries give rise to modal-mixing that may preclude component cascading. On the other hand, a mono-mode, thus narrow, waveguide is subject to higher losses. A fair compromise is found by employing W3 (three rows removed) multi-mode waveguides in place of single-mode W1 (one row removed): they are sufficiently large to pull down propagation losses and have yet not too many guided modes, so that bend modelling to pursue single-mode transmission can be feasible. Several attempts have been made for achieving single-mode transmission: bend smoothing by hole displacement [Moosburger, J., *et al.* (2001); Talneau, A., *et al.* A (2002); Benisty, H., *et al.* B (2002)], waveguide tapering [Talneau, A., *et al.* B (2002)] and, finally, slit bends [Happ, T., *et al.* (2002)]. Bend smoothed by hole displacement provide better transmission levels and less sensitivity to losses with respect to a sharp bend, but not yet single-mode transmission. It is noticeable that a comparison with experimental data shows good agreement with the finite-difference time-domain simulations. This proves the validity of the two-dimensional approximation and the accuracy of the experimental characterization. The tapered bend is based on the idea of having a single-mode cavity at the bend corner, which is able to couple only to the fundamental waveguide mode. Though this design attains single-mode transmission, the transmission level is too much sensitive to losses and the band-width is too narrow. The slit design, instead, exploits a one-dimensional Bragg mirror placed at the bend corner: the mirror builds up a ray-reflection-like mechanism for bending of light, in place of the usual resonant scattering induced by the cavity formed by the bend itself. This yields a nice high and flat transmission. Finally, efficient single-mode transmission is achieved by using tapered slits at the bend.

The same ideas can be applied to combiners and splitters. In particular, efforts are spent in the design of a photonic-crystal combiner for a multi-wavelength-source laser. The device is part of the demonstrators of the EU IST Project PCIC. The major issue is to minimize the cross-talk below -30dB, to avoid interference effects between the two active cavities. By using the slit-taper design for both bends and junction, the cross-talk is reduced below -30dB for a fair band-width, yet pre-

serving high and single-mode transmission. Such device is also under experimental characterization.

In conclusion, the hope is that this work offer some interesting results on the physics of semiconductor-based photonic-crystals, in particular, as regards the weak-confinement configuration. Though the study covers a wide set of aspects, from the photonic band structure to wave propagation, there are many attracting perspectives for continuing and extending the present analysis. First of all, a better assessment of photonic-crystal slabs requires a direct calculation of out-of-plane losses for both bulk states and defect states. This is already well underway in collaboration with Andreani L. C., who extended his numerical method to compute out-of-plane losses using the perturbation theory formalism and Fermi's golden rule. Results for W1 waveguides in air bridge photonic crystals have been submitted for publication [Andreani, L. C., *et al.* B (2002)]. In the same context, it would be interesting to extend the method to photonic-crystal slabs having more than three layers, including air and substrate. This is rather important for studying weak-confinement photonic-crystals slabs, where the heterostructure is often composed by more layers than the air bridge. Furthermore, the above extension would allow to study the effect of finite etch-depth on the photonic band structure and on propagation losses, more quantitatively than what has been done with the scattering-matrix method here. Lastly, the numerical technique could be also applied to the analysis of point defects in photonic-crystal slabs. Indeed, such research could help to settle the controversy between using strong- or weak-confinement photonic-crystal slabs for making photonic integrated circuits.

Concerning wave propagation, the next goal is to accomplish the modal analysis by projecting the even modes on the fundamental guided mode. A similar approach could be exploited with a three-dimensional finite-difference time-domain method for studying the polarization mixing in asymmetric photonic-crystal slabs, like silicon-on-insulator for example... and the list could continue with many other nice things to do. After all, there is no reason to get bored while working on photonic crystals!

BIBLIOGRAPHY

Agio M. (1999). *Cristalli Fotonici Mono- e Bidimensionali*. Pavia, Italy: Università degli Studi di Pavia.

Agio M., Andreani L. C. (2000). Complete photonic band gap in a two-dimensional chessboard lattice. *Physical Review B, 61*(23), 15519–15522.

Agio M., Lidorikis E., and Soukoulis C. M. (2000). Impurity modes in a two-dimensional photonic crystal: coupling efficiency and Q factor. *Journal of the Optical Society of America B, 17*(12), 2037–2042.

Agio M., and Soukoulis C. M. (2001). Ministop bands in single-defect photonic crystal waveguides. *Physical Review E, 64*, R055603(4).

Agranovich V. M., and Kravtsov V. E. (1985). Notes on Crystal Optics of Superlattices. *Solid State Communications, 55*(1), 85–90.

Anderson C. M., and Giapis K. P. (1997). Symmetry reduction in group $4mm$ photonic crystals. *Physical Review B, 56*(12), 7313–7320.

Andreani L. C., Agio M., and Botti S. (2001). Symmetry Properties of Two-Dimensional Photonic Crystals in *Electrons and Photons in Solids*. Pisa, Italy: Quaderni – Scuola Normale Superiore, pp. 71–89.

Andreani L. C., and Agio M. (2002). Photonic Bands and Gap Maps in a Photonic Crystal Slab. *IEEE Journal of Quantum Electronics, 38*(7), 891–898.

Andreani L. C., and Pavarini E. (2002). Etched distributed Bragg reflectors as three-dimensional photonic crystals: photonic bands and density of states. *Physical Review E, 66*, 036602(7).

Andreani L. C., and Agio M. (2002). Intrinsic diffraction losses in photonic crystal waveguides with line defects. *Applied Physics Letters, submitted for publication.*

Astratov V. N., Whittaker D. M., Culshaw I. S., Stevenson R. M., Skolnick M. S., Krauss T. F., and De La Rue R. M. (1999). Photonic band-structure effects in the reflectivity of periodically patterned waveguides. *Physical Review B, 60*(24), R16255–R16258.

Astratov V. N., Culshaw I. S., Stevenson R. M., Whittaker D. M., Skolnick M. S., Krauss T. F., and De La Rue R. M. (1999). Resonant Coupling of Near-Infrared Radiation to Photonic Band Structure Waveguides. *Journal of Lightwave Technology, 17*(11), 2050–2057.

Astratov V. N., Stevenson R. M., Culshaw I. S., Whittaker D. M., Skolnick M. S., Krauss T. F., and De La Rue R. M. (2000). Heavy photon disperions in photonic crystal waveguides. *Applied Physics Letters, 77*(2), 178–180.

Baba T., Fukaya N., and Yonekura J. (1999). Light propagation characteristics in defect waveguides in a photonic crystal slab. *Electronic Letters, 27 controlla*(x), 654–657.

Baba T., Fukaya N., and Motegi A. (2001). Clear correspondence between theoretical and experimental light propagation characteristics in photonic crystal waveguides. *Electronic Letters, 37*(12), 761-762.

Bassani F., and Pastori Parravicini G. (1975). *Electronic States and Optical Transitions in Solids.* Oxford: Pergamon Press.

Benisty H. (1996). Modal analysis of optical guides with two-dimensional photonic band-gap boundaries. *Journal of Applied Physics, 79*(10), 7483–7492.

Benisty H., Weisbuch C., Labilloy D., Rattier M., Smith C. J. M., Krauss T. F., De La Rue R. M., Houdré R., Oesterle U., Jouanin C., and Cassagne D. (1999). Optical and Confinement Properties of Two-Dimensional Photonic Crystals. *Journal of Lightwave Technology, 17*(11), 2063–2077.

Benisty H., Labilloy D., Weisbuch C., Smith C. J. M., Krauss T. F., Cassagne D., Béraud A., and Jouanin C. (2000). Radiation losses of waveguide-based two-dimensional photonic crystals: Positive role of the substrate. *Applied Physics Letters, 76*(5), 532–534.

Benisty H., Lalanne Ph., Olivier S., Rattier M., Weisbuch C., Smith C. J. M., Krauss T. F., Jouanin C., and Cassagne D. (2002). Finite-depth and intrinsic losses in vertically etched two-dimensional photonic crystals. *Optical Quantum Electronics, 34*, 205–215.

Benisty H., Olivier S., Weisbuch C., Agio M., Kafesaki M., Soukoulis C. M., Qiu M., Swillo M., Karlsson A., Jaskorzynska B., Talneau A., Moosburger J., Kamp M., Forchel A., Ferrini R., Houdré R., and Oesterle U. (2002). Models and Measurements for the Transmission of Submicron-Width Waveguide Bends Defined in Two-Dimensional Photonic Crystals. *IEEE Journal of Quantum Electronics, 38*(7), 770–785.

Berger V. (1998). Nonlinear Photonic Crystals. *Physical Review Letters, 81*(19), 4136–4139.

Birner A., Grüning U., Ottow S., Schneider A., Müller F., Lehmann V., Föll H., and Gösele U. (1998). Macroporous silicon: a two-dimensional photonic bandgap material suitable for the near-infrared spectral range. *Physica Status Solidi A, 165*, 111–117.

Birner A., Wehrspohn R. B., Gösele U., and Busch K. (2001). Silicon-Based Photonic Crystals. *Advanced Materials, 13*(6), 377–388.

Blanco A., Chomski E., Grabtchak S., Ibisate M., John S., Leonard S. W., Lopez C., Meseguer F., Miguez H., Mondia J. P., Ozin G. A., Toader O., and van Driel H. M. (2000). Large-scale synthesis of a silicon photonic crystal with a complete three-dimensional bandgap near 1.5 micrometers. *Nature, 405*, 437–439.

Bogaerts W., Bienstman P., Taillaert D., Baets R., and De Zutter D. (2001). Out-of-plane scattering in photonic crystal slabs. *IEEE Photonic Technology Letters, 13*(6), 565–567.

Boscolo S., Midrio M., and Someda C. G. (2002). Coupling and Decoupling of Electromagnetic Waves in Parallel 2-D Photonic Crystal Waveguides. *IEEE Journal of Quantum Electronics, 38*(1), 47–53.

Broderick N. G. R., Ross G. W., Offerhaus H. L., Richardson D. J., and Hanna D. C. (2000). Hexagonally Poled Lithium Niobate: A Two-Dimensional Nonlinear Photonic Crystal. *Physical Review Letters, 84*(19), 4345–4348.

Busch K., and John S. (1998). Photonic band gap formation in certain self-organizing systems. *Physical Review E, 58*(3), 3896–3908.

Busch K., Vats N., John S., and Sanders B. C. (2000). Radiating dipoles in photonic crystals. *Physical Review E, 62*(3), 4251–4260.

Cao J. R., Lee P.-T., Choi S.-J., Shafiiha R., Choi S.-J., O'Brien J. D., and Dapkus P. D. (2002). Nanofabrication of photonic crystal membrane lasers. *Journal of Vacuum Science and Technology B, 20*(2), 618–621.

Cardona M., and Yu P. Y. (1996) *Fundamentals of Semiconductors*. Berlin: Springer-Verlag.

Cassagne D., Jouanin C., and Bertho D. (1996). Hexagonal photonic-band-gap structures. *Physical Review B, 53*(11), 7134–7141.

Chow E., Lin S.-Y., Johnson S. G., Villeneuve P. R., Joannopoulos J. D., Wendt J. R., Vawter G. A., Zubrzycki W., Hou H., and Alleman A. (2000). Three-dimensional control of light in a two-dimensional photonic crystal slab. *Nature, 407*, 983–986.

Chow E., Lin S.-Y., Wendt J. R., Johnson S. G., and Joannopoulos J. D. (2001). Quantitative analysis of bending efficiency in photonic-crystal waveguide bends at $\lambda = 1.55\mu$m wavelengths. *Optics Letters, 26*(5), 286–288.

Chutinan A., Noda S. (2000). Waveguides and waveguide bends in two-dimensional photonic crystal slabs. *Physical Review B, 62*(7), 4488–4492.

Chutinan A., Okano M., and Noda S. (2002). Wider bandwidth with high transmission through waveguide bends in two-dimensional photonic crystal slabs. *Applied Physics Letters, 80*(10), 1698–1700.

Conti C., Trillo S., and Assanto G. (2000). Energy Localization in Photonic Crystals of a Purely Nonlinear Origin. *Physical Review Letters, 85*(12), 2502–2505.

Coquillat D., Ribayrol A., De La Rue R. M., Le Vassor d'Yerville M., Cassagne D., Jouanin C. (2001). First Observations of 2D Photonic Crystal Band Structure in GaN-Sapphire Epitaxial Material. *Physica Status Solidi A, 183*(1), 135–138.

Cowan A. R., and Young J. F. (2002). Mode matching for second-harmonic generation in photonic crystal waveguides. *Physical Review B, 65*, 085106(6).

Datta S., Chan T. C., Ho K. M., and Soukoulis C. M. (1993). Effective dielectric constant of periodic composite structures. *Physical Review B, 48*(20), 14936–14943.

Dumeige Y., Sagnes I., Monnier P., Vidakovic P., Abram I., Mériadec C., and Levenson A. (2002). Phase-Matched Frequency Doubling at Photonic Band Edges: Efficiency Scaling as the Fifth Power of the Length. *Physical Review Letters, 89*(4), 043901(4).

D'Urso B., Painter O., O'Brien J., Tombrello T., Yariv A., and Scherer A. (1998). Modal reflectivity in finite-depth two-dimensional photonic-crystal microcavities. *Journal of the Optical Society of America B, 15*(3), 1155–1159.

Espinola R. L., Ahmad R. U., Pizzuto F., Steel M. J., and Osgood R. M. Jr. (2001). A study of high-index-contrast 90° waveguide bend structures. *Optics Express, 8*(9), 517–528.

Erchak A. A., Ripin D. J., Fan S., Rakich P., Joannopoulos J. D., Ippen E. P., Petrich G. S., and Kolodziejski L. A. (2001). Enhanced coupling to vertical radiation using a two-dimensional photonic crystal in a semiconductor light-emitting diode. *Applied Physics Letters, 78*(5), 563–565.

Fan S., Villeneuve P. R., Joannopoulos J. D., and Schubert E. F. (1997). High extraction efficiency of spontaneous emission from slabs of photonic crystals. *Physical Review Letters, 78*(17), 3294–3297.

Fan S., Villeneuve P. R., Joannopoulos J. D., and Haus H. A. (1998). Channel Drop Tunneling through Localized States. *Physical Review Letters, 80*(5), 960–963.

Fan S., Villeneuve P. R., Joannopoulos J. D., Khan M. J., Manolatou C., and Haus H. A. (1999). Theoretical analysis of channel drop tunneling processes. *Physical Review B, 59*(24), 15882–15892.

Fan S., and Joannopoulos J. D. (2002). Analysis of guided resonances in photonic crystal slabs. *Physical Review B, 65*, 235112(8).

Fano U. 1961. Effects of configuration interaction on intensities and phase shifts. *Physical Review, 124*(6), 1866–1878.

Ferrini R., Leuenberger D., Mulot M., Qiu M., Moosburger J., Kamp M., Forchel A., Anand S., and Houdré R. (2002). Optical Study of Two-Dimensional InP-based Photonic Crystals by Internal Light Source Technique. *IEEE Journal of Quantum Electronics, 38*(7), 786–799.

Figotin A., and Goren V. (2001). Resolvent method for computations of localized defect modes of H-polarization in two-dimensional photonic crystals. *Physical Review E, 64*, 056623(16).

Fleming J. G., Lin S. Y., El-Kady I., Biswas R., and Ho K. M. (2002). All-metallic three-dimensional photonic crystals with a large infrared band gap. *Nature, 417*, 52–55.

Foresi J. S., Villeneuve P. R., Ferrera J., Thoen E. R., Steinmeyer G., Fan S., Joannopoulos J. D., Kimerling L. C., Smith H. I., and Ippen E. P. (1997). Photonic-bandgap microcavities in optical waveguides. *Nature, 390*, 143–145.

Foteinopoulou S., and Soukoulis C. M. (2002). Theoretical Investigation of One-Dimensional Cavities in Two-Dimensional Photonic Crystals. *IEEE Journal of Quantum Electronics, 38*(7), 844–849.

Lalanne Ph., and Talneau A. (2001). Structure à cristal photonique pour la conversion de mode. *French Patent 0115057.*

Galli M., Agio M., Andreani L. C., Belotti M., Guizzetti G., Marabelli F., Patrini M., Bettotti P., Dal Negro L., Gaburro Z., Pavesi L., Lui A., and Bellutti P. (2002). Spectroscopy of photonic bands in macroporous silicon photonic crystals. *Physical Review B, 65*, 113111(4).

Galli M., Agio M., Andreani L. C., Atzeni L., Bajoni D., Guizzetti G., Businaro L., Di Fabrizio E., Romanato F., and Passaseo, A. (2002). Optical properties and photonic bands of GaAs photonic crystal waveguides with tilted square lattice. *European Physical Journal B, 27*, 79–87.

Gourley P. L., Wendt J. R., Vawter G. A., Brennan T. M., and Hammons B. E. (1994). Optical properties of two-dimensional photonic lattices fabricated as honeycomb nanostructures in compound semiconductors. *Applied Physics Letters, 64*(6), 687–689.

Grüning U., Lehmann V., Ottow S., and Busch K. (1996). Macroporous silicon with a complete two-dimensional photonic band gap centered at 5 mm. *Applied Physics Letters, 68*(6), 747–749.

Halevi P., Krokhin A. A., and Arriaga J. (1999). Photonic Crystal Optics and Homogenization of 2D Periodic Composites. *Physical Review Letters, 82*(4), 719–722.

Happ T, Moosburger J., Kamp M., and Forchel A. (2002). Private communication.

Ho K. M., Chan C. T., and Soukoulis C. M. (1990). Existence of a Photonic Gap in Periodic Dielectric Structures. *Physical Review Letters, 65*(25), 3152–3155.

Ho K. M., Chan C. T., Soukoulis C. M., Biswas R., and Sigalas M. (1994). Photonic Band Gaps in Three Dimensions: New Layer-by-Layer Periodic Structures. *Solid State Communications, 89*, 413–416.

Hwang J.-K., Hyun S.-B., Ryu H.-Y., and Lee Y.-H. (1998). Resonant modes of two-dimensional photonic bandgap cavities determined by the finite-element method and by use of the anisotropic perfectly matched layer boundary condition. *Journal of the Optical Society of America B, 15*(8), 2316–2324.

guest editors Krauss T., and Baba T. (2002). Feature section on photonic crystal structures and applications. *IEEE Journal of Quantum Electronics, 38*(7).

Imada M., Chutinan A., Noda S., and Mochizuki M. (2002). Multidirectionally distributed feedback photonic crystal lasers. *Physical Review B, 65*, 195306(8).

Jackson J. D. (1975) *Classical Electrodynamics*. New York: John Wiley & Sons.

Joannopoulos J. D., Meade R. D., and Winn J. N. (1995). *Photonic Crystals – Molding the flow of light*. Princeton, NJ: Princeton Universty Press.

Joannopoulos J. D., Villeneuve P. R., Fan S. (1997). Photonic crystals: putting a new twist on light. *Nature, 386*, 143–149.

John S. (1987). Strong localization of photons in certain disordered dielectric superlattices. *Physical Review Letters, 58*(20), 2486–2489.

John S., and Rangarajan R. (1988). Optimal structures for classical wave localization: an alternative to the ioffe-regel criterion. *Physical Review B, 38*(14), 10101–10104.

Johnson S. G., Fan S., Villeneuve P. R., Joannopoulos J. D., and Kolodziejski L. A. (1999). Guided modes in photonic crystal slabs. *Physical Review B, 60*(8), 5751–5758.

Johnson S. G., Villeneuve P. R., Fan S., and Joannopoulos J. D. (2000). Linear waveguides in photonic-crystal slabs. *Physical Review B, 62*(12), 8212–8222.

edited by IEEE and OSA. (1999). Feature section on photonic band gap materials. *Journal of Lightwave Technology, 17*(11).

guest editors Bowden C. M., Dowling J. P., Everitt H. O. (1993). Development and applications of materials exhibiting photonic band gaps. *Journal of the Optical Society of America B, 10*(2).

guest editors Bowden C. M., Zheltikov A. M. (2002). Nonlinear Optics of Photonic Crystals. *Journal of the Optical Society of America B, 19*(9).

Kafesaki M., Agio M., and Soukoulis C. M. (2002). Waveguides in finite-height two-dimensional photonic crystals. *Journal of the Optical Society of America B, 19*(9), 2232–2240.

Kawai N., Inoue K., Carlsson N., Ikeda N., Sugimoto Y., Asakawa K., and Takemori T. (2001). Confined Band Gap in an Air-Bridge Type of Two-Dimensional AlGaAs Photonic Crystal. *Physical Review Letters, 86*(11), 2289–2292.

Kirchner A., Busch K., and Soukoulis C. M. (1998). Transport properties of random arrays of dielectric cylinders. *Physical Review B, 57*(1), 277–288.

Ko D. Y. K., and Inkson J. C. (1988). Matrix method for tunneling in heterostructures: Resonant tunneling in multilayer systems. *Physical Review B, 38*(14), 9945–9951.

Koenderink A. F., Bechger L., Schriemer H. P., Lagendijk A., and Vos W. L. (2002). Broadband Fivefold Reduction of Vacuum Fluctuations Probed by Dyes in Photonic Crystals. *Physical Review Letters, 88*(14), 143903(4).

Kosaka H., Kawashima T., Tomita A., Notomi M., Tamamura T., Sato T., and Kawakami S. (1998). Superprism phenomena in photonic crystals. *Physical Review B, 58*(16), R10096–R10099.

Kosaka H., Kawashima T., Tomita A., and Sato T. (2000). Photonic-crystal spot-size converter. *Applied Physics Letters, 76*(3), 268–270.

Koster G. F., Dimmock J. O., Wheeler R. G., and Statz H. (1963). *Properties of the Thirty-Two Point Groups*. Cambridge, MA: MIT Press.

Kramper P., Birner A., Agio M., Soukoulis C. M., Müller F., Gösele U., Mlynek J., and Sandoghdar V. (2001). Direct spectroscopy of a deep two-dimensional photonic crystal microresonator. *Physical Review B, 64*, 233102(4).

Krauss T. F., De La Rue R. M., and Brand S. (1996). Two-dimensional photonic-bandgap structures operating at near-infrared wavelengths. *Nature, 383*, 699–701.

Labilloy D., Benisty H., Weisbuch C., Krauss T. F., De La Rue R. M., Bardinal V., Houdré R., Oesterle U., Cassagne D., and Jouanin C. (1997). Quantitative Measurement of Transmission, Reflection, and Diffraction of Two-Dimensional Photonic Band Gap Structures at Near-Infrared Wavelengths. *Physical Review Letters, 79*(21), 4147–4150.

Labilloy D., Benisty H., Weisbuch C., Krauss T. F., Houdré R., and Oesterle U. (1997). Use of guided spontaneous emission of a semiconductor to probe the optical properties of two-dimensional photonic crystals. *Applied Physics Letters, 71*(6), 738–740.

Labilloy D., Benisty H., Weisbuch C., Smith C. J. M., Krauss T. F., Houdré R., and Oesterle U. (1999). Finely resolved transmission spectra and band structure of two-dimensional photonic crystals using emission from InAs quantum dots. *Physical Review B, 59*(3), 1649–1652.

Lalanne Ph., and Benisty H. (2001). Out-of-plane losses of two-dimensional photonic crystals waveguides: Electromagnetic analysis. *Journal of Applied Physics, 89*(2), 1512–1514.

Lalanne Ph., and Talneau A. (2002). Modal conversion with artificial materials for photonic-crystal waveguides. *Optics Express, 10*(8), 354–359.

Lehmann V., and Föll H. (1990). Formation mechanism and properties of electrochemically etched trenches in *n*-type silicon. *Journal of the Electrochemical Society, 137*(2), 653–659.

Leonard S. W., van Driel H. M., Birner A., Gösele U., and Villeneuve P. R. (2000). Single-mode transmission in two-dimensional macroporous silicon photonic crystal waveguides. *Optics Letters, 25*(20), 1550–1552.

Leung K. M., and Liu Y. F. (1990). Photon band structures: The plane-wave method. *Physical Review B, 41*(14), 10188–10190.

Leung K. M., and Liu Y. F. (1990). Full Vector Wave Calculation of Photonic Band Structures in Face-Centered-Cubic Dielectric Media. *Physical Review Letters, 65*(21), 2646–2649.

Li L. (1996). Use of Fourier series in the analysis of discontinuous periodic structures. *Journal of the Optical Society of America A, 13*(9), 1870–1876.

Li Z.-Y., Gu B.-Y., and Yang G.-Z. (1998). Large Absolute Band Gap in 2D Anisotropic Photonic Crystals. *Physical Review Letters, 81*(12), 2574–2577.

Liao Z. P., Wong H. L., Yang B. P., and Yuan Y. F. (1984). A transmitting boundary for transient wave analyses. *Scientia Sinica A, XXVII*, 1063–1076.

Lidorikis E., Sigalas M. M., Economou E. N., and Soukoulis C. M. (1998). Tight-Binding Parametrization for Photonic Band Gap Materials. *Physical Review Letters, 81*(7), 1405–1408.

Lidorikis E., Sigalas M. M., Economou E. N., and Soukoulis C. M. (2000). Gap deformation and classical wave localization in disordered two-dimensional photonic-band-gap materials. *Physical Review B, 61*(20), 13458-13464.

Lin S. Y., J. G. Fleming, D. L. Hetherington, B. K. Smith, R. Biswas, K. M. Ho, M. M. Sigalas, W. Zubrzycki, S. R. Kurtz, and J. Bur. (1998). A three-dimensional photonic crystal in the infrared wavelengths. *Nature, 394*, 251-253.

Lin S.-Y., Chow E., Hietala V., Villeneuve P. R., and Joannopoulos J. D. (1998). Experimental Demonstration of Guiding and Bending of Electromagnetic Waves in a Photonic Crystal. *Science, 282*, 274–276.

Lončar M., Doll T., Vučković J., and Scherer A. (2000). Design and Fabrication of Silicon Photonic Crystal Optical Waveguides. *Journal of Lightwave Technology, 18*(10), 1402–1411.

Lončar M., Nedeljković D., Doll T., Vučković J., Scherer A., and Pearsall T. P. (2000). Waveguiding in planar photonic crystals. *Applied Physics Letters, 77*(13), 1937–1939.

Lončar M., Nedeljković D., Pearsall T. P., Vučković J., Scherer A., Kuchinsky S., and Allan D. C. (2002). Experimental and theoretical confirmation of Bloch-mode light propagation in planar photonic crystal waveguides. *Applied Physics Letters, 80*(10), 1689–1691.

López-Tejeira F., Ochiai T., Sakoda K., and Sánchez-Dehesa J. (2002). Symmetry characterization of eigenstates in opal-based photonic crystals. *Physical Review B, 65*, 195110(8).

Luo C., Johnson S. G., Pendry J. B., and Joannopoulos J. D. (2002). All-Angle Negative Refraction in Photonic Crystals. *Physical Review B, 65*, 201104R(4).

Malpuech G., Kavokin A., Panzarini G., and Di Carlo A. (2001). Theory of photon Bloch oscillations in photonic crystals. *Physical Review B, 63*, 035108(11).

Manolatou C., Johnson S. G., Fan S., Villeneuve P. R., Haus H. A., and Joannopoulos J. D. (1999). High-Density Integrated Optics. *Journal of Lightwave Technology, 17*(9), 1682–1692.

Martin O. J. F., Girard C., Smith D. R,, and Schultz S. (1999). Generalized Field Propagator for Arbitrary Finite-Size Photonic Band Gap Structures. *Physical Review Letters, 82*(2), 315–318.

Martorell J., Vilaseca R., Corbalán R. (1997). Second harmonic generation in a photonic crystal. *Applied Physics Letters, 70*(6), 702–704.

Meade R. D., Brommer K. D., Rappe A. M., and Joannopoulos J. D. (1991). Electromagnetic Bloch waves at the surface of a photonic crystal. *Physical Review B, 44*(19), 10961–10964.

Meade R. D., Brommer K. D., Rappe A. M., and Joannopoulos J. D. (1992). Existence of a photonic band gap in two dimensions. *Applied Physics Letters, 61*(4), 495–497.

Meade R. D., Rappe A. M., Brommer K. D., Joannopoulos J. D, and Alerhand O. L. (1993). Accurate theoretical analysis of photonic band-gap materials. *Physical Review B, 48*(11), 8434–8437; Erratum: Accurate theoretical analysis of photonic band-gap materials. *Physical Review B, 55*(23), 15942.

Meade R. D., Devenyi A., Joannopoulos J. D., Alerhand O. L., Smith D. A., and Kash K. (1994). Novel applications of photonic band gap materials: Low-loss bends and high Q cavities. *Journal of Applied Physics, 75*(9), 4753–4755.

Mekis A., Chen J. C., Kurland I., Fan S., Villeneuve P. R., and Joannopoulos J. D. (1996). High Transmission through Sharp Bends in Photonic Crystal Waveguides. *Physical Review Letters, 77*(18), 3787–3790.

Mekis A., Fan S., and Joannopoulos J. D. (1998). Bound states in photonic crystal waveguides and waveguide bends. *Physical Review B, 58*(8), 4809–4817.

Mekis A., Fan S., and Joannopoulos J. D. (2001). Tapered Couplers for Efficient Interfacing Between Dielectric and Photonic Crystal Waveguides. *Journal of Lightwave Technology, 19*(6), 861–865.

Moosburger J., Kamp M., Forchel A., Olivier S., Benisty H., Weisbuch C., and Oesterle U. (2001). Enhanced transmission through photonic-crystal-based bent waveguides by bend engineering. *Applied Physics Letters, 79*(22), 3579–3581.

Notomi M. (2000). Theory of light propagation in strongly modulated photonic crystals: Refraction-like behavior in the vicinity of the photonic band gap. *Physical Review B, 62*(16), 10696–10705.

Ochiai T., and Sakoda K. (2001). Dispersion relation and optical transmittance of a hexagonal photonic crystal slab. *Physical Review B, 63*, 125107(7).

Ochiai T., and Sakoda K. (2001). Nearly free-photon approximation for two-dimensional photonic crystal slabs. *Physical Review B, 64*, 045108(11).

Olivier S., Rattier M., Benisty H., Weisbuch C., Smith C. J. M., De La Rue R. M., Krauss T. F., Oesterle U., and Houdré R. (2001). Mini stopbands of a one dimensional system: the channel waveguide in a two-dimensional photonic crystal. *Physical Review B, 63*, 113311(4).

Olivier S., Smith C. J. M., Rattier M., Benisty H., Weisbuch C., Krauss T. F., Houdré R., and Oesterle U. (2001). Miniband transmission in a photonic crystal coupled-resonator optical waveguide. *Optics Letters, 26*(13), 1019–1021.

Olivier S., Benisty H., Rattier M., Weisbuch C., Qiu M., Karlsson A., Smith C. J. M., Houdré R., and Oesterle U. (2001). Resonant and nonresonant transmission through waveguide bends in a planar photonic crystal. *Applied Physics Letters, 79*(16), 2514–2516.

Olivier S., Smith C. J. M., Benisty H., Weisbuch C., Krauss T. F., Houdré R., and Oesterle U. (2002). Cascaded Photonic Crystal Guides and Cavities: Spectral Studies and their Impact on Integrated Optics Design. *IEEE Journal of Quantum Electronics, 38*(7), 816–824.

Pacradouni V., Mandeville W. J., Cowan A. R., Paddon P., Young J. F., and Johnson S. R. (2000). Photonic band structure of dielectric membrane periodically textured in two dimensions. *Physical Review B, 62*(7), 4204–4207.

Padjen R., Gerard J. M., and Marzin J. Y. (1994). Analysis of the filling pattern dependence of the photonic bandgap for two-dimensional systems. *Journal of Modern Optics, 41*(2), 295–310.

Painter O., Vučković J., and Scherer A. (1999). Defect modes of a two-dimensional photonic crystal in an optically thin dielectric slab. *Journal of the Optical Society of America B, 16*(2), 275–285.

Painter O., Husain A., Scherer A., O'Brien J. D., Kim I., and Dapkus P. D. (1999). Room temperature photonic crystal defect lasers at near-infrared wavelengths in InGaAsP. *Journal of Lightwave Technology, 17*(11), 2082–2088.

Palamaru M., and Lalanne Ph. (2001). Photonic crystal waveguides: Out-of-plane losses and adiabatic modal conversion. *Applied Physics Letters, 78*(11), 1466–1468.

edited by Palik E. D. (1985). *Handbook of optical constants of solids*. Orlando: Academic Press.

Patrini M., Galli M., Marabelli F., Agio M., Andreani L. C., Peyrade D., and Chen Y. (2002). Photonic Bands in Patterned Silicon-on-Insulator Waveguides. *IEEE Journal of Quantum Electronics, 38*(7), 885–890.

Patrini M., Galli M., Belotti M., Andreani L. C., Guizzetti G., Pucker G., Lui A., Bellutti P., and Pavesi L. (2002). Optical response of one-dimensional $(Si/SiO_2)_m$ photonic crystals. *Journal of Applied Physics, 92*(4), 1816–1820.

Pendry J. B., and MacKinnon A. (1992). Calculation of Photon Dispersion Relations. *Physical Review Letters, 69*(19), 2772–2775.

Pertsch T., Zentgraf T.,Peschel U.,Bräuer A., and Lederer F. (2002). Anomalous Refraction and Diffraction in Discrete Optical Systems. *Physical Review Letters, 88*(9), 093901(4).

Peyrade D., Chen Y., Talneau A., Patrini M., Galli M., Marabelli F., Agio M., Andreani L. C., Silberstein E., Lalanne Ph. (2002). Fabrication and optical measurements of silicon on insulator photonic nanostructures. *Microelectronic Engineering, 61-62*, 529–536.

Pottier P., Seassal C., Letartre X., Leclerq J. L., Viktorovitch P., Cassagne D., and Jouanin C. (1999). Triangular and Hexagonal High Q-Factor 2-D Photonic Bandgap Cavities on III-V Suspended Membranes. *Journal of Lightwave Technology, 17*(11), 2058–2062.

Qiu M., and He S. (2000). A nonorthogonal finite-difference time-domain method for computing the band structure of a two-dimensional photonic crystal with dielectric and metallic inclusions. *Journal of Applied Physics, 87*(12), 8268–8275.

Qiu M., and He S. (2000). Numerical method for computing defect modes in two-dimensional photonic crystals with dielctric or metallic inclusions. *Physical Review B, 61*(19), 12871–12876.

Qiu M. (2002). Effective index method for heterostructure-slab-waveguide-based two-dimensional photonic crystals. *Applied Physics Letters, 81*(7), 1163–1165.

Robertson W. M., Arjavalingam G., Meade R. D., Brommer K. D., Rappe A. M., and Joannopoulos J. D. (1993). Measurement of the photon dispersion relation in two-dimensional ordered dielectric arrays. *Journal of the Optical Society of America B, 10*(2), 322–327.

Robertson W. M., Arjavalingam G., Meade R. D., Brommer K. D., Rappe A. M., and Joannopoulos J. D. (1993). Observation of surface photons on periodic dielectric arrays. *Optics Letters, 18*(7), 528–530.

Romanato F., Businaro L., Di Fabrizio E., Passaseo A., De Vittorio M., Cingolani R., Patrini M., Galli M., Bajoni D., and Andreani L. C. (2002). Fabrication by means of X-Ray lithography of two-dimensional GaAs/AlGaAs photonic crystals with unconventional unit cell. *Nanotechnology, 13*(8), 644-652.

Rowson S., Chelnokov A., and Lourtioz J.-M. (1999). Two-Dimensional Photonic Crystals in Macroporous Silicon: From Mid-Infrared (10 μm) to Telecommunication Wavelengths (1.3-1.5 μm). *Journal of Lightwave Technology, 17*(11), 1989–1995.

Ryu H.-Y., Kim S.-H., Park H.-G., Hwang J.-K. Lee Y.-H., and Kim J.-S. (2002). Square-lattice photonic band-gap single-cell laser operating in the lowest-order whispering gallery mode. *Applied Physics Letters, 80*(21), 3883–3885.

Sakoda K. (1995). Optical transmittance of a two-dimensional triangular photonic lattice. *Physical Review B, 51*(7), 4672–4675; Transmittance and Bragg reflectivity of two-dimensional photonic lattices. *Physical Review B, 52*(12), 8992–9002.

Sakoda K. (2001). *Optical Properties of Photonic Crystals*. Berlin: Springer.

Saleh B. E. A., and Teich M. C. (1991). *Fundamentals of Photonics*. New York: John Wiley and Sons Inc.

Schilling J., Birner A., Müller F., Wehrspohn R. B., Hillebrand R., Gösele U., Busch K., John S., Leonard S. W., and van Driel H. M. (2001). Optical characterisation of 2D macroporous silicon photonic crystals with bandgaps around 3.5 and 1.3μm . *Optical Materials, 17*(1), 7–10.

Schilling J., Müller F., Matthias S., Wehrspohn R. B., and Gösele U. (2001). Three-dimensional photonic crystals based on macroporous silicon with modulated pore diameter. *Applied Physics Letters, 78*(9), 1180–1182.

Shkunov M. N., Vardeny Z. V., De Long M. C., Polson R. C., Zakhidov A. A., and Baughman R. H. (2002). Tunable, Gap-State Lasing in Switchable Directions for Opal Photonic Crystals. *Advanced Functional Materials, 12*(1), 21–26.

Silvestre E., Pottage J. M., Russel P. St., and Roberts P. J. (2000). Design of thin-film photonic crystal waveguides. *Applied Physics Letters, 77*(7), 942-944.

Smith C. J. M., Benisty H., Olivier S., Rattier M., weisbuch C., Krauss T. F., De La Rue R. M., Houdré R., and Oesterle U. (2000). Low-channel waveguides with two-dimensional photonic crystal boundaries. *Applied Physics Letters, 77*(18), 2813–2815.

Sondergaard T., Bjarklev A., Kristensen M., Erland J., and Broeng J. (2000). Designing finite-height two-dimensional photonic crystal waveguides. *Applied Physics Letters, 77*(6), 785–787.

edited by Soukoulis, C. M. (1996). *Photonic Band Gap Materials*, Vol. 315 of *NATO Advanced Studies Institute, Series E: Applied Sciences*. Dordrecht: Kluwer.

edited by Soukoulis C. M. (2001). *Photonic Crystals and Light Localization in the 21st Century*, Vol. 563 of *NATO Science Series, Series C: Mathematical and Physical Sciences*. Dordrecht: Kluwer Academic Publishers.

Sözüer H. V., Haus J. W., and Inguva N. (1992). Photonic bands: Convergence problems with the plane-wave method. *Physical Review B, 45*(24), 13962–13972.

Talneau A., Le Gouezigou L., and Bouadma N. (2001). Quantitive measurements of low propagation losses at 1.55μm on planar photonic crystal waveguides. *Optics Letters, 26*(16), 1259–1261.

Talneau A., Le Gouezigou L., Bouadma N., Kafesaki M., Soukoulis C. M., and Agio M. (2002). Photonic-crystal ultrashort bends with improved transmission and low reflection at 1.55 μm. *Applied Physics Letters, 80*(4), 547–549.

Talneau A., Lalanne Ph., Agio M., and Soukoulis C. M. (2002). Low-reflection Photonic-Crystal taper for efficient coupling between guide sections of arbitrary widths. *Optics Letters, 27*(17), 1522–1524.

Tavlove A. (1995). *Computational Electrodynamics – The Finite-Difference Time-Domain Method*. Norwood, MA: Artech House.

Thijssen M. S., Sprik R., Wijnhoven J., Megens M., Narayanan T., Lagendijk A., and Vos W. L. (1999). Inhibited Light Propagation and Broadband Reflection in Photonic Air-Sphere Crystals . *Physical Review Letters, 83*(14), 2730-2733.

Tokushima M., Kosaka H., Tomita A., and Yamada H. (2000). Lightwave propagation through a 120° sharply bent single-line-defect photonic crystal waveguide. *Applied Physics Letters, 76*(8), 952–954.

Vats N., John S., and Busch K. (2002). Theory of fluorescence in photonic crystals. *Physical Review A, 65*, 043808(13).

Villeneuve P. R., and Piché M. (1992). Photonic band gaps in two-dimensional square and hexagonal lattices. *Physical Review B, 46*(8), 4969–4972.

Villeneuve P. R., Fan S., and Joannopoulos J. D. (1996). Microcavities in photonic crystals: Mode symmetry, tunability, and coupling efficiency. *Physical Review B, 54*(11), 7837–7842.

Vlasov Y. A., Bo X.-Z., Sturm J. C., and Norris D. J. (2001). On-chip natural assembly of silicon photonic bandgap crystals. *Nature, 414*, 289–293.

Xu Y., Lee R. K., and Yariv A. (2000). Adiabatic coupling between conventional dielectric waveguides and waveguides with discrete translational symmetry. *Optics Letters, 25*(10), 755–757.

Yablonovitch E. (1987). Inhibited Spontaneous Emission in Solid-State Physics and Electronics. *Physical Review Letters, 58*(20), 2059–2062.

Yablonovitch E., and Gmitter T. J. (1989). Photonic band structure: The face-centered-cubic case. *Physical Review Letters, 63*(18), 1950-1953.

Yablonovitch E., Gmitter T. J., and Leung K. M. (1991). Photonic Band Structure: The Face-Centered-Cubic Case Employing Nonspherical Atoms. *Physical Review Letters, 67*(17), 2295–2298.

Yariv A., and Yeh P. (1984). *Optical Waves in Crystals*. New York: Wiley.

Yee K. S. (1966). Numerical solution of initial boundary value problems involving Maxwell's equations in isotropic media. *IEEE Transactions Antennas Propagation, AP-14*, 302–307.

Wang X.-H., Gu B.-Y., Li Z.-Y., and Yang G.-Z. (1999). Large absolute photonic band gaps created by rotating noncircular rods in two-dimensional lattices. *Physical Review B, 60*(16), 11417–11421.

edited by Weisbuch C., and Rarity J. (1996). *Microcavities and Photonic Band Gaps: Physics and Applications*, Vol. 324 of *NATO Advanced Studies Institute, Series E: Applied Sciences*. Dordrecht: Kluwer.

Whittaker D. M., and Culshaw I. S. (1999). Scattering-matrix treatment of patterned multilayer photonic structures. *Physical Review B, 60*(4), 2610–2618.

Wood R. W. (1902) *Philos. Mag., 4*, 396.

ACKNOWLEDGEMENTS

I would like to take this opportunity to express my thanks to those who helped me with various aspects of conducting research and the writing of this thesis. First and foremost, prof. Lucio C. Andreani and prof. Costas M. Soukoulis, for their guidance, patience and support throughout this research and the writing of this thesis.

I am grateful to Marta, Elena and my parents for their love and sharing.

I am pleased that I spent these years with very nice people, from both the Department of Physics "A. Volta" and the Department of Physics and Astronomy at Iowa State University. Besides their consulting and collaboration, I would better remind the impromptu snacks at the laboratory, under the expert guidance of prof. Guizzetti, with Cesare, Matteo, Dario, Maddalena, Davide, Daniele, Raffaella, Marco, Gabriele, and Eva, eating typical regional food and drinking good wine. We shall continue this way!

And I will never forget the months at Iowa State, the afternoons spent chatting with Marta, instead of working, the nice small house in Wisconsin Ave. with Janet and her weird guests (me included), specially Thomas, Victor Maximka and Peter. I would like to say thank also to Stavroula, who gave me the possibility to improve my patience (Voula, I'm kidding). Thanks also to Silvia, Joon, Ming, Giovanni, Joannis, Nikos, Daniele and the other guys for their great Greek hospitality (una faccia, una razza). Thanks to Rebecca, my favorite CMP secretary, for the kindness she had for me and, foremost, for reproaching my late morning arrivals at work. Thank you prof. Stassis, for your smiles and your "sermons". Thank you Angela and Costas, every time you invited me for dinner I felt like being at home.

Finally, I would like to thank all the people involved in the PCIC project. That was a chance to grow in experience and appreciate the importance of collaboration. Among them, I would like to expressly say my thanks to Rolando, Henri, Romuald, Ségolène, Anne, monsieur Weisbuch, and

David. Special thanks to Maria, who had to share the simulation burden with me.

I also would like to acknowledge those institutions and organizations that granted me financial support throughout these years and provided me with the appropriate equipment and resources for conducting this work: Department of Physics "A. Volta" and Università degli Studi di Pavia, Istituto Nazionale di Fisica della Materia (INFM), Department of Physics and Astronomy, Iowa State Univeristy, Ames Laboratory, and Foundation for Research and Technology Hellas (FORTH).
This research work was supported by the project MIUR-Cofin 2000 "One- and two-dimensional photonic crystals: growth, theory and optical properties," the project INFM-PAIS 2001 "Fabrication and Optical Characterization of two-dimensional photonic crystals," the European Union IST project PCIC "Photonic Crystal Integrated Circuits", and FORTH, at Heraklion, Crete.
This work was also in part supported and performed at Ames Laboratory under Contract No. W-7405-Eng-82 with the U.S. Department of Energy. The United States government has assigned the DOE Report number IS-T 2007 to this thesis.